Proceedings of the

3rd Joint Workshop on New Technologies for Computer/Robot Assisted Surgery

11-12-13 September 2013, Verona, Italy

this page was intentionally left blank

This workshop was made possible through the united efforts of following supporting EU funded projects on surgical robotics

3rd Joint Workshop on New Technologies for Computer/Robot Assisted Surgery

11-12-13 September 2013, Verona, Italy

September 11

8:45	9:00	registration
9:00	9:15	Word of Welcome by Prof. Franco Fummi, head of Computer Science Department, Univ. Verona
		Session 1 : segmentation and registration - D. Stoyanov - L. De Mattos
9:15	9:30	C. Barbalata and L.S. Mattos. Laryngeal Tumor Classification in Endoscopic Video
9:30	9:45	R. Melo, J. Barreto, G. Falcao. Camera calibration and real-time image distortion correction in medical endoscopy using exchangeable optics
9:45	10:00	M. Ourak, Br. Tamadazte, N. Andreff, C. Pieralli, O. Gaiffe and B. Wacogne. Towards registration of multimodal images of vocal folds based on mutual information
10:00	10:15	M. Allan, S. Ourselin, S. Thompson, D. Hawkes, J. Kelly and D. Stoyanov. Detection and Localization of Instruments in Minimally Invasive Surgery
10:15	10:30	A. Schoob, F. Podszus, D. Kundrat, L. A. Kahrs and T. Ortmaier. Stereoscopic Surface Reconstruction in Minimally Invasive Surgery using Efficient Non-Parametric Image Transforms
10:30	10:50	Coffee break
		Session 2: modelling - E. De Momi - S. Giannarou
10:50	11:05	M. Visentini-Scarzanella and D. Stoyanov. Stereo and Shape-from-Shading Cue Fusion for Dense 3D Reconstruction in Endoscopic Surgery
11:05	11:20	R. Mariën, M. Smoljkic, R. Geenens, M. Roeffaers, J. Vander Sloten, N. Famaey. Mechanical characterization of arterial tissue: Simultaneous confocal imaging and tensile testing
11:20	11:35	P. T. Tran, A. Devreker, G. Smoljkic, H. De Praetere, P. Herijgers, E. Vander Poorten and J. Vander Sloten. Patient-Specific Design of Multi-Component Steerable Catheters
11:35	11:50	C. Shi, S. Giannarou, S. Lee and G-Z Yang. Intravascular Modeling and Navigation for Transcatheter Aortic Valve Implantation
11:50	12:05	G. Smoljkic, C. Gruijthuijsen, E. Vander Poorten and J. Vander Sloten. Towards Intra-operative Use of Catheter Simulation
12:05	14:05	Lunch
		Session 3: active guidance & assistance - M. Capiluppi - B. Rosa
14:05	14:55	keynote Prof G-Z.Yang: Emerging Platforms for Surgical Robots
14:55	15:10	V. Strbac, J. Vander Sloten and N. Famaey. Towards Real-time FE for surgical applications
15:10	15:25	B. Rosa, J. Szewczyk and G. Morel. Precise navigation on soft tissues with an endomicroscopy probe
15:25	15:40	D. Dall'Alba, B. Maris and P. Fiorini. Needle Mounted Navigation System for Free Hand Percutaneous Procedures
15:40	15:55	A. Gijbels, E. Vander Poorten, P. Stalmans and D. Reynaerts. Application of a Robotic Comanipulation and Teleoperation System for Retinal Cannulations
15:55	16:10	D. De Lorenzo, S. Calò, A. Ciullo, M. D. Comparetti, M. Kunze, E. De Momi and G. Ferrigno. Redundancy management of a LWR4+ for safe, collision free, robotic surgical applications, using environmental sensors
16:10	16:30	Coffee break
		Session 4: Interfaces & Haptic Feedback - T. Haidegger - E. Vander Poorten
16:30	16:45	C. Belvedere, S. Tamarri and A. Leardini. Cutting Edge Technology in Computer Assisted Surgery for Total Knee Replacement. State-of-the-art of techniques and relevant results.
16:45	17:00	D.E. Barkana, D.G. Duru, A.D. Duru, A. Açık and M.Ozkan. Development and Evaluation of an Interface for Pre-Operative Planning of Cryoablation of a Kidney Tumor
17:00	17:15	G. Barresi, N. Deshpande, L. Mattos, L. Guastini, G. Peretti and D. Caldwell. Usability and Performance: Comparative Evaluation of Surgeon Interfaces in Laser Phonomicrosurgery
17:15	17:30	M. Li, M. Ridzuan, P. Dasgupta and K. Althoefer. Pseudo-Haptic Feedback for Tissue Stiffness Simulation
17:30	17:45	J. Konstantinova, M. Li, P. Dasgupta, K. Althoefer and T. Nanayakkara. Palpation Strategies for Artificial Soft Tissue Examination
17:45	18:00	S.P. Diez, E. Vander Poorten, B. Willaert and D. Reynaerts. Spatially distributed stiffness rendering system for handsfree palpation

3rd Joint Workshop on New Technologies for Computer/Robot Assisted Surgery

11-12-13 September 2013, Verona, Italy

September 12

8:45	9:00	Registration
9:00	9:05	Word of Welcome
		Session 5 - teleoperation and training - B. Herman - S. Speidel
9:05	9:20	F. Despinoy, J. Leon-Torres, M. Vitrani and B. Herman. Toward remote teleoperation with eye and hand: a first experimental study
9:20	9:35	S.Jordán, Á. Takács, I. Rudas and T. Haidegger. Modelling and Control Framework for Robotic Telesurgery
9:35	9:50	M. De Piccoli, F. Visentin, D. Zerbato and P. Fiorini. 3D vessel modeling for diagnosis and training
9:50	10:05	K. Baeck, P. Lopes, G. Biglino, C. Capelli and P. Verschueren. State of the art in 3D printing of compliant cardiovascular models: HeartPrint - Material characterization of HeartPrint models and comparison with arterial tissue properties
10:05	10:20	S. Suwelack, S. Röhl, S. Bodenstedt, D. Katic, H. Kenngot, B. Müller-Stich, A. Wekerle, M. Wagner, J. Wünscher, R. Dillmann and S. Speidel. Biomechanical simulations, soft tissue phantoms and open data - validating and benchmarking systems for computer assisted minimally invasive surgery
10:20	10:40	coffee break
		Session 6: novel robotic hardware (1) – M. Capiluppi - M. Sette
10:40	10:55	D. Zerbato, L. Vezzaro, L. Grespan, L. Gasperotti and P. Fiorini. Accurate and Low Cost Training System for Robotic Surgery
10:55	11:10	A. van Poelgeest, D. Kaltenbacher, T. Cuntz, C. Spindler, A. Sanagoo, J. Schaechtele and A. Rothfuss. Systems for handheld surgical robotics and man-machine OR teams
11:10	11:25	S. Tognarelli, P. Miloro, A. Verbeni, M. Mura, A. Cafarelli, G. Ciuti, P. Dario and A. Menciassi. Low invasive therapy under robotic guidance in the vascular district: a case study
11:25	11:40	M. Zenati. Medrobotics' FLEX Robotic System
11:40	11:55	A. Jiang, T. Nanayakkara, P. Dasgupta and K. Althoefer. Stiffness-controllable octopus-like robot arm for minimally invasive surgery
11:55	13:55	lunch
		Session 7: novel robotic hardware (2) - K. Althoefer - G. Ferrigno
13:55	14:00	intro
14:00	14:50	keynote speech : Anne Bajart 'EU-funded research programme in robotics: achievements and perspectives'
14:50	15:05	T. Ranzani, M. Cianchetti, G. Gerboni, I. De Falco, G. Petroni and A. Menciassi. A modular soft manipulator with variable stiffness
15:05	15:20	G. Lucarini, A. Tozzi, C. Bruni, A. Vallesi, E. Gaggini, G. Ciuti and A. Menciassi. Electromagnetic design for capsule endoscope navigation: a preliminary study
15:20	15:35	A. Sanchez, C. Liu, N. Zemiti, P. Poignet and E. Dombre. Control of meso-robots for endoluminal surgery
15:35	15:50	I.S.M. Khalil, V. Magdanz, S. Sanchez, O.G. Schmidt, L. Abelmann, and S.Misra. Magnetic Control of Potential Microrobotic Drug Delivery Systems
15:50	16:05	V. Meiser and D. Seatovic. System integration: A comparison of the SCATh and the CASCADE system architecture
16:05	16:25	coffee break
		Session 8: visionary works and systems - S. Misra – A. Menciassi
16:25	16:40	S. Weber, P. Brett, M. Caversaccio, D. Proops, B. Bell, X. Du, N. Gerber, T. Williamson, C. Coulson and A. Reid. Minimally invasive, robot assisted cochlear implantation
16:40	16:55	L.S. Mattos and N. Andreff. The µRALP Project: New Technologies and Systems for Robot-Assisted Laser Phonomicrosurgery
16:55	17:10	H. Wurdemann, E. Secco, T. Nanayakkara, K. Althoefer, K. Lis, L. Mucha, K. Rohr and Z. Nawrat. Mapping Tactile Information of a Soft Manipulator to a Haptic Sleeve in RMIS
17:10	18:00	round table

CONFERENCE DINNER AT GARDIA LAKE IN LA LOGGIA RAMBALDI – BUS DEPARTS AT 18.30 FROM ACCADEMIA.

3rd Joint Workshop on New Technologies for Computer/Robot Assisted Surgery

11-12-13 September 2013, Verona, Italy

September 13

8:45	9:00	Registration
9:00	9:05	Word of Welcome
		session 9: roadmapping - M. Zenati - E. Vander Poorten
9:05	9:20	J. Vander Sloten - Image-based Engineering in Surgery
9:20	9:35	M. Zenati and J. Maron. Communication and Teamwork Failure as a Barrier to Robotic Surgical Safety
9:35	9:50	B. Davies. The ACROBOT technology: a model for robotic surgery?
9:50	10:05	G. Ferrigno. ACTIVE: Active Constraints Technologies for Ill defined and Volatile Environments.
10:05	10:25	coffee break
		session 10: cogntive surgical robotics - Y. Kassahun - A. Van Poelgeest
10:25	10:40	J. Maron and M. Zenati. Framework for Managing Cognitive Load in a Data-Rich Robotic Operating Room
10:40	10:55	E. De Momi, R. Perrone, L. Schreiter, J. Raczkowsky, F. Boriero, M. Capiluppi and P. Fiorini. EuRoSurge Workflow: From ontology to surgical task execution
10:55	11:10	Y. Kassahun, B. Yu and E. Vander Poorten. Learning Catheter-Aorta Interaction Model Using Joint Probability Densities
11:10	11:25	L. Fichera, D. Pardo and L. Mattos. Artificial Cognitive Supervision during Robot-Assisted Laser Surgery
11:25	11:40	M. Bonfe, N. Preda, C. Secchi, F. Ferraguti, R. Muradore, L. Repele, G. Lorenzi, L. Gasperotti and P. Fiorini. Automated Surgical Task Execution: the Next Step in Robotic Surgery
11:40	13:40	lunch
		session 11: roadmapping & Multi-Annual Research agenda - P. Fiorini - J. Vander Sloten
13:40	14:30	keynote speech: Christophe Leroux 'Opportunities in the European Robotics Public Private Partnership (PPP) and the Topic Group on Healthcare robotics'
14:30	15:30	round table
15:30	15:50	coffee break
15:50	16:50	round table
16:50	16:55	closure of workshop

Program Chair

E. Vander Poorten, Marta Capiluppi, P. Fiorini

Organising Commitee

Kaspar Althoefer (KCL)	Stamatia Giannarou (ICL)	Sarthak Misra (Univ. of Twente)	E. Vander Poorten (KU Leuven)
Gianni Borghesan (KU Leuven)	Enrique Gomez (Univ. Madrid)	Philippe Poignet (LIRRM)	Marie-Aude Vitrani (ISIR, Paris)
Marta Capiluppi (Univ. Verona)	Tamas Haidegger (Obuda Univ)	Joerg Raczkowsky (KIT)	Jos Vander Sloten (KU Leuven)
Leonardo Mattos (IIT)	Yohannes Kassahun (UBremen)	Dominiek Reynaerts (KU Leuven)	Auguste van Poelgeest (IPA)
Elena De Momi (POLIMI)	Rainer Konietschke (DLR)	Mauro Sette (Medyria)	Guang-Zhong Yang (ICL)
Giancarlo Ferrigno (POLIMI)	Arianna Menciasi (SSSA, Pisa)	Jan Stallkamp (IPA)	Nabil Zemiti (LIRRM)
Paolo Fiorini (Univ. Verona)	Guillaume Morel (ISIR, Paris)	Danail Stoyanov (UCL)	
Roberto Foroni (Univ. Verona)	George Mylonas (ICL)	Stefano Stramigioli (Univ. of Twente)	

this page was intentionally left blank

Emerging Platforms for Surgical Robotics - Prof. G.Z.-Yang

Abstract

The Hamlyn Centre (http://www.imperial.ac.uk/robotics) directed by Prof Yang has been established for developing safe, effective and accessible imaging, sensing and robotics technologies that can reshape the future of healthcare for both developing and developed countries. Focusing on technological innovation but with a strong emphasis on clinical translation and direct patient benefit with a global impact, the centre is at the forefront of research in imaging, sensing and robotics for addressing global health challenges associated with demographic, environment, social and economic changes. The Centre plays an active role in international collaboration and outreach activities, as well as in the training of surgeons and engineers in robotic technologies, thereby facilitating a fully integrated clinical approach. It has extensive research, engineering laboratory spaces at the South Kensington campus of Imperial, large pre-clinical facilities at Northwick Park with state-of-the art imaging and surgical equipment for in vivo validation, and comprehensive clinical laboratories at the Surgical Innovation Centre at Imperial College St Mary's Hospital.

In addition to its core research activities, the Centre offers comprehensive PhD and MRes programmes for researchers with a strong technical or clinical background. These programmes are designed to develop cutting edge, disruptive technologies and blue-sky ideas; yet will be appropriate and accessible to both developing and developed countries for addressing different needs of the healthcare challenges with a common ground for technological innovations. Through its endowment fund and close working relationship with industry, government and non-government organisations, the Centre also offers Advanced Fellowships, International Fellowships, Faculty Exchange Programmes, and Research Secondment for specific research projects and technical areas.

Biography

Professor Guang-Zhong Yang (FREng, FIEEE, FIET, FAIMBE) is director and co-founder of the Hamlyn Centre for Robotic Surgery, Deputy Chairman of the Institute of Global Health Innovation, Imperial College London, UK. Professor Yang also holds a number of key academic positions at Imperial – he is Director and Founder of the Royal Society/Wolfson Medical Image Computing Laboratory, co-founder of the Wolfson Surgical Technology Laboratory, Chairman of the Centre for Pervasive Sensing. He is a Fellow of the Royal Academy of Engineering, fellow of IEEE, IET, AIMBE and a recipient of the Royal Society Research Merit Award and listed in The Times Eureka 'Top 100' in British Science.

Professor Yang's main research interests are in medical imaging, sensing and robotics. In imaging, he is credited for a number of novel MR phase contrast velocity imaging and computational modelling techniques that have transformed in vivo blood flow quantification and visualisation. These include the development of locally focused imaging combined with real-time navigator echoes for resolving respiratory motion for high-resolution coronary-angiography, as well as MR dynamic flow pressure mapping for which he received the ISMRM I. I Rabi Award. He pioneered the concept of perceptual docking for robotic control, which represents a paradigm shift of learning and knowledge acquisition of motor and perceptual/cognitive behaviour for robotics, as well as the field of Body Sensor Network (BSN) for providing personalized wireless monitoring platforms that are pervasive, intelligent, and context-aware.

EU-funded Research Programme in Robotics – Achievements and Perspectives –

Dr. A. Bajart

Abstract

The EU has been funding research in cognitive systems and robotics for more than 10 years, with the goal to make robots and cognitive systems more intuitive, robust, autonomous and acting in a real-world environments. This talk will present the main achievements of the programme and give some perspective on the current situation of robotics research in Europe, as well as future opportunities and challenges in particular in the context of H2020.

Biography

Anne Bajart has a PhD in Electronical Engineering. She is Research Programme Officer at the European Commission. Before working for the EC, she worked as lecturer, researcher and project manager at the University of Liège (BE), at the Ecole Polytechnique de Lausanne (CH) and at Philips Leuven (BE). She has expertise a.o. in systems control, digital signal processing, power electronics and speech recognition. Her main areas of interest today are robots, Human-Robot and Human-Computer Interaction, benchmarking and performance evaluation of systems, intelligent control of complex systems, dissemination of science, impact assessment and social acceptance of technology.

Opportunities in the European Robotics Public Private Partnership (PPP) and the Topic Group on Healthcare Robotics

Abstract

The of the presentation is to explain the interest the Topic Group on Healthcare Robotics being elaborated at the moment. The expose, will present the context of creation of this topic group, its connection with the euRobotics aisbl and the Robotics PPP. We will present and debate of the objectives, and of the organization foreseen. The presentation will be an introduction to an open discussion in a round table which will be an opportunity to organize the community.

Biography

Dr. Christophe LEROUX (PhD) is research correspondant for applications ICT and Health at CEA LIST. He obtained a PhD in 1990, in artificial intelligence. He has expertise in research in algorithms for robotics (supervision, computer vision and intuitive MMI) for hazardous environment and assistive robotics. Since 2003 he works at combining cognitive engineering and embedded cognition to provide automatic and intuitive mobile manipulation functions to assist severely handicapped people. He conducted several robotics experiments with quadriplegic and elderly people, caregivers, physicians in institutions. Member of the of EUROP ETP board and then of euRobotics AISBL Board of Directors up to 2013, he is involved in the elaboration of the robotics PPP since its beginning. He is member of the scientific board of IFR. In France he is member of the scientific committee of the APPROCHE association and of CENROB (robotics for handicapped people). He was involved in the FET Flagship Robocom responsible for the Technology Transfer mechanisms and links with the industry. He is also involved since 2010 in the study of ELS issues in robotics and participated to the elaboration of the green paper on legal issues in robotics in the euRobotics CA. He organizes now the Topic Group on Healthcare Robotics for the euRobotics aisbl and the robotics PPP.

this page was intentionally left blank

Laryngeal Tumor Classification in Endoscopic Video

Corina Barbalata[1] and Leonardo S. Mattos[2]
[1]VIBOT Erasmus Mundus: Univ. Burgundy, Univ. Girona, Heriot-Watt Univ.
[2]Department of Advanced Robotics, Istituto Italiano di Tecnologia, Genova, Italy
Email: corina.barbalata@gmail.com, leonardo.mattos@iit.it

I. INTRODUCTION

Laryngeal carcinoma is one of the most common type of head and neck cancers. Early diagnosis of any carcinoma is the most important factor involved in treatment planning and improves the quality of life of the patient. Moreover, abnormalities that start as benign lesions may develop to malignant tumors in 10% of the cases [6]. The standard diagnosis method is biopsy together with pathological analysis, but this does not represent a risk free procedure. Furthermore, the time needed to obtain the results of the pathological analysis vary from a few days to a few weeks.

Recently, the analysis of endoscopic videos has shown the development of abnormality in the larynx is closely related to an increase in the number of the micro-blood vessels around it. This is an interesting information that can lead to the development of optical biopsy systems. Progress in that direction has started with the development of imaging systems that enhance the visualization of blood vessel, such as the Narrow-Band Imaging (NBI) system patented by Olympus. NBI is based on differences in the penetration depth of different light wavelengths in tissue. Blue light, centred around 415 nm, passes through the mucosa and enhances the superficial blood vessels, while the narrow-band green light, centred around 540 nm, penetrates deeper into the tissue, enhancing the subephitelial vessels. The NBI technology is being increasingly used to locate and characterize lesions in the larynx. However, until present time physicians still do not have access to a statistical measurement system able differentiate between malignant and benign tumors.

The goal of this research is to develop an automatic system to help medical specialists diagnose lesions in the larynx. Similarly to the approach followed by doctors, our method is based on determining the approximate location of the lesion and performing a detailed analysis of the micro-blood vessels network within that region. This finally leads to the classification of the lesion as benign or malignant.

II. MATERIALS AND METHODS

In order to create a computer-aided-diagnosis system, an important step is to remove the specular reflections. In endoscopic imaging, due to the high-illumination, wet and very smooth environment, specular reflections are very common and can be disturbing for the physician. Furthermore, in the task of automatic segmentation and classification of lesions, reflections can cause difficulties. Therefore, removal of specular reflections is the first required step for further image processing.

Specular reflection removal algorithms can be divided according to the number of images used. The first group is based on multiple images, obtained in different conditions (different polarization angles, changing light source direction, etc.). Using any of the techniques in this group is challenging due to the fact that it may not be always possible to meet the required conditions in practice [9]. The second category removes the reflections based on one single image, the method used in this research belonging to this group.

In endoscopic images, specular reflections appear as bright regions in various parts of the image. The size of specular regions do not respect any pattern or size, making the segmentation task very challenging. Large specular regions can also overlap possible malignant tissue. Consequently, we have decided to compute the area of each detected specular region and if it is too large, the area is considered an abnormality and is not removed.

Based on the previous researches [1], [7], [8], in this project an efficient algorithm for reduction of specular reflections using a single image as input has been implemented. The first step is to determine the specular reflection regions based on adaptive thresholding in the HSV color space. The dimension of detected ROI is computed and additional pixels are added to specularities. The last step is to fill the remained ROI by propagation of information from the surrounding non-specular areas.

As stated in [5] the specular reflection have intense brightness and low saturation values, information that can be used in finding the region of interest. Consequently, the HSV color space offers advantages when specular reflections have to be removed. In this case, a region of interest can be defined applying thresholds on the saturation and value channels of the image. An adaptive threshold scheme [5] is used here to obtain accurate results. Based on experiments performed with endoscopic videos of the larynx, thresholds were cho-

sen as stated in Equation 1 and Equation 2.

$$V = 0.7 \cdot V_{max} \tag{1}$$

$$S = 0.35 \cdot S_{max} \tag{2}$$

In our algorithm, the results obtained with this thresholding scheme are improve based on image gradient information. Reflection regions are small bright spots, so they can be interpreted as high gradient regions in their neighborhood. An experimental threshold was chosen to segment the specular reflection based on the magnitude of the gradient of the gray images. In our case this value was set to 130.

After the regions of reflection were detected, the next step is to reconstruct the affected area. A filling scheme was used for that task considering texture preservation as a key feature to minimize disruption on the results of subsequent image processing. In this research, since specular reflections were assumed to be small, the color behind each reflection was considered constant and similar to the neighboring pixels. The result of this approach presents smooth regions substituting small reflection areas, as can be seen in Figure 1.

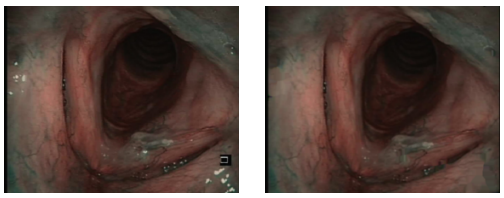

(a) Original image (b) Reconstruction

Fig. 1: Specular reflection removal and reconstruction.

Moreover, another important problem is solved with the help of this algorithm: removal of additional information provided by the endoscope equipment. After applying the algorithm proposed previously, both text and specular reflections are removed, due to the similar characteristic, being characterized as bright white areas. Results are presented in the figure 2, where the residual information and the specular reflections are removed, but the lesion is maintained, although it is characterized by a white bright region. As mentioned previous our algorithm is able to differentiate this lesions from specular reflections due to their large areas.

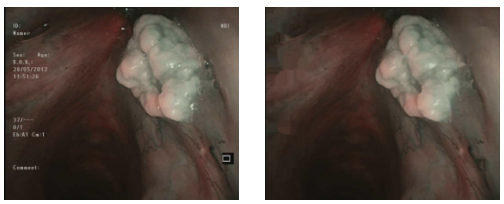

(a) Original image (b) Reconstruction

Fig. 2: Residual information removal and reconstruction.

After the specular reflections have been eliminated, the design of an automatic system for lesion classification was realized. Analyzing the characteristics of the micro-vascular patterns, abnormality growths can be identified and classified from an early stage. In order to obtain the classification, there is the need of detecting the region of interest and extracting the blood vessels, which represents the main focus of this research.

The presence of abnormality such as tumors, polyps, polypoid lesions results in appearance of rough surface in endoscopic image [4]. Detecting the region of interest is not a straightforward task, the main challenge represents the irregular shape of the tumour or in some cases the non-existence of a tumour. In the case of healthy vocal cords it is a very difficult task to determine which region should be closely analyzed. On the other hand, when abnormalities are present, the extraction of region of interest may assist the physician by suggesting an approximate location of the tumor. The region of interest is detected in most of the cases based on the outer boundaries that describe the lesions. Results from this processing step can be seen in Figure 3. Limitations are encountered when no clear boundaries are present and the characteristics of the abnormality are similar with the surrounding tissue, further research being needed to solve this challenging situations.

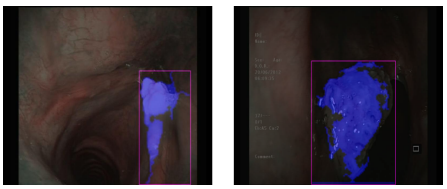

Fig. 3: Region of interest detection.

The next step of the processing algorithm consists in extracting image features from the marked region of interest. Blood vessels vary in shape, length and diameter, so the design of this stage is also challenging. The most important operation performed in this case is edge detection. In this research a number algorithms were merged together in order to detect and segment both very small and large blood vessels. From the problems encountered, the hardest was distinguishing between small vessels and noise. Both present many similarities, tending to produce false positives. Nevertheless, our final algorithm is able distinguish between the two situations, as can be seen in Figure 4. Its final implementation uses Matched Filter based on the First-Order Derivative of Gaussian (MFFODG), as presented in [10]. Moreover, the output of the filter is subsequently thresholded and validated using a Gabor filter and the morphological Black-Top-Hat operation. This combination of algorithms proved to be effective in generating blood vessels maps of the appropriate quality for further processing.

Once segmented, the blood vessels map is used to

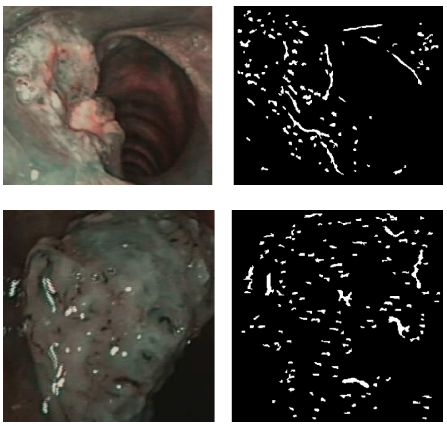

Fig. 4: Micro-blood vessel segmentation.

classify the observed lesion. This is done by quantitative measurements of the blood vessels characteristics, including width and tortuosity, which have been shown correlated to lesion development, i.e., the presence of dilated or highly tortuous blood vessels are signs of lesion development. Here, these measurements are used to classify lesions based on confidence levels, which are computed according to the method proposed in [2]. If the confidence level is over 0.5, the lesions can be considered as malignant. Otherwise, the lesion is considered benign.

III. RESULTS

A collection of narrow-band endoscopic videos of the larynx was provided by the San Martino Hospital of Genoa, including videos acquired from different patients with a wide range of tumors. These videos were used to create a database of 50 images of lesions of vocal cords with both benign and malignant tumors, which were extracted randomly without following any criteria for selecting good frames. Consequently, the dataset contained images far from ideal for processing, some showing only small and distant lesions, some others not perfectly in focus, and others presenting relatively low contrast and motion artefacts. The videos were acquired using rigid endoscopes, the Olympus OTV-S7ProH-HD-10E camera, and the Olympus Visera Elite CLV-S190 video system.

Based on the described database, each part of the developed tumor segmentation and classification system was evaluated. The tumor localization system demonstrated an overall success rate of 78%, and the feature extraction system achieved 87% specificity and 78% accuracy. Finally, the overall accuracy of the tumor classification system was 84.3%.

IV. CONCLUSION

This research proposes a new system for the localization, segmentation and classification of lesions in the larynx based on endoscopic narrow-band imaging video. The developed algorithm starts by detecting the approximate location of the lesion in the vocal cords, which is followed by the segmentation of the blood vessels present in that region. The algorithm continues with the measurement of geometric features of the blood vessels map, based on which an statistical analysis provides the probability of malignancy. To our best knowledge, this is the first system developed for the segmentation and analysis of the blood vessels in the vocal cords.

Considering the experimental results, we can conclude the proposed method is capable of recognizing malignant tumors in the vocal cords with high accuracy. Nevertheless further research is still needed, specially to improve the sensitivity of the blood vessel extraction algorithm. Further development is also needed to create a system useful for medical specialists. Nonetheless, the system developed consists in a promising novel method for cancer detection and classification, representing an innovation in the medical imaging field.

V. ACKNOWLEDGMENT

The research leading to these results has received funding from the European Union Seventh Framework Programme FP7/2007-2013 - Challenge 2 - Cognitive Systems, Interaction, Robotics - under grant agreement uRALP - n288233.

REFERENCES

[1] J. Beach. Spectral reflectance technique for retinal blood oxygen evaluation in humans. In *Applied Imagery Pattern Recognition Workshop, 2002. Proceedings. 31st*, pages 117–123, 2002.

[2] E. Bullitt, S. R. Aylward, T. Van Dyke, and W. Lin. Computer-assisted measurement of vessel shape from 3T magnetic resonance angiography of mouse brain. *Methods (San Diego, Calif.)*, 43(1):29–34, September 2007.

[3] G. Dagnino, L.S. Mattos, and D.G. Caldwell. New software tools for enhanced precision in robot-assisted laser phonomicrosurgery. In *Engineering in Medicine and Biology Society (EMBC), 2012 Annual International Conference of the IEEE*, pages 2804–2807, 2012.

[4] B. V. Dhandra, R. Hegadi, M. Hangarge, and V. S. Malemath. Analysis of abnormality in endoscopic images using combined hsi color space and watershed segmentation. In *Pattern Recognition, 2006. ICPR 2006. 18th International Conference on*, volume 4, pages 695–698, 2006.

[5] Thomas M. Lehmann and Christoph Palm. Color line search for illuminant estimation in real-world scenes. *J. Opt. Soc. Am. A*, 18(11):2679–2691, Nov 2001.

[6] C Piazza, O Dessouky, G Peretti, D Cocco, L De Benedetto, and P Nicolai. Narrow-band imaging: a new tool for evaluation of head and neck squamous cell carcinomas. review of the literature. *Acta Otorhinolaryngol Ital*, 2008.

[7] Thomas H. Stehle. Specular Reflection Removal in Endoscopic Images. 2006.

[8] T. Taxt. Separation of the diffuse, specular and quasiperiodic signal components in medical ultrasound images. In *Ultrasonics Symposium, 1994. Proceedings., 1994 IEEE*, volume 3, pages 1639–1644 vol.3, 1994.

[9] Qingxiong Yang, Shengnan Wang, and Narendra Ahuja. Real-time specular highlight removal using bilateral filtering. In *Proceedings of the 11th European conference on Computer vision: Part IV*, ECCV'10, pages 87–100, Berlin, Heidelberg, 2010. Springer-Verlag.

[10] Bob Zhang, Lin Zhang, Lei Zhang, and Fakhri Karray. Retinal vessel extraction by matched filter with first-order derivative of gaussian. *Comput. Biol. Med.*, 40(4):438–445, April 2010.

Camera Calibration and Real-time Image Distortion Correction in Medical Endoscopy Using Exchangeable Optics

Rui Melo
Inst. for Systems and Robotics
University of Coimbra, Portugal
Email: rmelo@isr.uc.pt

João Barreto
Inst. for Systems and Robotics
University of Coimbra, Portugal
Email: jpbar@isr.uc.pt

Gabriel Falcão
Instituto de Telecomunicações
University of Coimbra, Portugal
Email: gff@deec.uc.pt

***Abstract*—Minimally invasive surgery (MIS) is highly beneficial for the patient but it is very difficult to execute by the doctor that have to undergo a long training till acquiring the required skills and hand-eye coordination. Computer-aided surgery (CAS) can play a major role in MIS by enabling more surgeons to practice the technique while decreasing errors of clinical consequence. Such systems will use as input the intra-operative endoscopic video stream, which means that the camera must be calibrated at all times in order to take full advantage of the received data. We argue that, although camera calibration is a mature topic, the problem is far from being solved in the context of surgical applications. We propose a solution that we believe will be important to transfer the existing research in image based CAS from the Labs to the Operating Rooms. In addition we present a system for distortion correction in endoscopic images that handles the high resolution/framerates of current equipment. The correction requires the accurate calibration of the optical system which is handled by our automatic calibration technique from a single image and our adaptive projection model to cope with the lens rotation during operation. Our first clinical trial showed significant improvements in the execution of surgical tasks in knee arthroscopy.**

I. Background

In minimally invasive surgery (MIS) the doctor executes the procedure guided by the images acquired by an endoscopic camera. Typically the endoscopic camera consists in autoclavable exchangeable optics that are mounted on a charge-coupled device (CCD) camera head just before the procedure starts. These optics can be forward-viewing, when they look up-front, or oblique-viewing if the tubular lens has a cut of 30°, 70° or 90° to enable a periscope-like view. The viewing direction of the oblique-viewing lenses can be changed without moving the camera head by simply rotating the endoscope around its symmetry axis [1]–[3]. This rotation is typically inferred by observing the position of a triangular mark on the periphery of the circular region. Oblique-viewing endoscopes are specially useful in inspecting narrow cavities, such as the articulations (arthroscopy) or the sinus (rhinoscopy), where the space to maneuver the probe is very limited.

Although being highly beneficial for the patient in terms of recovery time and risk of infection, the stats show that MIS is used only in 25% of the procedures eligible for this technique. The reason for this low penetration is the fact that MIS procedures are much more difficult to execute than the equivalent open surgery counterparts. The access to the organs is very limited and surgeons must use intra-operative video as only guidance. This poses severe problems in terms of hand-eye coordination and some surgeons are simply unable to make the visual-spatial leap needed to master this technique [4].

In this context, the use of systems for computer aided surgery (CAS) can make a significant difference in the adoption and clinical outcomes of MIS. We envision that such systems will receive as input the intra-operative endoscopic video, eventually register the image data with pre-operative models of targeted organs, and use the information for assisting the doctor during the procedures. Such assistance can take multiple forms, ranging from providing a better visualization of the observed cavities to granting that the surgery is executed according to a pre-plan, and passing by helping the doctor to navigate inside the human-body.

II. Endoscopic camera calibration and real-time correction of radial distortion

Image-based CAS requires the endoscopic camera to be properly calibrated. The camera intrinsic calibration enables to map each image pixel into a light-ray direction, being a necessary condition for inferring 3D information from the video stream. Most of the actual works in image-based CAS focus in higher-level problems, such as segmentation, reconstruction and registration, and disregard the camera calibration which is assumed to be known.

Although camera calibration is a well studied topic [5], the problem of calibrating an endoscopic camera with exchangeable lenses and keeping the parametrization accurate during the entire procedure is far from being trivial. The reasons are threefold: (i) the calibration must be carried in the OR because the lenses are exchangeable, (ii) since the calibration must be carried by a medical non-expert user the procedure must be fast and robust, meaning that standard lab procedures that require acquiring tenth of images of a grid and clicking points are not suitable, and (iii) in the case of oblique-viewing endoscopes the lens rotate with respect to the camera head changing the camera parameters during operation.

We present a method for endoscopic camera calibration that overcomes the above mentioned difficulties of usability and constant updating during the procedure. It is important to refer that providing an effective solution for the camera calibration problem in the context of surgery is fundamental

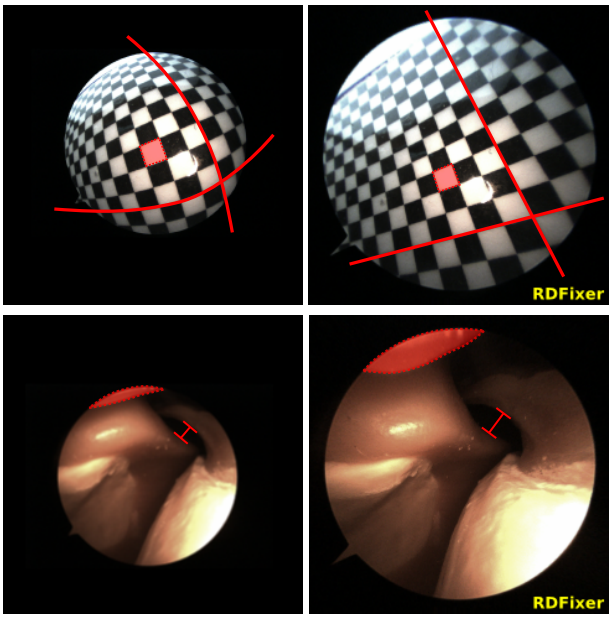

Figure 1. RDFixer distortion correction in a chessboard pattern and a knee model. Left - Original image. Right - Corrected image using RDFixer. It can be noticed, in red, the differences when the distortion is corrected.

for image-based CAS to become a reality in the future. Our solution aims at enabling this key step to be performed in the OR, a subject that has been overlooked up until now.

As a first application for the calibration, we present a system for the improvement of the visualization during endoscopy through the correction of image distortion in real-time. In many situations endoscopic video suffers from severe radial distortion (RD), an optical aberration due to limitations in optical construction technology. Optics cannot eliminate this pernicious effect when the lens are small and have a wide field of view (FOV). The problem is that RD severely hinders depth perception. We therefore propose a software-based system that combines calibration information with an hybrid GPU+CPU architecture for removing the distortion in real-time.

III. System overview

The system used for distortion correction, dubbed RDFixer, consists in an add-on device that is installed in between the camera control unit and the display, that captures the endoscopic video, updates the projection model according to the lens rotation and corrects the RD in real time. The procedure starts with the acquisition of one calibration image, similar to the one presented in the top row of Fig. 1. The calibration processes is completely automatic and after a few seconds the systems is ready for distortion correction. The bottom row of Fig. 1 shows the distortion correction result in the knee model, with some of the differences in the anatomical structures outlined in red.

The camera calibration is conducted using the single image calibration (SIC) algorithm proposed in [6]. Let $\mathbf{X}$ be the vector of homogeneous coordinates of a 3D point represented in a world reference frame. Point $\mathbf{X}$ is projected into point $\mathbf{x}$ in the endoscopic image such that

$$\mathbf{x} \sim \mathsf{K}_0 \, \mathbf{\Gamma}_\xi(\mathsf{P}\,\mathbf{X}) \,. \tag{1}$$

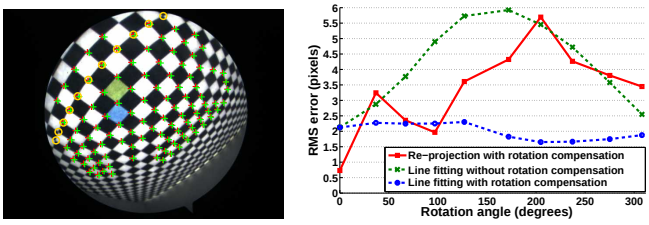

(a) Test image (1280 × 960) (b) Root Mean Square (RMS) Errors

Figure 2. Experimental validation of the model for updating the camera calibration. The red curve in the graphic of (b) shows the RMS value of the re-projection error for different angular displacements α of the lens probe. The two other curves refer to the error of fitting a line to a set of collinear points (the yellow circles in (a)) after correcting the image distortion and without taking into account the lens rotation.

P denotes the standard 3×4 projection matrix [7], $\mathbf{\Gamma}_\xi$ is a nonlinear projective function that accounts for the image radial distortion, and K_0 is the matrix of intrinsic parameters with the following structure

$$\mathsf{K}_0 \sim \begin{pmatrix} a\,f & s\,f & c_x \\ 0 & a^{-1}\,f & c_y \\ 0 & 0 & 1 \end{pmatrix} \tag{2}$$

where f, a, and s, stand respectively for the focal length, aspect ratio, and skew, and $\mathbf{c} = (c_x, c_y)^\intercal$ are the non-homogeneous coordinates of the image principal point. The calibration consists in determining this projection model parameters and this is accomplished using a single image of a checkerboard pattern.

Since the endoscopic lens may rotate relatively to the camera head, assuming unitary aspect ration and zero skew, we decompose the intrinsics matrix into:

$$\mathsf{K}_0 \sim \begin{pmatrix} f & 0 & c_x \\ 0 & f & c_y \\ 0 & 0 & 1 \end{pmatrix} , \tag{3}$$

then it can be factorized as

$$\mathsf{K}_0 \sim \mathsf{K_h}\,\mathsf{K_c} \sim \begin{pmatrix} f_h & 0 & c_x \\ 0 & f_h & c_y \\ 0 & 0 & 1 \end{pmatrix} \begin{pmatrix} f_c & 0 & 0 \\ 0 & f_c & 0 \\ 0 & 0 & 1 \end{pmatrix} , \tag{4}$$

with f_c being the focal length of the endoscopic lens, and f_h being the focal length of the camera head that converts metric units into pixels.

The intrinsic matrix of the compound optical system formed by the camera head and the rotated endoscope becomes

$$\mathsf{K} \sim \mathsf{K}_h \, \mathsf{R}_{\alpha,\mathbf{q}'} \, \mathsf{K}_c \,, \tag{5}$$

with $\mathsf{R}_{\alpha,\mathbf{q}'}$ being a plane rotation by α and around the point $\mathbf{q}'$, where the optical axis intersects the image plane.

During operation, this rotation is tracked in the endoscopic image by searching for the triangular mark as it moves and the projection model is updated accordingly. Fig. 2(a) shows the change in the re-projection error while rotating the lens as well as the result of fitting a line to a set of points after distortion correction using the adaptive projection model presented [8].

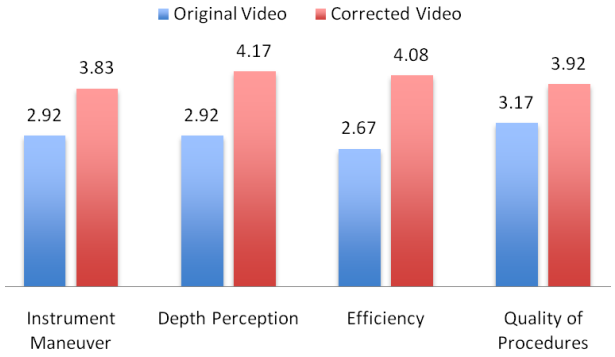

Figure 3. Performance evaluation by the supervisor using the Global Rating Score [10]. The performance is evaluated in a scale from 1 to 5, with 5 representing the greatest performance for each indicator. The values are the mean score for all subjects in each visualization.

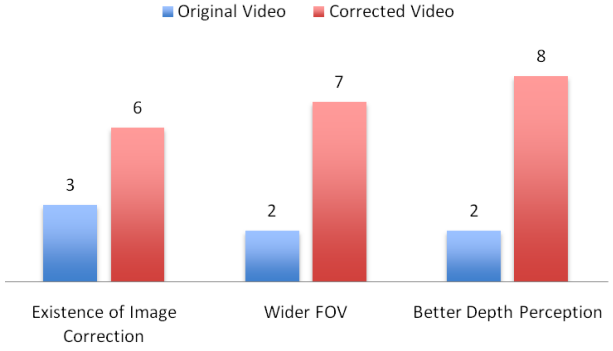

Figure 4. Subject survey results. The count above each column represents the number of "Yes" answers among all subjects when prompted about the subjective impressions depicted.

Given the initial calibration, we track the triangular mark, update the projection model and correct the distortion using the approach proposed in [9]. The heterogeneous system presented in [9] uses both CPU and GPU to process the 1080p@60Hz video stream in real tme. This requires efficient memory access patterns on the GPU to cope with such high data throughput without delaying the stream.

IV. First clinical trial in the impact of RD correction in surgical performance

We evaluated the performance impact of correcting the RD in a common surgical procedure - the loose bodies removal during the arthroscopy of the knee. Loose bodies are another name for free floating pieces of debris in the knee joint. They are tissues that have torn away from their original location and move around the joint causing pain, swelling, and locking. The procedure consists in removing the loose bodies using a 3.4mm soft tissue grasper, which requires a considerable skill in hand-eye manipulation.

The trial involved a group of 12 training interns, which were supervised by an experienced orthopaedic surgeon, and aimed to validate the improvements in visualization and depth perception. Each subject was individually called to a separate room and asked to remove the same free body using the original and corrected visualization. The visualization mode sequencing was properly balanced across subjects to maintain the statistical reliability of the results. The procedure was conducted without the trainee knowing the purpose of the test, or the type of visualization used for each trial. After each successful removal the supervisor scored the clinical performance of the subject according to an adaptation of the Global Rating Scale presented in [10], and the trainee also filled a subjective questionnaire about the visualization experience. Figures 3 and 4 show the results of the trial, where an improvement of over 30% can be observed in the procedure quality (Fig. 3).

The results of this trial supported our assumption that removing the RD provides a better visualization experience that is clearly noticed by the clinician, and that influences the surgical performance.

V. Conclusions

This paper describes an effective solution for camera calibration in the OR, which is crucial to enable future image-guided CAS applications. We use the calibration in a first CAS application where the camera model is used to correct the lens distortion via software. Our first trial shows that this visualization application has a significant impact in the surgical outcome.

Acknowledgments

The authors gratefully acknowledge the Portuguese Science Foundation (FCT) that generously funded this work through project PTDC/EIA-CCO/109120/2008.

References

[1] T. Yamaguchi *et al.*, "Camera Model and Calibration Procedure for Oblique-Viewing Endoscope," in *MICCAI*, 2003, pp. 373–381.

[2] C. Wu, B. Jaramaz, and S. G. Narasimhan, "A Full Geometric and Photometric Calibration Method for Oblique-viewing Endoscope," *Int Journal of Computer Aided Surgery*, vol. 15, pp. 19–31, 2010.

[3] N. Fukuda, Y. Chen, M. Nakamoto, and T, "A scope cylinder rotation tracking method for oblique-viewing endoscopes without attached sensing device," *Software Eng and Data Mining*, pp. 684–687, 2010.

[4] (2012, Jan) Surgeons don 3D glasses, get 'remarkable' depth perception for keyhole surgery. http://www.huffingtonpost.ca/2012/01/24/surgeons-don-3d-glasses-_n_1229173.html.

[5] J.-Y. Bouguet. Camera Calibration Toolbox for Matlab. [Online]. Available: http://www.vision.caltech.edu/bouguetj/calib_doc/index.html#ref

[6] J. Barreto, J. Roquette, P. Sturm, and F. Fonseca, "Automatic Camera Calibration Applied to Medical Endoscopy," in *BMVC*, 2009.

[7] R. I. Hartley and A. Zisserman, *Multiple View Geometry in Computer Vision*, 2nd ed. Cambridge University Press, ISBN: 0521540518, 2004.

[8] R. Melo, J. P. Barreto, and G. Falcao, "A new solution for camera calibration and real-time image distortion correction in medical endoscopy - initial technical evaluation," *Biomedical Engineering, IEEE Transactions on*, vol. 59, no. 3, pp. 634 –644, march 2012.

[9] R. Melo, G. Falcao, and J. P. Barreto, "Real-time HD image distortion correction in heterogeneous parallel computing systems using efficient memory access patterns," *Journal of Real-Time Image Processing*, december 2012.

[10] A. Insel, B. Carofino, R. Leger, R. Arciero, and A. Mazzocca, "The development of an objective model to assess arthroscopic performance," *J Bone Joint Surg Am*, vol. 91, pp. 2287–95, 2009.

Towards registration of multimodal images of vocal folds based on mutual information

M. Ourak*[1], B. Tamadazte[1], N. Andreff[1], C. Pieralli[1], O. Gaiffe[2] and B. Wacogne[2]

[1]FEMTO-ST institute-UFC/CNRS/ENSMM/UTBM. 24, rue Alain Savary, 25000 Besançon, France.
[2]University Hospital Besançon (CHU). 3, boulevard Alexandre Fleming, 25000 Besançon, France.
(*)Corresponding author : mouloud.ourak@femto-st.fr

***Abstract*— This paper deals with mutual information-based registration of multimodal images for laser phonomicrosurgery of the vocal folds. The images to be registered are white light images (white light camera) versus fluorescence images. This work is carried out within the framework of the European project μRALP which involves the use of microrobotic system for endoluminal laser phonosurgery. The designed system includes two fiber bundles connected to a high speed camera and one fiber bundle used for fluorescence image. Using the mutual information based registration method, it will be possible to represent the visible information in the fluorescence image and use it in the other image.**

I. INTRODUCTION

A phonosurgery system uses a stereo-microscope and a semi-automatic system to control the laser source positioned at 400 mm outside the patient (see Fig. 1). This technique relies completely on the skills of surgeons who must operate through a microscope, control the laser directly by hand, and deals with the associated poor ergonomics of the operating setup [1], [2]. The μRALP project will enable to overcome such limitations by developing a more intuitive system (inserted through the mouth into the laryngo-pharyngeal cavity) that allows to position the laser close to the vocal chords (*ie.* 20 mm). Mainly, the proposed system includes a piezoelectric actuated mirror (two degrees of freedom), two fiber bundles for high frequency imaging, one fiber bundle for fluorescence image, and a Helium-Neon (HeNe) laser (see Fig. 2).

The developed system will work as follows: the surgeon defines a trajectory around the tumor to incise, in the fluorescence image. Thereby, the objective of μRALP system is to control automatically the displacement of the laser beam along the pre-defined trajectory. In order to ensure a better accuracy during automatic resection, it is required to close the control loop over an exteroceptive sensor (high speed camera in our case). Namely, this so-called visual servoing (vision-based robot control) is robust to robot calibration errors and to robot environment variations [3].

In general, visual servoing requires defining a reference features (points, lines, image, 3D pose, etc.) that allows the system to evolve from its current position to its target position. In our case, the reference can be defined (by the surgeon) in the fluorescence image frame R_f and the system will move in the high speed white light image frame R_s. Thus, it is necessary to compute the transformation $(\widehat{T}, \widehat{\rho})$ between both frames (*ie.* R_f and R_s). The mutual information-based method seems very appropriate for the computation of this transformation, especially when the images are of different modalities.

In the literature, the mutual information-based registration has been widely discussed. Zitova et *al.* [4] has classified the registration techniques for medical applications into two main categories: area-based and feature-based methods. Generally, a registration technique follows mainly these four steps: features detection, features matching, transformation estimation, and image resampling.

This paper focuses in the adaptation of the mutual information technique in the case of fluorescence images *vs.* high speed white light images. Thereby, it contains some basic definitions about the mutual information, the context of use,

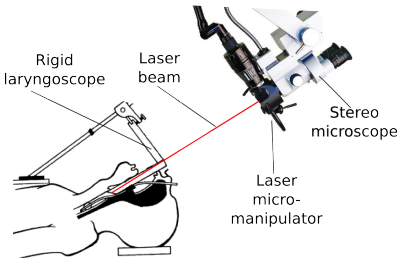

Fig. 1. Current laser phonosurgery setup.

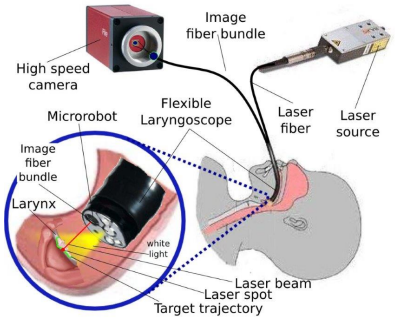

Fig. 2. New laser phonosurgery system proposed by the μRALP project.

some primary results and the future investigations of this work.

II. Mutual Information

The mutual information is inspired by the information theory domain. It is based on the measure of information, commonly called entropy, in a message. In the case of image processing, this allows to measure the similarity between two images I_1 and I_2.

A. Entropy

In information theory domain, the entropy was first introduced by Hartley [5]. There, he used it to measure the uncertainty of a signal s between a transmitter and a receiver. The first Hartley entropy function, is given by:

$$H_0(X) = log_b |X| \tag{1}$$

where X is a vector containing random values x_i.

Move over, the mean information quantity associated to each source value is the expectation of the own information of each event $X = x_i$. According to Shannon, adding a weight to the output of the Hartley entropy allows to rewrite the equation (1) as:

$$H = \sum_i p_i log_2(\frac{1}{p_i}) = -\sum_i p_i log_2(p_i) \tag{2}$$

where p_i is the associated probability of each event x_i.

Applied to the images, the measure of the entropy allows us to compute the degree of similarity information between two images (higher is the similarity between images, lower is the entropy).

B. Joint histogram

To estimate the joint probability distribution of the gray values between two images, it is possible to use the notion of joint histogram. This joint histogram is a 3D map ($\mathbb{N}^2$ in $\mathbb{N}$), whose 2D inputs are the grayscale value of each pixel of $I_1(i,j)$ and of the corresponding pixel in $I_2(i,j)$ and the output is the amount of such couple $(I_1(i,j), I_2(i,j))$ (see Fig. 3 and algorithm 1).

Thereby, the joint histogram allows illustrating the similarity between two images. In practice, lower the similarity between images, more the joint histogram is uniform (its graph is a plane). Conversely, if two images are perfectly similar, the joint histogram is represented by a diagonal line.

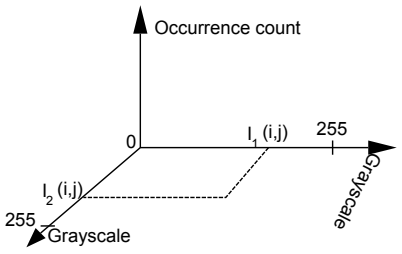

Fig. 3. Representation of the joint histogram.

Algorithm 1 Joint histogram algorithm

Require: I_1, I_2 two images
1: $init : binSize \leftarrow 255$;
2: $init : h(binSize, binSize)$;
3: $u \leftarrow height(I_1)$;
4: $v \leftarrow width(I_1)$;
5: **for** i from 0 to u **do**
6: **for** j from 0 to v **do**
7: $h(I_1(i,j), I_2(i,j)) = h(I_1(i,j), I_2(i,j)) + 1$;
8: **end for**
9: **end for**
10: **return** h

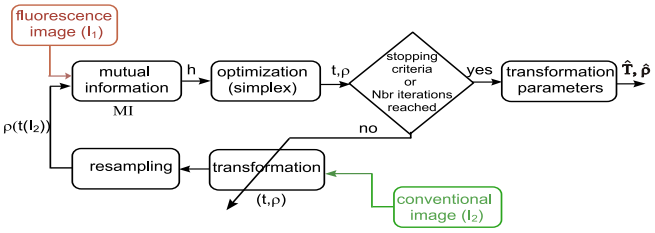

Fig. 4. Key steps of the proposed mutual information based registration.

C. Mutual information

Based on the entropy and the joint histogram principles, the mutual information can be defined following the three methods described in [6], [7].
However, for our work, we use the method using the marginal and joint entropy based on the value of the normalized joint histogram, given by (3).

$$MI(I_1, I_2) = H(I_1) + H(I_2) - H(I_1, I_2) \tag{3}$$

where $H(I_1)$ and $H(I_2)$ are the marginal entropy of I_1 and I_2, respectively, and $H(I_1, I_2)$ is joint entropy computed from the joint histogram.

Let us assume the rigid transformation $\widehat{T} \epsilon SE(3)$ between the images I_1 and I_2. Thereby, the transformation can be estimated by maximizing the mutual information $(MI)_i$.

$$\widehat{T} = arg \max_{t \in SE(3)} MI[I_1, t(I_2)] \tag{4}$$

where t is a possible rigid transformation. If we add a zoom factor, then we need to multiply the transformation matrix with the scaling factor:

$$zoom = \begin{pmatrix} \rho & 0 & 0 \\ 0 & \rho & 0 \\ 0 & 0 & 1 \end{pmatrix} \tag{5}$$

where ρ is the scale value. Hence, the equation (4) can evolve using the zoom parameter as:

$$(\widehat{T}, \widehat{\rho}) = arg \max_{t,\rho} MI[I_1, \rho(t(I_2))] \tag{6}$$

III. Optimization

Once the basics of the mutual information are addressed, it is necessary to establish an effective optimization method able to compute the maximum (respectively the minimum) of the joint information between both images. In this work, we opted to use a non-gradient-based optimization technique commonly known as *the simplex method* [8]. This choice is justified by the fact that the *simplex* is better fitted to an optimization problem with limited variables number [9].
The different steps of the presented mutual information based images registration are shown in Fig. 4.

IV. First Results

The experimental validation is performed with the objective to determine the estimated transformation $(\widehat{T}, \widehat{\rho})$ applied to image I_2 to be confounded with the image I_1. This transformation is here decomposed in translations (t_x and t_y), rotation θ_z and zoom ρ.

The validation tests were carried out using different images, between monomodal images acquired in various conditions (point of view, lighting illumination, adding objects onto the scene and scale changing), and between fluorescence images *vs.* white light image of vocal chords (images obtained from [11]). This paper show only the results using fluorescence *vs.* white light images. In this experiment, we added a fictive incision mark on the fluorescence image where the tumor is visible. To display the difference between image I_1 and the transformed image $\rho(t(I_2))$, we combine them as their checkerboard masked sum (Fig. 5). Thus a quality criterion of the registration is the continuity of the combined image a long the check-board lines.

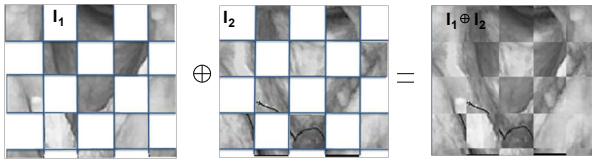

Fig. 5. Illustration of the construction of the result image ($\oplus$ operator to combine the two images I_1 and I_2).

By analyzing the Fig. 6, it can be noticed the continuity of the combination of I_1 in I_2 as shown in Fig. 6(b).

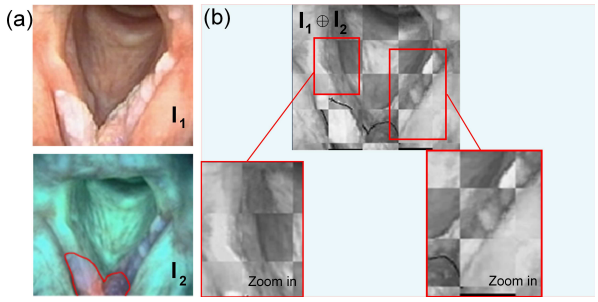

Fig. 6. Illustration of the registration results between I_1 and I_2. Column (a) represents the test images (*ie.* fluorescence image *vs.* white light image), and column (b) represents the obtained combined image with a zoom in to show the details.

Otherwise, the obtained values of the different parameters of $(\widehat{T}, \widehat{\rho})$ for the test shown in Fig. 6 are: t_x = -13.92 pixels, t_y = -1.31 pixels, θ_z = -0.0141°, and ρ = 0.158 pixels. This result is obtained in 110 seconds for a 170×150 image size using a 2.5 GHz PC.

V. Conclusion

This paper presented the initial results using the proposed mutual information registration method. The considered images are multimodal (*ie.* fluorescence image *vs.* white light image), and such image pairs will be used to detect the cancerous tumor in the vocal chords. The mutual information based registration method gives promising results and shows interesting robustness with respect to different kind and quality of the images.

The next step is to develop a new metric for visual servoing using the proposed technique. A new control law, which does not require any matching nor tracking step (direct visual servoing), based on mutual information will be designed. This is to ensure that the surgeon can plan a trajectory (*ie.* incision) on the fluorescence image and the endoluminal laser phonosurgery microrobot system will be able to follow this reference in the high speed white light images.

ACKNOWLEDGMENT

This work was supported by μRALP, the EC FP7 ICT Collaborative Project no. 288663 (`http://www.microralp.eu`), and by ACTION, the French ANR Labex no. ANR-11-LABX-01-01 (`http://www.labex-action.fr`).

References

[1] J. A. Burns, G. Har-El, S. Shapshay et al., *Endoscopic Laser Resection of Laryngeal Cancer: Is It Oncologically Safe? Position Statement From the American Broncho-Esophagological Association*, Annals of Otology Rhinology and Laryngology, vol. 118(6), pp. 399-404, 2009.
[2] M. C. Jackel, A. Martin, and W. Steiner, *Twenty-five Years Experience with Laser Surgery for Head and Neck Tumors*, European Archives of Oto-Rhino-Laryngology, vol. 264(6), pp. 577-585, 2007.
[3] Chaumette and S. Hutchinson. *Visual Servo Control, Part I: Basic Approaches*, IEEE Rob. and Auto. Mag., vol. 13(4), pp.8290, 2006.
[4] Barbara Zitova, Jan Flusser, *Image Registration Methods: a Survey*, Image and Vision Computing. vol. 977-1000, 2003.
[5] R. V. L. Hartley, *Transmission of Information,* Bell System Technical Journal, vol. 7, pp. 535563, 1928.
[6] Josien P. W. Pluim, J. B. Antoine Maintz and Max A. Viergever, *Mutual Information based Registration of Medical Images: a Survey*, IEEE Trans. on Medical Imag. 22(9), pp. 986-1004, 2003.
[7] Amaury Dame, Eric Marchand, *Second Order Optimization of Mutual Information for Real-time image Registration*, IEEE Transaction on image Processing, vol. 21(9), pp. 4190-4203, 2012.
[8] J. A. Nelder and R. Mead. *A Simplex Method for Function Minimization,* Computer Journal, vol. 7, pp. 308-313, 1965.
[9] Yang-Ming Zhu, and Steven M. Cochoff, *Influence of Implementation Parameters on Registration of MR and SPECT Brain Images by Maximization of Mutual Information*, IEEE Trans. on Medical Imag., 2001.
[10] R. John Koshel, *Enhancement of the Downhill Simplex Method of Optimization*, vol. 4832, pp. 270-282, 2002.
[11] C. Arens, T. Dreyer, H. Glanz, K. Malzahn, *Indirect Autofluorescence Laryngoscopy in the Diagnosis of Laryngeal Cancer and its Precursor Lesions*, European Archives of Oto-Rhino-Laryngology and Head & Neck, vol. 261(2), pp. 71-76, 2004.

Detection and Localization of Instruments in Minimally Invasive Surgery

Max Allan*, Sébastien Ourselin†, Steve Thompson†, David J. Hawkes†, John Kelly‡, Danail Stoyanov*

*Centre for Medical Image Computing and Dept. of Computer Science, UCL

†Centre for Medical Image Computing and Dept. of Medical Physics and Bioengineering, UCL

‡Division of Surgery and Interventional Science, UCL Medical School
{maximilian.allan.11,s.ourselin,s.thompson,j.d.kelly,danail.stoyanov}@ucl.ac.uk

***Abstract*—Integration of vision techniques for detection and localization of instruments in Minimally Invasive Surgery (MIS) can provide assistance to surgeons through motion control and guidance aids. In this study, we propose a framework for detecting and localizing the tool pose in 3D in the coordinate system of the observing camera. Using Random Forest classifiers to probabilistically label pixels in laparoscopic images as instrument or tissue, we recover the pose in 3D through a region based level-set segmentation technique. We demonstrate the effectiveness of the proposed system by comparison to ground truth tracking data obtained through an optical tracking system. This work is a continuation of the work in [1].**

I. Introduction

Minimally Invasive Surgery (MIS) has greatly improved surgical outcomes compared to open surgery by reducing the trauma of the procedure by accessing the surgical site through small keyhole ports [2]. However difficulties arising from the removal of direct access to the underlying anatomy has complicated surgery. Precise control of the instruments and tissue is more difficult to achieve with minimally invasive instruments and perceptive information such as force feedback and field of view is reduced. Robotic and computer assisted surgery have improved the surgeon's ability to navigate and operate [3], [4] through the introduction of HD stereoscopic video cameras and motion control systems that reduce hand tremors and remove the motion inversion of controlling a pivoting instrument.

As MIS is introduced to more complex procedures, the benefits of integrating preoperative information and navigation assistance become more prominent. Real-time knowledge of the instrument position and orientation with respect to both the surgical camera and the underlying anatomy becomes increasingly important as a means of introducing these systems. Computer vision techniques have demonstrated themselves to be effective methods of obtaining this information with minimal modification to existing surgical workflows.

There have been numerous proposals in the literature to adapt computer vision techniques to the minimally invasive environment. Several methods have attempted to integrate low level image features as part of point-based pose estimation methods [5], [6] and have achieved successful results on surgical images. Template tracking has also been attempted [7], [8]. However, one of the major shortcomings of this type of technique is that small scale features are vulnerable to occlusions so often found in surgical environments due to tissue, blood and smoke.

An alternative approach which makes use of region statistics when localizing pose presents a solution to this problem. [9] suggested an approach that involves aligning a model with a class probability map and achieve robust results. However, the method suffers from a non-differentiable cost function which leads to slow and unpredictable optimizations. Approaches which make use of level-set based region alignments have been successful in the computer vision literature [10], [11] and it is the approach of [12] which we follow most closely. The motivation behind following these methods is that the level set function can be smoothly differentiated with respect to the pose parameters of the target object leading to minimization techniques that simultaneously find the optimal 3D pose.

In this work we propose a 3 stage method of localizing medical instruments in 3D given a simple shape and appearance model. We perform detection with a random forest classifier after extensive experimentation to select suitable features, a 2D initialization with a shape analysis approach and 3D pose refinement with a level-set based segmentation.

II. Method

A. Detection

Random Forests (RF) [13] were chosen as the method of discriminating the regions of the image which correspond to the instrument and the tissue. They provide an accurate, fast and potentially parallelizable method which can be easily extended to handle multi-class training data, a useful feature when classifying multiple distinct tool or tissue types.

1) Feature selection: The complexity of light reflectance in the scene leads to some visual ambiguities between the instrument and areas of the tissue surface which makes classification challenging. As such, feature selection for the random forest becomes extremely important to ensure that the classification is accurate enough to enable good pose estimation.

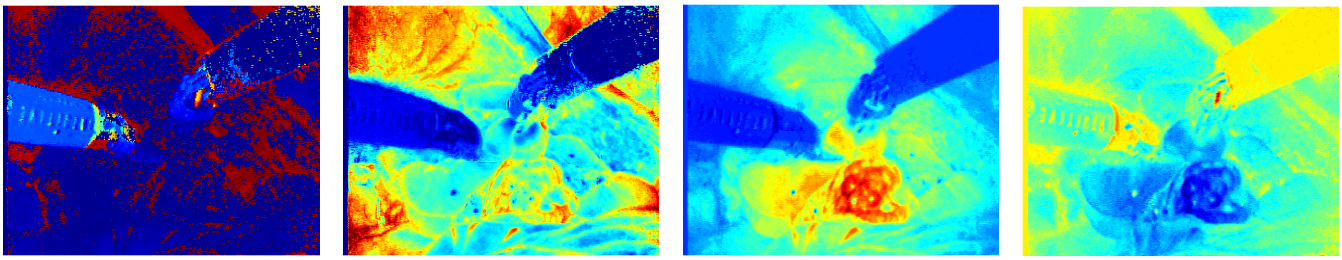

(a) Hue (b) Saturation (c) Opponent 2 (d) Opponent 3

Fig. 1: Visualisations of the discriminative power of the chosen colourspaces.

We tested several different features across distinct regions of MIS images: lightly colored tool shafts, darkly colored tool shafts, instrument tips and tissue. We performed our tests on several color features: RGB, HSV, CIE XYZ, Opponent 2 and Opponent 3, further details on these color spaces are reported in [14], [15].

2) Forest Implementation: We made use of the Random Forest implementation of the OpenCV library [1] and limit our forest size to 50 trees of no more than 10 levels to increase speed of both training and classification.

B. Instrument Pose Detection

1) Parametrization: We choose the standard parametrization of the instrument using the Euler angles (θ, ψ, ϕ) and a translation $\mathbf{t}$ in the camera coordinate system. As we have so far only modelled the instrument shaft as a featureless cylinder (without considering articulation of the instrument head) we are unable to detect the axial rotation parameter ϕ leaving our model with 5 recoverable degrees of freedom.

2) 2D Initialization: As our 3D pose estimation technique relies on a gradient descent based method to refine the pose, it is important to obtain a good initial estimate to avoid local minima and to reduce the time taken to converge. We achieve this by selecting the largest connected regions of the classification map and then finding their principal axes using the moment of inertia tensor. Then by assuming that the connected region can be approximated by a 2D cylinder, we can estimate its width and height (in pixels) from the eigenvalues of the tensor as $r = \sqrt{2I_2/m}$ and $l = \sqrt{12I_1/m - 3r^2}$. The estimate of width can be used to estimate the depth of the instrument given that we know the width of the instrument in metric units a priori. From this initialization we obtain an estimate of $\mathbf{t}$ as well as the rotational parameter θ.

3) 3D Refinement: To estimate the additional rotational degree of freedom ψ as well as refine the estimates of θ and $\mathbf{t}$ we employ the 3D pose estimation technique of [12]. Given an estimate of image pose and a known 3D model of the target object, a segmentation can be defined through the outer contour of the its projection onto the image plane. The quality of the segmentation can be defined using an image functional:

$$E(g(\mathbf{p})) = -\sum_{\mathbf{p}\in\Omega} \Big(\log \left(H_e(g(\mathbf{p}))P_f + (1 - H_e(g(\mathbf{p}))P_b \right) \Big) \tag{1}$$

where $P_{f|b}$ refers to the confidence of a pixel belonging to the instrument class and the tissue class respectively and is computed by the random forest as the fraction of trees which voted for each class. $g(\mathbf{p})$ represents the level set function and, as usual, is represented by a signed distance function (negative values for the exterior, positive for the interior). $H(.)$ is a smoothed Heaviside function which filters the distance values into interior/exterior regions with the smoothing allowing for uncertainty in the location of the contour. To find the minimum of Eq. 1 from the set of possible projections of the target object we search the space of its pose parameters with gradient descent.

III. Results

The results were collected by a C++ implementation of the algorithm without any parallelization or optimization of the code and as such is not real-time. Random Forest mean classification time is 3.47 seconds for an SD image and pose estimation takes 1-20 seconds, with the large variation due to differences in accuracy of the starting estimate.

A. Features for Classification

We performed several experiments to determine the most discriminative visual features to use for classification. We used the general statistical technique for measuring the distance between histograms of the Bhattacharyya distance [16] and also an internal estimator provided by all decision tree methods known as variable importance [17]. To ensure we considered a range of tissue types and instrument appearances we perform tests on 97 manually labelled images from 6 different surgical procedures.

Our investigations showed that the most discriminative colour spaces appear to be the hue, saturation and the opponent 2 and 3 colour spaces.

B. Laboratory experiments

Validation of the pose estimation was achieved with an experiment where data was acquired from an NDI Optotrak Certus[2] optical tracking system. We manufactured rigid bod-

[1] www.opencv.willowgarage.com

[2] http://www.ndigital.com/lifesciences/certus-motioncapturesystem.php

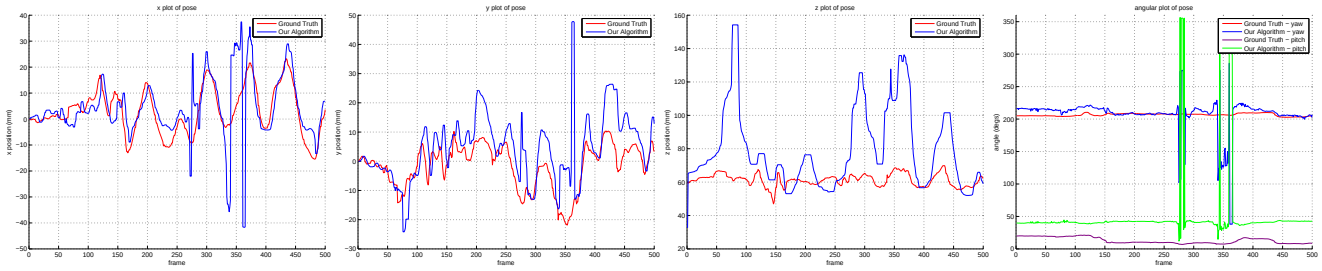

(a) (b) (c) (d)

Fig. 2: The error plots for the Optotrak calibrated pose. As can be seen the errors are quite low, particularly in x and y. The z error occasionally moves far from the true estimate (which in turn distorts the x and y estimates). The positional estimates have been median filtered to smooth out some of the errors.

ies with embedded optical markers and attached one to the proximal end of a Viking Systems 3DHD laparoscope and one to the proximal end of an Ethicon monopolar dissector. The experimental setup can be seen in Figure 3. Camera and hand eye calibration between the camera and Optotrak coordinate systems were obtained using toolboxes available online to allow comparison of measurements made by our method using the camera and those from the Optotrak [3] [4]. Camera calibration reprojection error was 0.2 pixels and additionally, the instrument was calibrated to measure the offset between the tool's tip and the attached rigid body with a calibration error of 0.17mm $\pm$ 0.18mm.

Experiments were performed by translating and rotating the instrument between the camera and an *ex vivo* lamb liver tissue sample while the Optotrak system recorded the instrument pose in the camera coordinate system for each frame. An instrument appearance model was learned from images of the tool in front of a homogeneous background and a background appearance model was learned from separate images of the liver.

By computing the 3D pose of the instrument at each frame and comparing to data from the Optotrak system we show motion plots of the tip position and error plots in Figure 2. To compensate for calibration error, which results in a constant offset, we show the motion after the coordinate systems have been matched for the first frame. The plots visibly show that our method correctly localises to the ground truth pose in the majority of frames. The mean and standard deviation of the error for the instrument are 0.171mm and 0.182mm whereas for the camera they are 0.981mm and 0.002mm respectively. These are promising results considering we are estimating 3D information from a monocular image and this explains the larger error visible in the z axis. Occasional errors are also visible as spikes in our measurements, particularly around frames 280 and frame 350. These occur when the instrument is moved out of the view of the camera and the pose localisation system incorrectly recognises part of the shadow in the image as an instrument. These errors could easily be removed by incorporating a simple tracking framework such as Kalman filtering.

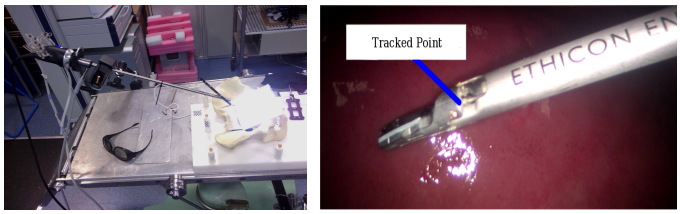

(a) (b)

Fig. 3: (a) shows the laboratory experimental setup with the laparoscope complete with optical tracking markers. (b) shows a frame from the laparoscope showing the instrument in front of a lamb's liver. The marker indicates the point on the instrument which is tracked by our system.

IV. Conclusion

In this study we have proposed a method for detecting and localizing instruments in surgical images. Experimentation with optically calibrated data shows that our method is robust and generally accurate with some inaccuracy in the depth estimation. As typical surgical systems are equipped with stereo cameras our future work will include integrating stereo constraints to improve accuracy. We further hope to make use of temporal tracking estimates to reduce the error from noisy estimates and additionally we plan to integrate extensive GPU parallelization to achieve real time performance of our work, as has been reported in the literature.

References

[1] M. Allan, S. Ourselin, S. Thompson, D. J. Hawkes, J. Kelly, and D. Stoyanov, "Toward detection and localization of instruments in minimally invasive surgery," *IEEE transactions on bio-medical engineering*, vol. 60, pp. 1050–1058, Apr. 2013. PMID: 23192482.

[2] A. Darzi and S. Mackay, "Recent advances in minimal access surgery," *BMJ*, vol. 324, pp. 31–34, Jan. 2002.

[3] D. J. Mirota, M. Ishii, and G. D. Hager, "Vision-based navigation in image-guided interventions," *Annual Review of Biomedical Engineering*, vol. 13, pp. 297–319, Aug. 2011. PMID: 21568713.

[3] http://www0.cs.ucl.ac.uk/staff/Dan.Stoyanov/calib/

[4] http://www.vision.ee.ethz.ch/software/calibration_toolbox//calibration_toolbox.php

[4] D. Stoyanov, "Surgical vision," *Annals of Biomedical Engineering*, vol. 40, pp. 332–345, Feb. 2012.

[5] S. Voros, J. Long, and P. Cinquin, "Automatic detection of instruments in laparoscopic images: A first step towards high-level command of robotic endoscopic holders," *The International Journal of Robotics Research*, vol. 26, pp. 1173 –1190, Nov. 2007.

[6] A. Reiter, P. K. Allen, and T. Zhao, "Learning features on robotic surgical tools," in *Computer Vision and Pattern Recognition*, 2012.

[7] R. Sznitman, K. Ali, R. Richa, R. Taylor, G. Hager, and P. Fua, "Data-driven visual tracking in retinal microsurgery," in *Medical Image Computing and Computer-Assisted Intervention - MICCAI 2012* (N. Ayache, H. Delingette, P. Golland, and K. Mori, eds.), vol. 7511 of *Lecture Notes in Computer Science*, pp. 568–575, Springer Berlin / Heidelberg, 2012.

[8] D. Burschka, J. J. Corso, M. Dewan, W. Lau, M. Li, H. Lin, P. Marayong, N. Ramey, G. D. Hager, B. Hoffman, D. Larkin, and C. Hasser, "Navigating inner space: 3-D assistance for minimally invasive surgery," in *In: Workshop Advances in Robot Vision, in conjunction with the IEEE/RSJ International Conference on Intelligent Robots and Systems*, pp. 67–78, 2004.

[9] Z. Pezzementi, S. Voros, and G. D. Hager, "Articulated object tracking by rendering consistent appearance parts," in *IEEE International Conference on Robotics and Automation, 2009. ICRA '09*, pp. 3940 –3947, May 2009.

[10] S. Dambreville, R. Sandhu, A. Yezzi, and A. Tannenbaum, "Robust 3D pose estimation and efficient 2D region-based segmentation from a 3D shape prior," in *Proceedings of the 10th European Conference on Computer Vision: Part II*, ECCV '08, (Berlin, Heidelberg), pp. 169–182, Springer-Verlag, 2008.

[11] B. Rosenhahn, T. Brox, and J. Weickert, "Three-dimensional shape knowledge for joint image segmentation and pose estimation," in *Pattern Recognition, volume 3663 of LNCS*, p. 109116, Springer, 2005.

[12] V. A. Prisacariu and I. D. Reid, "PWP3D: Real-Time segmentation and tracking of 3D objects," *International Journal of Computer Vision*, vol. 98, pp. 335–354, Jan. 2012.

[13] L. Breiman, "Random forests," *Mach. Learn.*, vol. 45, pp. 5–32, Oct. 2001.

[14] G. W. Meyer and D. P. Greenberg, "Perceptual color spaces for computer graphics," in *Proceedings of the 7th annual conference on Computer graphics and interactive techniques*, SIGGRAPH '80, (New York, NY, USA), p. 254261, ACM, 1980.

[15] T. Gevers and H. Stokman, "Classifying color edges in video into shadow-geometry, highlight, or material transitions," *Multimedia, IEEE Transactions on*, vol. 5, pp. 237 – 243, June 2003.

[16] A. Bhattacharyya, "On a measure of divergence between two statistical populations defined by their probability distributions," *Bulletin of the Calcutta Mathematical Society*, vol. 35, pp. 99–109, 1943.

[17] A. Verikas, A. Gelzinis, and M. Bacauskiene, "Mining data with random forests: A survey and results of new tests," *Pattern Recognition*, vol. 44, pp. 330–349, Feb. 2011.

Stereoscopic Surface Reconstruction in Minimally Invasive Surgery using Efficient Non-Parametric Image Transforms

Andreas Schoob, Florian Podszus, Dennis Kundrat, Lüder A. Kahrs and Tobias Ortmaier

Abstract— **Intra-operative instrumentation and navigation in minimally invasive surgery is challenging due to soft tissue deformations. Therefore, surgeons make use of stereo endoscopy and adjunct depth perception in order to handle tissue more safely. Moreover, the surgeon can be assisted with visualized information computed from three-dimensionally estimated surgical site. In this study, a review of state-of-the-art methods dealing with surface reconstruction in minimally invasive surgery is presented. In addition, two real-time solutions based on non-parametric image transforms are proposed. A local method using an efficient census transform is compared to model-based tracking of disparity. The algorithms are evaluated on online available image sequences of a deforming heart phantom with known depth. Both approaches show promising results with respect to accuracy and real-time capability. Particularly, the model-based method is able to compute very dense depth maps if the observed surface is smooth.**

I. Introduction

Stereoscopic vision has become a key component in minimally invasive surgery providing three-dimensional visual feedback. The adjunct depth perception of the scene is beneficial when manipulating tissue with surgical instruments such as forceps or scalpels. Moreover, a dual imaging system can be utilized to reconstruct the surgical site in order to facilitate intra-operative guidance or augmented reality based on additional intra- and pre-operative data.

Due to soft tissue characteristics, current research especially addresses tissue motion tracking [1]–[4] as well as registration of pre- to intra-operative data [5]–[7]. These approaches mostly incorporate stereo-based depth estimation. For this purpose, correspondences between the left and right camera image have to be determined. This can be achieved by cost computation based on state-of-the-art methods [8]. In detail, depth of an object point projected to the image planes is computed based on intensity information obtained from the pixel's neighborhood. Common similarity measures for comparing left and right image are sum of squared differences (SSD) and normalized cross-correlation (NCC).

An early NCC based method models depth as a Gaussian distribution in order to detect and remove instruments from the endoscopic view [9]. Aside from observing instruments, the pose of the endoscope with respect to the target can be determined by applying NCC based feature matching on mono camera images [10]. Using a stereo fiberscope instead, NCC based correspondence search can be combined with simultaneous localization and mapping (SLAM) for estimating the tissue's surface as well as the endoscope's pose and motion [11]. A three-dimensional representation of the surgical site can also be computed with a NCC multiple resolution approach applied on images of a stereo camera capsule. Designed for augmented reality in laparoscopy, such a device is deployed inside the patient's abdominal cavity providing an increased field-of-view and depth-of-field [12]. Due to specular highlights on glossy tissue or lighting variations, obtaining an accurate and dense depth map with local similarity measures often leads to non-reliable results. Therefore, one can enhance local metrics by smoothness terms and a dynamic programming framework in order globally estimate depth [5]. In a more recent approach, discriminative matching in especially texture-less tissue regions is achieved by applying adaptive support windows [13]. Further on, depth information obtained at salient features can be propagated into a spatial neighborhood resulting in a semi-dense and smooth depth map of the surgical site [14]. In this particular case, once detected features additionally allow to temporally observe motion of the tissue. Aside from that, one can take both spatial and temporal disparity information into account. Combined with a hybrid CPU-GPU implementation, a powerful real-time reconstruction framework targeting on registration of pre-operative models can be implemented [15].

In contrast to methods combining locally applied similarity measures with spatial or temporal constraints, more global optimization is achieved with model-based methods. In minimally invasive surgery, the surface of the observed soft tissue is generally continuous and smooth. Following this assumption, tissue depth and deformation can be modeled by applying hierarchical free-form registration with piecewise bilinear maps [16]. Especially for cardiac surface deformation, disparity can be described by B-splines and tracked by a first order optimization based on a SSD error function [17]. Even a set of tracked features is sufficient to observe cardiac motion [18]. Despite using features, region-based tracking with elastic deformation modeling and an efficient minimization scheme also guarantees real-time cardiac motion estimation [4]. However, model-based three-dimensional tracking is computationally complex and limited due to depth discontinuities arising at borders of instruments in the surgical field of view.

In general, stereo-based tissue depth estimation is prone to specular highlights, texture-less surface, instrument occlusions, bleeding or fume during laser interventions. If those methods fail, literature provides alternative solutions applicable for intra-operative vision-based navigation. For a comprehensive overview, we recommend [19,20].

All authors are with the Institute of Mechatronic Systems, Leibniz Universität Hannover, Germany. andreas.schoob@imes.uni-hannover.de

Disadvantageously, most of above mentioned methods are evaluated on different image data complicating comparison. In order to provide a structured evaluation framework, a medical data set containing ground truth has been established [6,14]. Unfortunately, only few further methods are verified on this data [15,21]. In addition, literature review has shown that, apart from common similarity measures (i.e. NCC), especially non-parametric metrics based on the efficient rank or census transform are hardly used within image-guided minimally invasive surgery.

In this study, accurate and real-time capable techniques for dense surface reconstruction of surgical scenes are presented. Contrary to the commonly used NCC, a solution comprising a locally applied, more simple and efficient census transform is briefly presented in Sec. II. Providing more dense and smooth depth information, a model-based implementation using thin plate splines (TPS) and fast optimization applied on rank transformed images is introduced subsequently. In Sec. III, both methods are evaluated with respect to accuracy as well as real-time capability using the aforementioned online available image sequences [6,14]. Sec. IV summarizes this contribution.

II. Materials and Methods

In Sec. II-A both rank and census transform are introduced. Subsequently, Sec. II-B and II-C describe our proposed methods for stereoscopic surface reconstruction based on those non-parametric image transforms. To simplify implementation, calibrated and rectified images are used. Thus, disparity computation is reduced to an one-dimensional search problem.

A. Rank and census transform

In contrast to estimating disparity relying on absolute intensities, the rank and census transform of an image $\boldsymbol{I}$ show improved robustness to radiometric differences, lighting changes and noise [22]. For both transforms, the image intensities $\boldsymbol{I}(N(\boldsymbol{p}))$ within a local $M \times N$ neighborhood $N(\boldsymbol{p})$ are compared to the center pixel's $\boldsymbol{p} = (x,y)^{\mathrm{T}}$ intensity $\boldsymbol{I}(\boldsymbol{p})$. The rank transform of image $\boldsymbol{I}$ is defined by

$$\boldsymbol{I}_{\mathrm{R}}(\boldsymbol{p}) = \sum_{j=-N/2}^{N/2} \sum_{i=-M/2}^{M/2} \xi\left(\boldsymbol{I}(\boldsymbol{p}), \boldsymbol{I}(\boldsymbol{p}+(i,j)^{\mathrm{T}})\right). \quad (1)$$

Subsequently, the census transform is given by

$$\boldsymbol{I}_{\mathrm{C}}(\boldsymbol{p}) = \bigotimes_{j=-N/2}^{N/2} \bigotimes_{i=-M/2}^{M/2} \xi\left(\boldsymbol{I}(\boldsymbol{p}), \boldsymbol{I}(\boldsymbol{p}+(i,j)^{\mathrm{T}})\right) \quad (2)$$

with $\bigotimes$ denoting concatenation to a bit string. The function ξ for comparing the two intensities is denoted as

$$\xi(I_1, I_2) = \begin{cases} 0, & \text{if } I_1 \leq I_2 \\ 1, & \text{else.} \end{cases} \quad (3)$$

B. Local census-based disparity computation

For computational efficiency, a sparse census transform is applied resulting in a shortened bit string. Hereby, only every second column and row of the neighborhood $N(\boldsymbol{p})$ are considered. Hamming distance H is used as similarity measure between a pixel $\boldsymbol{p}_\ell = (x_\ell, y_\ell)$ in the left image $\boldsymbol{I}_{\mathrm{C},\ell}$ and a pixel $\boldsymbol{p}_r = (x_r, y_r)^{\mathrm{T}} = \boldsymbol{p}_\ell - (d,0)^{\mathrm{T}}$ in the right image $\boldsymbol{I}_{\mathrm{C,r}}$ (4). Disparity is denoted as d.

$$H(\boldsymbol{p}_\ell, d) = \sum_{i=1}^{M\times N-1} \boldsymbol{I}_{\mathrm{C},\ell}(\boldsymbol{p}_\ell, i) \oplus \boldsymbol{I}_{\mathrm{C,r}}(\boldsymbol{p}_\ell - (d,0)^{\mathrm{T}}, i) \quad (4)$$

Index i defines the appropriate bit in string $\boldsymbol{I}_{\mathrm{C}}(\boldsymbol{p})$ whereas $\oplus$ denotes XOR operation. Smoothness and unambiguous matching are achieved in a cost aggregation by summing up the Hamming distances $H(\boldsymbol{p}_\ell, d)$ within a certain pixel neighborhood. Additionally, our disparity computation comprises a consistency check, a sub-pixel refinement, a removal of disparity speckles and a winner-takes-all (WTA) strategy. Further smoothing is done by bilateral filtering.

C. Model-based disparity computation

An elastic model-based computation is able to provide a dense and reliable disparity map if the observed surface is smooth [17]. Furthermore, such an approach facilitates real-time three-dimensional tissue motion tracking [4]. However, accuracy strongly depends on the number of parameters describing the elastic deformation.

In this study, disparity is estimated by a thin plate spline (TPS) based tracking following the ideas introduced in *Lau et al.* and *Richa et al.* [17,4]. Our algorithm uses rank transformed images and an extended inverse compositional parametrization.

Assuming a rank transformed image region $\boldsymbol{I}_{\mathrm{R}}$ described by n pixels $\boldsymbol{p}_{\ell,i} = (x_{\ell,i}, y_{\ell,i})^{\mathrm{T}}$ in the left and n pixels $\boldsymbol{p}_{\mathrm{r},i} = (x_{\mathrm{r},i}, y_{\mathrm{r},i})^{\mathrm{T}}$ in the right image with $i \in \{1,...,n\}$, mapping between both pixel sets can be formulated by an elastic transformation (5) [23]. Since images are rectified, corresponding points will have the same y-coordinate with $y_{\mathrm{r},i} = y_{\ell,i}$. As a result, disparity is simply defined by $d_i = x_{\ell,i} - x_{\mathrm{r},i}$. One-dimensional mapping for $x_{\mathrm{r},i}$ is then denoted as

$$x_{\mathrm{r},i}(\boldsymbol{p}_{\ell,i}) = \begin{bmatrix} a_1 & a_2 & a_3 \end{bmatrix} \begin{bmatrix} x_{\ell,i} \\ y_{\ell,i} \\ 1 \end{bmatrix} + \sum_{j=1}^{\alpha} w_j \cdot u(\left\|\boldsymbol{c}_{\ell,j} - \boldsymbol{p}_{\ell,i}\right\|) \quad (5)$$

with TPS basis function $u(r) = r^2 \log r^2$ and parameter vector $\boldsymbol{t} = (w_1, ..., w_\alpha, a_1, a_2, a_3)^{\mathrm{T}}$ [23]. So-called control points $\boldsymbol{c}_{\ell,j} = (\widehat{x}_{\ell,j}, \widehat{y}_{\ell,j})^{\mathrm{T}}$ with $j \in \{1,...,\alpha\}$ are initially set in the left image. According to current depth of the scene, control points $\boldsymbol{c}_{\mathrm{r},j} = (\widehat{x}_{\mathrm{r},j}, \widehat{y}_{\mathrm{r},j})^{\mathrm{T}}$ in the right image need to be estimated . Once correspondence between $\boldsymbol{c}_\ell$ and $\boldsymbol{c}_{\mathrm{r}}$ is known, a mapping for any pixel $\boldsymbol{p}_{\mathrm{r},i}^{\mathrm{T}} = m(\boldsymbol{p}_{\ell,i}, \boldsymbol{c}_{\mathrm{r}})$ can be formulated with a linear system [4,23]. In general, temporal disparity changes between consecutive frames are described by deviation $\Delta\boldsymbol{c}_{\mathrm{r}}$ with respect to prior control point configuration $\boldsymbol{c}_{\mathrm{r}}$. For real-time estimation of $\boldsymbol{c}_{\mathrm{r}} + \Delta\boldsymbol{c}_{\mathrm{r}}$, an

inverse compositional parametrization is implemented [24]. In detail, a virtual warping of image $\boldsymbol{I}_{\mathrm{R},\ell}(m(\boldsymbol{p}_{\ell,i}, \boldsymbol{c}_\ell + \Delta\boldsymbol{c}_\ell))$ describes disparity changes by shifting $\Delta\boldsymbol{c}_\ell$ with respect to $\boldsymbol{c}_\ell$. Since compositional frameworks cannot be applied to TPS directly, $\boldsymbol{c}_\mathrm{r} = f(\boldsymbol{c}_\ell, \Delta\boldsymbol{c}_\ell)$ is subsequently estimated in a closed-form solution [25]. Thus, our optimization aims on finding $\Delta\boldsymbol{c}_\ell$ instead. As a result, the alignment error to be minimized can be formulated with (6). Before, a sparse rank transform is applied to both left and right image in order to increase robustness to lighting variations without introducing further parameters.

$$\min_{\Delta\boldsymbol{c}_\ell} \epsilon = \sum_{i=1}^{n} \left[\boldsymbol{I}_{\mathrm{R},\ell}(m(\boldsymbol{p}_{\ell,i}, \boldsymbol{c}_\ell + \Delta\boldsymbol{c}_\ell)) - \boldsymbol{I}_{\mathrm{R,r}}(m(\boldsymbol{p}_{\ell,i}, \boldsymbol{c}_\mathrm{r}))\right]^2 \quad (6)$$

For rectified images, one has just to consider the x-components of $\Delta\boldsymbol{c}_\ell = (\Delta\widehat{\boldsymbol{x}}_\ell, \Delta\widehat{\boldsymbol{y}}_\ell)$ where $\Delta\widehat{\boldsymbol{x}}_\ell$ describes a column vector of stacked $\widehat{x}_{\ell,j}$. Performing first order Taylor expansion on (6), this least-squares problem can be iteratively solved by computing $\Delta\widehat{\boldsymbol{x}}_\ell$ as follows

$$\Delta\widehat{\boldsymbol{x}}_\ell = (\boldsymbol{J}(\boldsymbol{I}_{\mathrm{R},\ell}, \boldsymbol{p}_\ell, \boldsymbol{c}_\ell))^+ \begin{bmatrix} \boldsymbol{I}_{\mathrm{R,r}}(m(\boldsymbol{p}_{\ell,1}, \boldsymbol{c}_\mathrm{r})) - \boldsymbol{I}_{\mathrm{R},\ell}(\boldsymbol{p}_{\ell,1}) \\ \vdots \\ \boldsymbol{I}_{\mathrm{R,r}}(m(\boldsymbol{p}_{\ell,n}, \boldsymbol{c}_\mathrm{r})) - \boldsymbol{I}_{\mathrm{R},\ell}(\boldsymbol{p}_{\ell,n}) \end{bmatrix} \quad (7)$$

with pseudoinverse $\boldsymbol{J}^+$ of the Jacobian matrix $\boldsymbol{J}$. Corresponding to pixel $\boldsymbol{p}_{\ell,i}$, the i-th row of $\boldsymbol{J}$ is defined by

$$\boldsymbol{J}_i(\boldsymbol{I}_{\mathrm{R},\ell}, \boldsymbol{p}_{\ell,i}, \boldsymbol{c}_\ell) = \left[\frac{\partial \boldsymbol{I}_{\mathrm{R},\ell}(m(\boldsymbol{p}_{\ell,i}, \boldsymbol{c}_\ell)}{\partial \widehat{x}_{\ell,1}} \cdots \frac{\partial \boldsymbol{I}_{\mathrm{R},\ell}(m(\boldsymbol{p}_{\ell,i}, \boldsymbol{c}_\ell)}{\partial \widehat{x}_{\ell,\alpha}}\right]. \quad (8)$$

Compared to conventional gradient based optimization, Jacobian $\boldsymbol{J}$ and its pseudoinverse $\boldsymbol{J}^+$ has to be computed just once between consecutive frames. As a result, computation time is significantly reduced.

D. Image processing and sequences

The proposed methods are implemented in C++ using NVIDIA CUDA and OpenCV [26]. For highly parallel computing a NVIDIA GTX TITAN is deployed accessing both global and shared GPU memory. Quantitative evaluation is conducted on two online available image sequences of a deforming silicon heart phantom with an image resolution of 320×288 pixels (see Fig. 1) [6,14,27]. Obtained by CT scans and registered to camera frame, there are 20 ground truth depth maps each used for multiple images of a sequence.
In the following, the implemented algorithms will be denoted as *local* (see Sec. II-B) and *TPS* method (see Sec. II-C). The *local* method computes depth for the whole scene. Due to reduced overlapping of the left and right camera image, the *TPS* algorithm cannot be initialized considering the entire region. Here, 200×200 pixels are computed. However, the size of image region being reconstructed strongly depends on the surgical task. During robot-assisted actions, e.g. incisions by surgical tools, depth computation of a target region might be sufficient whereas registration to pre-operative images often requires the whole 3D scene.

III. Results

A. Image sequences with known ground truth

In our experiments, mean disparity and depth errors as well as their standard deviations are determined with respect to ground truth. The results are shown in Fig. 1 and listed in Table I which also contains the percentage of matched points and computation time per frame. Since the heart phantom's surface is smooth, the *TPS* method outperforms the *local* one with respect to accuracy and density of reconstruction. Due to more global optimization, image noise is intrinsically compensated and depth in sparsely textured surface can be estimated by the help of a discriminative neighborhood. Once initialized, tracking of disparity is even robust in dynamically changing tissue surface. Nevertheless, if the scene is sufficiently illuminated, the *local* method is able to compute dense disparity information in real-time, too.
Compared to methods from literature, our errors are within same order of magnitude. For instance, *Stoyanov et al.* estimate disparity with an error of $0.89 \pm 1.13\,px$ for *Heart 1* and $1.22 \pm 1.71\,px$ for *Heart 2* [14]. *Röhl et al.* report a depth error of $1.45\,mm$ for *Heart 1* and $1.64\,mm$ for *Heart 2* [15].

TABLE I
Computational results of the proposed methods

	Heart 1		*Heart 2*	
	local	TPS	local	TPS
Disp. err. $[px]$	1.86 ± 0.94	1.38 ± 0.72	0.96 ± 0.27	0.69 ± 0.26
Depth err. $[mm]$	1.87 ± 0.80	1.74 ± 0.70	1.68 ± 0.47	1.52 ± 0.52
Matched $[\%]$	67.6 ± 9.40	54.4 ± 0.50	67.5 ± 12.3	57.2 ± 0.83
Time $[ms]$	25.6 ± 0.98	34.0 ± 5.77	25.6 ± 0.91	29.7 ± 6.56

B. In vivo image sequence

A qualitative experiment is conducted on an online available *in vivo* porcine sequence [20]. Fig. 2 show that if the number of control points is increased to 4×4, the error between *TPS* and *local* depth estimation is significantly reduced.

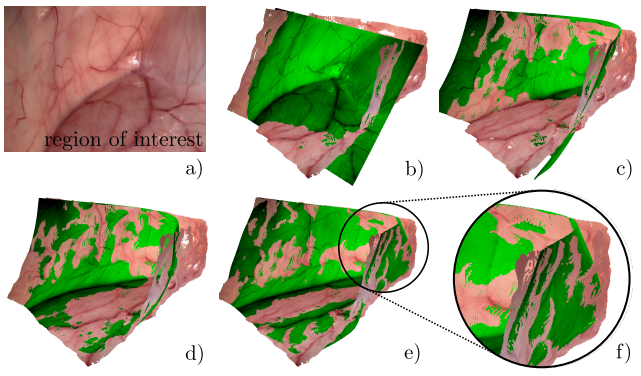

Fig. 2. Qualitative validation on *in vivo* porcine procedure [20]; reconstructed depth with *local* method (natural color) and *TPS* method (green color) with a) selected frame, b) 2×2, c) 3×2, d) 3×3 and e) 4×4 control points with f) improved depth estimation compared to b), c) and d)

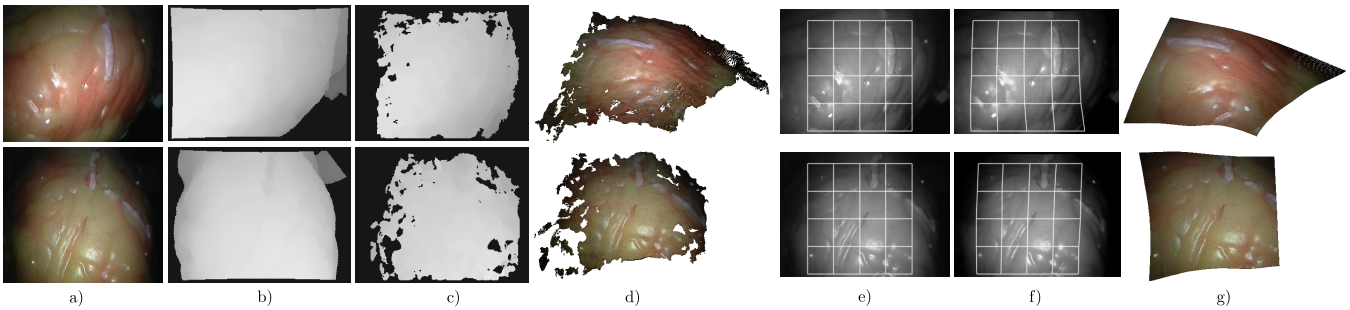

Fig. 1. Results of disparity and depth computation; top: *Heart 1* sequence; bottom: *Heart 2* sequence; a) frame of left camera b) ground truth disparity map; c) computed disparity with *local* method; d) reconstructed depth with *local* method; e) left image with 5×5 control points of *TPS* method; f) corresponding control points in the right image; g) reconstructed depth with *TPS* method

IV. Conclusion and Outlook

In this study, surface reconstruction of surgical scenes based on non-parametric image transforms is evaluated. The proposed methods are fast and provide dense surface estimation. If the observed surface is sufficiently smooth, our model-based algorithm is highly accurate. Although it uses non-deterministic optimization, real-time capability is achieved by an inverse compositional framework. However, the choice between these two methods strongly depends on the surgical task and tissue properties. Future work will deal with incorporation in an intra-operative system for laser phonomicrosurgery.

Acknowledgment

This research has received funding from the European Union FP7 under grant agreement μRALP - n^{o} 288663. The authors thank the Visual Information Processing Group at the Imperial College in London for providing image data.

References

[1] M. Groeger, T. Ortmaier, W. Sepp, and G. Hirzinger, "Tracking local motion on the beating heart," *Proceedings of SPIE Medical Imaging*, pp. 233–241, 2002.

[2] D. Stoyanov, G. Mylonas, F. Deligianni, A. Darzi, and G. Yang, "Soft-tissue motion tracking and structure estimation for robotic assisted mis procedures," in *Proceedings of MICCAI*, 2005, vol. 3750, pp. 139–146.

[3] P. Mountney and G.-Z. Yang, "Soft tissue tracking for minimally invasive surgery: Learning local deformation online," in *Proceedings of MICCAI*, 2008, vol. 5242, pp. 364–372.

[4] R. Richa, P. Poignet, and C. Liu, "Deformable motion tracking of the heart surface," in *IEEE/RSJ International Conference on Intelligent Robots and Systems, IROS*, 2008, pp. 3997 –4003.

[5] G. Hager, B. Vagvolgyi, and D. Yuh, "Stereoscopic video overlay with deformable registration," *Medicine Meets Virtual Reality*, 2007.

[6] P. Pratt, D. Stoyanov, M. Visentini-Scarzanella, and G.-Z. Yang, "Dynamic guidance for robotic surgery using image-constrained biomechanical models," in *Proceedings of MICCAI*, vol. 6361, 2010, pp. 77–85.

[7] S. Speidel, S. Roehl, S. Suwelack, R. Dillmann, H. Kenngott, and B. Mueller-Stich, "Intraoperative surface reconstruction and biomechanical modeling for soft tissue registration," in *Proc. Joint Workshop on New Technologies for Computer/Robot Assisted Surgery*, 2011.

[8] J. Banks, M. Bennamoun, and P. Corke, "Non-parametric techniques for fast and robust stereo matching," in *Proceedings of IEEE TENCON*, vol. 1, 1997, pp. 365–368.

[9] F. Mourgues, F. Devernay, and È. Coste-Manière, "3D reconstruction of the operating field for image overlay in 3D-endoscopic surgery," in *IEEE and ACM International Symposium on Augmented Reality (ISAR)*, 2001, p. 191.

[10] T. Thormaehlen, H. Broszio, and P. Meier, "Three-dimensional endoscopy," *Medical imaging in gastroenterology and hepatology, 124th Falk Symposium Hannover, Germany*, 2002.

[11] D. Noonan, P. Mountney, D. Elson, A. Darzi, and G.-Z. Yang, "A stereoscopic fibroscope for camera motion and 3D depth recovery during minimally invasive surgery," in *IEEE International Conference on Robotics and Automation, ICRA*, 2009, pp. 4463 – 4468.

[12] B. Tamadazte, S. Voros, C. Boschet, P. Cinquin, and C. Fouard, "Augmented 3-d view for laparoscopy surgery," in *Augmented Environments for Computer-Assisted Interventions*, 2013, vol. 7815, pp. 117–131.

[13] S. Bernhardt, J. Abi-Nahid, and R. Abugharbieh, "Robust dense endoscopic stereo reconstruction for minimally invasive surgery," in *MICCAI workshop on MCV*, 2012, pp. pp. 198–207.

[14] D. Stoyanov, M. Scarzanella, P. Pratt, and G.-Z. Yang, "Real-time stereo reconstruction in robotically assisted minimally invasive surgery," in *Proceedings of MICCAI*, 2010, vol. 6361, pp. 275 – 282.

[15] S. Rohl, S. Bodenstedt, S. Suwelack, H. Kenngott, B. P. Muller-Stich, R. Dillmann, and S. Speidel, "Dense gpu-enhanced surface reconstruction from stereo endoscopic images for intraoperative registration," *Medical Physics*, vol. 39, p. 1632, 2012.

[16] D. Stoyanov, A. Darzi, and G. Yang, "Dense 3d depth recovery for soft tissue deformation during robotically assisted laparoscopic surgery," in *Proceedings of MICCAI*, 2004, vol. 3217, pp. 41–48.

[17] W. Lau, N. Ramey, J. Corso, N. Thakor, and G. Hager, "Stereo-based endoscopic tracking of cardiac surface deformation," in *Proceedings of MICCAI*, 2004, vol. 3217, pp. 494–501.

[18] D. Stoyanov, A. Darzi, and G. Z. Yang, "A practical approach towards accurate dense 3d depth recovery for robotic laparoscopic surgery," *Computer Aided Surgery*, vol. 10, no. 4, pp. 199–208, 2005.

[19] D. Stoyanov, "Surgical vision," *Annals of Biomedical Engineering*, vol. 40, no. 2, pp. 332–345, 2012.

[20] P. Mountney, D. Stoyanov, and G.-Z. Yang, "Three-dimensional tissue deformation recovery and tracking," *Signal Processing Magazine, IEEE*, vol. 27, no. 4, pp. 14 –24, july 2010.

[21] M. C. Yip, D. G. Lowe, S. E. Salcudean, R. N. Rohling, and C. Y. Nguan, "Tissue tracking and registration for image-guided surgery," *IEEE Transactions on Medical Imaging*, vol. 31, no. 11, pp. 2169–2182, 2012.

[22] C. Pantilie and S. Nedevschi, "Optimizing the census transform on cuda enabled gpus," in *IEEE International Conference on Intelligent Computer Communication and Processing (ICCP)*, 2012, pp. 201–207.

[23] F. Bookstein, "Principal warps: Thin-plate splines and the decomposition of deformations," *IEEE Transactions on Pattern Analysis and Machine Intelligence*, vol. 11, no. 6, pp. 567–585, 1989.

[24] S. Baker and I. Matthews, "Lucas-kanade 20 years on: A unifying framework," *International Journal of Computer Vision*, vol. 56, no. 3, pp. 221 – 255, 2004.

[25] F. Brunet, V. Gay-Bellile, A. Bartoli, N. Navab, and R. Malgouyres, "Feature-driven direct non-rigid image registration," *International Journal of Computer Vision*, vol. 93, pp. 33–52, 2011.

[26] G. Bradski, "The OpenCV Library," *Dr. Dobb's Journal of Software Tools*, 2000. [Online]. Available: http://www.opencv.org

[27] S. Giannarou, D. Stoyanov, D. Noonan, G. Mylonas, J. Clark, M. Visentini-Scarzanella, P. Mountney, and G.-Z. Yang, "Hamlyn Centre Laparoscopic / Endoscopic Video Datasets," 2012. [Online]. Available: http://hamlyn.doc.ic.ac.uk/vision/

Stereo and Shape-from-Shading Cue Fusion for Dense 3D Reconstruction in Endoscopic Surgery

Marco Visentini-Scarzanella, *Member, IEEE,* and Danail Stoyanov, *Member, IEEE*

***Abstract*—Dense 3D reconstruction of the surgical site is important for providing image-guidance, augmented reality and, in robotic surgery, active constraints. The challenge with endoscopic images is that soft-tissue surfaces do not always have salient characteristics and computational techniques fail to achieve unique correspondence. In this paper, we propose a novel method for handling homogenous regions by fusing visual cues using a combination of Shape-from-Shading (SFS) and stereo. A sparse reconstruction of the underlying structure is performed with a feature-based algorithm and used to initialise and guide two independent SFS modules, which infer monocular dense relative depth. The two reconstructions are then registered with nearest neighbour 3D matching, which is directly translated into a dense 2D disparity estimate. Our only assumption is consistency of the two reconstructions and this is sufficient for the overall scheme to be effective. We validate the approach quantitatively with benchmark phantom data and comparison against the state-of-the-art endoscopic reconstruction algorithms.**

I. Introduction

RECONSTRUCTING dense 3D information from intra-operative endoscopic videos is a fundamental building block for computer-assisted endoscopic interventions including image-guided navigation and dynamic active constraints [1], [2]. Active techniques such as structured light, time-of-flight and photometric methods can recover depth information without complex computational algorithms but they require significant adaptation to instrumentation which is a barrier to clinical translation. Vision-based techniques are currently an attractive approach for recovering the *in vivo* tissue morphology since they rely only on image information that is inherently used by the surgeon during procedures. The challenge of vision approaches is that surgical scenes are non-rigid, dynamic, have complex reflectance and surgical instruments create large discontinuities and occlusions.

Different visual cues can be used for reconstructing 3D geometry in endoscopic images [1], [3]. Stereoscopic approaches have received particular attention recently [4], [5] because stereo-laparoscopes are part of robotic surgery systems and are also now available for conventional laparoscopic instruments. One advantage of computational stereo is that tissue deformation due to breathing, peristalsis or the cardiac cycle can be dealt with on a per frame basis. This overcomes some of the difficulties in non-rigid Structure-from-Motion techniques that solve a complex and computationally intensive reconstruction problem [6]. While local propagation based computational stereo techniques have been shown to yield promising results for recovering 3D and motion [4], [3] such methods rely on salient tissue textures and produce results dependent on aggregation or correlation window sizes. Shape-from-Shading (SFS) on the other hand does not require textured surfaces but relies on homogeneous intensity variation to infer dense depth and the surface normals [7], [8], [9], [6], [10]. Recent applications of SFS to endoscopic data have attempted to use specularities to register the reconstructed surface in metric space [7], recovering the surface albedo through pre-operative calibration procedures [9], and methods to model the light source and estimate non-Lambertian BRDF parameters [10], [6] have been presented. Nevertheless, the numerical sensitivity of SFS makes it unsuitable for systems relying exclusively on it for reconstruction [10]. Attempts to combine the complementary attributes of stereo and SFS in endoscopy have been reported [11], [12] but were limited to local SFS assuming orthographic projection and suffered from cumulative errors because of the gradient propagation strategy. However, fusing visual cues is critical for building robust algorithms that can perform reliably like the human visual system even in difficult surgical images.

In this paper, we propose a novel method for combining stereo and SFS reconstruction to robustly recover dense 3D surface information from endoscopic videos. We exploit stereo vision by accurately reconstructing salient areas with strong texture and use this information to provide an initial estimate of the tissue albedo. Then each independent monocular channel is recovered via SFS reconstructions and aligned within the same frame of reference, providing estimates for textureless areas not recovered from stereo. Given the assumption that SFS is consistent between the two channels, which is strengthened further the common stereo initialisation of the two reconstructions, the two dense SFS reconstructions are registered together and their voxels matched in 3D. We validate our method quantitatively with phantom data and measure performance against image noise comparing it to state-of-the-art dense stereo reconstruction algorithms.

II. Method

The proposed method is schematically presented in Figure 2. Given a stereo image pair (I_L, I_R) from a calibrated laparoscope (C_L, C_R) images are fed into a sparse reconstruction algorithm **(1)** [4]. Each image is then processed independently by a SFS module together [7] with the sparse depth information **(2)**. The sparse stereo reconstruction initialises

M. Visentini-Scarzanella is with the Communications and Signal Processing Group, Imperial College London, London, UK, e-mail: (see http://www.commsp.ee.ic.ac.uk/ marcovs/contacts/).

D. Stoyanov is with the Centre for Medical Image Computing, University College London, UK, e-mail: (see http://www0.cs.ucl.ac.uk/staff/Dan.Stoyanov/).

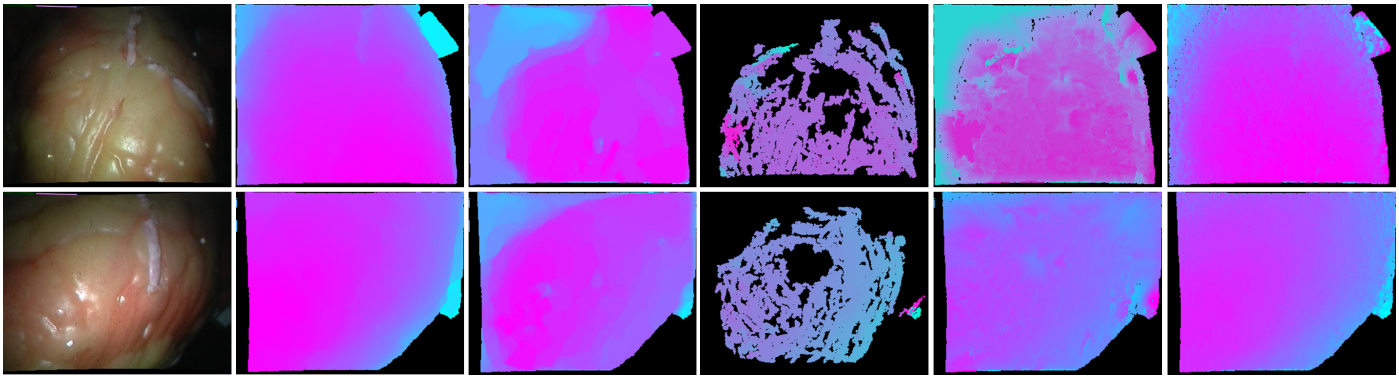

Fig. 1: From left to right: frame from the 'f5' and 'f7' datasets, ground truth disparity, disparities from the TV-L1 [13] algorithm, initial stereo reconstruction [4], SFS reconstruction initialised with stereo data, SFS reconstruction initialised with 5% of ground truth data.

depth and local albedo information for propagation by the SFS module to the remaining pixels. The two SFS reconstructions are then projected in 3D space and registered together for matching **(3)** with the ICP algorithm. As long as the SFS reconstructions are consistent between the two views, they should align perfectly after registration. This allows voxel matching from the two reconstructions via nearest neighbour search and immediately translates to matching between pixels through calibrated projection. A final step can be performed to optimise pixel matches with sub-pixel accuracy and these can be triangulated for the final 3D reconstruction.

III. Results

We evaluate our approach quantitatively on phantom data from the Hamlyn dataset (http://hamlyn.doc.ic.ac.uk/vision/). This consists of two stereo videos with ground truth from aligned dynamic CT data. We test the performance of the algorithm in two different scenarios: by initialising the SFS with different proportions of ground truth data and by initialising the SFS with the sparse stereo reconstruction instead. We further compare our approach with the dense stereo TV-L1 algorithm [13].

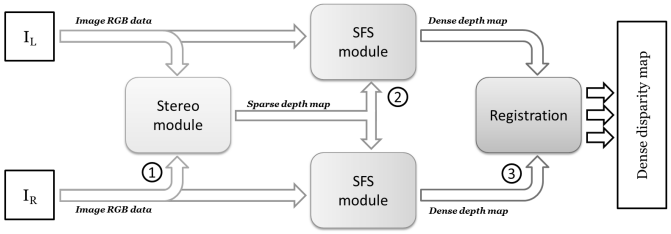

Fig. 2: Workflow for the proposed algorithm. (**1**) An input stereo image pair (I_L, I_R) is used to obtain an initial sparse stereo reconstruction. (**2**) The obtained depth map is then used with each image for a guided Shape-from-Shading dense depth estimate. (**3**) The two depth maps are then registered together for dense disparity map estimation.

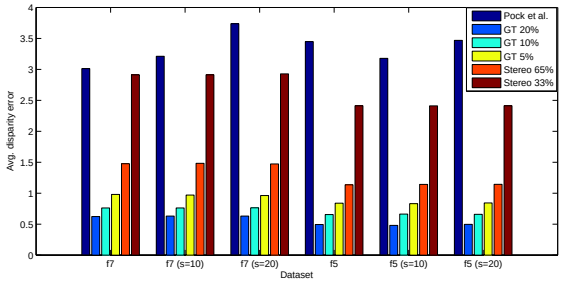

Fig. 3: Average pixel disparity error for the proposed method with different proportions of ground truth (GT) or stereo seeds and state-of-the-art dense stereo [13].

As shown in Figure 3, the ground truth initialisation allows the SFS algorithm to perform well even with very low proportions of initialised elements. The average disparity error was found to be below 2 pixels whenever more than 1% of the total image pixel count is supplied as seeds. The disparity error was measured exclusively on the reconstructed pixels. When the algorithm is initialised by very sparse stereo data, the performance degrades, since even with relatively accurate 3D information the surface normals estimated from stereo data for the albedo calculations are significantly different from the ground truth data. This can be handled by outlier rejection schemes and our current work does not incorporate this and wrong initial stereo matches can be propagated to the dense depth map. Nevertheless, our results show the capabilities of the proposed algorithm even in the presence of such initialization errors compared to the state-of-the-art. Indeed, global variational methods such as [13] suffer from the general lack of texture typical of endoscopic data, and the smoothness constraints imposed by such schemes confers the final disparity map a characteristically blotchy appearance. A visual representation of the dense disparities for the phantom and on *in vivo* data is shown in Figure 1.

IV. Conclusion

Robust reconstruction algorithms that can perform reliably, like the human visual system, in difficult surgical scenes are important for surgical vision and visual cue fusion is a critical element in realising robustness. Here we have proposed a method for 3D tissue surface reconstruction in endoscopic surgery using a novel combination of stereo and SFS. We have reported validation results on benchmark phantom data and compared our method against the state-of-the-art in endoscopic scene 3D reconstruction. In our future work we will focus on *in vivo* experimentation and on building discontinuity models into the framework so that instruments and occlusions do not perturb our reconstruction results.

References

[1] P. Mountney and G.-Z. Yang, "Motion compensated slam for image guided surgery," in *Medical Image Analysis and Computer-Assisted Intervention (MICCAI)*, Beijing, China, 2010, pp. 496–504.

[2] D. J. Mirota, M. Ishii, and G. D. Hager, "Vision-based navigation in image-guided interventions," *Annual Review of Biomedical Engineering*, vol. 13, no. 1, pp. 297–319, 2011.

[3] D. Stoyanov, "Stereoscopic scene flow for robotic assisted minimally invasive surgery," in *Medical Image Analysis and Computer-Assisted Intervention (MICCAI)*, Nice, France, 2012, pp. 479–486.

[4] D. Stoyanov, M. Visentini-Scarzanella, P. Pratt, and G.-Z. Yang, "Real-time stereo reconstruction in robotically assisted minimally invasive surgery," in *Medical Image Computing and Computer-Assisted Intervention (MICCAI)*, Beijing, China, 2010, pp. 275–282.

[5] S. Röhl, S. Bodenstedt, S. Suwelack, and *et al.*, "Dense gpu-enhanced surface reconstruction from stereo endoscopic images for intraoperative registration," *Medical Physics*, vol. 39, no. 3, pp. 1632–1645, 2012.

[6] A. Malti and A. Bartoli, "Estimating the cook-torrance brdf parameters in-vivo from laparoscopic images," in *Workshop on Augmented Environment in Medical Image Computing and Computer Assisted Intervention (MICCAI)*, Nice, France, 2012.

[7] M. Visentini-Scarzanella, D. Stoyanov, and G.-Z. Yang, "Metric depth recovery from monocular images using shape-from-shading and specularities," in *IEEE International Conference on Image Processing (ICIP)*, Orlando, USA, 2012, pp. 25 –28.

[8] C. Wu, S. Narasimhan, and B. Jaramaz, "A multi-image shape-from-shading framework fornear-lighting perspective endoscopes," *International Journal of Computer Vision*, vol. 86, pp. 211–228, 2010.

[9] G. Ciuti, M. Visentini-Scarzanella, A. Dore, A. Menciassi, P. Dario, and G.-Z. Yang, "Intra-operative monocular 3d reconstruction for image-guided navigation in active locomotion capsule endoscopy," in *IEEE RAS EMBS International Conference on Biomedical Robotics and Biomechatronics (BioRob)*, 2012, pp. 768 –774.

[10] T. Collins and A. Bartoli, "Towards live monocular 3d laparoscopy using shading and specularity information," in *International Conference on Information Processing in Computer-Assisted Interventions (IPCAI'12)*, Pisa, Italy, 2012, pp. 11–21.

[11] M. Visentini-Scarzanella, G. P. Mylonas, D. Stoyanov, and G.-Z. Yang, "*i*-brush: A gaze-contingent virtual paintbrush for dense 3d reconstruction in robotic assisted surgery," in *Medical Image Computing and Computer-Assisted Intervention (MICCAI)*, London, UK, 2009, pp. 353–360.

[12] B. P. L. Lo, M. Visentini-Scarzanella, D. Stoyanov, and G.-Z. Yang, "Belief propagation for depth cue fusion in minimally invasive surgery," in *Medical Image Computing and Computer Assisted Intervention (MICCAI)*, New York, USA, 2008, pp. 104–112.

[13] T. Pock, D. Cremers, H. Bischof, and A. Chambolle, "Global solutions of variational models with convex regularization," *SIAM Journal on Imaging Sciences*, vol. 3, no. 4, pp. 1122–1145, 2010.

Mechanical characterization of arterial tissue: Simultaneous confocal imaging and tensile testing

Rosalien Mariën, Marija Smoljkic, Rachel Geenens, Maarten Roeffaers, Jos Vander Sloten, Nele Famaey
Biomechanics Section, Department of Mechanical Engineering KU Leuven, Belgium
Molecular Imaging and Photonics, Faculty of Bioscience Engineering KU Leuven, Belgium

***Abstract*—To avoid damage as a consequence of a surgical procedure, it is important to define loading thresholds that can safely be applied to soft tissues. The goal of this research is to determine the mechanical properties of cardiovascular tissue, more specifically the sensitivity of the tissue to damage. To be able to quantify this sensitivity to damage, an experimental setup was designed. This setup can stretch a piece of cardiovascular tissue stepwise. After each elongation of the tissue a microscopic image can be taken with a confocal microscope. These images can then be analyzed in order to determine the strain of the tissue, the orientation of the fibers and the damage to the tissue. To study the elasticity of the tissue, the stress-strain curve was calculated for one of the tissue samples. The orientation of the fibers was compared at different depths in the sample. To determine the damage of the tissue, the number of microruptures in the tissue were analyzed. These first results are promising and serve as a proof of concept of the experimental setup.**

I. Introduction

Accurate mechanical characterization of cardiovascular tissue at micro-level is necessary for numerous applications. One of these applications is robotic surgery, where there is currently still a lack of haptic feedback, with tissue overload as a consequent risk. By means of an online finite element simulation with a realistic material model, extra information about damage to the tissue can be handed to the surgeon, based on forces measured during the surgical procedure. Another application for this model is the prediction of the behavior of aneurysms, to avoid rupture [1].

To obtain realistic results from this model, it is important that the material parameters of the model are known. Several testing devices exist to acquire the material parameters for the different constituents of the aorta.

Commonly material parameters are obtained by performing mechanical experiments using a uniaxial or biaxial test bench or a pressure-diameter test setup. However, this method provides only information about the passive tissue response. The active behavior of the smooth muscle cells is examined with a myograph. The histology of the tissue can be examined with a microscope [1]. To determine the parameters that take the damage of the tissue into account however, not many methods are available.

To obtain more information concerning these damage parameters and to examine the stress-strain relationship of the aortic tissue, an experimental setup was designed. With this setup it is possible to look at cardiovascular tissue on a microscopic level. These microscopic images can be analyzed to determine some of the damage parameters.

II. Materials and methods

A. Tissue preparation

Rat aortic tissue is used since its dimensions are similar to those of human arteries often encountered during surgery. The rats used in the experiments were all male and weighed 500 g. After excising the aortic tissue, a segment of the aorta was cut open. The surface of each sample is approximately 5 mm by 5 mm. All samples are stained with propidium iodide (excitation 536 nm; emission 617 nm) and Hoechst33342 (excitation 346 nm; emission 460 nm) [3]. Propidium iodide (PI) will color only the dead cells, the Hoechst staining the living cells. The staining protocol starts with rinsing the sample twice in fresh phosphate buffered saline (PBS). Afterwards, the tissue is placed in a PI solution for 30 minutes. The PI is diluted with PBS (1/100). The sample is then rinsed again in PBS, before it is placed in a Hoechst solution for one minute. The Hoechst is diluted with PBS (1/500). Finally the tissue is rinsed once more with PBS. The samples are preserved in PBS at a temperature of 4°C.

Prior to staining the samples were punctured with a needle to provide some reference points. To determine the optimal diameter of this needle, 3 needles with different diameters (1.1 mm, 0.45 mm and 0.15 mm) were used to puncture three different tissue samples. The needle with diameter 0.45 mm gave the best result: clearly defined regions of dead cells that are easily recognized. These reference points can be used to calculate the strain of the tissue, when strain mapping based on image correlation fails. They can also be used to keep track of the orientation of the tissue, e.g. by placing two points along the axial axis.

B. Testing device

A testing device, consisting of a uniaxial tensile test bench and a microscope, was built. The goal of this device is to enable stretching of the tissue in small steps, while simulateneously allowing a confocal microscope to take an image after each elongation step. During the experiments, a load cell continuously records the forces on the tissue. This setup can be seen in figure 1.

The two linear actuators ensure that the tissue can be stretched symmetrically up to 200% for a tissue sample of size 5 mm by 5 mm. The chosen actuators are the microslide series from Newmark Systems Inc, with steppermotor. Only one load cell is necessary due to the symmetric application

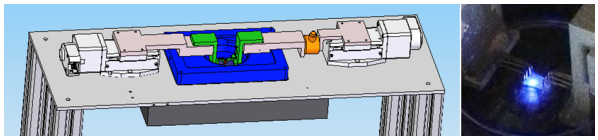

Fig. 1. (Left) Uniaxial tensile device: table with adjustable height (gray), stage of microscope (black), actuators (white), load cell (orange), clamps (green) and perfusion chamber (blue). The total length of the tensile test bench is 215mm.; (right) Snapshot of a mounted sample.

of force. The 'Model 31 mid-range precision load cell' from Honeywell is used. This load cell can measure forces up to 23 N, using four strain gauges in a full Wheatstone bridge. The tissue can be fixed to the tensile test bench with the aid of two clamps, see figure reffig:testsetup, which in turn are connected to the device through magnets. The clamps have several hooks (diameter: 0.9 mm) attached to them, used to mount the sample. The aortic tissue can be placed inside a heated perfusion chamber (the 'Heating Insert M' from Pecon) to keep it viable. The system is placed under an Olympus Fluoview1200 IX81- ZDC confocal microscope.

C. Imaging protocol

The wavelengths of the lasers of the microscope used during the experiments, are 405 nm and 552 nm. The beamsplitter splits the beam of light into two beams, one with frequencies above 490 nm, one with frequencies below 490 nm. Since the experiments are dynamic, the pinhole is completely opened. The image is magnified 10 times.

D. Data analysis

Three analyses are executed on the microscopic images. The stress-strain relationship is examined, as well as the orientation of the fibers and the damage to the tissue.

Stress-strain analysis: The one-dimensional second Piola-Kirchoff stress S_{11} and the lagragrian strain E_{lag} are calculated.

$$S_{11} = \frac{FL_0}{A_0 L} \tag{1}$$

$$\mathbf{E}_{lag} = \frac{1}{2}(\mathbf{U}^2 - \mathbf{I}) \tag{2}$$

with F being the force, L_0 the initial length of the tissue, L the current length of the tissue, A_0 the initial surface size of the tissue, $\mathbf{I}$ the identity tensor and U the right Green-Lagrange strain tensor. More information about these tensors can be found in [1].

The lagrangian strain is calculated based on digital image correlation with Vic-2D, a software from Correlated Solutions. The program tries to find a certain gray value pattern in consecutive images. Based on the correlation between two images, the software calculates the displacement vector for all points and consequently the strain in the images [4].

Orientation of the fibers: In the images, elastin and collagen fibers can be recognized. Since both contribute to the mechanical properties of the tissue, it is important to study them. The orientation of the fibers is studied with the program ImageJ, more specifically with OrientationJ. The hessian matrix is calculated for each point in the image. The

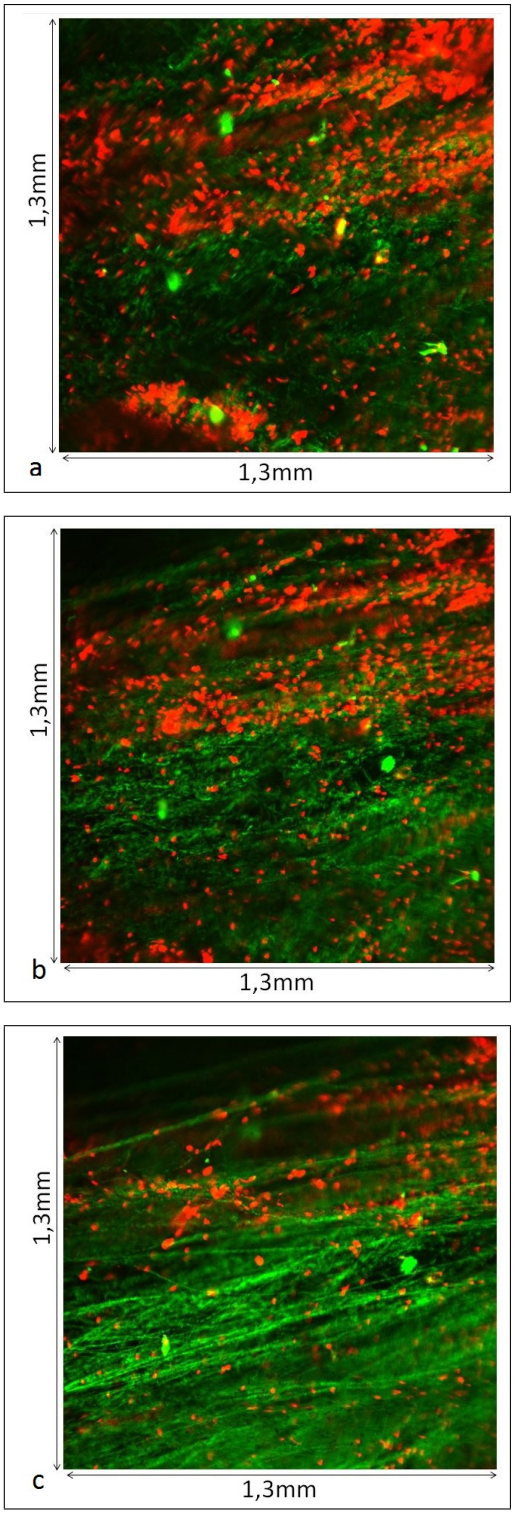

Fig. 2. Segment (1.3 mm by 1.3 mm) of a specimen (5 mm by 5 mm) stained with PI and Hoechst. The depth of the image is 125-150 micron. The tissue is stretched under the confocal microscope: a) unstretched, b) 1.3 mm stretched and c) 2.6 mm stretched.

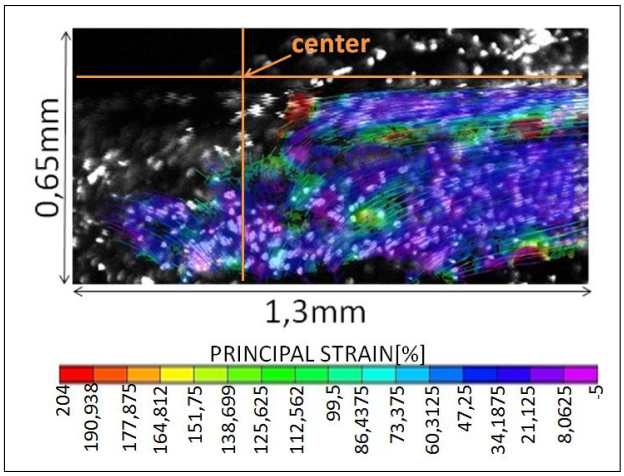

Fig. 3. Strain and displacement, calculated with Vic-2D for the image taken at a motor displacement of 1.3mm. The depth of the image is 125-150 micron.

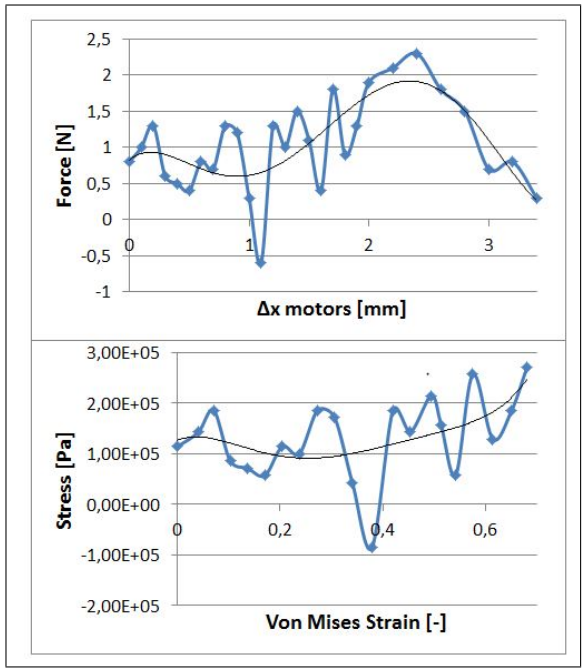

Fig. 4. (Top) Force as a function of motor displacement (Bottom)Stress-strain curve for a depth of 125-150 micron.

eigenvalues of this matrix correspond to the curvature values, the eigenvectors to the principal directions [5].

Damage to the tissue: The damage can be determined in two ways. A first possibility is to look at the evolution of the number of dead cells. A second possibility is to look at the evolution of the number of micro-ruptures in the tissue.

III. RESULTS

The analyses described above have been performed on data from one tissue sample. The results in this section are therefore *not* statistically relevant, but serve as a proof of concept. Microscopic images of this sample in the unstretched condition and in two stretched conditions can be seen in figure 2.

A. Stress-Strain

Lagrangian strain From the microscopic images the strain can be calculated with Vic-2D. The strain in the principal direction is depicted in figure 3 with a colormap. Only the top half of the microscopic image is depicted, since only at the top half of the image enough dead cells were visible to calculate the correlation between consecutive images. The small vestors in this figure depict the displacement compared to the unstretched condition. The strain calculated by Vic-2D is on average 0.129 mm smaller than the displacement of the motors. This is due to the fact that the sample ruptures around the hooks of the clamps. To determine where the center of the tissue is in the image, one can look at the orientation of the displacement vectors on figure 3. The y-axis (the axial axis) can be found in the region where the displacement vectors move apart. One part of the displacement vectors moves towards the left side, the other part towards the right side. The displacement vectors don't move horizontally, but a slightly upwards. This is due to the poisson effect. The x-axis (the transversal axis) lies at the top of the image where the the displacement vectors run horizontally.

Second Piola-Kirchoff stress Using the force data recorded during the experiments, the second Piola-Kirchoff stress can be calculated. The measured force has a large variability (see top figure 4), this can be explained by the fact that the experiments were performed pseudo-statically. It took about 60 seconds to take an image after displacement of the motors. During this time the tissue had time to relax.

Stress-strain curve The stress-strain curve can be seen in figure 4.

B. Fiber orientation

In the microscopic images (figure 2), it can clearly be seen that the fibers start to align during stretching. The fibers visible on the images are elastin and collagen fibers. They are autofluorescent and their emission spectra are in the same region as that of the Hoechst staining (elastin: 405 nm; collagen: 390 nm) [6]. Therefore they are visible in the green spectrum.

The orientation can be calculated with OrientationJ. Since it is interesting to compare the orientation of the fibers at different depths, this analysis was executed for three slices, 25 micron between each slice (figure 5).

The measured fiber angles of these slices are similar, therefore it is probable that the fibers from the three different depths belong to the same fiber family. In literature, the angles of the fibers with reference to the axial axis are located between $-5°$ and $-5°$ [8]. As can be seen on the figure, the values obtained with OrientationJ are in line with these results.

C. Damage to the tissue

The damage to the tissue can be quantified by looking at the evolution of the number of dead cells and the number of

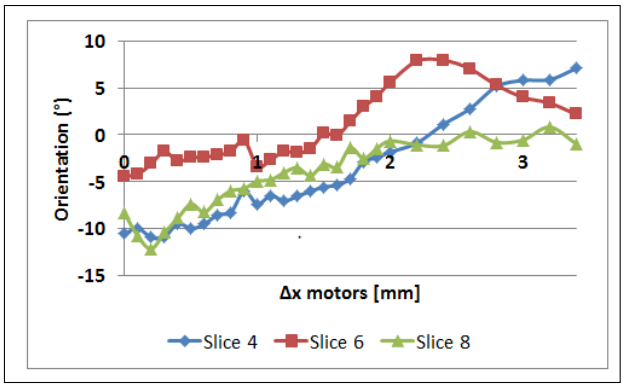

Fig. 5. Comparison of the orientation of the fibers: slice 4 (depth: 75-100 micron), slice 6 (depth: 125-150 micron) and slice 8 (depth: 175-200 micron).

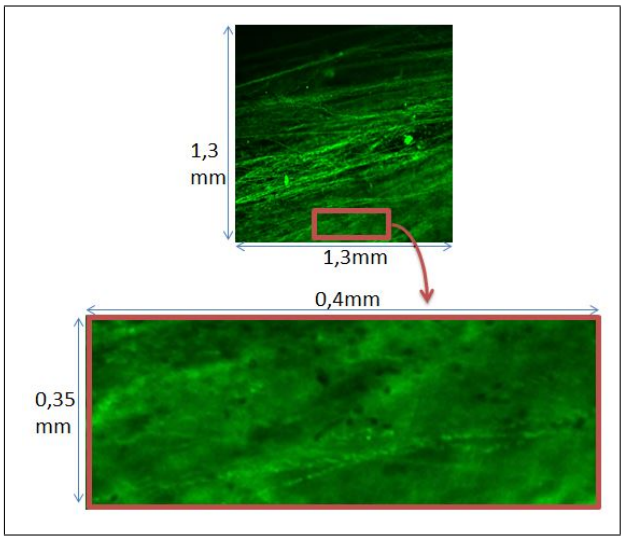

Fig. 6. Black dots appearing in images: possible micro-ruptures.

micro-ruptures.

Evolution of micro-ruptures It is possible to see more and more black dots appearing in the images, as the tissue gets stretched further, see figure 6. It is hypothesized that these dots are micro-ruptures. The decrease in the force around the time these dots appear, seems to support this theory. Further testing is necessary to confirm this.

Assuming that these black dots are indeed micro-ruptures, the evolution in the number of micro-ruptures can be seen in figure 7. The drop in the curve can be explained by several smaller micro-ruptures combining into some larger micro-ruptures.

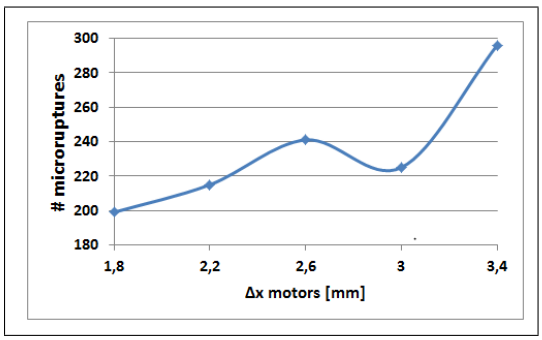

Fig. 7. Damage to the tissue: evolution in the number of micro-ruptures

Evolution of dead cells To be able to see more dead cells appearing as the tissue gets stretched and thus damaged more, the staining protocol needs to be adapted as described in [2]. The PI is than diluted in Hank's Balanced Salt Solution (HBSS) with a concentration of 1.5 M. The staining happens inside the perfusion chamber and is added 30 minutes prior to the start of the experiments. The tissue is not rinsed after applying the staining.

This protocol was not yet applied in the executed experiments.

D. Determination of damage-parameters

With the information from the images and the recorded forces, several parameters of the material model can be derived. The material model requires for example information about the angle of the collagen fibers. The results from the analysis in OrientationJ can directly be implemented here. Information about the damage parameters can also be accessed with the testing device. For example, one of the parameters that needs to be defined, is a dimensionless variable that brings the damage to the fibers into account. This parameter can be determined by looking at the occurrence of micro-ruptures. Another damage parameter is a dimensionless variable that brings the damage to the extracellular matrix into account. To fill this parameter in, more tests need to be performed with PI staining, continuously surrounding the tissue, as described above. That way the ratio of the number of dead cells and the total number of cells can be used to derive this dimensionless parameter.

IV. CONCLUSION

The designed setup was able to capture the deformation in the aortic tissue on a micro-level during stretching. This setup is of great assistance in determining realistic material parameters for cardiovascular tissue.

REFERENCES

[1] N. Famaey, Soft tissue damage prevention in surgery: an experimental and computational framework with application to arterial clamping, Ph.D. dissertation, Dept. Biom. Eng., KULeuven, 2012.
[2] R.T.A. Megens, Two-Photon Microscopy of Vital Murine Elastic and Muscular Arteries, Journal of Vascular Research 2007, 44:87-98, DOI: 10.1159 / 000098259.
[3] Dojindo, Cell Staining, URL: www.dojindo.com.
[4] B. Pan, Two-dimensional digital image correlation for in-plane displacement and strain measurement: a review, IOP publishing: measurement scienceand technology, 2009, doi:10.1088/0957-0233/20/6/062001.
[5] F. Daniels, Quantification of Collagen Orientation in 3D Engineered Tissue, Master thesis, Eindhoven university of technology, 2006.
[6] F.W.D. Rost, Fluorescence microscopy. 2, Cambridge University Press, 1995, ISBN 0 521 42277 9.
[7] MK. OConnell et al., The three-dimensional micro- and nanostructure of the aortic medial lamellar unit measured using 3d confocal and electron microscopy imaging, Matrix Biol 27(3):171181, 2008

Patient-Specific Design of Multi-Component Steerable Catheters

Phuong Toan Tran*, Alain Devreker*, Gabrijel Smoljkic*, Herbert De Praetere†, Paul Herijgers†,
Emmanuel Vander Poorten*, Jos Vander Sloten*
*Department of Mechanical Engineering, KU Leuven,
†Experimental Cardiac Surgery, University Hospital Leuven, Leuven, Belgium

***Abstract*—Catheter-based diagnostic and therapeutic interventions are gaining in popularity due to the limited invasive nature of the approach. This evolution persists despite limited visualisation and manoeuvrability of the catheter within the vasculature. 2D X-ray angiographic and fluoroscopic imaging methods expose patients to increased levels of radiation [1] and require injection of contrast agent prone to allergic reactions [2]. To overcome the absence of depth information, notable efforts are being conducted to fuse real-time 2D fluoroscopic images with pre-operatively reconstructed 3D models [3]. When deformations of the cardiovascular system occur due to physiological phenomema, the intervention, or due to the introduction of fairly stiff instruments, it becomes difficult to rely on pre-operative data. To overcome the abovementioned issues, CASCADE, a recent EU-funded FP7 project, investigates the development of *self-aware* robotic catheters. These steerable catheters embark several sensors to intra-operatively capture and reconstruct the vasculature *from within* the vessel. The development of such catheters is challenging, as the additional sensors should not interfere with the catheter's main diagnostic or therapeutic purpose. For trans-catheter aortic valve implantation (TAVI), the catheter should still be able to safely reach the implantation site to implant the replacement valve. Furthermore, since patients and implants differ, solutions should be patient-specific. This abstract presents a method to design patient-specific multi-component steerable catheters. Results suggest that for TAVI a pair of adequately-placed short 2-DoF actuators can substantially limit the interaction with the vasculature. Where the current approach is geometric, it should be expanded to better account for the dynamics of and the interaction with the cardiovascular system.**

I. Introduction

For the last decades, minimally invasive interventional techniques have been increasingly adopted all over the world. With smaller incisions and reduced tissue dissection, these procedures allow not only faster recovery and better patient satisfaction, but also treatment of patients that would be considered inoperable with classical surgery. However, due to the reduced field of view and restrained access to the patient's anatomy, minimally invasive approaches require alternative imaging systems and increased dexterity to appropriately control the instruments. In general, long learning curves are associated to these procedures. In particular, this is true for catheter-based endovascular procedures where conventional catheters provide very limited manoeuvrability and where fluoroscopic and echographic images give few insights about the location of the catheter within a dynamic and deformable vascular environment. Recent steerable catheter technology allows overcoming some of these limitations. Through internal actuation, these catheters can adapt the shape of their distal extremity [4]. However, also here safe operation relies on accurate visualization and registration of catheter pose relative to the environment. Research conducted within the CASCADE project departs from traditional fluoroscopic and echographic imaging and focuses on the integration of embedded sensors into steerable catheters, providing them with real time proprioceptive and exteroceptive senses. One of the challenges is to incorporate actuators and sensors while not interfering with the original diagnostic or therapeutic purpose.

In this paper, we present a method for designing multi-component steerable catheters for TAVI. TAVI treats stenosis of an aortic valve by implanting a stent-mounted bioprosthetic valve delivered on-site by a catheter. The latter is inserted through a vascular access site (e.g. the femoral artery) and guided up to the stenotic native valve where the implant is released [5]. The proposed approach allows patient-specific selection of a catheter configuration based on a geometric analysis of the interactions between the catheter distal extremity and the vascular environment.

In the remainder of this paper, section II describes the vessel and catheter models, as well as the developed optimization program. Section III presents the results of our simulations. Finally, section IV concludes this report by discussing directions for future developments.

II. Methods and Materials

A. Catheter Specifications

An envisioned catheter for efficient and safe TAVI integrates at its distal extremity a force sensor monitoring the interactions between the catheter distal tip and the vessel wall, a flow sensor for localisation of vessel branches, an intravascular ultrasound (IVUS) probe imaging successive aorta cross-sections during the procedure, and electromagnetic position sensors for registering the catheter position. Although several mechanisms for catheter steering have been developed in the past [4], the present work focuses on hydraulic McKibben actuators [6] with constant curvature deflection. Without loss of generality modules with 2 degrees of freedom (DoFs) to adjust the bending radius and the bending direction are considered. Table I presents typical dimensions used for the components of the envisioned catheter. McKibben actuators are enclosed by rigid spacers that serve as a base to attach the actuators to the catheter. Note that given their small dimensions, flow and position sensors are not modeled here.

TABLE I. DIMENSIONS AND MODELS OF CATHETER COMPONENTS

Rigid cylinder		
Component	**Diameter[mm]**	**Length[mm]**
Force sensor (EndoSense TactiCath)	2.5	20
IVUS (Volcano Visions PV 8.2F)	2.5	15
Position sensor (NDI Aurora 5DoF)	0.9	12
Valve (Edwards SAPIEN)	6	25
McKibben spacer	5	5
Section of torus		
Component	**Diameter[mm]**	**Length[mm]**
McKibben actuator	5	10 - 90
Rectangular plate		
Component	**Dimensions[mm]**	
Flow sensor (M7 Devices)	1.6×1×0.5	

The particular nature of TAVI and cardiovascular procedures in general constrains already the number of possible catheter configurations. To minimize surgical risks during TAVI, the catheter distal tip should ideally not intrude more than 50mm into the heart chamber when deploying the valve implant (in this first approach, this constraint is relaxed to 75mm). In addition, when using a force sensor, this must be placed at the very tip of the catheter, while the IVUS probe should be as close as possible to the tip. Given these constraints, possible configurations, starting from the catheter tip are:

Force sensor - IVUS - Valve - n McKibben (1)

Force sensor - IVUS - m McKibben - Valve - p McKibben (2)

with $m + p = n$, the number of 2-DoF McKibben modules.

B. Optimization Goal and Principle

The objective is now to determine the number, the length and the order of occurence of the McKibben actuators, so that minimal contact between the catheter and the vessel wall can be achieved while the former is being advanced along the vessel up to the heart chamber. All possible combinations of lengths according configurations (1), (2) and within the ranges of Table I are investigated. It is hypothesized that if at least theoretically (in the absence of gravity) the catheter can adopt a shape maximally coinciding with the center line, such configuration possesses excellent properties to also in reality limit the contact with the vasculature. In search for an ideal configuration we therefore solve for each configuration and for each place along the center line the actuation angles needed to maximally align both. At any point on this trajectory, if collisions between the catheter and the vessel wall occur, the penetration depth is evaluated. In combination with other design constraints, such as length and actuator bending radius, the penetration depth is used to compute an overall quality score for each configuration.

C. Aorta Model

A triangular surface mesh of the vessel wall is reconstructed using a CT scan provided by the Department of Radiology of the University Hospital. The center line is generated by taking the center of circles that approximate successive aorta cross-sections along the entire aorta. The resulting center line is resampled to obtain the desired resolution (Fig.1). Generation of the aorta mesh and center line is performed using Mimics (Materialise - Leuven, Belgium) and pyFormex [7].

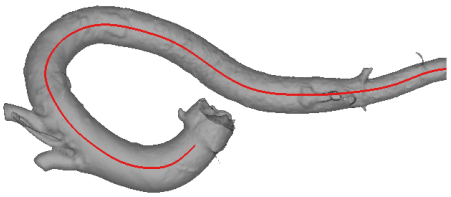

Fig. 1. Aorta mesh and center line (red) reconstructed from a CT scan.

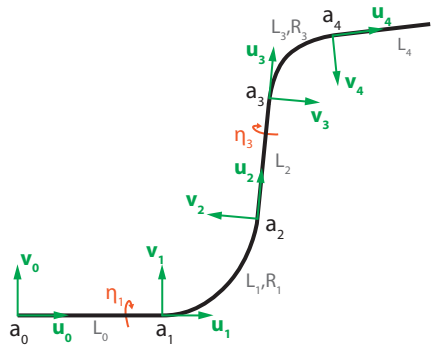

Fig. 2. Center line for catheter with 2 McKibben actuators. Part i of the catheter has a length L_i and is associated with a local reference frame $(\boldsymbol{u_i}, \boldsymbol{v_i}, \boldsymbol{n_i})$. Each actuator (here 1 and 3) possesses 2 DoFs: R_i and η_i.

D. Catheter Model

Two different representations of the catheter are used in the simulation. The catheter center line is used to simulate the catheter motion inside the aorta. A catheter mesh is used to detect and evaluate penetrations with the aorta.

1) Catheter Center Line: The catheter center line is modeled as a succession of line segments and circular arcs representing the different rigid components (sensors, McKibben spacer, valve) and the McKibben actuators respectively. This leads to a set of piece-wise parametrized vectorial equations of lines and circular arcs. Fig.2 shows the center line of a catheter with 2 McKibben actuators. Unit vectors $\boldsymbol{u_i}$ are defined such that each part of the center line is tangent to the previous one. Vectors $\boldsymbol{u_i}$ and $\boldsymbol{v_i}$ are orthogonal and form a plane in which the catheter part i lays. Together with $\boldsymbol{n_i} = \boldsymbol{u_i} \times \boldsymbol{v_i}$, they define a local reference frame on each part at $\boldsymbol{a_i}$. Each McKibben actuator has 2 DoFs: the bending radius R_i and the bending direction modeled by the angle η_i between $\boldsymbol{v_{i-1}}$ and $\boldsymbol{v_i}$. The angle η_i is the angle of rotation about vector $\boldsymbol{u_i}$.

2) Catheter Mesh: The catheter mesh is used to detect and evaluate collisions between the catheter and the vessel wall. Meshes of components described in Table I are obtained by folding a plane of triangular elements and closing the resulting surface with appropriate disks. Individual components are then automatically assembled using local frames defined at the extremities of each component. Parametric generation of such meshes is realized with pyFormex (Fig.3).

E. Catheter Motion

1) Optimization Program: Given one catheter configuration with n_{arcs} McKibben actuators, let $\boldsymbol{p_i}$ $(i = 0, \ldots, n-1)$ be n points of the catheter center line C_1, starting from the catheter proximal tip. $\boldsymbol{q_j}$ $(j = 0, \ldots, m-1)$ are m points of the aorta center line C_2, starting from the abdominal aorta

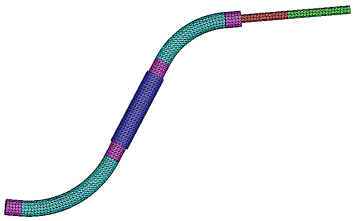

Fig. 3. Catheter mesh with force sensor (green), IVUS probe (red), valve implant (blue), McKibben spacers (magenta) and McKibben actuators (cyan).

to the heart valve. The proximal tip $\boldsymbol{p_0}$ of the catheter is fixed to a point $\boldsymbol{q_j} \in C_2$. The objective is then to find the transformation parameters to apply to C_1 to maximally fit C_1 to C_2. By finding these parameters for every point $\boldsymbol{q_j}$ of the aorta center line and applying these parameters to C_1, catheter motion along the aorta center line is simulated.

In total $3+2n_{arcs}$ DoFs are to be solved by this optimization problem, namely: 3 rotations about point $\boldsymbol{q_j}$ described by unit quaternion $z = (z_0\,; z_1\,; z_2\,; z_3)$ and transformation matrix $T(z)$; the change of the n_{arcs} radii R_k and n_{arcs} axial rotations η_k about the catheter center line. Let C_1' be the catheter center line after applying these transformations. By defining the distance between point $\boldsymbol{a}$ and curve C with points $\boldsymbol{b_j}$ as:

$$\mathrm{d_{min}}\left(\boldsymbol{a},\, C\right) = \min_j \|\boldsymbol{a} - \boldsymbol{b_j}\|, \tag{3}$$

a function F that must be minimized can be defined as the bidirectional point to curve mean squared distance:

$$F(z, R_k, \eta_k) = \frac{1}{2}\left[\frac{1}{n}\sum_{i=0}^{n-1} \mathrm{d_{min}}\Big(T(z)\boldsymbol{p_i}(R_k, \eta_k),\, C_{2,r}\Big)^2 + \frac{1}{t}\sum_{l=j}^{j+t-1} \mathrm{d_{min}}\Big(\boldsymbol{q_l},\, C_1'(z, R_k, \eta_k)\Big)^2\right] \tag{4}$$

The aorta center line C_2 is restrained to the portion of interest $C_{2,r}$ containing t points from $\boldsymbol{q_j}$ to $\boldsymbol{q_{j+t-1}}$. The minimization of (4) is subject to the following constraints and boundaries:

$$\|z\| = 1 \tag{5}$$
$$T(z)\boldsymbol{u_0} \cdot (\boldsymbol{q_{j+1}} - \boldsymbol{q_j}) \geq 0 \tag{6}$$
$$-1 \leq z_i \leq 1 \text{ for } i = 0, \ldots, 3 \tag{7}$$
$$R_{min} \leq R_k \;(k = 2l+1 \text{ for } l = 0, \ldots, n_{arcs}-1) \tag{8}$$
$$-\pi < \eta_k \leq \pi \;(k = 2l+1 \text{ for } l = 0, \ldots, n_{arcs}-1) \tag{9}$$

Equation (6) constrains the first segment of C_1' to the local direction of C_2 at $\boldsymbol{q_j}$. R_{min} in (8) is defined as $R_{min}{=}\frac{L_k+\Delta}{2\pi}$ where L_k is the arc length and Δ=20mm.

2) Optimization Algorithm: The optimization program that minimizes objective function (4) under constraints (5-6) and within boundaries (7-9) is numerically solved within pyFormex with the sequential least squares programming (SLSQP) solver of the SciPy library [8], [9]. The initial guess required for such numerical solver is based either on a geometric analysis of the aorta center line shape or on the results of previous optimization steps. The set of initial parameters that allows achieving the minimal objective function value after optimization is used to determine the optimal parameter set.

TABLE II. CHARACTERISTICS OF MESHES AND CENTER LINES

	Aorta		Catheter	
	Mesh	**CenterLine**	**Mesh**	**CenterLine**
Resolution[mm]	0.97	3.97	1.09	2.15
Vertices	99556	113	1353-4396	37-125
Faces	199100	-	2916-9252	-
Length[mm]	-	445	-	80-260

F. Catheter Penetration Depth

For each point $\boldsymbol{q_j}$ on the aorta center line C_2, the catheter mesh is generated according to the result of the optimization program described in section II-E. Potential collisions with the aorta are detected and evaluated using ray tracing algorithms based on the Jordan curve theorem [10], [11] and Kd-tree nearest neighbors [12]. For our purpose of comparing different catheter configurations in a vessel with relatively limited tortuosity, the penetration depth $d_{p,j}$ of the catheter inside the aorta wall for position $\boldsymbol{q_j}$ can be defined as

$$d_{p,j} = \sum_{h=0}^{n_{out,j}-1} \min_g \left\|\boldsymbol{m_{cath,h}} - \boldsymbol{m_{aorta,g}}\right\|^2 \tag{10}$$

with $\boldsymbol{m_{cath,h}}$ $(h = 0, \ldots, n_{out,j}-1)$ the location of the $n_{out,j}$ vertices of the catheter mesh that lie outside the aorta for the simulated step $\boldsymbol{q_j}$ and with $\boldsymbol{m_{aorta,g}}$ the locations of the vertices of the aorta mesh.

G. Characterization of Catheter Configurations

By defining $d_p^{ci} = \sqrt{\sum_j d_{p,j}}$ and $\theta^{ci} = \max_k \frac{L_k}{R_{k,min}}$, each configuration ci is characterized by a score

$$S^{ci} = \alpha\frac{d_p^{ci}}{\max_{ci} d_p^{ci}} + \beta\frac{\theta^{ci}}{\max_{ci}\theta^{ci}} \tag{11}$$

The lower the score, the better the configuration is. The α-term relates to the amount of collisions that the catheter produces when following the aorta center line. The β-term accounts for the design constraints of the actuators. Shorter length L_k of actuators k allows easier local position control. On the other hand it is harder to manufacture actuators k that can generate a very small bending radius $R_{k,min}$.

III. RESULTS

Fig.4 compares the scores obtained for each catheter configuration. For this evaluation, α and β were set to $\alpha = 0.7$ and $\beta = 0.3$, putting thus a relative high weight β on ease of manufacturing. A maximum of 2 McKibben actuators is considered. Their respective length varies from 10 to 90mm with a 10mm step. Following the catheter specifications described in section II-A, 110 different configurations are compared. Characteristics of meshes and center lines generated during the simulations are presented in Table II. The resolution is the mean distance between adjacent vertices. The vessel center line is restricted from the abdominal aorta to the aortic valve. Simulations are performed on a PC with 2 Intel Xeon CPU E5-2620 @ 2.00GHz and 32GB RAM. The total computation time was about 110 hours (thus about 1 hour per configuration). We expect that there are still substantial opportunities to further speed up the current implementation. Collisions between

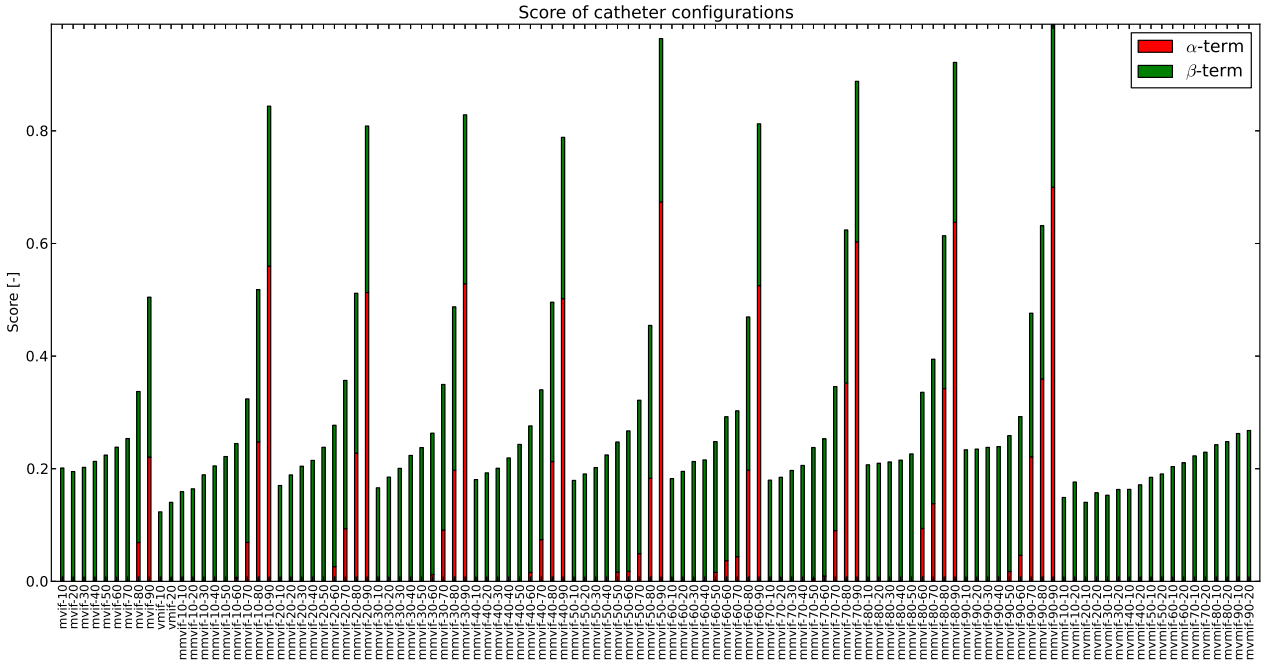

Fig. 4. Score of each catheter configuration. Each configuration is identified by an acronym stating which components are in the catheter (m: actuator, v: valve, i: IVUS sensor, f: force sensor), the relative order (from proximal part to distal tip), and the actuator length (from proximal part to distal tip) in mm.

catheter and vasculature occur when the actuator length limits the catheter manoeuvrability. This occurs when there is no actuator between valve and sensors. Such an actuator would allow better controllability since rigid parts of the catheter are shorter and can be steered more efficiently to avoid contact. The required bending angle generally increases with actuator length, since longer actuators have to bend more to follow the aorta center line, especially in the region of the aortic arch. These results thus suggest that an optimal catheter configuration for TAVI should include short actuators adequately located to deal with the rigid parts of the catheter.

IV. Conclusion

This paper describes a first approach to design multi-component steerable catheters comprising 2-DoF actuators with constant curvature deflection. Current simulation results favor adequately placed short actuators. However, the results are based on a pure geometric analysis, assuming that the catheter's proximal part always lays on the aorta center line. A simulation incorporating the mechanical properties of the catheter, such as described in [13], and more efficient and precise collision detection would allow better estimates of the contact and interactions with the vessel. Although illustrated for TAVI, the presented method can be applied to other procedures that would benefit from multi-component catheters.

Acknowledgment

This research was supported by the EU's Seventh Framework Programme under GA No. 601021 (CASCADE).

References

[1] I. Pantos, G. Patatoukas, D. Katritsis, and E. Efstathopoulos, "Patient radiation doses in interventional cardiology procedures," *Current Cardiology Reviews*, vol. 5, no. 1, pp. 5–11, 2009.

[2] M. Saljoughian, "Intraveous radiocontrast media: A review of allergic reactions," *US Pharmacist*, vol. 37, no. 5, pp. 14–16, 2012.

[3] S. Liao, R. Miao and Z. Y., "Automatic and efficient contrast-based 2-d/3-d fusion for trans-catheter aortic valve implantation (tavi)," *Computerized*, vol. 37, pp. 150–161, 2013.

[4] Y. Fu, H. Liu, W. Huang, S. Wang, and Z. Liang, "Steerable catheters in minimally invasive vascular surgery," *The International Journal of Medical Robotics and Computer Assisted Surgery*, vol. 5, no. 4, pp. 381–391, Jul. 2009.

[5] C. R. Smith, M. B. Leon, M. J. Mack, D. C. Miller, J. W. Moses, L. G. Svensson, E. M. Tuzcu, J. G. Webb, G. P. Fontana, R. R. Makkar *et al.*, "Transcatheter versus surgical aortic-valve replacement in high-risk patients," *New England Journal of Medicine*, vol. 364, no. 23, pp. 2187–2198, Jun. 2011.

[6] A. Moers, M. De Volder, and D. Reynaerts, "Integrated high pressure microhydraulic actuation and control for surgical instruments," *Biomedical Microdevices*, vol. 14, no. 4, pp. 699–708, Aug. 2012.

[7] B. Verhegghe. pyFormex Homepage. [Online]. Available: http://www.nongnu.org/pyformex/

[8] D. Kraft, "A software package for sequential quadratic programming," DLR German Aerospace Center – Institute for Flight Mechanics, Koln, Tech. Rep. DFVLR-FB 88-28, 1988.

[9] E. Jones, T. Oliphant, P. Peterson *et al.* (2001) SciPy: Open source scientific tools for python. [Online]. Available: http://scipy.org/

[10] J. O'Rourke, *Computational geometry in C*. Cambridge university press, 1998.

[11] C. J. Ogayar, R. J. Segura, and F. R. Feito, "Point in solid strategies," *Computers & Graphics*, vol. 29, no. 4, pp. 616–624, Aug. 2005.

[12] J. L. Bentley, "Multidimensional binary search trees used for associative searching," *Communications of the ACM*, vol. 18, no. 9, pp. 509–517, Sep. 1975.

[13] T. Alderliesten, M. K. Konings, and W. J. Niessen, "Modeling friction, intrinsic curvature, and rotation of guide wires for simulation of minimally invasive vascular interventions," *Biomedical Engineering, IEEE Transactions on*, vol. 54, no. 1, pp. 29–38, Jan. 2007.

Intravascular Modeling and Navigation for Transcatheter Aortic Valve Implantation

Chaoyang Shi, Stamatia Giannarou, Su-Lin Lee, Guang-Zhong Yang

***Abstract*—This paper proposes a new vasculature modeling scheme based on the data fusion from intravascular ultrasound (IVUS) and electromagnetic (EM) tracking for Transcatheter Aortic Valve Implantation (TAVI). The system is suitable for obtaining inner cross section images of blood vessels, as well as capturing the corresponding pose of the probe from an electromagnetic sensor. Three-dimensional (3D) modeling of blood vessels is provided to facilitate intra-operative surgical guidance for the alignment of the artificial and native valves. A hybrid probe consisting of an IVUS sensor and an EM sensor has been integrated to capture data from both sensors simultaneously. An image processing method based on the gradient vector flow (GVF) snake method has been proposed, followed by the use of kinematic transformations to convert the image coordinates into 3D coordinates to reconstruct the anatomical model. The method could reduce the time of valve alignment, improve the precision for positioning, minimize the use of contrast agent and assess the status of deployed valve after surgery.**

I. Introduction

Aortic valve stenosis is characterized by the narrowing and obstruction of the valve between the left ventricle of the heart and the ascending aorta, leading to cardiac decompensation, chest pain and even sudden death. The standard procedure for surgical Aortic Valve Replacement (AVR) requires making a large incision by opening the chest, cutting off the ascending aorta from the heart, and using a cardiopulmonary bypass. This leads to significant trauma, long postoperative recovery time and a high mortality rate. Moreover, around 30% to 60% of patients cannot undergo this therapy, due to advanced age, left ventricular dysfunction, or the presence of multiple coexisting conditions [1].

To overcome these problems, the new technology of TAVI has been proposed to offer an alternative to minimize the trauma induced in traditional approaches [2]. The implantation procedure involves accessing a femoral artery and performing balloon valvuloplasty, followed by advancing a compressed bioprosthetic valve and then deployed by inflating the balloon on a catheter when reaching the native aortic valve. This new technology carries a significantly reduced mortality rate, with a mortality figure of 30.7% compared to 50.7% for the conventional standard treatment in one year [2].

For TAVI, however, there are also several challenges associated with this new technology. For instance, the width of the native valve and its annulus is small. High or low valve placement relative to the native valve annulus will destroy the artificial valve or obstruct the coronary artery, leading to disastrous complications. Therefore, visualization and localization of the native valve annulus, and precise alignment and placement of the artificial valve on the correct location relative to this annulus is a crucial and time-consuming step. During the TAVI procedure, contrast enhanced C-arm fluoroscopy is usually used to provide intraoperative guidance. However, such technology can only provide 2D information for visualization of the complex aortic root, adding difficulties and consuming a considerable amount of time to locate and align the valve annulus. In addition, the contrast enhanced technique requires a significant amount of contrast agent, which can lead to adverse reactions due to its nephrotoxicity, especially to patients with kidney impairments [3]. Therefore, a more efficient technique for 3D vascular visualization and reduction in the use of contrast agent is desirable.

In recent years, intravascular ultrasound catheter imaging technology has been employed to obtain two-dimensional cross-section images of the blood vessels, providing anatomical information of the lumen morphology [4, 5]. This enables disease diagnosis with much less contrast agent compared to 3D angiography. It also permits the assessment of the interventions and evaluation of treatments after surgery. Vascular modeling technology based on IVUS has shown significant advantages for characterization of vascular diseases such as atherosclerosis [4]. It can also provide planning and navigation information for stent and stent graft deployment, as well as valve implantation.

Thus far, there is significant research in the use of IVUS for intra-operative guidance. For example, Sanz-Requena et al captured IVUS images by pulling back an IVUS catheter with constant speed of 0.5 mm/s and built a 3D reconstruction of artery models [6]. This method, however, is based on the assumption that the captured cross sections are parallel to each other. Therefore, it can be applied only to vessels with relatively small curvatures. Other groups have worked on the data fusion of IVUS and angiography [7-9], and estimated the pose of the IVUS probe tip in angiography images to obtain the approximate location of the IVUS images. However, the estimation of the pose of the IVUS probe remains difficult.

To overcome these limitations, we propose a new method

Manuscript received July 14, 2013. This work was supported by FP7-EU Project "Cognitive AutonomouS CAtheter operating in Dynamic Environments (CASCADE)".

The authors are with the Hamlyn Centre for Robotic Surgery, Imperial College London, UK. Email: {c.shi, stamatia.giannarou, su-lin.lee, g.z.yang}@imperial.ac.uk

based on information fusion from both IVUS and electromagnetic motion capture sensors (MMCS). The purpose of this work is to provide 3D visualization of blood vessels based on the fusion of anatomical information obtained from IVUS with corresponding pose from an electromagnetic sensor. Such a method can be applied to the characterization of valve stenosis and surgical navigation, as well as the localization of the annulus for easy alignment and placement during valve implantation.

The proposed system has been validated on phantom data captured within a silicone model of the aorta. The 3D model of the phantom was reconstructed with this hybrid probe to evaluate the effectiveness of the proposed method.

II. Materials and Methods

A. Hardware Configuration of Experimental Setup

The hardware configuration of the proposed system is shown in Fig.1. The hybrid probe consists of an IVUS sensor and an electromagnetic sensor. The IVUS imaging probe of Volcano Catheter Visions PV 8.2 with a working frequency of 10MHz and a detection range of 60mm, was connected with the Volcano s5™ system (Volcano Corporation, CA, USA) to obtain the inner cross sections of the blood vessels. A mini electromagnetic sensor with 6 degrees of freedom (DOFs) was connected with the Aurora Electromagnetic Tracking System (NDI Corporation, CA) to collect the corresponding pose information.

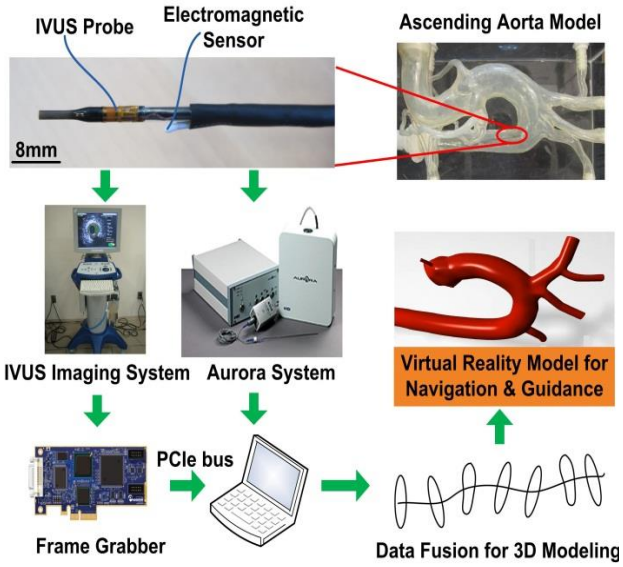

Fig. 1: The hardware configuration for the whole system. The hybrid probe consisting of two sensors is shown on the top left.

A DVI2PCIe frame grabber was connected with the IVUS Imaging System to record video data of the cross sections of blood vessels at 20 frames per second (fps). The corresponding pose information was recorded at the same frequency simultaneously.

A silicone-based, transparent, anthropomorphic phantom (Elastrat Sarl, Geneva, Switzerland) representing an ascending aorta was applied for this study, shown in the right top in Fig.1. Such a membrane model is suitable for evaluating the proposed method. This silicone model was immersed into a water tank and no flow was circulated inside it during imaging with the hybrid probe.

B. Image Processing for Extracting Coordinate of Contour

A sample video frame with a resolution of 1280 x 1024 pixels captured from the IVUS imaging system is shown in Fig.2. The IVUS probe appears as a hollow and circular shape in the center of the region of interest (ROI) ROI1. The ROI of ROI2 shows the cross section of the blood vessel. The scale in the 2D images is presented by the distance between the blue markers, and is equal to 5mm in our experiment.

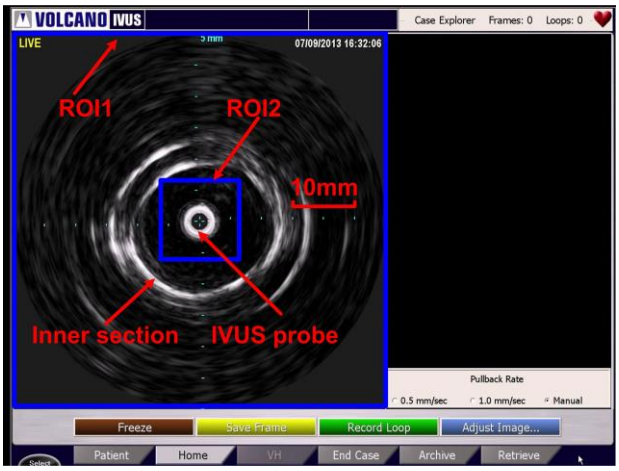

Fig.2: A video frame captured from blood vessel cross section

According to the properties of the captured images, a new image processing method has been implemented. The main steps of this process can be listed as follows.

Step 1: Obtain an IVUS video frame and the corresponding pose of the hybrid probe from the two sensors

Step 2 : Determine the center of the IVUS probe:

Select the ROI1, convert it into grey scale, apply a median filter, then perform Hough Circle transform in ROI1 to calculate the IVUS probe center location O_I and the radius r_1 for the circular black area in the center and estimate the radius r_2 of the white points (noise) surrounding r_1

Step 3: Pre-processing for Canny algorithm:

Select ROI2, convert it into grey scale, remove the image part of IVUS probe and the surrounding noise by drawing a black solid circle centered in O_I with radius r_2 and then apply the an average filter to remove the scale markers and the remaining noise

Step 4: Apply the Canny edge detection algorithm to obtain the rough contour of the cross section captured from the blood vessel model, and remove the scale makers and noise inside the inner cross section according to their length information

Step 5: Create a circle centered in O_I with radius r_3 , equal or larger than r_2 as an initial contour, and apply the Gradient Vector Flow (GVF) snake [10] to obtain a continuous and smooth contour

Step 6: Calculate the kinematics to convert the image coordinates of the contour into 3D coordinates

Step 7: Create a point cloud from the anatomical and pose information, mesh and render it into a 3D model.

C. Kinematics for Converting Image Coordinate into 3D Global Coordinate

Then, we need to calculate the pose for each contour and convert the contour points into 3D coordinates. Fig.3 shows the relationship of the coordinate systems among the Aurora emitter, the electromagnetic sensor and the IVUS emitter. The kinematic transformation can be expressed as:

$$ {}^{O}T_{I} = {}^{O}T_{M} \cdot {}^{M}T_{I} \quad (1) $$

$$ {}^{O}P_{I} = {}^{O}T_{I} \cdot {}^{I}P_{C} \quad (2) $$

where, ${}^{O}T_{M}$ stands for the transformation between the electromagnetic tracker and the Aurora coordinate system. There are seven parameters $T_x, T_y, T_z, Q_0, Q_x, Q_y, Q_z$ acquired from the electromagnetic sensor. The first three parameters represent the position, and the others are used to express the orientation using quaternion conventions. The quaternion information is converted into a transformation matrix to obtain ${}^{O}T_{M}$. After the assembly of the hybrid probe, these two sensors share the same orientation. ${}^{M}T_{I}$ expresses the transformation matrix between the electromagnetic sensor system and the IVUS emitter coordinate system, and it can be measured directly.

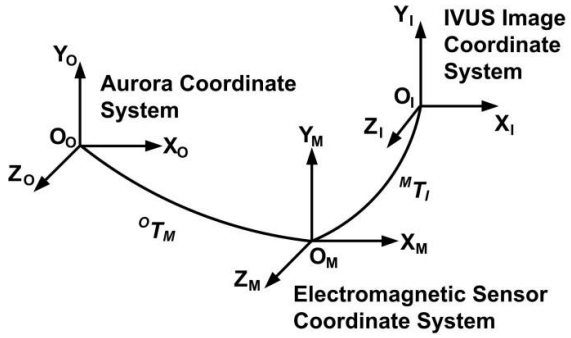

Fig.3: Kinematic relationship among Aurora emitter, Electromagnetic sensor coordinate and IVUS emitter coordinate systems

To transform these coordinates from pixels to millimeters, the following equation is used:

$$ {}^{I}P_{C}(X_P, Y_P, Z_P, 1) = P_{C}(k * \Delta x, k * \Delta y, 0, 1) \quad (3) $$

where, Δx and Δy stand for the coordinates of the contour relative to the image center in pixels. k expresses the real distance in millimeters that every image pixel stands for, and can be obtained from the image processing for the scale marks on the raw image. In our experiment, it is equal to 0.077 mm/pixel. ${}^{I}P_{C}$ represents the pixel coordinates expressed in millimeters, and uses the homogeneous coordinate format for convenience for the kinematic transform.

After obtaining these parameters, we can calculate ${}^{O}T_{I}$ and multiply it with ${}^{I}P_{C}$ in (3) to calculate the 3D physical coordinates according to equations (1)-(2). ${}^{O}P_{I}$ expresses the coordinate of a pixel on the contour measured in millimeters in the global coordinate system.

III. Results

A. Image Processing for Extracting and Locating Coordinate for Contour

The results of *Step 2* to *Step 5* of the image processing are shown in Fig.4. The radius r_2 was calculated as 70 pixels. A circle with a larger radius was used as the initial contour in *Step 5*, and the contour result shown in blue was obtained after applying the GVF snake. This algorithm runs at about 0.2 fps on an Intel(R) Core(TM) i5-2520M @2.5 GHz with 4 GB RAM.

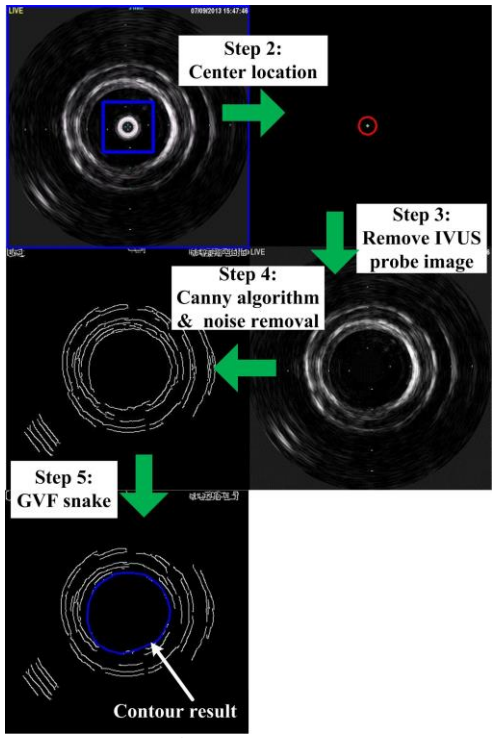

Fig. 4: Image processing for IVUS images

B. Data Fusion for 3D Modeling

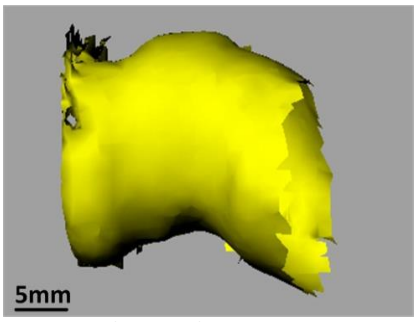

Fig. 5: 3D modeling for part of descending aorta based on sensor fusion method

The integrated probe was used to scan inside the descending aorta to collect data. After applying *Step 6* and *Step 7* in the image processing method, the 3D structure of the blood vessel can be reconstructed. The preliminary modeling for part of descending aorta is shown in Fig.5. A complete scan inside both of ascending and ascending aorta will be conducted in the near future.

IV. Discussion

In this work, we have proposed a system to obtain the inner cross sections of blood vessels and capture the corresponding catheter pose for locating these cross sections. The 3D reconstruction of the blood vessel can provide both morphological information and relative position information

between the blood vessel and the catheter tip. This can assist the surgeons to manipulate and advance the deployed devices within the blood vessel. During the alignment and valve placement in TAVI, the 3D reconstruction of the vessels can support precise localization and easy observation of the valve stenosis and annulus. Therefore, the hybrid probe can be used as a visualization aid to improve the efficiency in the implantation of artificial valves. After image registration, the virtual environment can be used to provide morphological information and navigate the operations of surgical tools, facilitate the implantation in the following steps. This method can support the use of non-contrast enhanced imaging and prevent reinjection of contrast media, reducing the use of contrast media.

The proposed image processing method is simple and fully automatic, advancing previous works which require the manual selection of the initial contour to converge to the real contour. Besides, when the IVUS probe is near to or comes in contact with the inner cross section, parts of the contour will converge on the IVUS probe image, leading to incorrect contour estimations. Our method has been proven to solve this problem.

This integrated sensor can be also deployed as an assessment tool to evaluate the status of the deployed valve after surgery. Misalignment of the implanted valve will cause valve migration, an important complication after the TAVI procedure. This would result in moderate and severe aortic regurgitation, which is one of the most important predictors of mortality and can cause serious consequences [11]. This technology can provide essential information for surgeons to take precautions in advance. It can also be applied to abdominal aortic aneurysms and thoracic aortic aneurysms. The proposed visualization framework can provide 3D modeling of the blood vessels and facilitate the location of branches to improve the efficiency in the installation of stent graft on the secondary branches of blood vessel for these two diseases.

The disadvantage of this system is that the IVUS probe and electromagnetic sensor are assembled in series with around 10 mm distance between them. When the catheter is confronted with large forces, the coordinate relationship between the two sensors will be affected by deformation. This issue could be tackled by estimating the deformation using force feedback from sensors installed in the affected area. If the surgeon can insert the integrated sensor with a relatively slow velocity away from the vasculature walls, such obstacle and deflection can be neglected.

In the future, additional electromagnetic sensors will be attached along the IVUS probe to estimate its shape [12] and realize Simultaneous Catheter and Environment Mapping (SCEM), which can provide both catheter localization and vessel geometry reconstruction. This would provide 3D visualization imaging of the artificial valve with respect to the stenosed valve for precise alignment.

V. Conclusion

A practical solution for 3D intravascular modeling of the aorta has been proposed based on the sensor fusion between images from an IVUS imaging probe and pose information from an electromagnetic sensor. An effective image processing pipeline was proposed to realize fully automatic processing of IVUS images. Experiments were carried out in an in-vitro environment to evaluate the effectiveness of proposed method. It should be noted that the current implementation of the IVUS image processing algorithm is not yet real-time because of the computational complexity of the GVF snake method. Our future work will focus on the improvement of the hardware platform, the IVUS image processing algorithm and the 3D surface modeling to enable real-time processing, as well as the evaluation of the modeling accuracy.

VI. Acknowledgments

The authors would like to acknowledge Dr. Philip Pratt and Dr. Alessio Dore for their contribution to this work. This research has been supported by the Commissions 7th Framework Programme FP7-ICT, by the project CASCADE under grant agreement No.601021.

References .

[1] E. Charlson, A. T. Legedza, and M. B. Hamel, "Decision-making and outcomes in severe symptomatic aortic stenosis," *J Heart Valve Dis*, vol. 15, pp. 312-21, May 2006.

[2] M. B. Leon, C. R. Smith, M. Mack, D. C. Miller, J. W. Moses, L. G. Svensson, *et al.*, "Transcatheter Aortic-Valve Implantation for Aortic Stenosis in Patients Who Cannot Undergo Surgery," *New England Journal of Medicine*, vol. 363, pp. 1597-1607, 2010.

[3] M. R. Rudnick, J. S. Berns, R. M. Cohen, and S. Goldfarb, "Contrast media-associated nephrotoxicity," *Curr Opin Nephrol Hypertens*, vol. 5, pp. 127-33, Mar 1996.

[4] J. T. Lee and R. A. White, "Basics of intravascular ultrasound: An essential tool for the endovascular surgeon," *Seminars in Vascular Surgery*, vol. 17, pp. 110-118, 2004.

[5] S. E. Nissen, "Application of intravascular ultrasound to characterize coronary artery disease and assess the progression or regression of atherosclerosis," *The American Journal of Cardiology*, vol. 89, pp. 24-31, 2/21/ 2002.

[6] R. Sanz-Requena, D. Moratal, D. R. Garcia-Sanchez, V. Bodi, J. J. Rieta, and J. M. Sanchis, "Automatic segmentation and 3D reconstruction of intravascular ultrasound images for a fast preliminar evaluation of vessel pathologies," *Comput Med Imaging Graph*, vol. 31, pp. 71-80, Mar 2007.

[7] A. Wahle, G. P. M. Prause, S. C. DeJong, and M. Sonka, "Geometrically correct 3-D reconstruction of intravascular ultrasound images by fusion with biplane angiography-methods and validation," *Medical Imaging, IEEE Transactions on*, vol. 18, pp. 686-699, 1999.

[8] C. J. Slager, J. J. Wentzel, J. C. H. Schuurbiers, J. A. F. Oomen, J. Kloet, R. Krams, *et al.*, "True 3-Dimensional Reconstruction of Coronary Arteries in Patients by Fusion of Angiography and IVUS (ANGUS) and Its Quantitative Validation," *Circulation*, vol. 102, pp. 511-516, August 1, 2000.

[9] B. Godbout, J. A. de Guise, G. Soulez, and G. Cloutier, "3D elastic registration of vessel structures from IVUS data on biplane angiography," *Acad Radiol*, vol. 12, pp. 10-6, Jan 2005.

[10] C. Xu and J. L. Prince, "Snakes, shapes, and gradient vector flow," *Image Processing, IEEE Transactions on*, vol. 7, pp. 359-369, 1998.

[11] M. Gotzmann, M. Lindstaedt, and A. Mugge, "From pressure overload to volume overload: aortic regurgitation after transcatheter aortic valve implantation," *Am Heart J*, vol. 163, pp. 903-11, Jun 2012.

[12] A. Dore, G. Smoljkic, E. V. Poorten, M. Sette, J. V. Sloten, and Y. Guang-Zhong, "Catheter navigation based on probabilistic fusion of electromagnetic tracking and physically-based simulation," in *Intelligent Robots and Systems (IROS), 2012 IEEE/RSJ International Conference on*, 2012, pp. 3806-3811.

Towards Intraoperative Use of Surgical Simulators: Evaluation of Catheter Insertion Models

G. Smoljkic, C. Gruijthuijsen, J. Vander Sloten and E. Vander Poorten

***Abstract*—Accurate and precise control of a catheter's position inside the vasculature remains a difficult and important task. Current manual approaches rely very much on the surgeon's expertise as visual information is extremely limited. The intraoperative use of fluoroscopy for real-time visualization of the catheter and the vasculature leads to safety issues, both for the patient and for the surgeon. By introducing robotically steered catheters these disadvantages can be at least partially alleviated. Also, robotics could improve the repeatability and accuracy of the catheter motion inside the vasculature. Due to the complexity of the catheter-vessel interaction current robotic steering relies completely on the surgeon's skills and experience. Based on the own experience and fluorscopic imaging surgeons form themselves mental maps of the catheter-vessel system. Within these maps the robot's joints are commanded one at a time. In order to introduce more sophisticated and coordinated steering capability the intraoperative use of a catheter insertion model originating from surgical training has been evaluated. The validation of the insertion model on a simplified test-bed showed a good predictive capability. The final objective is to use such approach for real-time guidance or even robotic catheter control. Speeding up the algorithm for intra-operative use remains therefore a major challenge.**

***Index Terms*—mechanical modeling, surgical simulation, catheter control, navigation assistance**

I. Introduction

In recent years minimally invasive cardiovascular procedures have gained dramatically in popularity. Faster patient recovery, reduced surgical costs and the possibility of using only local anesthesia are amongst the major advantages compared to open heart surgery. In minimal invasive procedures long, thin and flexible instruments or catheters are introduced and advanced into the endovascular system to perform diagnostic or therapeutic tasks. The limited visibility upon and maneuverability of the catheter in combination with the complex and fragile nature of the vasculature has raised the interest in robotic assisted catheterization. More advanced catheters featuring more degrees of freedom (DOFs) than conventional catheters can be controlled robotically hence allowing in principle more precise, repeatable and efficient catheter motion. This potential is at present far from realised as surgeons can only control one DOF at a time. Efficient operation of these devices requires thus still considerable insight and expertise. The knowledge that would be needed to allow coordinated multi-DOF control e.g. needed to closely follow an optimal trajectory inside the vasculature is still lacking. A first requirement is here the presence of realistic models of both the catheter and the vessel wall, formulated in such a way that they allow easy and fast computation of the catheter robot's kinematics.

In the literature a number of interesting algorithms to simulate catheter motion have been proposed. Cotin *et al.* use Finite Element Method (FEM) to model the catheter as a series of connected 3D beam elements[6]. The positions of these beams are geometrically constrained by the vessel model. To take into account the geometric nonlinearities arising from large catheter deformations, the authors propose an incremental FEM approach. This however results in a cumulative error on the catheter shape. Luboz and Wang use mass-spring models for the catheter [9], [11]. Such approaches encounter problems in preserving the constant catheter length as this turns the equations numerically stiff. The catheter can also be modeled as a set of discrete Elastic Kirchhoff Rods [8], [10], but no experimental validation was performed of these models. Finally in [7] the authors designed a method for catheter simulation searching the minimum energy state of a catheter that is represented as a set of rigid links interconnected with springs. Because of the extensive validation of this algorithm and the need for an accurate simulation, this last algorithm is selected and adjusted for catheter position control. In the remainder of the paper, the adjusted simulation model is described in subsection II-A. The model has been implemented. Experimental validation and results are discussed in subsection II-B. Finally, in section III the paper is concluded and directions for further work are discussed.

II. Minimum energy model

While the catheter is inserted into the vasculature, it flexes and bends passively adapting its shape to the geometry of the vasculature. The shape and tip position are largely dependent on the forces that act on the catheter, but also on its motion history. Konings *et al.* derived a semi-analytic simulation that can accurately predict the motion of a catheter inside the vasculature [1], [2], [3], [4], [7]. Starting from a known geometrical and material model of the vessel, the algorithm calculates the catheter shape after a forced motion of the catheter such that the total potential energy of the combined catheter and vessel wall is minimal. The simulation algorithm has been designed for training purposes. This abstract extends its applicability to steering of active catheters.

A. The relaxation algorithm

Under the assumption of high axial and torsional stiffness, a catheter can be represented as a series of i rigid links of constant length λ_i connected by spherical joints (Fig.1.a). An angular spring is attached at each joint as illustrated in Figure 1.b. The original catheter model of Konings, restricted

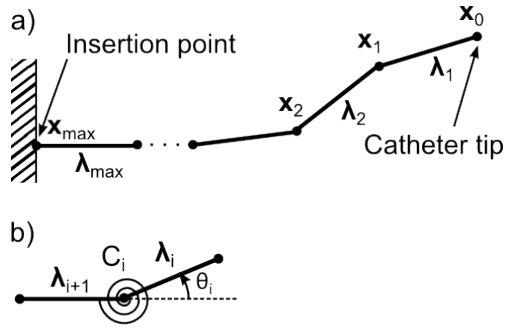

Fig. 1. (a) representation of a catheter as a series of rigid links of length $\boldsymbol{\lambda}_i$ at positions $\boldsymbol{x}_i$ (b) angular springs with stiffness c_i connect the joints.

to the modeling of straight guidewires, was later extended to also include intrinsic curvature and rotation about the catheter axis. The fixed intrinsic curvature angle used to characterize pre-shaped guidewires, is made adaptable here in order to replicate the behavior of active catheters with a proximal DOF and e.g. a locally bending of the catheter tip. After this adaptation an input-output map between the displacements of the actuating cables, embedded in the catheter, and the tip motion is derived. Similarly a change in rotation of the catheter about its longitudinal axis at the proximal side, is achieved by adjusting the internal rotation angle as proposed in [4]. The original approach to represent rotation fails to correctly determine the direction of the intrinsic curvature after deformation of the catheter in interaction with the vasculature. This is due to the fact that the local rotation angle at the active side of catheter is always described w.r.t. to the fixed reference frame placed at the insertion point. To solve this issue, the approach is adapted by attaching a frame to every joint, based on a discrete version of the theory of Bishop frames [5]. The intrinsic curvature at each joint is then expressed easily with respect to these frames. The relaxation algorithm is an iterative minimization algorithm estimating the catheter shape based on the assumption that the equilibrium state corresponds to a minimal energy state of the combined catheter-vessel system. The total energy is thus composed of the vessel energy and the energy of the deformed catheter. The final shape estimate is found after executing an adequate number of relaxation steps. In each relaxation step, all bending angles $\boldsymbol{\theta}_i$ are calculated consecutively, starting from the tip of the catheter (i $= 0$) and propagating to the proximal end of the catheter and the insertion point. Additional relaxations can be imposed to further refine the shape estimates and obtain more accuracte predictions. The new implementation is evaluated next.

B. Model validation

In order to evaluate the accuracy of the catheter-vessel simulation approach an *in-vitro* experimental test-bed was made from a segmented MR-scan of a human aorta. The projection of the model on a 2D-plane was made and a centerline extracted. A 20mm thick aorta-model was constructed along this centerline. The contour of the aorta was cut out from a 3mm thick polycarbonate plate and embedded in a sandwich structure. An Ethernet GigE Prosilica GC650C with 6mm lens and resolution of 659×493 pixels was placed above the test-bed to compute the ground truth. The camera was placed on a customized mount 720mm above the aorta phantom. Figure 2 shows a raw image obtained from the camera and the results of the segmentation and comparison with the insertion model. The camera images have been segmented and the shape of the

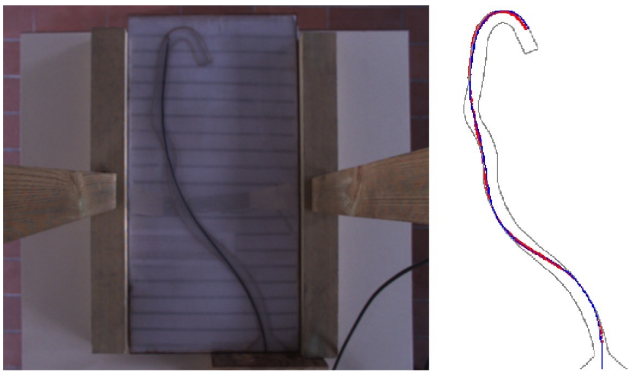

Fig. 2. Raw image of the setup with the test catheter inserted in the 2D aorta mock-up (Left). Overlay of the simulated catheter (blue) over the real catheter (red) for an insertion length of 700mm (Right).

catheter has been obtained after the insertion of 700mm into the phantom. The resulting catheter shape obtained from the camera was compared to the position and shape predicted by the insertion model. Two measures have been used to quantify the similarity: the Hausdorff distance d_h and the Root Mean Square (RMS) of the deviation between both shapes d_{RMS}. The results show a RMS deviation stays below 2.5mm whereas the Hausdorff distance is 4.4mm. These findings correspond to the results obtained by the Konings group.

III. Conclusion

In this paper a catheter insertion model proposed by Konings has been evaluated. The simulation model iteratively searches for a quasi-static equilibrium state of a catheter and vasculature after a set of forced actions of the catheter robot. The model was expanded to simulate catheter insertion, retraction, rotation and distal bending of the catheter tip. In validation experiments the catheter shape obtained by the insertion model was compared to the measured catheter shape. A good fidelity of the model was obtained. In future work the model will be applied for actual catheter position control. Further effort needs to be paid to speed up computations though as current computations are far from real-time.

Acknowledgments

This research has been supported by the Commission's 7th Framework Programme FP7-ICT, by the project CASCADE under grant agreement No.601021.

References

[1] T. Alderliesten, P. A N Bosman, and W.J. Niessen. Towards a real-time minimally-invasive vascular intervention simulation system. *Medical Imaging, IEEE Transactions on*, 26(1):128–132, 2007.

[2] T. Alderliesten, M.K. Konings, and W.J. Niessen. Simulation of minimally invasive vascular inventions for training purposes. *Comput Aided Surg*, 9(1–2):3–15, 2004.

[3] T. Alderliesten, M.K. Konings, and W.J. Niessen. Robustness and complexity of a minimally invasive vascular intervention simulation system. *Medical Physics*, 33(12):4758–4769, 2006.

[4] T. Alderliesten, M.K. Konings, and W.J. Niessen. Modeling friction, intrinsic curvature, and rotation of guide wires for simulation of minimally invasive vascular interventions. *Biomedical Engineering, IEEE Transactions on*, 54(1):29–38, 2007.

[5] Richard L. Bishop. There is more than one way to frame a curve. *The American Mathematical Monthly*, 82(3):246–251, 1975.

[6] S. Cotin, C. Duriez, J. Lenoir, P. Neumann, and S. Dawson. New approaches to catheter navigation for interventional radiology simulation. In *Proceedings of the 8th international conference on Medical image computing and computer-assisted intervention - Volume Part II*, MICCAI'05, pages 534–542, Berlin, Heidelberg, 2005. Springer-Verlag.

[7] M.K. Konings, E.B. Kraats, T. Alderliesten, and W.J. Niessen. Analytical guide wire motion algorithm for simulation of endovascular interventions. *Medical and Biological Engineering and Computing*, 41(6):689–700, 2003.

[8] Shun Li, Jing Qin, Jixiang Gao, Yim-Pan Chui, and Pheng-Ann Heng. A novel fem-based numerical solver for interactive catheter simulation in virtual catheterization. *Journal of Biomedical Imaging*, 2011:3:3–3:3, jan 2011.

[9] Vincent Luboz, Rafal Blazewski, Derek Gould, and Fernando Bello. Real-time guidewire simulation in complex vascular models. *Vis. Comput.*, 25(9):827–834, jul 2009.

[10] Wen Tang, Pierre Lagadec, Derek Gould, Tao Ruan Wan, Jianhua Zhai, and Thien How. A realistic elastic rod model for real-time simulation of minimally invasive vascular interventions. *Vis. Comput.*, 26(9):1157–1165, sep 2010.

[11] F. Wang, L. Duratti, E. Samur, U. Spaelter, and H. Bleuler. A computer-based real-time simulation of interventional radiology. In *Conf Proc IEEE Eng Med Biol Soc*, 2007.

Towards Real-time FE for surgical applications

Vukasin Strbac, Jos Vander Sloten, Nele Famaey
Biomechanics Section, Department of Mechanical Engineering KU Leuven, Belgium
Email: vule.strbac@mech.kuleuven.be

***Abstract*—As the Finite Element(FE) method is becoming more pervasive in scientific and engineering endeavours the application space of the method increases as well. This work provides indication that real-time surgical application is also possible. The challenge is reducing the solution times of this, generally computationally expensive method, such that FE on patient organs under the influence of surgical instruments can provide valuable information to the interventionalist during surgery.**

We present an implementation of a Total Lagrangian Explicit Dynamic Finite Element algorithm implemented on General Purpose Graphics Processing Units(GPGPUs) that suggests the fulfillment of this constraint. The usability of the method is demonstrated by conducting a broad assay on ranging model sizes and GPGPUs and comparing to an industry-proven FE code Abaqus.

I. Introduction

Modern surgical theaters today are capable of providing electromagnetic or optical position tracking systems that can be used to locate the position of instruments under the control of the surgeon. Likewise, current imaging techniques are capable of producing highly detailed geometries of patient specific anatomy. By combining these data with an appropriate material model of the organ or organs under consideration all boundary condition requirements for FE in surgery are met. Providing near-instantaneous response on the state of the tissue under mechanical load (pressing, pulling, cutting...) is instrumental in ensuring patient safety, thus creating the need for a real-time FE system.

Successful real-time implementations of nonlinear finite elements have been sparse in publications, mostly likely due to the limited computational power of hardware and the high arithmetic intensity of conventional FE algorithms. The Total Lagrangian Explicit Dynamic(TLED) [1] tackles this problem in part by using the total lagrangian spatial discretization scheme. It ensures that shape function derivatives do not need to be recomputed every time step, thus additionally reducing the number of operations. By using explicit time integration (the central difference method), the nonlinearities are handled in a simple way, provided a small enough time step is chosen. Another benefit of explicit integration is that per-element computations can be done somewhat independently, adding individual contributions gradually to form the global force matrix. This feature along with the per-node fully independent computations lends itself well to parallelization. The explicit nature of the solution also facilitates the tracking of one or mode variables throughout the solution, e.g. the accumulation of damage [2].

Nvidia CUDA [3] technology enables us to use the massively parallel architecture of modern GPUs to conduct general-purpose floating-point computations in an accessible and simplified way. By distributing the computations over the cores of the card, most calculations of the same time step can be done at the same time, providing significant speed-up to the algorithm.

In section II, we present details on the algorithm and implementation, hardware and the boundary conditions of the simulation, followed by results (III) and the conclusions (IV) on the topic.

II. Materials and methods

A. Mechanical model

For the purposes of validating the accuracy of the proposed method we solve a uniaxial compression problem on a cube of uniform size and increasing element density. The material employed is a hyperelastic Neo-Hookean material(ref. eq.1, 2), often used as an estimate of the behavior of most soft tissues.

$$\Psi = \frac{\mu}{2}(\overline{I}_1 - 3) + \frac{\kappa}{2}(J-1)^2, \tag{1}$$

where μ and κ are material constants - shear and bulk modulus, respectively. $\overline{I}_1$ is the first invariant of the right Cauchy-Green deformation tensor $\mathbf{C}$. The second Piola-Kirchoff stress tensor $\mathbf{S}$ can be derived from the SEDF as:

$$\mathbf{S} = 2\frac{\partial \Psi}{\partial \mathbf{C}} = \mu J^{-\frac{2}{3}}(\mathbf{I} - \frac{tr(\mathbf{C})}{3}\mathbf{C}^{-1}) + \kappa J(J-1)\mathbf{C}^{-1}. \tag{2}$$

The elements used in the simulations are under-integrated hexahedra, which offer good results for a relatively low number of computing operations. No hourglassing preventive algorithms have been implemented. A smooth loading curve up to 20% strain was used to minimize inertial effects and enabling us to study the phenomena under quasi-static conditions.

The simple boundary conditions in our simulations prescribe no displacements in the axial direction (Z) for the bottom nodes and enforces displacements along the same axis for the top nodes, all other degrees of freedom are non-constrained.

The critical time step was computed by using linear theory [4] and proving sufficient to maintain the convergence.
Each model has identical material properties and was loaded in a time span of 5 seconds. The critical time step c size was determined by using the following formula.

$$L_e = \frac{V_e}{A_e}; c = sqrt\frac{\lambda + 2\mu}{\rho}; \Delta t = \frac{L_e}{c} \tag{3}$$

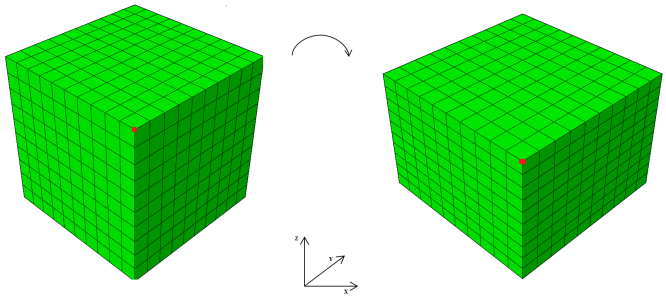

Fig. 1. Initial and deformed geometry and a reference point on a 10x10x10 model

Where L_e is the characteristic length, computed using the smallest element area in the model A_e and it's volume V_e, ρ is the mass density of the element. The 5 second loading time is therefore distributed along around 6000 to more than 50000 steps in different models.

B. Total Lagrangian Explicit Dynamic algorithm

The system to be solved is:

$$\mathbf{M}\ddot{\mathbf{u}} + c_d\mathbf{M}\dot{\mathbf{u}} + \mathbf{P}(\mathbf{u}) = \mathbf{R}, \tag{4}$$

where $\mathbf{M}$ is the diagonalized mass matrix, c_d is the damping coefficient, $\mathbf{u}$ are the nodal displacements, $\mathbf{P}$ are the internal forces and $\mathbf{R}$ are the external forces. [1], [5], [6], [4], for example, provide additional detail on the topic. A pseudo-code of the solution of the system in equation 4 is provided below.

Pre-computation phase:

1) Shape function derivatives in global coordinates from isoparamatric coordinates and positions, using the Jacobian matrix:

$$^0\mathbf{J}_e = \frac{\partial(x,y,z)}{\partial(\xi,\eta,\zeta)} = \nabla\mathbf{N}_{Iso}\mathbf{p}_e \tag{5}$$

$$\nabla\mathbf{N}_{Glo,e} = {}^0\mathbf{J}_e^{-1}\nabla\mathbf{N}_{Iso} \tag{6}$$

2) Construct strain-displacement matrix: $\mathbf{B}_e$
3) Compute element volumes and diagonalized mass matrix $\mathbf{M} = M_e\mathbf{I}$
4) Central difference method coefficients:

$$a = -\frac{2(\Delta t^2)}{2t\Delta t M_e}; \qquad b = \frac{1+(2-q\Delta t)}{2+q\Delta t}; \tag{7}$$

$$c = -\frac{2-q\Delta t}{2+q\Delta t}; \qquad q = \frac{2(1-{C_r}^2)}{\Delta t(1+C_r)} \tag{8}$$

Iteration phase:

4) Deformation gradient:

$$^t\mathbf{F}_e = \mathbf{I} + \nabla\mathbf{N}^t\mathbf{u}_e \tag{9}$$

5) Cauchy-Green strain tensor, Jacobian determinant:

$$^t\mathbf{C}_e = {}^t\mathbf{F}_e^{T\,t}\mathbf{F}_e\ ,\ {}^tJ_e = det(^t\mathbf{F}_e) \tag{10}$$

6) Second Piola-Kirchoff stress:

$$^t\mathbf{S}_e = 2\frac{\partial^t\mathbf{\Psi}_e}{\partial^t\mathbf{C}_e} \tag{11}$$

7) Force contribution:

$$^t\mathbf{P}_e = 8det(^0J_e)\mathbf{B}_e^{T\,t}\mathbf{S}_e \tag{12}$$

8) Summation of elemental contributions into the global force vector:

$$^t\mathbf{P} = \sum {}^t\mathbf{P}_e \tag{13}$$

9) New displacements:

$$^t\mathbf{u} = a\,{}^t\mathbf{P} + b\,{}^t\mathbf{u} + c\,{}^{t-\Delta t}\mathbf{u} \tag{14}$$

10) Displacement loading for next step:

$$^{t+\Delta t}\mathbf{u}_{BC} = {}^{t+\Delta t}\mathbf{d}_{BC} \tag{15}$$

In the above notation the left superscript denotes the time step, the right subscript denotes element scope. C_r is the convergence rate of the central difference scheme, and set close to 1, as relaxation effects were not considered and a small enough time step was used.

In light of increasing the speed of the algorithm, pre-computing all possible values is essential. Due to the spatial discretization scheme chosen, the shape function derivatives do not change accross the time steps, therefore we compute them here. The central difference method coefficients are also pre-computed as they too do not change throughout.

Single point Gaussian integration is used to obtain element nodal forces from element stress in step 7, which was in turn computed from the right Cauchy-Green tensor and deformation gradient in steps 4-6. Depending on the material model used, the stress computation in step 7 can vary. In our implementation, the Neo-Hookean material with and without damage are used, according to equation 2. After the computation of the global force vector in step 8, the nodal displacements are calculated using the central difference scheme. Finally, new displacement boundary conditions are assigned to the boundary nodes, to prepare for the next step. For a more detailed discussion on TLED, the reader is referred to [1].

C. Hardware and implementation

The pseudocode described in section II-B is implemented using Nvidia Compute Unified Device Architecture (CUDA). The GPGPU cards used for this purpose are an Nvidia Tesla C2075, K20c and GTX680 capable of running thousands of threads concurrently. For a detailed overview of CUDA, the reader is referred to [3].

The two most important factors in speeding up a program by using a GPGPU is replacing loops with parallel functions (kernels) and the pre-computation of all possible values for later use in the algorithm. Albeit, the former can be used only if iterations are independent from one another. For this

Parameter	Value
μ	1006.7e-6 MPa
κ	50e-3 MPa
λ	49.3e-3 MPa

TABLE I
MATERIAL PARAMETERS

reason we can parallelize over elements and nodes and not over time steps. The most suitable portions of code to implement in parallel are: obtaining the global force matrix (steps 4-8) using element-level granularity, updating of displacements (step 9) and loading for the next step (10), both using node-level granularity.

The granularity of parallelization in the computation of force contributions in the global force matrix assembly is one element, meaning that each thread run by the hardware computes the values of force for one element. The interconnectivity of elements mandates storage problems when summing force contributions on a node from surrounding elements in a parallel setting. A reduction scheme has been implemented for this reason that avoids the serialization of storage writes.

In the second kernel, we obtain per-node displacements using coefficients computed in the pre-computation phase. Using the central difference method we compute future displacements of nodes based on the global force matrix and the pre-computed coefficients in step 3. Here, the granularity is one node.

The last kernel executes the loading of the nodes under boundary conditions. Much like the previous kernel, it is executed per-node and it is a pleasingly parallel task due to no communication requirements between nodes.

An Abaqus finite element simulation code was used to validate the newly implemented code. Identical boundary conditions and smooth loading curve were used in both solution regimes, as well as the material parameters (I). The Abaqus jobs were run on a system with an Intel i7-3740QM processor and 4GB of RAM.

III. RESULTS

The results obtained through simulation in Abaqus/Explicit are regarded as benchmark. The accuracy of the newly implemented algorithm was evaluated by comparing the displacement vector in the XY plane of one top node at the corner. For all simulations the deviation from Abaqus solutions never exceeds 0.3%. The initial configuration and the loaded, converged configuration are symmetric with respect to all orthogonal planes and vertical edges remain vertical.

The results in Figure 2 show a speed up factor of TLED versus Abaqus on a per-time step basis. The total solution times speed up are proportional to these values and range from 1 second to 1h22m40s for Abaqus and from 0.2s to 50s for the parallel solver on the fastest K20c device.

IV. CONCLUSION

We have presented an integral part of a computer integrated system for monitoring of any mechanical stress-related

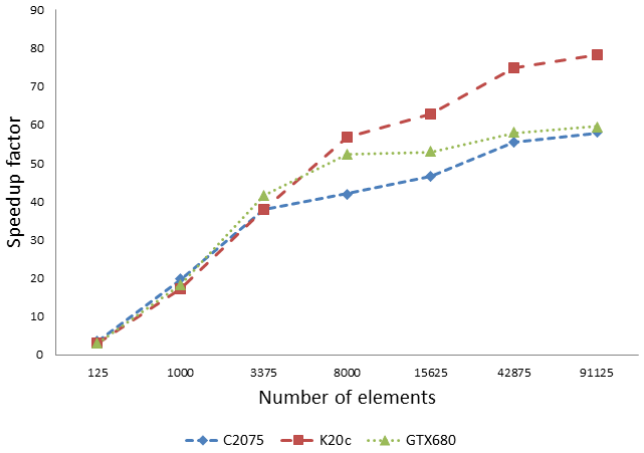

Fig. 2. Speed up factors versus Abaqus as a function of model element density

variable in patient tissues in an intraoperative setting. The nonlinear Finite Element algorithm employed was described in detail and results on a single loading scenario of a cube using a range of element densities and execution GPGPUs was presented.

The results show significant speedups and good accuracy in comparison to stable and reliable solutions. This work, therefore, encourages the prospect of the described technology soon becoming implemented in the modern surgical theater.

ACKNOWLEDGMENT

This research was supported by the EUs Seventh Framework Programme under GA No. 601021 (CASCADE). The authors would like to thank Prof. K.Miller and Dr. G.Joldes for considerable instruction and assistance with the details of the TLED algorithm.

REFERENCES

[1] K. Miller, G. Joldes, D. Lance, and A. Wittek, "Total lagrangian explicit dynamics finite element algorithm for computing soft tissue deformation," *Communications in Numerical Methods in Engineering*, 2007.

[2] N. Famaey, J. Vander Sloten, and E. Kuhl, "A three-constituent damage model for arterial clamping in computer-assisted surgery." *Biomech Model Mechanobiol*, Mar 2012. [Online]. Available: http://dx.doi.org/10.1007/s10237-012-0386-7

[3] Nvidia, *CUDA C Programming Guide 4.2*, Nvidia Corporation, 2012. [Online]. Available: http://developer.nvidia.com/nvidia-gpu-computing-documentation

[4] T. J. Hughes, *The Finite Element Method - Linear Static and Dynamic Finite element Analysis*. Dover publications, Inc., 1987.

[5] G. R. Joldes, A. Wittek, and K. Miller, "Suite of finite element algorithms for accurate computation of soft tissue deformation for surgical simulation." *Med Image Anal*, vol. 13, no. 6, pp. 912–919, Dec 2009. [Online]. Available: http://dx.doi.org/10.1016/j.media.2008.12.001

[6] T. Belytchko and T. J. Hughes, Eds., *Computational methods for transient analysis*, 1983.

Precise Navigation on Soft Tissues with an Endomicroscopy Probe

Benoît Rosa*†, Jérôme Szewczyk*, Guillaume Morel*
*Institute of Intelligent Systems and Robotics, UPMC - University Pierre et Marie Curie, CNRS - UMR 7222, Paris, France
†Department of Mechanical Engineering, KU Leuven

***Abstract*—Probe-based Confocal Laser Endomicroscopy (pCLE) is a recent image modality that could allow to perform optical biopsies, without taking a tissue sample. This is of particular interest in laparoscopy, to diagnose and grade cancer in the abdominal cavity.**

Among the different problems that arise when trying to take optical biopsies inside the abdominal cavity, the control of the probe motion is of upmost importance. Indeed, it is not only necessary to stabilize the images on the organs, but also to move the probe along the tissue surface to reconstruct large field of view images needed by pathologists. This can be done using a mosaicking algorithm.

This paper presents a visual servo control scheme for controlling the probe navigation on the tissue. Its robustness is challenged in an *ex vivo* setup using a high-accuracy industrial robot. The achieved precision is good enough to allow for reconstructing large field of images with controlled shape and size, and high resolution.

I. Introduction

In oncology, biopsy is a standard procedure that aims at determining the cancer nature and development stage of a suspected tissue. It consists in taking a tissue sample out of the patient in order to analyze it under a microscope. Anatomopathologists usually analyze the cells themselves but also their relative organization from a larger picture to make their diagnosis. Prior to this, they need to prepare the tissue for microscope examination. Usually, the tissue is frozen or fixed using paraffin and cut in thin slices of a few microns, then stained using special markers that highlight cellular structures (for instance, hematoxylin-eosin staining which is used un clinical routine).

In digestive surgery, extemporaneous biopsies can be carried out, i.e. biopsies made during the operating time. In that case, the surgeon takes the tissue sample, sends it to the anatomopathologist, and waits for his/her answer that will orient the following of the procedure. For instance, in the event of a tumor resection, the surgeon must be sure that the resection margins are free of tumour cells. The time that the pathologist spends preparating the tissue is then just a waiting time during which the patient is under global anesthesia. Moreover, taking a tissue sample is invasive, which limits the number of biopsies that can be done on a same organ. This is particularly problematic for staging laparoscopies, in which the surgeon explores the abdominal cavity and needs to take several biopsies in order to find metastases and properly grade the cancer development stage [1], [2].

To circumvent those limitations, it has been proposed to take "optical biopsies", i.e. without taking a tissue sample. The surgeon then needs to bring an image modality, here a microscope, *in situ* in order to take images that can directly be transmitted to the surgeon. Different image modalities can be used, for instance OCT [3] and confocal endomicroscopy (pCLE) [4], [5]. In this paper, we focus on confocal endomicroscopy. This image modality works with fluorescence imaging, which is interesting because functional imaging can be realized by using the proper fluorescent agent. This image modality is currently used in clinical practice during endoluminal examinations, for instance for diagnosis of Barrett's esophagus [6], [7]. It tipycally has a resolution of one micron, and a field of view of 200x240 microns. The images are acquired at a 12 Hz rate.

Several problems arise when trying to use pCLE in endoscopic examinations. First, contrarily to endoluminal examinations, the flexible probe is not in a tube. Therefore, organ motions must be taken into account. In the abdominal cavity, organs move in a range of a few centimeters each second due mainly to breathing and persitaltis. This particular problem has been the subject of many research, and solved either using passive [8] or force-controlled [9] stabilization. Second, the field of view in the pCLE images is usually too narrow for the pathologist to analyze the cellular structures properly. It has been reported previously that pathologists need a $1-3\ mm^2$ field of view, whereas a single image is only $0.04\ mm^2$. The same problem had already been reported in endoluminal examinations, and mosaicking algorithms have been developped in order to enhance the field of view [10], [11]. The principle is to move the probe along the tissue – while staying in contact, which is needed for acquiring images – and to register images together in order to reconstruct a large field of view image. Moving the probe inside a laparoscopic instrument can be done using specific microactuators [8], [12], but it has been shown in [13] that even with a very precise control of the probe motion, tissue deformations prevent from making high quality mosaics.

In this paper, we present a visual servoing approach that allows to control the probe trajectory on the tissue with microscopic precision.

This work was supported by OSEO (Maisons-Alfort, France) under ISI Project PERSEE (number I0911038W) and by French state funds managed by the ANR within the Investissements d'Avenir programme (Labex CAMI) under reference ANR-11-LABX-0004

II. Endomicroscopy-based visual servoing

This section presents the visual servoing scheme that is used for controlling the probe motion. First, a quick look at the mosaicking algorithm from [10] helps to understand image metrics and scan requirements, then the visual servoing control loop is presented.

A. Notations

In the following, V refers to speeds whereas X refers to positions. They both are vectors. Subscripts $_r$, $_p$, $_a$ and $_0$ refer to the robot holding the probe, the probe, the anatomical tissue and a fixed base, respectively. For instance, $V_{p/a}$ denotes the relative velocity between the probe and the anatomical tissue.

B. Mosaicking algorithm

The mosaicking algoithm used in this work was published in [10]. The main part of the problem is reconstructing the trajectory that has been followed in the images. This is done in two steps (see fig. 1).

First, successive images are registered together (real-time mosaicking, fig. 1a) using normalized cross-correlation [14]. This computation is made in one pass with a Fourier transform, so it has a fixed computational budget and is suited for real-time. This allows to compute an estimation $\widehat{V}_{p/a}$ of $V_{p/a}$, and therefore to estimate $X_{p/a}$ by simply integrating it (eq. 1).

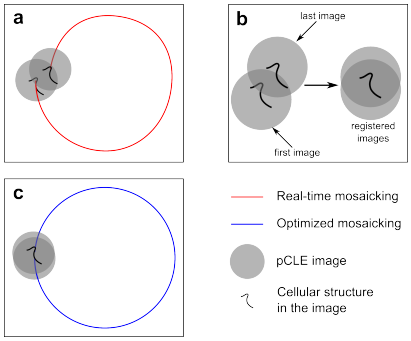

Figure 1. General principle of the mosaicking algorithm. a: real-time mosaicking; b: registration of spatially but not temporally closed images; c: optimized mosaicking.

$$\widehat{X}_{p/a}(t) = \widehat{X}_{p/a}(0) + \int_0^t \widehat{V}_{p/a}(\tau)d\tau \tag{1}$$

The problem of registering successive images together to sum the registration results, as in eq. 1, is that the total error at the end of the trajectory is the sum of each registration error. It can be seen in fig. 1a that cellular structures are not properly aligned due to this cumulative error. The second part of the mosaicking algorithm is meant to eliminate this drift. By analyzing the real-time mosaicking trajectory, one can find images that are spatially close but not temporally close. Registering those images together (fig. 1b) and then performing an optimization scheme (fig. 1c) leads to an enhanced mosaic. This is particularly important, because mosaic images reconstruction leads to blurred and duplicate structures in the images if cumulative errors are not taken into account.

C. Scanning requirements

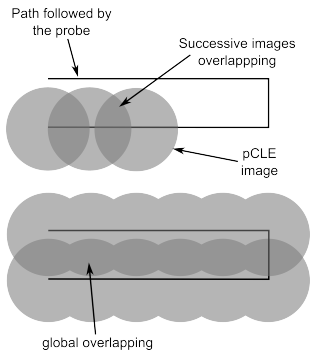

Figure 2. Scanning requirements in terms of overlapping

Scanning a tissue in order to make a mosaic needs specific requirements (see fig. 2). First, sucessive images should overlap of approximately 80% to obtain good results with open-loop mosaicking. This leads to a scanning speed on the tissue of approximately 0.3 mm/s or less. 0.3 mm/s is preferred because a lower speed means a larger scanning time.

Second, overlap between scan lines (global overlap) must be sufficient to compute mosaics (50-100 microns overlap between scanning lines). To make a 3 mm^2 mosaic, a raster scan trajectory of 15 straight parallel lines of 1500 microns length is proposed. It has been shown in [15] that drift in the real-time mosaicking is low enough to allow for computing optimized mosaics if such a trajectory can be followed with approximately 50 microns precision.

D. Position-based visual servoing (PBVS)

It has been shown in [13] that tissue deformations play an important role when scanning at the contact of the tissue. Therefore, we propose here to use the measurements of the real-time mosaicking algorithm to control the probe motion.

The setup that we have here is a robot r controlling the movements of a probe p relatively to a fixed base 0 in order to follow a trajectory on a tissue a. In other words, we want to compute the required speed $V_{r/0}$ so that the estimated image position $X_{p/a}$ follows a given scanning trajectory X_d. Usually, in visual servoing, a simple proportional controller ensures an exponential convergence of the error towards zero. Here, since the image velocity is not null, a feedforward term should be added. However, we have here additional disturbances with the tissue deformations. Exponential convergence of the error cannot be obtained with a simple proportional gain since probe motions don't necessary make the image move. Therefore, an additional integral gain is added. The resulting control loop then writes, with K_P and K_I being repsectively the proportional and integral gains:

$$\begin{aligned} V_{r/0} = \frac{\mathrm{d}X_d}{\mathrm{d}t} + K_P\left(X_d(t) - \widehat{X}_{p/a}(t)\right) + \\ K_I \int_0^t \left(X_d(\tau) - \widehat{X}_{p/a}(\tau)\right) d\tau \end{aligned} \tag{2}$$

III. Experimental setup and results

A. Experimental setup

The experimental setup is presented on fig. 3. The confocal imaging system is a Cellvizio with a UHD probe (Mauna Kea Technologies, France). The probe is fixed at the end effector of a TX40 robot (Stubli, Faverges, France), through a prototype probe holder. The robot has 6 Degrees of Freedom (DoF) and exhibits a 20 µm repeatability at its end effector. The tissue samples are put on a rough surface that is fixed with respect to the robot base and parallel to the horizontal plane. Considering the small size of the scanned areas (a few square millimeters), the scanned tissues are considered as planar in this study. Therefore, the robot movements are generated at a constant height z_0 . Meanwhile, the probe orientation is kept constant, which finally results in a 2 DoF planar positioning problem. The cartesian position of the optical head is controlled by the on-board controller of the TX40 robot which is interfaced for allowing real-time update. Tissues are stained with Acriflavine for fluorescence.

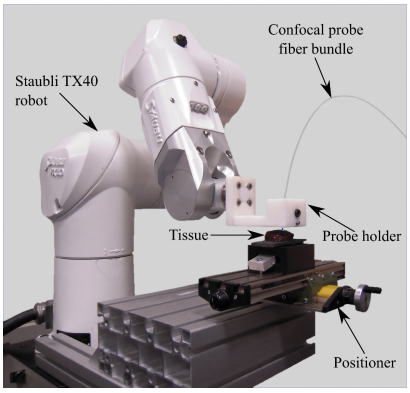

Figure 3. Experimental setup with a TX40 robot

B. Ex vivo experiments on soft tissues

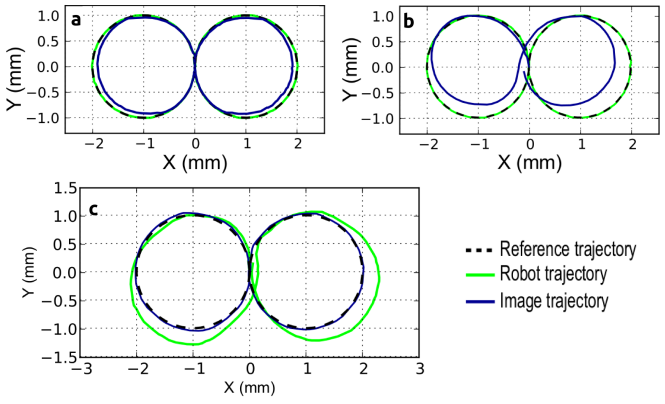

Figure 4. Data recorded during the performing of 8-shape trajectories. a: on a piece of paper glued to a rigid surface. b: on a piece of beef liver with open-loop control. c: on a piece of beef liver with closed-loop control.

1) Simple trajectory: On figure 4 can be seen the results of several scans with an 8-shape trajectory formed of two circles of 1 mm each. The results on paper (fig. 4a) clearly indicate that the robot control is very precise, according to its own measurements. A marginal error of 140 microns occurs at the farthest point of the trajectory, indicating a possible deformation of the probe holder or a robot modeling error. Most importantly, drift due to real-time mosaicking between first and last image is less than 10 microns, which has been observed in repeated experiments.

As expected, results on soft tissue (fig. 4b) show a very large shift relatively to the reference trajectory. The mean distance error between the image trajectory and the reference trajectory is more than 300 µm, and the final error is 150 µm. This shows that the tissue deformation has a direct and non negligible impact on the trajectory effectively followed by the probe relative to the tissue.

Finally, applying visual servoing allows to follow the reference trajectory with high accuracy (fig. 4c). The error between the first and the last image is 15 µm and the mean tracking position error is 30 µm. This improvement with respect to the open-loop results from fig. 4a and fig. 4b shows that the tissue and probe holder deformations are rejected by the visual control algorithm.

2) Large field of view mosaics: The next experiment is a mosaic obtained by servoing the image to follow the 3 mm^2 raster scan desired trajectory described previously. The two mosaics (real-time and optimized) are presented in fig. 5. The performance of the visual servo control allows to make sure that each line will overlap with the next one, thus making the computation of an optimized mosaic possible. This results in an optimized mosaic that has very low drift : the gain can be observed on fig. 5 when zooming to particular regions. The general shape of the optimized mosaic does not change with respect to the real-time mosaic, but blurred regions disappear. This gain in resolution is expected to make the analysis of the images by a pathologist easier.

IV. Conclusion

This paper presents a visual servo control scheme for navigating precisely on a soft tissue, for large field of view mosaicking purposes. A particular problem that has to be taken into account is the tissue deformation phenomenon, which is evidenced in the paper and acts as a disturbance to be rejected by the controller.

A simple PI closed loop control and a feedforward action is sufficient for rejecting unmodelled tissue deformations. The precision of the tracking allows for computing large mosaics with proper overlapping. Resulting mosaics are of good quality thanks to subsequent optimization of the images positions in the mosaic.

Future research will direct towards integrating the tissue model that has been proposed and validated in [13] in order to enhance the tracking performances of this visual servo control scheme. Integration in minimally invasive instruments for *in vivo* evaluation is also considered.

Acknowledgement

The authors thank their partners in the PERSEE project: Mauna Kea Technologies (project leader, Paris, France), Endocontrol Medical (Grenoble, France), Institut Mutualiste Montsouris (Paris, France) and Institut Gustave Roussy.

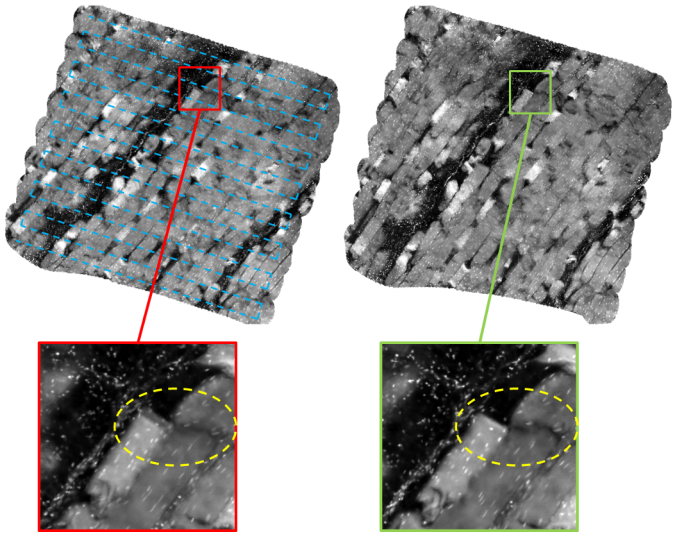

Figure 5. Square 1.7 x 1.7 mm raster scan mosaics constituted with 1600 images obtained under visual servoing (chicken breast). Left: real-time mosaic with the raster scan desired trajectory in dashed blue; right: optimized mosaic. Zooming on details show that, for the optimized mosaic, the precision of the off-line registration allowed by proper layer overlapping leads to see microscopic details with reduced blur, for example in the yellow dashed ellipse.

The project also largely benefits from the interaction with three anthropologists, Marie-Christine Pouchelle, Caroline Moricot and Marina Maestrutti, who are warmly thanked (support from CNRS, PE/PS program of INSHS and from INCA – the national institute of cancer).

REFERENCES

[1] Y. Hori, "Diagnostic laparoscopy guidelines," *Surgical Endoscopy*, vol. 22, no. 5, pp. 1353–1383, 2008.

[2] V. Muntean, A. Mihailov, C. Iancu, R. Toganel, O. Fabian, I. Domsa, and M. Muntean, "Staging laparoscopy in gastric cancer. accuracy and impact on therapy," *J. Gastrointestin. Liver Dis.*, vol. 18, no. 2, pp. 189–195, 2009.

[3] L. Hariri, G. Bonnema, K. Schmidt, A. Winkler, V. Korde, K. Hatch, J. Davis, M. Brewer, and J. Barton, "Laparoscopic optical coherence tomography imaging of human ovarian cancer," *Gynecologic oncology*, vol. 114, no. 2, pp. 188–194, 2009.

[4] G. L. Goualher, A. Perchant, M. Genet, B. Viellerobe, B. Abrat, and N. Ayache, "Towards optical biopsies with an integrated fibered confocal fluorescence microscope," in *Proc. IEEE International Conference on Medical Image Computing and Computer-Assisted Intervention (MICCAI'04)*, 2004, pp. 761–768.

[5] M. Wallace, P. Fockens *et al.*, "Probe-based confocal laser endomicroscopy." *Gastroenterology*, vol. 136, no. 5, p. 1509, 2009.

[6] R. Kiesslich, L. Gossner, M. Goetz, A. Dahlmann, M. Vieth, M. Stolte, A. Hoffman, M. Jung, B. Nafe, P. Galle *et al.*, "In vivo histology of barrett's esophagus and associated neoplasia by confocal laser endomicroscopy," *Clinical Gastroenterology and Hepatology*, vol. 4, no. 8, pp. 979–987, 2006.

[7] P. Sharma, A. Meining, E. Coron, C. Lightdale, H. Wolfsen, A. Bansal, M. Bajbouj, J. Galmiche, J. Abrams, A. Rastogi *et al.*, "Real-time increased detection of neoplastic tissue in barrett's esophagus with probe-based confocal laser endomicroscopy: final results of an international multicenter, prospective, randomized, controlled trial," *Gastrointestinal endoscopy*, vol. 74, no. 3, pp. 465–472, 2011.

[8] B. Rosa, B. Herman, J. Szewczyk, B. Gayet, and G. Morel, "Laparoscopic optical biopsies: in vivo robotized mosaicing with probe-based confocal endomicroscopy," in *Intelligent Robots and Systems (IROS), 2011 IEEE/RSJ International Conference on*. IEEE, 2011, pp. 1339–1345.

[9] W. Latt, T. Chang, A. Di Marco, P. Pratt, K. Kwok, J. Clark, and G. Yang, "A hand-held instrument for in vivo probe-based confocal laser endomicroscopy during minimally invasive surgery," in *Intelligent Robots and Systems (IROS), 2012 IEEE/RSJ International Conference on*. IEEE, 2012, pp. 1982–1987.

[10] T. Vercauteren, A. Perchant, G. Malandain, X. Pennec, and N. Ayache, "Robust mosaicing with correction of motion distortions and tissue deformations for in vivo fibered microscopy," *Medical Image Analysis*, vol. 10, no. 5, pp. 673–692, Oct. 2006.

[11] K. E. Loewke, D. B. Camarillo, W. Piyawattanametha, M. J. Mandella, C. H. Contag, S. Thrun, and J. K. Salisbury, "In vivo micro-image mosaicing," *IEEE Trans. Biomed. Eng.*, vol. 58, no. 1, pp. 159–171, Jan. 2011.

[12] M. Erden, B. Rosa, J. Szewczyk, and G. Morel, "Mechanical design of a distal scanner for confocal microlaparoscope: a conic solution," in *IEEE International Conference on Robotics and Automation (ICRA)*, 2013, to appear.

[13] ——, "Understanding soft tissue behavior for application to microlaparoscopic surface scan," *IEEE Transactions on Biomedical Engineering*, vol. 60, no. 4, pp. 1059 – 1068, 2013.

[14] J. P. Lewis, "Fast template matching," in *Proceedings of the International Conference on Vision Interface (VI'95)*, 1995, pp. 120–123.

[15] B. Rosa, M. Erden, T. Vercauteren, B. Herman, J. Szewczyk, and G. Morel, "Building large mosaics of confocal endomicroscopic images using visual servoing," *IEEE Transactions on Biomedical Engineering*, vol. 60, no. 4, pp. 1041 – 1049, 2013.

Needle Mounted Navigation System for Free Hand Percutaneous Procedures

Diego Dall'Alba, Bogdan Maris et Paolo Fiorini

***Abstract*— In this work we have designed and developed a new navigation system for interventional radiology, implemented in a light and compact device. The system attached to the needle is composed by a small screen that gives hints about the position and the orientation, a controller that commands the screen and interfaces with the computer, and a marker that communicates with a tracking system. By using a real time software the user is guided to move the needle along the desired position and orientation. To the best of our knowledges, this is the first system to have the navigation display integrated directly on the tool. The in-vitro tests we have performed, show how such a system yields a higher precision in the execution of the task and a reduction of the time required to complete the procedure.**

I. Introduction

Clinical practice is increasingly replacing traditional open surgical procedures with minimally invasive techniques. This development results in a transition from direct visual feedback to image-based feedback. Image-guided percutaneous procedures are used for both diagnosis and treatment. The most known diagnostic procedure is biopsy, which is used to collect samples of tissues presumed to be malignant. Therapeutic procedures include tumor ablation based on different technologies such as radiofrequency ablation (RFA), cryoablation (CA) or tumor embolization. These procedures require precise insertion of an elongate instrument, usually referred as ablation probe or simply needle, into the target region. The success of the ablation is constrained by the precise positioning of the needle. Needle based procedures could be subdivided in 3 main steps: localization of the entry point on the patient's skin, orientation toward the target point of the needle and needle insertion. As reported in [1], one of the most underestimated challenges of surgical guidance is the intraoperative display. Different navigation systems have been proposed in literature, based on different tracking technologies or image modalities (see [2], [3] and [4]). All these works prove that the introduction of a navigation system during the procedure improve the performance in the needle insertion task. Anyway, no work addresses the specific problem of providing the navigation information to the user in an intuitive and ergonomic way. The positioning of the needle is still a key issue and most of the time the percutaneous procedure is human based, therefore we propose an integrated navigation system that provides information directly on the tool. The system helps the user to execute the procedure with high accuracy and precision.

This research has received funding from the European Union Seventh Framework Programme (FP7/2007-2013) under grant agreement no. 248960

Diego Dall'Alba, Bogdan Maris, and Paolo Fiorini are with the Department of Computer Science, University of Verona, Italy. diego.dallalba@univr.it, bogdan.maris@univr.it, paolo.fiorini@univr.it

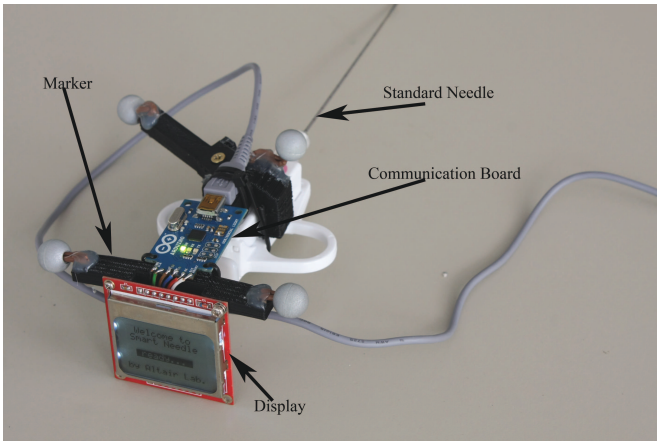

Fig. 1. A standard 18 gauge biopsy needle equipped with the compact navigation system.

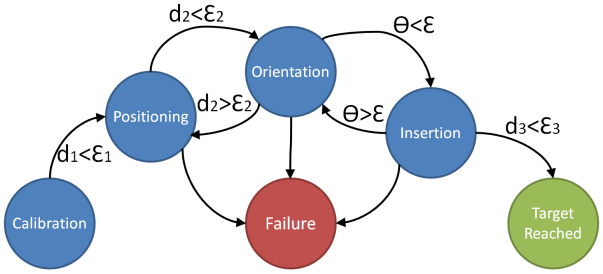

Fig. 2. State machine diagram. The threshold error depends on the current state and on the accuracy of the positioning ($\epsilon_1, \epsilon_2, \epsilon_3$) and orientation ($\epsilon$) to be reached(e.g. $\epsilon_1 < 1mm, \epsilon_2 < 3mm, \epsilon_3 < 4mm$). The on-line value of the target distance is given by the parameters d_1, d_2, d_3 for the positioning and θ for the orientation and is continuously updated on the display by a suitable graphical representation.

II. Materials and Methods

The position and the orientation of the needle are tracked with a passive optical tracking system from NaturalPoint (Corvallis, OR, US) composed by 12 USB infrared (IR) cameras. The precision of the tracking system is less than one millimeter. The proposed navigation system (Fig. 1) is designed to be attached to any type of needle (the first prototype is designed for biopsy needles). This characteristic requires the precise identification of the needle geometry (calibration phase) together with a method to map the navigation information on the display attached to the tool (navigation phase). The purpose of the calibration phase is

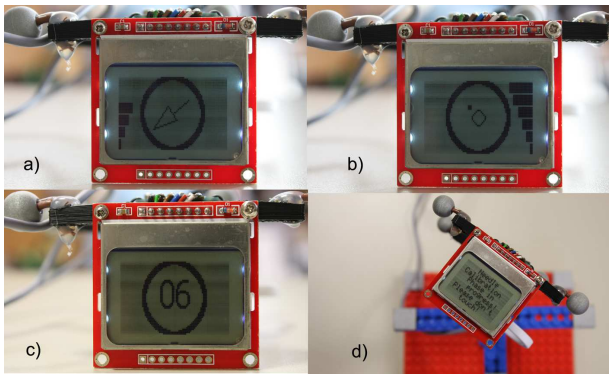

Fig. 3. State machine display a) positioning state. b)orientation state. c) insertion step. d) calibration step.

to identify the rigid transformation that links needle reference system with tracker measurements. This transformation will be used to display the correct information on the screen. The navigation process is modeled as a state machine (see Fig. 2) and to pass from one state to another a threshold is defined depending on the accuracy we want to reach. The first step of the navigation is the positioning of the needle to the entry point. It is advantageous to perform the aligning step after finding the entry point, because the instrument can be pivoted around the contact point between its tip portion and the surface without losing the entry point, which has already been located. When the accurate orientation is found the insertion will take place. For each step of the needle insertion and calibration, different representations are displayed on the screen, as shown in Fig. 3. For more details about the design of the compact navigation system and the calibration method please refer to [5]. The performances of the developed device were tested in-vitro. A polypropylene phantom with a thickness of 2 cm has been chosen for this experiment since it allows the needle to keep the same orientation after insertion. To localize a target point inside the phantom it was used the tip of a second calibrated needle. Five entry positions on the surface of the phantom were fixed. Each of the entry point together with the target point defines an orientation. For each of the 5 entry points positions, the needle insertion was repeated 5 times, for a total of 25 insertions for each user.

III. Results

In the experimental setup no. 1 the needle insertion was performed with the use of a PC monitor placed in front of the user on the same table of the phantom. The 3D information about the tool and the points (entry and target) are represented on the monitor, as in a standard image guided procedure. The experimental setup no. 2 was performed as the setup no. 1 but with the use of the new system that integrates the display applied on the needle. An important measure was the deviation from the desired orientation, once the target point was reached. Since the planning phase defines the safe orientation, we have computed the angle between the planned orientation and the final orientation. The positioning error was measured as the Euclidean distance between the needle tip position and the entry or the target point position, while the orientation error is measured as the dot product between the normalized vector represented by the entry point and target point and the vector representing the orientation of the needle given by the calibration transformation. Six subjects without previous experience have tested the system after the oral explanation of the task. We have compared the results in terms of accuracy in entry and target points localization. In Table I we report the accuracy and precision results of the experiment. We report the entry point localization error (ELE), the target point localization error (TLE) and angular orientation error (AOE). The results of experimental setup 2 show that the mean and STD of the error is lower than in setup 1 for all the errors considered. The use of the proposed system reduces the error (both in the position and in the orientation) and also reduces the influence of the users experience in needle insertion execution. In fact the standard deviation of the data is lower and more stable than in the case without display on the needle. The needle insertion time with the display mounted on the needle is about 40% lower than without the display.

Setup 1 with PC monitor						
	ELE [mm]		TLE [mm]		AOE [degree]	
User	Mean	STD	Mean	STD	Mean	STD
U1	5.114	1.453	4.50	2.542	5.839	1.667
U2	4.006	2.187	5.464	1.410	5.758	1.146
U3	5.081	2.321	4.506	2.187	6.259	2.869
U4	4.136	3.194	5.614	2.739	5.727	2.778
U5	5.147	1.492	4.497	1.665	5.420	1.726
U6	3.876	4.261	5.315	1.765	5.790	1.955
All	4.56	2.485	4.983	2.051	5.799	2.007
Setup 2 with PC monitor and display on the needle						
User	Mean	STD	Mean	STD	Mean	STD
U1	2.79	1.091	3.637	1.121	1.734	1.309
U2	2.703	1.114	3.079	1.677	2.456	1.856
U3	2.697	1.462	2.467	1.578	2.902	1.068
U4	2.727	1.257	3.916	1.988	1.833	1.576
U5	2.916	1.725	2.991	2.091	2.52	1.848
U6	2.627	2.111	3.043	1.26	4.036	0.918
All	2.746	1.46	3.196	1.619	2.58	1.429

TABLE I

Comparison of Error Values in the two experimental setups.

IV. Discussion

This work proposed a new system for an accurate needle placement. We have designed, tested and evaluated the system in an in-vitro experiment. The experiments we have done validate the utility of the tool that can be used in a more complex procedure. The main advantages of the navigation system we have presented are:

- gives the information directly on the tool.
- there is no need for the user to move the eyes from the interventional area.
- improves the accuracy and the precision to reach the desired position and orientation.
- reduces the procedure's time.

In the future works the electronic components will be miniaturized, and also the display should have a higher resolution and a higher refresh rate. The rigid body design will provide more protection to the electronic components. The needle device is being redesigned to take into account cleaning and sterilization requirement imposed by the operation room environment.

REFERENCES

[1] S. D. Herrell, R. L. Galloway, and L.-M. Su, "Image-guided robotic surgery: update on research and potential applications in urologic surgery." *Current Opinion in Urology*, vol. 22, no. 1, pp. 47–54, 2012. [Online]. Available: http://www.ncbi.nlm.nih.gov/pubmed/22080871

[2] A. Tekbas, A. Seitel, A. M. Franz, B. Radeleff, F. Pianka, and S. A. Müller, "Computer-Assisted Needle Insertion for Abdominal Interventions," *IFMBE Proceedings*, no. Vol. 25, pp. 159–162, 2009.

[3] F. Banovac, E. Wilson, H. Zhang, and K. Cleary, "Needle biopsy of anatomically unfavorable liver lesions with an electromagnetic navigation assist device in a computed tomography environment." *Journal of vascular and interventional radiology JVIR*, vol. 17, no. 10, pp. 1671–1675, 2006. [Online]. Available: http://www.ncbi.nlm.nih.gov/pubmed/17057009

[4] M. J. Wallace, S. Gupta, and M. E. Hicks, "Out-of-plane computed-tomography-guided biopsy using a magnetic-field-based navigation system." *CardioVascular and Interventional Radiology*, vol. 29, no. 1, pp. 108–113, 2006. [Online]. Available: http://www.ncbi.nlm.nih.gov/pubmed/16328686

[5] D. Dall'Alba, B. Maris, and P. Fiorini, "A compact navigation system for free hand needle placement in percutaneous procedures," in *IEEE/RSJ International Conference onIntelligent Robots and Systems (IROS)*, 2012.

Development of a Robotic Comanipulation and Teleoperation System for Vitreoretinal Surgery

A. Gijbels[1], E.B. Vander Poorten[1], P. Stalmans[2], D. Reynaerts[1]
[1]Dept. of Mechanical Engineering, Katholieke Universiteit Leuven, Belgium
[2]Dept. of Ophthalmology, University Hospitals Leuven, Belgium
Email: andy.gijbels@mech.kuleuven.be

I. Vitreoretinal Surgery

During vitreoretinal surgery, the surgeon performs procedures at the retina which acquire extreme precision. For some diseases, the most appropriate treatment is even too difficult to be performed manually and alternative but less effective treatments need to be applied. One of those diseases is called Retinal Vein Occlusion (RVO). Retinal Vein Occlusion is an eye condition which affects an estimated 16.4 million adults worldwide [1]. The disease occurs when a clot is formed in a retinal vein. This causes the patient to slowly lose his/her sight. Fig. 1 shows a healthy retina on the left and a retina suffering from RVO on the right. Today, there is no proven effective

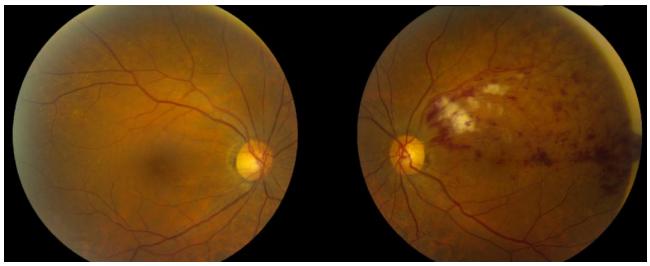

Fig. 1. Retinal Vein Occlusion (RVO): when a retinal vein gets blocked, the circulation of blood through the affected vein is reduced or stopped. The blockage causes the walls of the vein to leak blood and excess fluid into the retina. When the fluid collects in the macula (the area of the retina responsible for central vision), vision becomes blurry.
Left: healthy retina. Right: retina with RVO.

treatment available for this disease [2]. A promising treatment is retinal vein cannulation. During this procedure the surgeon inserts a needle through the sclera and injects a small dose of t-PA, a clot-dissolving agent, directly into the blocked vein [3]. Fig. 2 conceptually demonstrates this procedure. Several research groups report successful cannulations in animal and human models. However, due to safety issues, the procedure is not performed clinically today. The needle needs to be inserted in a vein with a diameter smaller than 500 µm and kept there for several minutes for the fluid to be fully injected [4]. Unintended movements make it extremely difficult to insert and maintain the needle into the vein. They can cause serious damage to the retina during this procedure. Two relevant types of unintended movements can be distinguished. Firstly, the human suffers from physiological tremor. Hand vibrations with an rms amplitude of 182 µm during vitreoretinal procedures

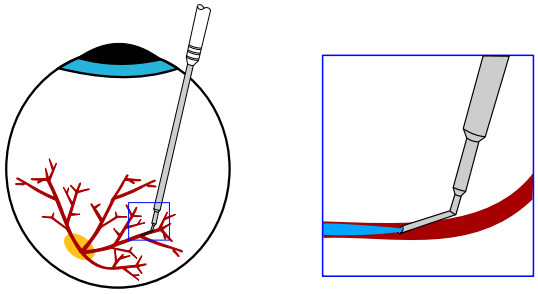

Fig. 2. Retinal Vein Cannulation: a hollow needle is inserted through the sclera and used to inject a clot-dissolving agent directly into the affected vein to remove the blockage causing RVO.

have been reported [5]. Secondly, the eye tends to rotate during the procedure due to the lateral forces applied by the instrument on the incision point. These rotations cause the retina to move which makes the surgeon to aim at a dynamic target.

II. Robot-assisted retinal cannulations

Abovementioned problems can be overcome by attaching the instrument to a surgical manipulator that assists the surgeon during the procedure. The manipulator can hold the eye stationary during the procedure by virtue of a Remote Center of Motion (RCM) incorporated in the manipulator. An RCM is a geometric point at a fixed location about which the instrument can pivot and translate through without a physical joint being present at this location [6]. When this RCM is made to coincide with the incision point in the sclera, the degrees of freedom (DOFs) of the instrument will be restricted to three rotations Θ, Φ and Ψ around the RCM and a translation R through the RCM as shown in Fig. 3. In this way, the eye and thus the retina are stabilized such that aiming at the blocked vein becomes easier.

Several surgical manipulators for vitreoretinal surgery have been reported [7]–[12]. Most of those, using a mechanism to implement the RCM, fail to keep the end-effector compact enough due to the kinematics of these mechanisms. This is problematic because of the very confined workspace typically for vitreoretinal surgery. The operating scene is populated by the patient, the surgeon and the microscope that the surgeon

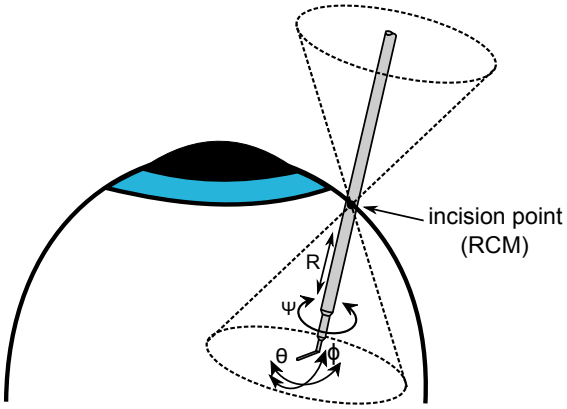

Fig. 3. Vitreoretinal surgeons only need 4 DOFs to manoeuvre the instrument in the eye: three rotations Θ, Φ and Ψ around the incision point and a translation R through the incision point. The remaining DOFs, which cause unintended eye rotations, can be blocked by aligning the RCM of the surgical manipulator with the incision point.

uses to navigate the instruments inside the patient's eye. To overcome these space limitations, an innovative RCM mechanism is incorporated in the surgical manipulator allowing a compact construction of the manipulators end-effector (see Fig. 4).

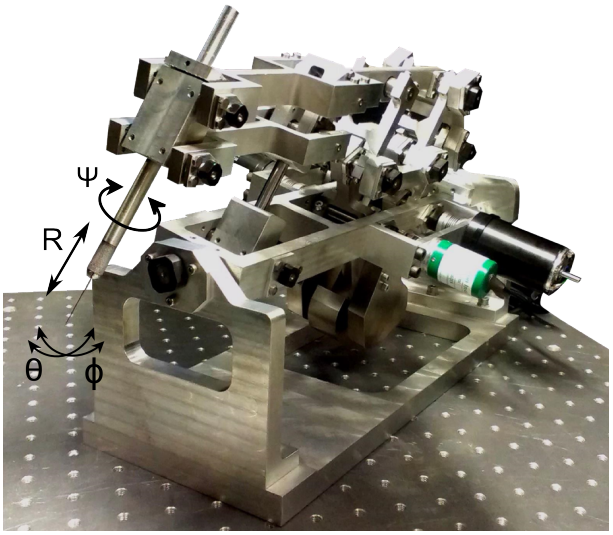

Fig. 4. The surgical manipulator relies on a novel RCM mechanism which implements the translational DOF of the instrument at the base of the mechanism instead of implementing it at the end-effector. In this way the end-effector is held very compact which is particularly interesting for retinal surgery where the instrument needs to be manoeuvred in a highly confined space.

The surgeon can choose to co-operatively move the instrument by gripping and manipulating the instrument directly (comanipulation strategy) or to control the movements of the surgical manipulator indirectly using a joystick (teleoperation strategy). For this purpose, the surgical manipulator is actuated in all its DOFs. When using the comanipulation strategy, virtual damping is implemented in the surgical manipulator to filter out the unintended hand vibrations. This damping also slows down the intended movements facilitating a slow and precise approach of the vein. When using the teleoperation strategy, motion scaling is used to scale down the hand vibrations and to slow down the intended hand movements. For this purpose a 4 DOF haptic joystick was developed (see Fig. 5). The DOFs of this joystick correspond to those shown on Fig. 3. Because of the haptic property of the joystick, scaled force feedback of the interaction forces between the instrument and the retina is possible. In this way, the surgeon is able to feel forces which are normally to small for humans to perceive. This feature will be implemented in the near future using a force sensor integrated in the surgical instrument. Currently, we are testing both the comanipulation and the teleoperation system to determine which technique is the most appropriate one for robotic vitreoretinal surgery.

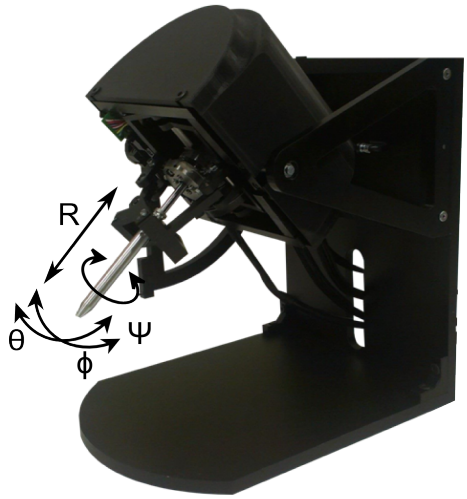

Fig. 5. The kinematical design of the joystick is such that its DOFs correspond to those used during vitreoretinal surgery. The movements of the joystick handle are mapped on the movements of the needle rather than on the movements of the instrument handle. In this way motion inversion between the movements of the surgeon and the instrument, which is typical for this kind of surgery, is eliminated.

III. Acknowledgments

This work was supported by an FP7-People Marie Curie Reintegration Grant, PIRG03-2008-231045 and by a PhD grant from the Institute for the Promotion of Innovation through Science and Technology in Flanders (I.W.T.-Vlaanderen), 101445.

References

[1] R. Sophie, "The prevalence of retinal vein occlusion: Pooled data from population studies from the united states, europe, asia, and australia," *Ophthalmology*, vol. 117, pp. 313– 319, 2010.

[2] B. Nilufer and B. Cosar, "Surgical treatment of central retinal vein occlusion," *Acta Ophthalmologica*, vol. 86, pp. 245–252, 2008.

[3] L. A. Bynoe, R. K. Hutchins, H. S. Lazarus, and M. A. Friedberg, "Retinal endovascular surgery for central retinal vein occlusion: Initial experience of four surgeons," *Retina*, vol. 25, pp. 625–32, 2005.

[4] M. R. Glucksberg, R. Dunn, and C. P. Giebs, "In vivo micropuncture of retinal vessels," *Graefe's Archive for Clinical and Experimental Ophthalmology,*, vol. 231, pp. 405–407, 1993.

[5] C. N. Riviere and P. S. Jensed, "A study of instrument motion in retinal microsurgery," *Proc. of the 22nd Annual EMBS Int. Conf.*, 2000.

[6] G. Zong, X. Pei, J. Yu, and S. Bi, "Classification and type synthesis of 1-dof remote center of motion mechanisms," *Mechanism and Machine Theory*, vol. 43, pp. 1585 – 1595, 2008.

[7] W. Wei, R. Goldman, N. Simaan, H. Fine, and S. Chang, "Design and theoretical evaluation of micro-surgical manipulators for orbital manipulation and intraocular dexterity," *ICRA*, pp. 3389–3395, 2007.

[8] K. Grace, J. Colgate, M. Glucksberg, and J. Chun, "A six degree of freedom micromanipulator for ophthalmic surgery," *IEEE Int. Conf. on Robotics and Automation*, vol. 1, pp. 630–635, 1993.

[9] M. Wapler, V. Urban, T. Weisener, J. Stallkamp, M. Durr, and A. Hiller, "A stewart platform for precision surgery," *Transactions of the Institute of Measurement & Control*, vol. 25-4, p. 329, 2003.

[10] Y. Ida, N. Sugita, T. Ueta, Y. Tamaki, K. Tanimoto, and M. Mitsuishi, "Microsurgical robotic system for vitreoretinal surgery," *Int. Conf. of Computer Assisted Radiology and Surgery*, pp. 27–34, 2012.

[11] A. Uneri, M. Balicki, J. Handa, P. Gehlbach, R. Taylor, and I. Iordachita, "New steady-hand eye robot with microforce sensing for vitreoretinal surgery research," *Int. Conf. on Biomedical Robotics and Biomechatronics*, pp. 814–819, 2010.

[12] Meenink, H.C.M., Rosielle, P.C.J.N., Steinbuch, and M. Smet, "Instrument manipulator for a master-slave robot for vitreo-retinal ophthalmic surgery," *Proc. of the 21st Int. Conf. on Medical Innovation and Technology 2009, Romania,*, p. 53.

Redundancy management of a LWR4+ for safe, collision free, robotic surgical applications, using environmental sensors

Danilo De Lorenzo, Simone Calò, Andrea Ciullo, Mirko Daniele Comparetti, Elena De Momi, Giancarlo Ferrigno
Department of Electronics, Information and Bioengineering
Politecnico di Milano
Milan, Italy
danilo.delorenzo@polimi.it

Mirko Kunze
Institute for Process Control and Robotics
Karlsruhe Institute of Technology
Karlsruhe, Germany

Abstract— **In surgical robotics, workspace sharing between robots and humans asks for safety-oriented control of the physical interaction. In this paper, a ROS – OROCOS system architecture for collision avoidance is presented for safe human-robot coexistence inside the operating room. A Microsoft Kinect sensor allows to track the user hand and to exploit the redundancy of the Kuka LWR4+ 7DoF manipulator moving the robot links far from a possible collision.**
Results show that the reaction time of the robot is about 80ms, when the user hand enters the collision risk region. A calibration between the Kinect and the robot workspace allows not to track the robot links with the Kinect sensor, reducing possible human-robot tracking occlusions.

Keywords—human-robot interaction; robotic surgery; redundancy; collision avoidance.

I. INTRODUCTION

In neurosurgery, several procedures can be performed with the help of robotic assistance. The robotic support can act directly on the surgeon tasks or in tool holding or for teaching [1][2]. In all these scenarios, the surgeon and the robot share the same workspace and safe human-robot interaction strategies must be considered. Collision detection and collision avoidance are needed inside an operating room where robots and clinicians work close together. In literature, collision detection and collision avoidance strategies have already been analyzed. Proprioceptive robot sensors are used for collision detection [3]. When the impact occurs, torque sensors detect the real torque on each joint; if the difference between this torque and the commanded torque is bigger than a threshold, the robot stops its movement.

In [4], the pose of the robot is computed in real time with a Kinect sensor. The pose of the operator's hand and the entire structure of the robot are extracted using a depth space approach. A repulsive vector is computed when there is a risk of collision between the robot and the operator. For real-time computation of this repulsive vector, Reflexxes Motion Libraries [5] are used. Both hand position and robot position are extracted using a depth camera. This approach could lead to risky situations in case the operator body overlaps the robot structure, compromising robot and skeleton detection.

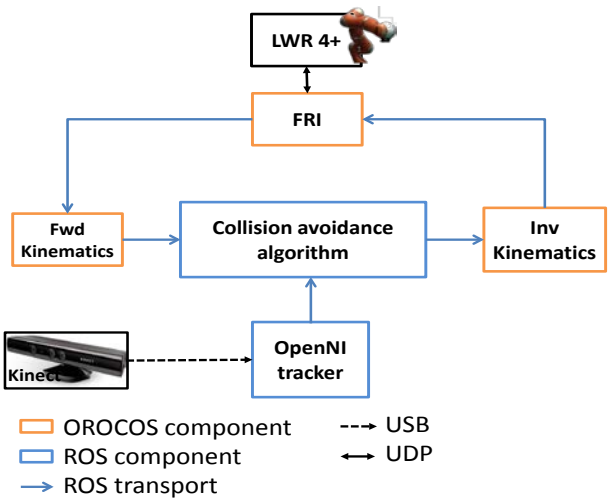

Fig. 1 ROS and OROCOS system software components and architecture.

The work here presented fits inside the Active EU project [6]. One of the purpose is to combine the ability of neurosurgeons with robotic instrument precision and repeatability and to exploit the 7th degree of freedom (redundancy) of a KUKA LWR4+ to improve robot maneuverability and avoid collision with operating room (OR) operators. If the robot is autonomously driven without any environmental information, it can accidentally hit the OR staff and/or the patient, leading to unsafe situations. Therefore, a high level controller to assure safe movements of the robot, avoiding any collision with the surgeon can be mandatory.

We introduce a preliminary system for collision avoidance, based on ROS and OROCOS platforms [7][8], which exploits the kinematic redundancy [9][10] of the Kuka LWR4+ and a

This work was partially funded by the ACTIVE FP7-ICT-2009-6-270460 European Project.

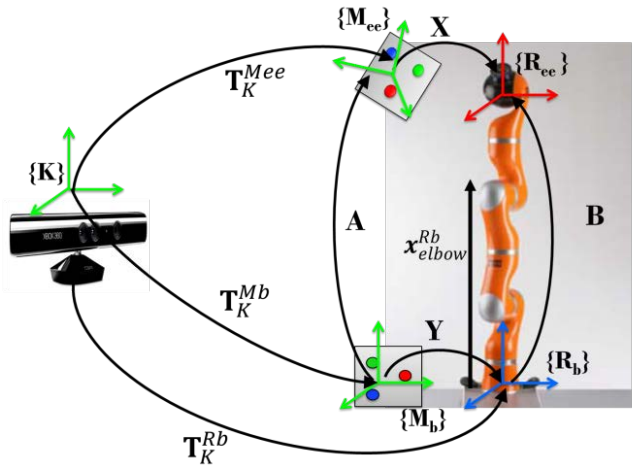

Fig. 2 Transformations involved in the calibration setup between the Kinect sensor and the LWR. **T, A, B, X, Y** are the transformations used during calibration procedure, {M} are the reference frames (RFs) of the markers, {R} are the RFs of the robot.

Microsoft Kinect sensor, calibrated inside the operational space of the robot.

II. Materials and Methods

The complete system is composed of a Microsoft Kinect sensor (Microsoft Corp., Redmond, WA, USA) and a KUKA Light-Weight-Robot 4+ (LWR) (Kuka Robotics, Augsburg, Germany). The system architecture is based on ROS and OROCOS platforms which communicate between them via ROS-transport (Fig. 1). OROCOS components are in charge of real-time communication with the LWR and of forward and inverse kinematic computation, while ROS modules are in charge of managing the information coming from the Kinect camera, using the OpenNI libraries [11] and the Point Cloud libraries [12]. We used the ROS `openni_tracker` component to gather the 3D Cartesian positions of the human body segments. In particular, the 3D position of an operator hand.

A. Kinect-robot calibration

As a first step, the calibration between the robot operational space and the Kinect camera space was performed. The goal of the calibration procedure was to compute the transformation ($\boldsymbol{T}_k^{Rb}$) from the Kinect reference frame (RF), {K}, to the robot base RF, {R_b} (Fig. 2). We glued paper colored (blue, green, red) 3 cm diameter circles on two rigid cardboards. Each cardboard was then attached onto the base and the end-effector (EE) of the robot. The three circles were used to build the two reference frames, {M_b} and {M_{ee}} and to compute the homogeneous transformations $\boldsymbol{T}_K^{Mb}$ and $\boldsymbol{T}_K^{Mee}$. With $\boldsymbol{T}_K^{Mb}$ and $\boldsymbol{T}_K^{Mee}$ known, we computed the **A** transformation between {M_b} and {M_{ee}} as:

$$\mathbf{A} = \mathrm{T}_{\mathrm{K}}^{\mathrm{Mb}\,-1} \cdot \mathrm{T}_{\mathrm{K}}^{\mathrm{Mee}} \qquad (1)$$

B is known via the forward kinematics while **X** and **Y** were determined using an hand-eye calibration procedure [13]. For the hand-eye procedure, the robot was moved in 14 different poses, exploring large part of the entire robot workspace. Once **Y** was known, it was possible to compute the calibration matrix between the robot base RF {R_B} and Kinect RF{K} ($\boldsymbol{T}_k^{Rb}$) as:

$$\mathrm{T}_{\mathrm{k}}^{\mathrm{Rb}} = \mathrm{T}_{\mathrm{K}}^{\mathrm{Mb}} \cdot \mathbf{Y} \qquad (2)$$

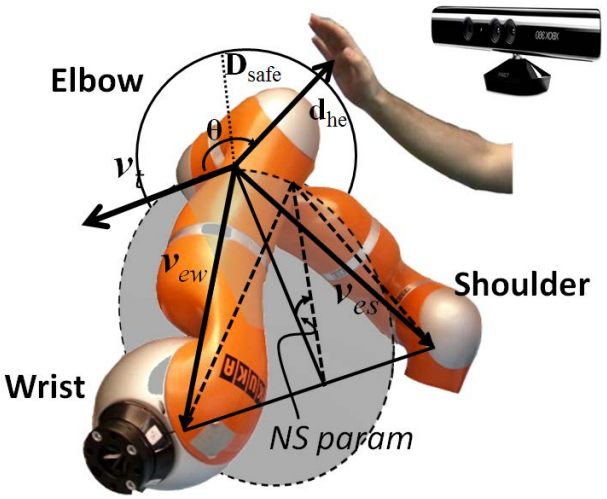

Fig. 3 Collision avoidance algorithm parameters. The null space parameter [10] (*NS param*) is the angle spanned by the triangle plane built as the virtual connection of the shoulder, the elbow and wrist of the robot. $\boldsymbol{v}_{es}$ is vector from elbow to the shoulder, $\boldsymbol{v}_{ew}$ is the vector from elbow to wrist, $\boldsymbol{v}_t$ is the tangent vector to the circumference virtually spanned by the robot elbow, while keeping fixed the wrist pose. $\boldsymbol{d}_{he}$ is the distance vector between the user hand and the elbow.

B. Collision avoidance algorithm

The collision avoidance strategy is aimed at exploiting the kinematic redundancy of the robot in order to keep the links of the robot far from the obstacle, while maintaining the same position of the EE.

As an exemplary scenario, we considered the robot with a fixed pose of its EE on the body of a patient (during a surgery) and the surgeon moving his hand close to the robot. The final goal was to update the value of the null space parameter (*NS param* in Fig. 3) [10] according to a high level control law.

The control law is based on the concept of "safe distance". We defined a spherical region of surveillance with a radius, D_{safe} = 35 cm around the elbow of the robot (Fig. 3). As soon as the hand of the operator enters in the virtual safety sphere, it is identified as an obstacle and the robot changes its configuration. The control law algorithm is detailed in Fig. 4. As a first step, the cartesian pose of the elbow, $\boldsymbol{x}_{elbow}^{Rb}$, is given in {R_b}, via the Fast Research Interface (FRI) [14]. The hand position, $\boldsymbol{x}_{hand}^{K}$, is acquired by the Kinect sensor with respect to {K} RF. Then, using the calibration matrix $\boldsymbol{T}_K^{Rb}$, the elbow position vector $\boldsymbol{x}_{elbow}^{Rb}$(Fig.1), is transformed into the {K} RF:

$$\mathrm{x}_{\mathrm{elbow}}^{\mathrm{K}} = \mathrm{T}_{\mathrm{K}}^{\mathrm{Rb}} \cdot \mathrm{x}_{\mathrm{elbow}}^{\mathrm{Rb}} \qquad (3)$$

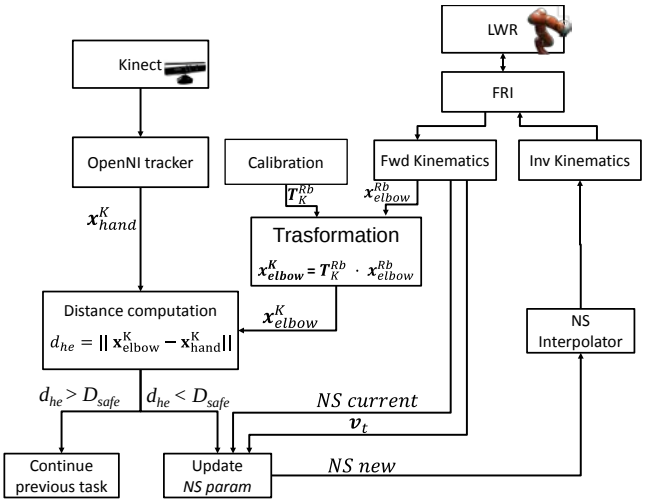

Fig. 4 Collision avoidance scheme.

Thus, the distance d_{he} between the hand and the robot elbow is computed. If d_{he} is less than D_{safe} the robot moves away changing its NS parameter, otherwise it keeps the current position.

The current joint positions are the inputs for the forward kinematics component which computes the current NS parameter (*NS current*) and a tangent vector ($\boldsymbol{v}_t$) (Fig. 3). The latter is the vector constructed as the cross product between the elbow-shoulder vector ($\boldsymbol{v}_{es}$) and the elbow-wrist vector ($\boldsymbol{v}_{ew}$) (Fig. 3):

$$\mathbf{v}_t = \mathbf{v}_{es} \times \mathbf{v}_{ew} \tag{4}$$

$\boldsymbol{v}_t$ is the tangent vector to the circle drawn by the movement of the elbow keeping the wrist and the shoulder fixed in position. $\boldsymbol{v}_t$ and the current *NS param* are published as ROS topics to the component in charge of updating the *NS param* value (*NS new*). The *NS param* value is updated starting from the *NS current*, with the following update rule:

$$NS\,new = NS\,current \mp k\left(\frac{D_{safe}}{d_{he}}\right) \tag{5}$$

with k being the proportional gain set to 0.05. The rule increases or descreases the *NS current* depending on the sign and the value of the cosine of the angle, θ, between $\boldsymbol{d}_{he}$ and $\mathbf{v}_t$ (Fig. 3).

We defined three regions for the possible *cos(θ)* values:

$\bar{c} < cos(\theta) < 1$ (Region 1),
$-\bar{c} < cos(\theta) < \bar{c}$ (Region 2),
$-1 < cos(\theta) < -\bar{c}$ (Region 3).

The complete *NS param* update rule is given by the following pseudo code:

```
If (d_he, < D_safe)
    If  (c̄ < cos(θ) < 1)
        NS new = NS current − k(D_safe / d_he);
    If  (−1 < cos(θ) < −c̄ )
        NS new = NS current + k(D_safe / d_he);
    Else
    Continue previous task
End
```

Region 2 is needed in order to avoid instability, due to the continuous change of the *NS param* from a positive value to a negative value due to the noise on $\boldsymbol{d}_{he}$.

Once the new *NS param* is known, the ROS component publish the new value (*NS new*) to the OROCOS component in charge of the interpolation (NS interpolator), according to the update rate of the FRI component (500 Hz). Then, the inverse kinematics component computes the new joint positions.

C. Experimental setup

a) Kinect hand tracking error

An operator freely moved both the hands in 3D space, handling a rigid cable of 50cm length at 1.2m distance from the Kinect sensors. Hand coordinates were acquired for 45s at 30Hz. The distance ($d_{H\text{-}H}$) between the two hands was computed, expecting $d_{H\text{-}H}$ to be equal to the length of the cable.

b) Kinect hand tracking error after calibration

An operator freely moved one hand in 3D space handling the LWR EE in order to overlap the hand position origin, $\boldsymbol{x}_{hand}^K$, with the {R_{ee}} RF origin; For this task, the robot was set to gravity compensation modality [14]. Hand positions were recorded for 120s with respect to {K} RF, while the EE position, $\boldsymbol{x}_{EE}^{R_b}$, were acquired via forward kinematics and then transformed in the {K} RF via the calibration matrix T_K^{Rb}. Then, the error distance between the hand position x_{hand}^K, and the EE origin x_{ee}^K was computed in {K} operational space:

c) Collision avoidance evaluation

The entire system was tested asking the operator to freely approach the robot elbow with his hand. The robot was approached 5 times from the left side and 5 from the right side, inside the safety zone. The trials were repeated at seven different update frequencies of the ROS component (10, 20, 30, 50, 100, 250, 500 Hz). The maximum allowed angular speed of the elbow was 1.4rad/s and the maximum Cartesian velocity was 0.2m/s, for safety reasons. We evaluated the time delay, T_d, as the time interval which starts as soon as the distance d_{he} is smaller than D_{safe} and ends when the robot starts to move (i.e. when *NS param* starts to change, Fig. 5).

I. Results

The Kinect hand tracking error showed accuracies which depends on hand velocities. The maximum median error was about 8 mm with interquartile range up to 8 cm.

Hand tracking error after calibration showed a median error of about 22 cm (16 cm and 30 cm, 25th and 75th percentile respectively).

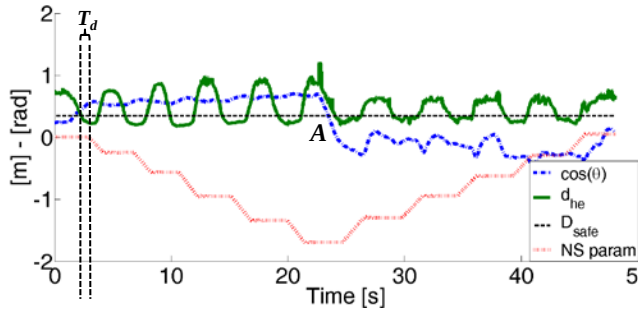

Fig. 5 Example of collision avoidance trial. The hand-elbow distance d_{he}, the safe threshold D_{safe} , the value of the *NS param* and the *cos(θ)* are shown . In A, there is a smooth change of the sign of the cos(θ) , when the user moved the hand on the other side of the robot.

Fig. 5 shows the results of a collision avoidance trial. As soon as the distance d_{he} goes below D_{safe} the robot start to move, changing the *NS param* (after T_d delay).
The time delay T_d (Fig. 6) quickly decreases with the ROS update rate, reaching a plateau below 0.1 ms at 100 Hz (80ms), without considerable improvement for higher frequencies.

II. Discussion and Conclusion

In this work, we showed a collision avoidance strategy able to change configuration of a Kuka LWR4+ robot, keeping fixed the pose of its EE. The calibration between the robot operational space and the Kinect sensor space allows not to track the robot skeleton with the Kinect sensor, avoid possible human – robot occlusions, since the robot link positions are always known from the robot kinematics.
Results showed that the time delay, T_d, between the detection of the possible collision and the actual motion of the robot links was below 0.1s for high update rates of the ROS modules. Given this time delay, it is possible to compute the minimum hand cartesian velocity to hit the robot as $\mathbf{v}_h = D_{safe}/T_d = 3.5$ m/s. We could not find references of speed of motions inside the OR, however, if this hand velocity can happen inside the OR, higher values of D_{safe} should be considered, since lower value of T_d. are not reachable in this architecture. Once the robot starts to move, the maximum speed of the user hand should be kept below the maximum allowed velocity of the elbow, se to 0.2 m/s. It should be noted that in the time delay, T_d, we neglected the delay due to the Kinect sensor computation of the hand position. This delay will be further evaluated tracking both the hand and the robot with an accurate external optical localization system. The collision avoidance method is not affected by the high Kinect tracking error (about 20cm), unless a specific safety distance is chosen to be considerably higher than the tracking accuracy.

The work is a preliminary study on the possibility to use such a system in the real OR, extending the algorithm to multi-body distance computation from all the joints of the robot. This will require increased computational costs that will be evaluated in further tests.

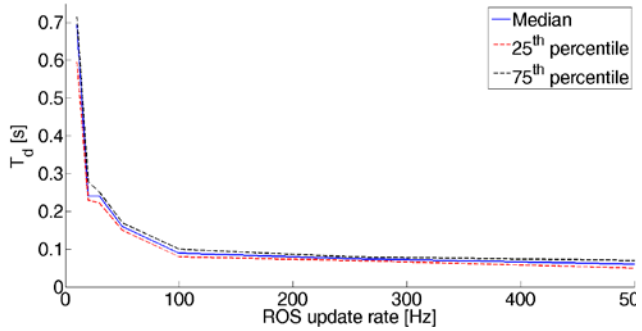

Fig. 6 Time delay T_d with respect to the ROS components update rate. Above 100Hz, the delay reaches a plateau of about 0.08s as median value.

References

[1] T. R. K. Varma, P. R. Eldridge, A. Forster, S. Fox, N. Fletcher, M. Steiger, P. Littlechild, P. Byrne, A. Sinnott, K. Tyler, S. Flintham, "Use of the NeuroMate Stereotactic Robot in a Frameless Mode for Movement Disorder Surgery," Stereotact Funct Neurosurg, vol. 80, pp. 132-135, 2003.

[2] G. R. Sutherland, I. Latour, A.D Greer, "Integrating an image-guided robot with intraoperative MRI: a review of the design and construction of neuroArm," IEEE Eng Med Biol Mag., vol. 27(3), pp.59-65, 2008.

[3] A. De Luca, A. Albu-Schaffer, S. Haddadin, G. Hirzinger, "Collision Detection and Safe Reaction with the DLR-III Lightweight Manipulator Arm," IEEE/RSJ International Conference on Intelligent Robots and Systems, 2006, pp.1623-1630, Oct. 2006, doi: 10.1109/IROS.2006.

[4] F. Flacco, T. Kroger, A. De Luca and O.Khatib, "A depth space approach to human-robot collision avoidance," IEEE International Conference on Robotics and Automation (ICRA), pp.338-345, 14-18 May 2012, doi: 10.1109/ICRA.2012.6225245

[5] T. Kröger, "Opening the door to new sensor-based robot applications — The Reflexxes Motion Libraries", in Proc. of the IEEE International Conference on Robotics and Automation, Shanghai, China, May 2011.

[6] G. Ferrigno, G. Baroni, F. Casolo, E. De Momi, G. Gini, M. Matteucci and A. Pedrocchi, "Medical Robotics and Computer-Aided Therapy", IEEE PULSE, vol. 2(3), pp. 55-61, 2011.

[7] M. Quigley, B. Gerkey, K. Conley, J. Faust, T. Foote, J. Leibs, E. Berger, R. Wheeler, and A. Y. Ng, "ROS: an open-source Robot Operating System," in Proc. Open-Source Software workshop of the International Conference on Robotics and Automation (ICRA), 2009.

[8] H. Bruyninckx, P.Soetens and B. Koninckx. The Real-Time Motion Control Core of the Orocos Project. IEEE International Conference on Robotics and Automation, p. 2766—2771, 2003

[9] A. De Luca and L. Ferrajoli, "Exploiting robot redundancy in collision detection and reaction," IEEE/RSJ International Conference on Intelligent Robots and Systems. IROS 2008, pp.3299-,3305, 22-26 Sept. 2008, doi: 10.1109/IROS.2008.4651204

[10] M. Shimizu, H. Kakuya, Y. Woo-Keun, K. Kitagaki and K. Kosuge, "Analytical Inverse Kinematic Computation for 7-DOF Redundant Manipulators With Joint Limits and Its Application to Redundancy Resolution," IEEE Transactions on Robotics, vol. 24(5), pp.1131-1142, Oct. 2008, doi: 10.1109/TRO.2008.2003266.

[11] OpenNi Framework, Documentation Homepage "http://www.openni.org (accessed: Nov. 2012)", Internet, 2012.

[12] R. B. Rusu, and S. Cousins, "3D is here: Point Cloud Library (PCL)," 2011 IEEE International Conference on Robotics and Automation (ICRA), pp. 1-4, 9-13 May 2011, doi: 10.1109/ICRA.2011.5980567

[13] M. D. Comparetti, A. Vaccarella, I. Dyagilev, M. Shoham, G. Ferrigno, and E. De Momi, "Accurate multi-robot targeting for keyhole neurosurgery based on external sensor monitoring," Proc Inst Mech Eng H., vol. 226(5), pp. 347-59, May 2012.

[14] G. Schreiber, A. Stemmer, and R. Bischoff, "The fast research interface for the kuka lightweight robot", IEEE International Conference on Robotics and Automation (ICRA 2010) Workshop on Innovative Robot Control Architectures, 2010.

Cutting Edge Technology in Computer Assisted Surgery for Total Knee Replacement

State-of-the-art of techniques and relevant results

Claudio Belvedere, Silvia Tamarri, Alberto Leardini
Movement Analysis Laboratory, Istituto Ortopedico Rizzoli
Bologna, Italy
belvedere@ior.it

Andrea Ensini, Antonio Timoncini, Sandro Giannini
I Orthopedics Clinic, Istituto Ortopedico Rizzoli
Bologna, Italy
giannini@ior.it

***Abstract* — After the initial exploitation of robotic assistance, computer assisted surgery in total knee replacement has proposed recently a number of surgical navigation systems and patient-specific instrumentations. These have contributed to achieve more accurate alignments than those obtained with conventional procedures. The present work wants to report on current intra- and post-operative measurements and analyses with these two technologies, aimed also at investigating the tracking of additional structures, as well as accuracy and efficacy of the surgical results. In a first study, a novel procedure to trace patello-femoral joint kinematics during navigated knee replacement is described, together with the initial very encouraging results in initial surgical case. From these measurements, an original procedure is proposed also to describe slackening and tightening of patellar tendon fibers. In a second, two patient-specific instrumentation procedures are evaluated by comparing the alignments planned preoperatively and achieved perioperatively, by using traditional and original techniques based on medical imaging. Both techniques demonstrated to be feasible, reliable, safe, and accurate enough for the purposes.**

Keywords* — *Human knee joint; patello-femoral joint; osteoarthritis - rheumatoid arthritis; joint replacement; knee prostheses; patient-specific instrumentation; surgical navigation; gait analysis; three-dimensional video-fluoroscopy

I. INTRODUCTION

Computer assisted surgery has investigated a number of different technologies after the initial exploitation of robotic assistance [1]. This is particularly true in total knee replacement (TKR), likely because of the huge number of operations, suitable traditional operative techniques, and the interest of vendors and surgeons. Surgical navigation systems (SNS) has been largely utilized since the late nineties to track the tibio-femoral joint (TFJ) together with corresponding bone cutting guides, for the three-dimensional (3D) alignment of the knee prosthesis components to the bones and of the whole lower limb to be targeted and assessed carefully according to anatomical reference frames defined at the beginning of the operation [2,3]. More recently, a so-called patient-specific instrumentation (PSI) has been proposed, with the aim of positioning prosthetic components according to the patient lower-limb and single bone alignments [1]. Computer models of the distal femur and proximal tibia are defined from scan acquisitions using computer tomography (CT) or magnetic resonance imaging (MRI) [1]. Based on these models, pre-surgical planning is then arranged by the TKR vendor and offered to the examination and adjustment of the surgeon via web-based interfaces. Corresponding patient- matched cutting guides are then manufactured and delivered to the hospital for guiding unequivocally bone resections during the operation. The final objective is to eliminate the standard huge instrumentation sets [1], which have to be taken sterilized in the operating theatre, for the surgeons to use simply the patient-matched guides and the corresponding TKR implant.

Both these computer-assisted technologies apparently have resulted in more accurate alignments than those after conventional implantation. However, surgical navigation still needs to exploit the tracking of the patella [4,5], known to be fundamental for the final patient outcome, much affected by a good restoration of the extensor apparatus (extensor muscles, patello-femoral joint – PFJ, patellar tendon). PSI has not demonstrated yet its final accuracy and efficacy in terms of restoration of physiological joint function [6]. The present work wants to contribute to these issues by reporting on current intra- and post-operative measurements and analyses in TKR patients operated with these technologies.

II. Knee Extensor Mechanism: In-vivo measures

A. PFJ tracking

1) *Rationale* - TKR also alters normal PFJ kinematics within the extensor mechanism resulting frequently in PFJ disorders and TKR failure [4]. Patellar tracking in case of resurfacing is further affected by patellar bone preparation and relevant component positioning. The traditional technique used to perform patellar resurfacing, even using SNS, is based only on visual inspection of its articular aspect for clamping the cutting jig and on a simple caliper to check for the thickness before and after bone cut, and, thus, without any computer assistance [4]. Although the inclusion in in-vivo navigated TKR of a procedure for supporting also patellar resurfacing via patient-specific bone morphology seems fundamental, this have been completely disregarded so far [7]. A novel procedure for measuring the effects of every surgical action on PFJ kinematics during navigated TKR using an extension of current SNS will be reported together with

relevant software and surgical instrumentation, and relevant results of the first applications in-vivo in patients.

2) *Materials and Methods* – Sixteen patients affected by primary gonarthrosis were implanted with a TKR prosthesis (10 and 6 patients, respectively, with NRG® and Triathlon®, Stryker®-Orthopaedics, Mahwah, NJ-USA) with patellar resurfacing. All TKR were performed by means of two SNS (Stryker®-Leibinger, Freiburg, Germany; 0.5°/0.5mm accuracy) with the standard femoral/tibial trackers, the pointer, and an original specially-designed patellar tracker [7]. The novel procedure for patellar tracking was approved by the local ethical committee; the patients gave informed consent prior the surgery. This procedure implies the use of a second system, i.e. the patellar SNS (PSNS), with dedicated software for supporting patellar resurfacing and relative data processing/storing (Fig. 1), in addition to the traditional knee SNS (KSNS) [7]. TFJ anatomical survey and kinematics were assessed according reccomandations [4,7] and data are shared between the two. The procedures for standard navigation were performed to calculate preoperative joint deformities and TFJ kinematics. The anatomical survey was performed also with PSNS, with relevant patellar anatomical reference frame definition and PFJ kinematics assessment (Fig. 2). After standard procedures for femoral and tibial component implantation, the procedure for patellar resection was performed with the support of the PSNS to plan a most proper level and orientation of the patellar cut and location of the patellar component. For all this, TFJ and PFJ kinematics were assessed, and possible adjustments in component positioning performed, until both kinematics were satisfactory.

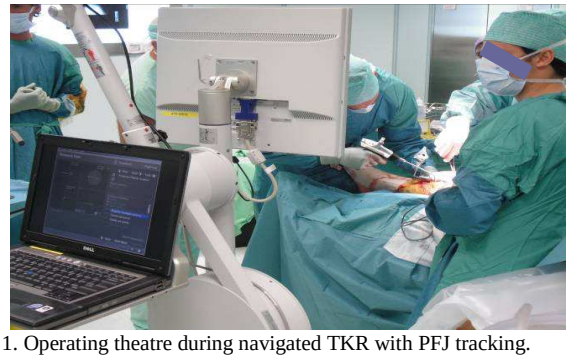

Fig. 1. Operating theatre during navigated TKR with PFJ tracking.

3) *Findings* - The novel procedure was performed successfully in all cases without complications, resulting in about 30 min longer than standard TKA. The final lower limb misalignment was within 0.5°, resurfaced patella was 0.4±1.2 mm thinner than the native, and patellar cut was 0.4°±4.1° laterally tilted. Final PFJ kinematics after patellar resurfacing was taken the reference normality. This showed a mean range of flexion, tilt and medio-lateral shift of 66.9°±8.5° (mean of minimum ÷ maximum values, 15.6°÷82.5°), 8.0°±3.1° (-5.3°÷2.8°), and 5.3±2.0 mm (-5.5÷0.2 mm), respectively. Significant correlations were found between the internal/external rotation of the implanted femoral component and the range of PFJ tilt ($p=0.05$; $R^2=0.41$). The goodness of patellar implantation parameters were confirmed also by successive X-ray inspections. Discrepancies in thickness up to 5 mm were observed between SNS- and calliper-based, i.e. not computer assisted, measurements.

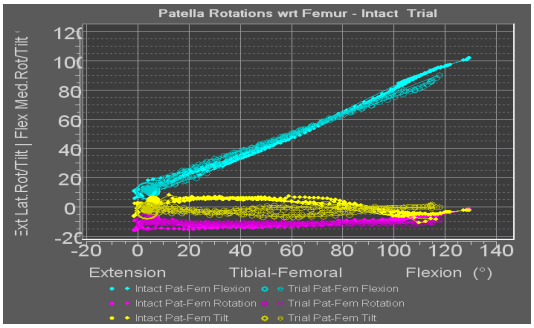

Fig. 2. Real-time PFJ rotations on the SNS monitor during surgery.

B. *Patellar Tendon tracking*

1) *Rationale* – The mobility and the stability of the human knee are controlled not only by a synergic interaction between TFJ and PFJ surfaces, but also between these and a number of important knee soft tissues [5]. Among these, the patellar tendon (PT) plays an important role in transmitting tensile forces within the extensor apparatus [5]. A thorough anatomy-based mapping of PT attachments is essential for a reliable assessment of fibres location and deformation during knee motion, to understand its contribution to knee function, and to restore physiological knee kinematics after TKR. Past methodologies did not allow the acquisition of accurate, natural and continuous movements over a large flexion range in the assessment of PT biomechanics. The inaccessibility of important anatomical landmarks prevented 3D PT mapping, robust anatomical reference definitions, and, ultimately, the identification of reliable patterns for PT fibre deformations and orientations [5]. Among possible measuring devices, current SNS enable direct digitization of bony landmarks and surfaces [4] together with the relevant attachment areas for PT [5]. A novel procedure for thorough description of lengthening and orientation patterns via careful anatomy-based PT fibre mapping will be reported below together with relevant results of the first applications in-vivo in patients.

2) *Materials and Methods* - Six patients affected by primary gonarthrosis were implanted with TKR prosthesis with patellar resurfacing using a Stryker®-Leibinger SNS. Similarly to what reported in the previous section, before TKR the standard trackers were pinned onto the femur and the tibia [4], and an additional novel tracker cluster was rigidly fixed onto patellar anterior aspect [7]. A pointer was used for system control and landmark digitization. Anatomical and articular definitions were according to recommendations [4]. Series of 3 trials of manually driven knee flexion-extension cycles in a 0°-140° arc were recorded with the intact and replaced knee. For PT fibre recruitment analysis, points on the proximal attachment on the patella were digitized together with distal attachment on the tibia. Point strips were also collected along the medial, central and lateral PT fibres. The centroids of the proximal/distal attachments and the strips extremities were assumed as fibre origins and insertions. Corresponding distances were calculated over flexion and reported as % of the

corresponding maximum length at the intact knee (L_{max}). Location of the most isometric fibres (ISO) was also investigated. Fibre orientation was calculated in tibial frontal and sagittal planes with respect to the proximo-distal axis, anterior and lateral inclination being positive.

		Pre TKR		Post TKR	
		At full ext.	***At full flex.***	***At full ext.***	***At full flex.***
Elongation (%$_{Lmax}$)	*Lat*	78.1 ± 10.8	99.4 ± 0.4	89.0 ± 5.5	99.7 ± 2.7
	Med	78.7 ± 7.4	99.4 ± 0.2	91.5 ± 4.2	100.9 ± 3.8
	Cent	78 ± 9.5	99.5 ± 0.2	90.3 ± 3.6	100.5 ± 2.8
Frontal Inclination (°)	*Lat*	-14.1 ± 17.8	-6.1 ± 6.8	-8.6 ± 6.3	-1.8 ± 4.3
	Med	-7.5 ± 7.9	-2.0 ± 4.3	-3.0 ± 6.4	1.9 ± 6.2
	Cent	-10.7 ± 11.8	-4.0 ± 3.5	-5.6 ± 2.5	0.1 ± 3.2
Sagittal Inclination (°)	*Lat*	20.0 ± 9.3	-4.9 ± 6.3	20.5 ± 8.8	-2.2 ± 5.6
	Med	21.5 ± 5.7	-8.6 ± 7	17.7 ± 5.1	-7.1 ± 10.5
	Cent	20.9 ± 7	-6.8 ± 6.2	19.2 ± 6.6	-4.7 ± 7.9

3) *Findings* - Repeatable patterns of TFJ, PFJ and PT kinematics were observed versus flexion within each knee, standard deviation over trials being smaller than 1.0 mm and 1.0°, both at the intact and replaced knees. The corresponding values over specimens were larger due to the different status of the diseased knees, these being about 7 mm and 9°. At the natural knees, PT lengthening occurred with different extents mainly in the initial 30°-40° of flexion for all fibres. This was observed also after TKR, although at near full extension all fibres were about 15% tighter than by in the intact knee (see Table). Fibres in the intact knee inclined laterally and posteriorly of about 11° and 30°, respectively; after TKA, an extra lateral inclination of 4° was observed. ISO had no anatomical consistency. PT kinematics was always correlated to TFJ flexion. After TKR, frontal orientation was correlated to medio-lateral PFJ shift, but this was not observed at the intact knees, likely due to the eroded status of the native patella.

III. Patient-Specific Instrumentation (PSI) tests

Recent improvements in the biomechanical understanding of mobility and stability of the knee joint, prosthetic design and surgical technique have contributed to the success of TKR [1]. There is still debate about the maximum admitted misalignment for the lower limb mechanical axis, although alignment errors larger than 3° would result in a more rapid implant wear and mobilization [6]. In the last decade, SNS has been exploited to improve prosthesis component positioning. Recent studies have revealed that these systems are able to reduce outliers in prosthetic component alignments and result in a better mechanical axis when compared to conventional instrumentations [6]. Nevertheless, the majority of surgeons continue to prefer the conventional technique because of the lack of long-term functional results. The most recent advance in TKR is Patient-Specific Instrumentation (PSI, Fig. 3), which claims to achieve better positioning of prosthetic components while avoiding complex instrumentation in the operating theatre [1]. These technologies offer original patient-matched cutting blocks that are expected to generate more accurate bone cuts and better alignments of the prosthesis components. Particularly, these cutting blocks are derived from lower-limb computer tomography (CT) or magnetic resonance imaging (MRI). Computer-aided design (CAD) models of the distal femur and proximal tibia are reconstructed from the image scanning techniques [1] (Fig. 4). Relevant cutting blocks are, then, designed and manufactured based on surgeon's recommendations with only one fitting position on the patient native anatomy. To date, only a few studies have reported early relevant results, whereas the actual effectiveness has yet to be demonstrated [6].

Here below two different PSI systems for TKR are assessed and compared, particularly the accuracy with which of two procedures result in positions and alignments of the components consistent with the corresponding in the preoperative plan. For this purpose two evaluating techniques were used, and two studies were conducted accordingly: A. intra- and post-operative measures by using respectively SNS and measurements on radiographs, and B. post-operative bi-planar video-fluoroscopy for final 3D poses.

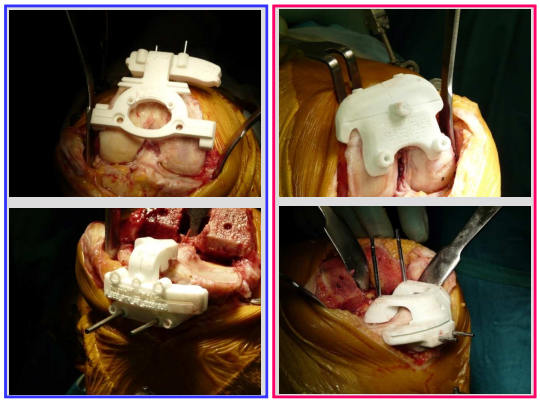

Fig. 3. MyKnee® (left) and VISIONAIRE® (right) PSI: fixation on bones.

A. *Intra- and post-operative accuracy assessment using SNS and radiographs*

1) *Purpose* - The aim of the first study is to assess and compare the accuracy of two different PSI systems for TKR both intra-operatively for bone preparation and post-operatively for final component alignment, with the main hypothesis being that a good accuracy can be achieved by these two PSI systems in all three anatomical planes.

2) *Materials and Methods* - Fifty patients affected by primary gonarthrosis were recruited for unilateral TKR using PSI systems and signed relevant informed consent. Two different patient groups consisting of twenty-five subjects each were created. Each group was associated to a different PSI system and TKA prosthesis design. Particularly, in Group A, these were MyKnee® and GMK®, both by Medacta®-International, Castel S. Pietro, CH; in Group B, these were VISIONAIRE® and Journey®, both by Smith&Nephew®, London, UK (Fig. 3). PSI systems in Group A and Group B were derived from a CT-based and an MRI/X-Ray-based system technique, respectively (Fig. 4). At both the femur and the tibia, alignments on the three anatomical planes and resection thickness at the cutting blocks and at the resulting bone cuts were recorded intra-operatively by a SNS [3]. Corresponding alignments of the prosthetic components and

mechanical axis were also measured post-operatively on radiographs [3]. All measurements were compared with those of the corresponding pre-operative planning. Discrepancies larger than 3° were considered as outliers.

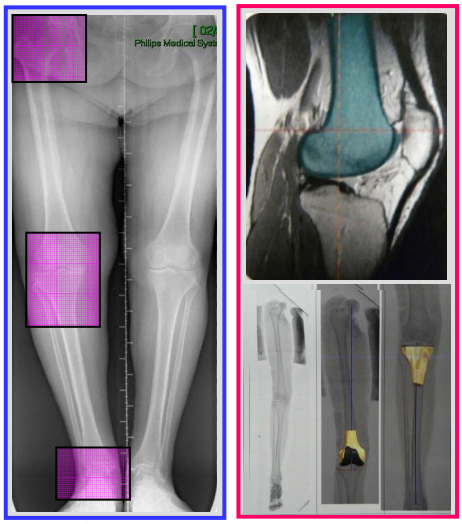

Fig. 4. MyKnee® (left) and VISIONAIRE® (right) PSI: model creation.

3) *Findings* - In both groups, the mean absolute differences between pre-operatively planned alignments and corresponding intra- and post-operatively measurements, ranged between 1.2° and 2.9° in all three anatomical planes. In both groups, both at the femur and the tibia, the plane with the smallest percentage of outliers was the coronal. The comparison between two groups was statistically significant ($p<0.05$) in the femoral sagittal plane, where group B showed smaller alignment discrepancies at the cutting blocks. Generally, both PSI systems showed good alignments in the coronal plane. Slight better performances were observed in the MRI-based system.

B. *Post-operative accuracy assessment using 3D video-fluoroscopy*

1) *Purpose* - The aim of the second evaluating technique is to assess and compare the accuracy of the two different PSI systems described in the previous for TKR also post-operatively for final component alignment using accurate 3D video-fluoroscopy.

2) *Materials and Methods* – Patients groups are the same of the previous point. For each patient, starting from two quasi-orthogonal fluoroscopic images, i.e. the coronal and the sagittal view of the replaced knee, and by a standard shape-matching technique in each of these images, the position and orientation of the femur and tibial two metal components and of the two prepared bones were estimated [8]. Component-to-bone relative positions and orientations were then obtained in 3D. Assuming the corresponding values at the preoperative plan equal to zero, small discrepancies were indication of highly accurate overall instrumentation. A repeatability test was performed to assess the reliability of this evaluation technique.

3) *Findings* - The repeatability test revealed that the present technique was reliable enough. The range over all patients for the position and orientation discrepancies was from zero to respectively 5.9 mm, i.e. femoral component in proximal-distal direction, and 4.2°, i.e. the femoral component in flexion. The comparison revealed also larger ($p<0.05$) antero-posterior and medio-lateral positions at the tibia in group A than in B. Generally, good match in three-dimensional position and orientation was found between the final implantation and the corresponding preoperative plans, with mean discrepancies smaller than 3.1 mm and 1.9°, respectively.

IV. Concluding Remarks

Surgical navigation systems and patient-specific instrumentations are augmenting the available technologies for advanced computer-assisted TRK [7]. In addition to fully controlled operations via surgical robots, hospitals and surgeons have now the options of navigated surgery via optical cameras and trackers, or of patient-specific cutting-blocks obtained from careful 3D computer based planning starting from medical imaging. All these three procedures can provide a valuable support to surgeons for achieving a successful TKR, with good fixation of the components, and mobility and stability at the replaced knee joint. These results however should be assessed at follow-ups, by means of the available gait analysis and 3D video-fluoroscopy [8]. The relevant evident advantages shall be opposed with costs of the instrumentation, time and arrangement of the procedures, and the learning curve. Definitely, the integration in these technologies of current biomechanical models for the knee joint, particularly those able to assess mobility and stability in terms of the mutual contribution of articulating surfaces and ligaments, can provide in the future further support for a best possible knee joint replacement.

References

[1] Walker PS, Yildirim G, Arno S, and Heller Y, “Future directions in knee replacement” Proc Inst Mech Eng H, vol. 224(3):393-414, 2010.

[2] Sparmann M, Wolke B, Czupalla H, Banzer D and Zink A, “ Positioning of total knee arthroplasty with and without navigation support. A prospective, randomised study” J Bone Joint Surg Br., vol. 85(6), pp. 830-5, Aug 2003.

[3] Belvedere C, Ensini A, Leardini A, Bianchi L, Catani F, et al., “Alignment of resection planes in total knee replacement obtained with the conventional technique, as assessed by a modern computer-based navigation system” Int J Med Robot, vol. 3(2), pp.117-24, Jun 2007.

[4] Belvedere C, Leardini A, Ensini A, Bianchi L, Catani F, et al., “Three-dimensional patellar motion at the natural knee during passive flexion/extension. An in vitro study”, J Orthop Res., vol. 27(11), pp.1426-31, Nov 2009.

[5] Belvedere C, Ensini A, Feliciangeli A, Cenni F, D'Angeli V, et al., “Geometrical changes of knee ligaments and patellar tendon during passive flexion”, J Biomech., vol. 45(11), pp.1886-92, Jul 2012.

[6] Ensini A, Timoncini A, Belvedere C, Cenni F, Leardini A, et al., “A new technology in the implant positioning for total knee replacement: comparison between two custom-fit techniques”, J Bone Joint Surg Br., vol. 94-B no. SUPP XL 191, 2012.

[7] Belvedere C, Ensini A, Moctezuma De La Barrera JL, Feliciangeli A, Leardini A, et al.. F, “Patellar tracking assessment in surgical navigation for total knee replacement: initial experience in patients”, J Bone Joint Surg Br vol. 94-B no. SUPP XLIV 66, 2012

[8] Catani F, Ensini A, Belvedere C, Feliciangeli A, Benedetti MG, et al., “In vivo kinematics and kinetics of a bi-cruciate substituting total knee arthroplasty: a combined fluoroscopic and gait analysis study” J Orthop Res., vol. 27(12), pp. 1569-75, Dec 2009.

Development and Evaluation of an Interface for Pre-Operative Planning of Cryoablation of a Kidney Tumor

Duygun Erol Barkana[1], Dilek Göksel Duru[2], Adil Deniz Duru[3], Alper Açık[4], and Mehmed Özkan[2], *Member, IEEE*

[1]Electrical and Electronics Engineering Department, Yeditepe University, Istanbul, 34755 TURKEY
[2] Institute of Biomedical Engineering, Bogazici University, Istanbul, 34684 TURKEY
[3] School of Physical Education and Sport, Sport Health Sciences Department, Marmara University, Istanbul, 34800 TURKEY
[4] Psychology Department, Yeditepe University, Istanbul, 34755, TURKEY

{ duygunerol@yeditepe.edu.tr}

***Abstract*—Surgical interfaces are used for the interpretation and quantification of the patient information, and for the presentation of an integrated workflow where all available data are combined to enable optimal treatments. Human factors research provides a systematic approach to design user interfaces with safety, accuracy, satisfaction and comfort. One of the human factors research called user-centered design approach is used to develop a surgical interface for pre-operative planning of cryoablation of a kidney tumor. Two experiments of a simulated cryoablation of a tumor task have been performed with surgeons to evaluate the proposed surgical interface using subjective (questionnaires) and objective (eye tracking) methods to obtain the best surgical interface configuration.**

Keywords—surgical interface; human factor analysis; user-centered approach; eye tracking; mental workload; situation awareness

I. INTRODUCTION

Minimally invasive surgical procedures have been evolved for reducing hospitalization time and surgical complexities. In a conventional minimally invasive surgery however, a surgeon operates on deeply located lesions without actually seeing or touching. Thus, an easy to use surgical interface (SI), which benefits maximally from the surgeons' skills while providing all necessary information that can be perceived and processed by the surgeon during the intervention in the operation theatre, is needed. Surgical interfaces are designed to improve surgical treatments in all the stages of a clinical workflow, which ranges from preoperative diagnosis and planning of the surgical interventions up to postoperative evaluation. In this work, SI is used for the interpretation and quantification of the patient information, and for the presentation of an integrated workflow where all available data are combined to enable optimal treatments. Recently, several SIs that consist of functions for identification of liver segments and planning of liver surgery have been developed.

CAScination is a well-known commercial system that integrates stereotactic technology in complex liver interventions and surgery [1]. A preoperative surgical simulator has been designed to allow surgeons to plan the surgical interventions for liver surgery in PAtient Specific Simulation and PreOperative Realistic Training (PASSPORT) project [2]. LiverAnalyzer™ (MeVis Medical Solutions AG, Germany) and Synapse Vincent™ (FUJIFILM Co., Japan) surgical interfaces have functions that can segment the liver, vessels, biliary system, and tumors, volumetry of the remnant and/or graft, evaluate vascular territories, and plan the surgery. Note that not only inclusion of functions for liver surgery, but also incorporating these functions systematically into interface design by considering the surgeon's requirements is an essential issue. Thus, recently, a user-centered virtual liver surgery planning system for liver surgery called Dr. Liver, has been developed, that considers human factors research, usability and time efficiency issues [3].

Human factors research describes how much and what kind of information a person can use effectively, and how information should be organized and presented to make it usable [4]. Human factors research has previously been used to provide design solutions for the disciplines of medicine, psychology and ergonomics in which human-machine interactions affect performance and usability [5]. The human factors research focus on the physical and sensory characteristics through displayed symbols, audibility and perceptual and cognitive abilities (human perception, sustained attention) through arrangement of displays, alarms, information presentation, information processing during the design of interfaces. Therefore, the human factors activities should be incorporated into surgical interface during the design process from an early stage. Various traditional, sociotechnological systems, user-centered design, computer-supported design and ecological interface design approaches in human factors research have been developed to design interfaces [5]. In this work, we use user-centered design (UCD) approach to develop a surgical interface for pre-operative planning of cryoablation of a kidney tumor.

SI has been developed considering the four phases of user-centered design approach, which are analysis, design, implementation and deployment. Possible configurations of the SI, which comprise various combinations of menu-based command controls, visual display of multi-modal medical

This work is supported in part by European Union Seventh Framework Programme FP7/2007-2013 under grant agreement n. 270396 (I-SUR).

images, 2D and 3D models of the surgical environment, graphical or tabulated information, visual alerts, etc., has been developed. We conduct two experiments of a simulated cryoablation of a tumor task with surgeons to evaluate the proposed SI. Surgeons are asked to find the tumor on the left kidney (target point) that is displayed on SI, and to determine a suitable entry point to start the ablation. Subjective (questionnaires) and objective (eye tracking) methods have been used to obtain the best surgical interface configuration.

II. Materials and Methods

In this section, initially development of SI considering the UCD approach has been given. Then experimental set-up, procedure, participants, and data collection and analysis details are provided.

A. *Development of SI Using User-Centered Design (UCD) Approach*

UCD approach consists of four main phases, i) analysis - determine SI modules and define the important usability and functionality factors, ii) design – begin to develop SI prototypes, iii) implementation – construct a heuristic evaluation, whereby usability experts work together with the SI developers and surgeons to analyze the various dimensions of the prototype SIs, and previously-used products with similar functionality of SI, and iv) deployment – use surveys or other evaluation techniques to get surgeons' feedback about SI for modifications (Fig. 1).

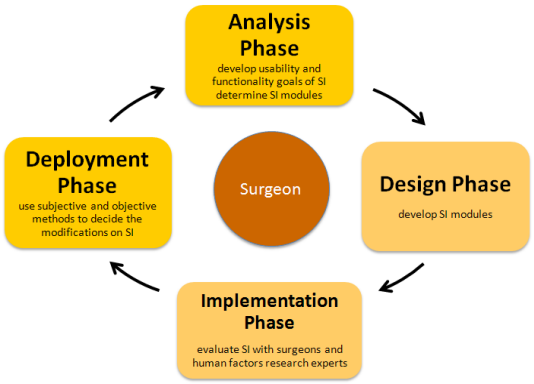

Fig. 1. User-Centered Approach during Design of SI

SI modules that satisfy the surgeons' need and important usability and functionality factors to design SI modules have been determined in the analysis phase of the UCD approach. SI consists of Medical Image Module, 3D View Module, Phantom Model Module, Robot CAD Model Module, Visualization Module, Entry-Target Selection Module, Run-Time (Real-Time) Module, and Needle Force Tracking Module. The response time, ease of use, and efficiency have found to be the most important factors among the usability and functionality factors [6]. Thus SI modules are designed considering these usability and functionality factors.

Medical Image Module, 3D View Module, Phantom Model Module, Robot CAD Model Module, Visualization Module, Entry-Target Selection Module, Run-Time (Real-Time) Module, and Needle Force Tracking Module have been developed in the design phase of UCD approach (Fig. 2).

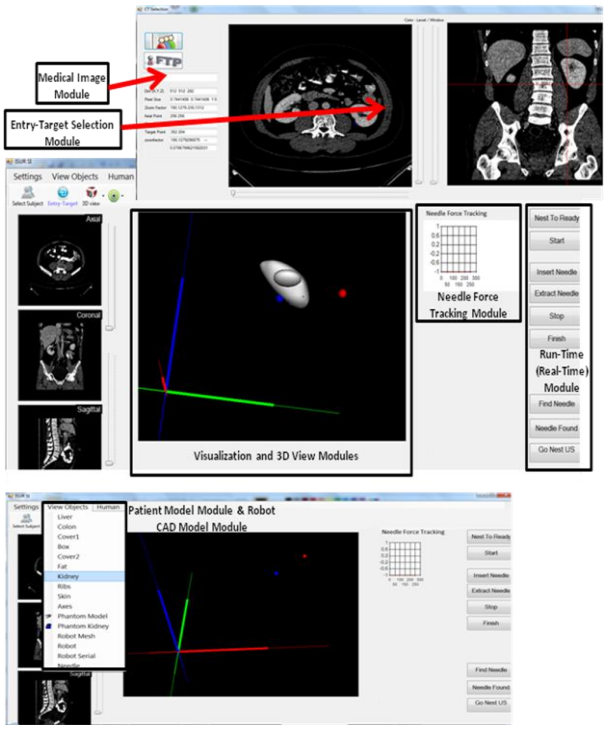

Fig. 2. Surgical Interface Modules

SI modules, menu and screen layout are reviewed with the surgeons, and experts in the implementation phase of the UCD approach. The button size, color, font size and information that are displayed on SI, which form the infrastructure of SI modules, have been decided considering the response time, ease of use, and efficiency factors. SI has been developed using Microsoft Visual Studio 2010 Development Environment to improve response time and efficiency. The visualization toolkit (VTK), which is an open source and freely available software, is used for 3D image processing and visualization to increase ease of use and efficiency.

Subjective and objective methods are used to evaluate the developed SI in deployment phase of UCD approach. An eye tracking system, which provides quantitative data, can help to understand visual and display-based information processing, and the factors that may impact upon the usability of interfaces. It could be possible to trace the surgeons' attention and automate assessments for example, based on "how much certain areas of an interface have been watched by the surgeons", with an eye tracking system. It is possible to learn where surgeons target on SI using eye tracking system, which will help us to remove the unnecessary information on SI, and obtain the optimum SI configuration.

B. *Experimental Set-Up*

Participants are seated on a non-adjustable chair while viewing a 22" LCD monitor set at 1680 x 1050 resolution from a distance of 70 cm (Fig. 3). Thus, the screen covered approximately 37.5° of the visual field horizontally. Participants are seated in front of a remote eye tracker and the

computer screen with their head resting on the chin-rest to ensure the accuracy of the data recording. The remote eye tracker Sensomotoric Instruments (SMI) 500 have been used to sample the participants' eye gaze at 500 Hz. SMI's control and analysis software BeGaze has been used to extract the fixation counts and fixation time.

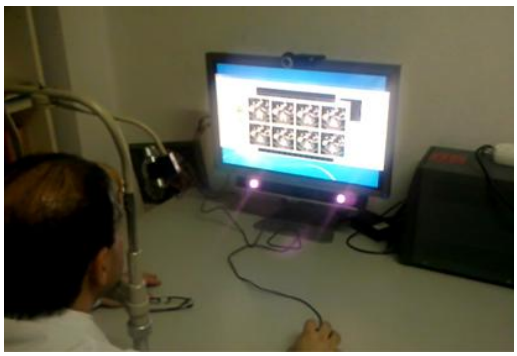

Fig. 3. Surgeon Performing Experiments on SMI 500 Eye Tracking System

C. Procedure

Participants are asked to find the tumor on the left kidney (target point), that has been displayed on SI, and to determine a suitable entry point to start the ablation. The eye position and pupil size of the participants have been saved to a log file with the eye tracker device during the task execution. Two experiments have been conducted. In the first experiment, the aim is to evaluate the SI to determine the necessary modifications on it. Participants are required to perform the cryoablation task with the developed SI. In the second experiment, the SI has been modified in terms of visual display, button size, color etc considering the first experiment results. Participants are required to perform the cryoablation task with the modified SI. The visual information acquisition and time to complete the task have been used to evaluate the configuration of SI in two experiments.

D. Participants

3 surgeons (all male) (Participant A (PA), Participant B (PB) and Participant C (PC)) from Urology Department of Faculty of Medicine, Istanbul University have attended the first experiment. 3 radiologists (two female and one male) (Participant D (PD), Participant E (PE) and Participant F (PF)) from Radiology Department of Faculty of Medicine, Istanbul University have attended the second experiment. All the participants are right-handed, and have normal vision. All urologists have experience with laparoscopic surgery, and radiologists have experience in kidney biopsy process.

E. Data Collection and Analysis

We have used eye tracking data to decide whether all or some of the information displayed on the SI has been relevant for the participants performing the cryoablation task. The Behavioral and Gaze Analysis (SMI BeGaze™) analysis software has been used to visualize, extract and analyze the eye tracking parameters [7]. Areas of interest (AOI) on the SI have been defined before the task execution started. Dwell time, fixation counts and average fixation duration concerning each AOI have been measured. The dynamic attention maps summarize the information about the most time-spent areas of the SI. Additionally, the fixation patterns and statistical parameters have been visualized by altering the color of the grid of AOIs (Gridded AOI) overlaid on the SI screen considering the amount of fixations. It is possible to compare the varying stimuli such as CTs, cursor movement through various slices independent of its content using Gridded AOI. Fixation counts and durations have also been used to quantify aspects of gaze behavior that reflect efficient use of the SI. We have also used subjective evaluation techniques, National Aeronautics and Space Administration Task Load Index (NASA-TLX) to measure the mental workload, and Short Post-Assessment Situational Awareness (SPASA) to measure situation awareness (SA) of the surgeons during the use of SI.

III. Results

The participant specific fixation counts and the results of the statistical analysis were presented in Fig. 4. The circles showed the amount of fixations in each CT image AOI separately for each participant. The gray dashed line showed the uniform distribution. The green dots represented the fixation counts, which are significantly ($p < 10^{-3}$) larger than what would be expected by chance. For each significant data-point, the black error bars provided 95% bootstrap confidence intervals (CIs) of the null-hypothesis distribution of maximum fixations in a AOI. Thus, the green dots would be expected to fall into these intervals, if all AOIs had received similar amount of fixations. The CI images shifted along the y-axis since the number of fixations was different for each CI image computation. The data clearly showed that participants focus on 2 or 3 AOIs, and neglected the rest. Importantly, participants' selected AOIs differed to some degree. Three of the images used by PA were in the upper row, the only looked-at CT image in the bottom-row receiving 7 fixations only. Both PB and PC spent time looking at two CT images shown in the lower row; but the favorite CT image of PB was yet another CT image in the lower part. These results conclusively showed that the presentation of 8 CT images was redundant for the participants. As a result of the first experiment, SI has been revised and the number of CT images displayed for entry and target point selection for kidney cryoablation was reduced to two.

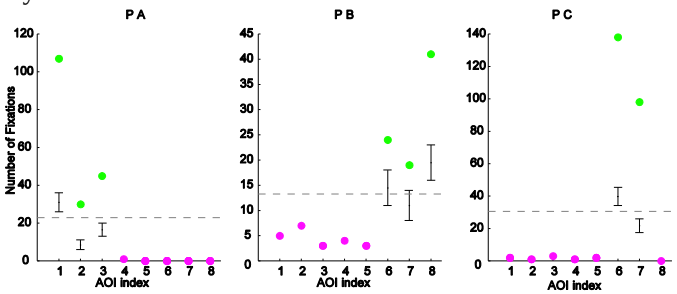

Fig. 4. Participant Specific Fixation Counts for First Experiment

When SI had been revised, time required to complete the task by the participants had been decreased (Table I). In the first experiments, the three participants (PA, PB, and PC) had

completed the task in 100, 72, and 159 seconds, respectively. When the SI had been modified, the participants (PD, PE, PF) needed only 62, 38 and 32 seconds, respectively, to complete the task.

TABLE I. TOTAL TIME EACH PARTICIPANT SPENT DURING TASK EXECUTION

	Total Time (s)	Relative time on CT images (%)	Median Fixation Duration (ms)
PA	100	**61**	168
PB	72	**55**	172.5
PC	159	**59**	169
PD	62	**28**	144
PE	38	**73**	262
PF	32	**79**	302

The amount and duration of fixations on displayed CT images displayed had shown differences between the first and second experiments. In the first experiment, the participants had spent 61%, 55%, and 59% of their total viewing time fixating the CT images. The fixations of two participants covered 73% (PE) and 79% (PF) of viewing time, indicating a relative increase in visual information acquisition after SI had been modified. Surprisingly, this statistic was a modest 28% for the PD because PD had used the sliders for changing the zoom level and the contrast of CT images frequently. A closer inspection of the fixation properties revealed that whereas PD made frequent use of both axial and coronal CT images (63 and 28 fixations, respectively), the other two participants (PE and PF) rarely visited the coronal CT images (one and four fixations on the coronal image respectively). Moreover, for PE and PF of the second experiment, the fixation durations were relatively longer, which suggested, that they received more continuous information upon the initiation of a fixation. Permutation tests revealed that the fixation durations of PE and PF were longer than the durations observed for the participants of the first experiment ($ps < 0.05$). The fixation durations of the PD were not significantly different than the fixation durations measured during the first experiment (all ps > 0.2). Thus, the decrease in the number of CT images presented on the SI led to shorter task execution times, and for two of the three subjects (PE and PF), the fixation data suggested that they benefited only from the axial CT image with relatively long lasting fixations.

Overall mental workload and situation awareness of participants had been evaluated when second experiment was completed. The overall workload was 3, 3.93 and 3 for PD, PE and PF, respectively. Overall mental workload of surgeons related with SI was low as it was aimed. Furthermore, overall SA scores of surgeons were 3.89, 3.7 and 3.78 for PD, PE and PF, respectively, which were considerably high.

IV. DISCUSSION AND CONCLUSIONS

This preliminary study highlights design of a SI for pre-operative planning of cryoablation of a kidney tumor using a user-centered approach (UCD), and evaluation of SI using subjective (questionnaires) and objective (eye tracking) methods to obtain the optimum SI configuration.

Possible configurations of the SI, which comprise various combinations of menu-based command controls, visual display of multi-modal medical images, 2D and 3D models of the surgical environment, graphical or tabulated information, visual alerts, etc., have been developed.

An eye tracking technology has been used to find an optimum SI configuration. Two experiments of a simulated cryoablation of a kidney tumor task with surgeons have been conducted to evaluate the proposed SI. Sequence, entry time, dwell time, revisits, average fixation, first fixation and fixation count parameters have been extracted from recorded eye movements through SMI BeGaze for scientific and statistical analysis. Specifically, by analyzing the distribution of fixation locations, we have revealed that the presence of 8 CT images in the first version of the SI has been redundant for the surgeon. The task execution time for the same task has decreased, and the participants have spent their time mostly on the AOI when the number for CT images on SI has been reduced. Furthermore, overall mental workload of surgeons related with SI has been found low, and situation awareness scores have found to be considerably high.

In the future, we plan to continue revision of the developed SI, include the real-time cryoablation protocol (intra-operative planning), and plan to collect eye tracking data in more difficult surgery-like tasks such as cryoneedle control.

ACKNOWLEDGMENT

We gratefully acknowledge the help of Prof. Fethi Calisir, who is in the Industrial Engineering Department of Istanbul Technical University, during the design, implementation and analysis of the questionnaires to investigate the importance of usability and functionality factors and to determine the mental workload and situation awareness. We acknowledge the help of Gokcer Eskikurt during data collection from the eye tracking system and analysis of the collected data.

REFERENCES

[1] M. Peterhans, A. Vom Berg, B. Dagon, D. Inderbitzin, C. Baur, D. Candinas, S. Weber, "A navigation system for open liver surgery: design, workflow and first clinical applications", The Inter. J. of Medical Robotics and Computer Assisted Surgery, vol. 7, pp. 7-16, 2011.

[2] J. B. Fasquel, J. Waechter, S. Nicolau, V. Agnus, L. Soler, J.A. Marescaux, "XML based component oriented architecture for image guided surgery: illustration for the video based tracking of a surgical tool", In Proc. of the 11th Inter. Conf. on Medical Image Computing and Computer Assisted Intervention: September 2008; New York.

[3] X. Yang, W. Lee, Y. Choi, H. You, "Development of A User-Centered Virtual Liver Surgery Planning System", In Proc. of the Human Factors and Ergonomics Society Annual Meeting, 56, pp. 1772-776, 2012.

[4] R. L. Klatzky, N. Kober, A. Mavor, "Safe, comfortable, attractive, and easy to use: improving the usability of home medical devices", Committee on Human Factors National Research Council (U.S.). Academic Press 1996, Washington, D.C.

[5] Handbook of human factors and ergonomics: Edited by Salvendy G: Wiley; 2006.

[6] D. Erol Barkana M. Ozkan., F. Calisir, D. Goksel Duru, A. D. Duru, "Development of a Surgical Interface for Cryoablation of Kidney Tumors", In Proc. of International Work-Conference on Bioinformatics and Biomedical Engineering: pp. 601-611, 2013.

[7] Experiment Center BeGaze Manual V3.0: Manual. SensoMotoric Instruments GmbH; June 2011.

Usability and Performance: Comparative Evaluation of Surgeon Interfaces in Laser Phonomicrosurgery

Giacinto Barresi[1], Nikhil Deshpande[1], Leonardo S. Mattos[1],
Luca Guastini[2], Giorgio Peretti[2], and Darwin G. Caldwell[1]
[1]Department of Advanced Robotics, Istituto Italiano di Tecnologia, Genova, Italy
[2]Department of Otorhinolaryngology, Università degli Studi di Genova, Italy
Email: {giacinto.barresi, nikhil.deshpande, leonardo.demattos, darwin.caldwell}@iit.it,
luca@guastini.eu, g.peretti@tin.it

***Index Terms*—Surgeon performance, ergonomic evaluation, unified rating, usability, SUS.**

I. Introduction

State-of-the-art Laser Phonomicrosurgery (LP) is a set of complex otolaryngological surgical techniques used in the treatment of laryngeal abnormalities, including cysts and tumors. The complexity of this surgical procedure influences its own outcome because of its peculiar issues: (i) the surgical site access can be difficult, (ii) the setting can cause surgeon discomfort, (iii) the outcome quality is totally dependent on the skills of the surgeon and is prone to errors, (iv) the operation methods require extensive training, and (v) the equipment characteristics themselves affect all the previous aspects [8]. The importance of the role of robot-assisted surgical systems is increasing in the operating room [7]. They provide significant advantages in effectiveness, efficiency and safety of surgery through, for instance, increased task precision, reduced tremor in gestures, and timely execution of repetitive tasks. Nevertheless, such recent advances still require an ergonomic approach for a user-centered design and evaluation of surgeon-machine interfaces [12]. The cognitive limits of human beings can become critical factors in excessive mental workload (the amount of cognitive resources used to accomplish a task) [10] and in human error [11]. Thus, human factor-oriented approach is required in user interface design and evaluation to increase both safety (for the surgeon and the patient) and performance of the system. It permits the analysis of the issues of user interface design in terms of human-machine interaction constructs like usability (a complex set of behavioural concepts, like execution time, user satisfaction and ease of learning, [1]) and the objective performance of the user (according to quantitative data automated collection, [4]). Such constructs are considered in this paper for the comparison of 2 user interfaces for LP, in the context of the European project - μRALP. At the Istituto Italiano di Tecnologia (IIT), this research has already resulted in new and improved computer-assisted LP systems. Mattos et al. [8] presented a novel surgeon interface, the Virtual Scalpel system, which replaces the traditional manual micromanipulator interface [6] with a motorized micromanipulator, controlled through a graphics stylus and a touch-screen tablet with live video of the surgical area. The immediate advantage offered by the new interface is that both the aiming and the activation of the laser are controlled by the graphics stylus. The analysis of this novel solution indicated that this system offers greater precision along with better ergonomics over the traditional laser micromanipulator [3], [8], [9]. Through a series of field trials involving a sample of potential users, the new Virtual Scalpel laser control interface [8] was compared with the AcuBlade [6], the traditional, state-of-the-art laser control interface with the manual micromanipulator for LP. This study defines the perceived usability of each interface and the performance of the users in surgery-like tasks. The subjective evaluation of the usability of the interface has been measured by means of questionnaires, and the objective evaluation of the performance of the interface by means of an imaging-based feature extraction method [4].

II. Evaluation Methodology

The experiments were designed to evaluate the effects on usability perception and user performance in two conditions of laser control in LP: (i) the AcuBlade condition (traditional user interface, consisting of microscope for visualization, a micromanipulator for laser aiming, a foot-pedal for surgical laser activation), and (ii) the Virtual Scalpel condition (novel user interface, consisting of a touch-screen laptop for visualization, and a stylus pen for both laser-aiming and activation). The trials were performed at the San Martino Hospital (Genova, Italy), involving a sample of potential end users of the surgical devices. The dependent variables were the scores of the System Usability Scale questionnaire (SUS) [2] and the objective values of performance which were processed through the imaging based metrics algorithm developed in Deshpande et al. [4].

Two dedicated rooms in the otolaryngology division were used for the trials, with complete control of the environmental and social context in order to avoid any disturbance and any effect of latent variables. The bigger room was used for the trials, and it contained a condition-specific chair for the subject (surgical intervention chair for the AcuBlade condition; an

office chair for the Virtual Scalpel condition), a table to support the experiment materials (plaster targets in both conditions, touch-screen laptop in Virtual Scalpel condition), the laser system column, the video column, a camera for video data recording (its orientation permitting the capture of relevant data on the subject's movements and posture). The smaller room consisted of a table and a chair, and it was used to collect the informed consent form and the questionnaires from the subjects.

24 medical students (undergraduate and graduate) with surgery training and experience as assistants in operation room were chosen as subjects for the trials. The subjects were divided into two groups, one per condition, AcuBlade group vs. Virtual Scalpel group, and each subject performed the trials in only one condition. The groups were composed in order to balance the study level (undergraduate and graduate) and the gender of the subjects.

The experimental task consisted of sets of trajectory following exercises wherein the subject performed maneuvers with the laser to follow preset random black traces on red plaster blocks. The traces were shaped as straight lines, C-curves, and S-curves, representative of real surgical actions. They were stamped on small plaster blocks, with each target block having 12 shapes, featuring one of five different randomized sequences of shapes and shape orientations. The subjects performed the trials in two sessions of two plaster blocks each, with a break of 10 minutes between the two, at least.

Before each experimental session, demographic and subject background data were collected by means of a information form. After the trials, the subject filled out an Italian version of the SUS questionnaire in order to collect information about his/her perception of the tool's usability. A question regarding the subjective evaluation of the time spent performing the tasks was also included.

The metrics introduced in [4] permitted to assess the quantitative performance of the subjects. Here, the metrics obtained from the image processing of the trials provided a quantitative basis for the assessment of the two conditions, comparing the trial times and the data of the laser-traced shapes against that of the desired shape along different dimensions (e.g. area, perimeter, orientation).

III. Data Analysis and Discussion

A t-test analysis was used in order to find the differences between the scores of the two groups from the SUS questionnaire and from the objective performance scores [4]. These analyses verify whether the users perceive a statistically significant difference in the level of usability for each interface (AcuBlade vs Virtual Scalpel) and if there is a statistically significant difference of quantitative performance between the two conditions.

The t-test analysis demonstrated the different level of usability of each interface, with a significant difference: the global score of subjective usability of Virtual Scalpel is higher than the score for Acublade. Further explorative analysis highlights the differences on 5 specific sub-scales of the SUS between the two interfaces. The users of the Virtual Scalpel system feel more confident than the users of AcuBlade during the tasks. The Virtual Scalpel interface is easier to use and easier to learn than the AcuBlade interface. The users of Virtual Scalpel would require to learn less processes than the users of AcuBlade as well. The sub-scale analysis clearly points to the ease-of-use and comfort of the Virtual Scalpel interface, over the AcuBlade interface.

In the objective performance assessment, the *unified rating* is used, a weighted sum of the individual metrics. This takes into account the natural performance variation in any human-operated equipment. Each individual laser-traced shaped contributes to the performance assessment analysis. Using equal weighting for each metric, the ideal value for the unified rating in this case is 60.

The two conditions again show a statistically significant difference on the unified rating for quantitative performance. The Virtual Scalpel condition permits a significantly better performance than the AcuBlade condition. Three individual metrics show a significant difference in performance between the two conditions: Perimeter Ratio (under the Virtual Scalpel condition, the laser-traced shapes conform to the length and thickness of the desired shapes, significantly better than in the AcuBlade condition), Orientation Measure (under the Virtual Scalpel condition, the laser-traced shapes are better aligned with the desired shapes than in the AcuBlade condition), Path Following Error (the Virtual Scalpel condition permits easier trajectory following with the laser than the AcuBlade condition).

The comparisons of SUS scores and of unified ratings between the two conditions is represented in Table I.

A t-test was also performed to understand the existence of significant differences between the perceived and actual times for trial completion effect in the two conditions. This result allows to infer the level of mental workload required in each condition [5]. The actual time spent in trials for

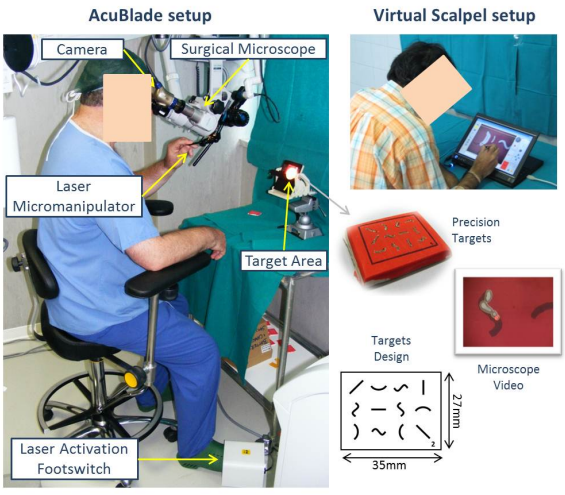

Figure 1. Experimental setup, video snapshot from a trial, and details of the precision targets stamped on a plaster block.

Table I
COMPARISON OF AVERAGE VALUES OF THE METRICS AND UNIFIED RATING SCORES

	AcuBlade condition	Virtual Scalpel condition		
	Means	Means	t	p
SUS Global Score	**65.56**	**83.06**	**4.83**	**0.009**
Unified Rating	**51.37**	**55.96**	**4.26**	**4e-4**

The *SUS Global scores* (subjective assessment of usability) and the *Unified Rating* (objective assessment of performance) for the two conditions. '100' and '60' are the respective maximum values.

Virtual Scalpel is significantly greater than the actual time in AcuBlade, while the estimated time taken for the trials with it is significantly lesser. Therefore, the Virtual Scalpel condition seems to induce less mental workload than the AcuBlade condition. This is advantageous for the acceptance and usability of the Virtual Scalpel condition since it is perceived as a low mental workload interface.

IV. CONCLUSIONS AND FUTURE WORK

In this paper, an integrative ergonomic evaluation of surgeon interfaces in LP was used to compare subjective usability and objective performance of a traditional system (AcuBlade) and a novel system (Virtual Scalpel). The results from the trials can be summarized as follows. (i) The usability of the Virtual Scalpel interface is demonstrated through the global usability value and the 5 different sub-scales of the SUS scale (e.g. the system is "easy to use" and "easy to learn"). (ii) The objective evaluation points to the clear advantage of the Virtual Scalpel interface over the AcuBlade interface. (iii) Both the interfaces show the same actual time for task performance, but the Virtual Scalpel interface is perceived to take significantly less time than the AcuBlade interface, implying that the Virtual Scalpel interface requires a much lower mental workload on part of the user. The t-test analysis showed the significant superiority of Virtual Scalpel in terms of the efficiency and safety aspects of its performance. (iv) Summing up, the subjective and objective evaluations classify the Virtual Scalpel interface as having superior usability and performance capability as a surgeon interface for more effective, efficient and safer laser microsurgeries. In the extension of this research, further studies are planned to better understand the relationships between subjective usability and objective performance in this specific interactive context.

ACKNOWLEDGMENT

The research leading to these results has received funding from the European Union Seventh Framework Programme FP7/2007-2013 – Challenge 2 – Cognitive Systems, Interaction, Robotics – under grant agreement μRALP - n°288233.

REFERENCES

[1] A. Abran, A. Khelifi, W. Suryn, and A. Seffah, "Usability Meanings and Interpretations in ISO standards," *Software Quality Journal*, vol. 11, no. 4, pp. 325–338, 2003.

[2] J. Brooke, "SUS: A "Quick and Dirty" Usability Scale," *Usability Evaluation in Industry*, 1995.

[3] G. Dagnino, L. S. Mattos, and D. G. Caldwell, "New Software Tools for Enhanced Precision in Robot-Assisted Laser Phonomicrosurgery," in *Proc. 34^{th} Intl. Conf. of IEEE Engineering in Medicine and Biology Society, (EMBC 2012)*, 2012, pp. 2804–2807.

[4] N. Deshpande, L. S. Mattos, G. Barresi, A. Brogni, G. Dagnino, L. Guastini, G. Peretti, and D. G. Caldwell, "Imaging based Metrics for Performance Assessment in Laser Phonomicrosurgery," in *Proc. Intl. Conf. on Robotics and Automation, (ICRA 2013)*, 2013.

[5] M. Lind and H. Sundvall, "Time estimation as a measure of mental workload," in *Engineering Psychology and Cognitive Ergonomics*. Springer, 2007, pp. 359–365.

[6] Digital AcuBlade System. Lumenis Inc. Israel. [Online] Available: http://www.surgical.lumenis.com. Accessed on 6-Sept-2012.

[7] S. Martelli, L. Nofrini, P. Vendruscolo, and A. Visani, "Criteria of Interface Evaluation for Computer assisted Surgery Systems," *International Journal of Medical Informatics*, vol. 72, no. 1-3, pp. 35–45, 2003.

[8] L. S. Mattos, G. Dagnino, G. Becattini, M. Dellepiane, and D. G. Caldwell, "A Virtual Scalpel System for Computer-assisted Laser Microsurgery," in *Proc. IEEE/RSJ Intl. Conf. on Intelligent Robots and Systems, (IROS 2011)*, Sep. 2011, pp. 1359–1365.

[9] L. S. Mattos, M. Dellepiane, and D. G. Caldwell, "Next-generation Micromanipulator for Computer-assisted Laser Phonomicrosurgery," in *Proc. 33^{rd} Intl. Conf. of IEEE Engineering in Medicine and Biology Society, (EMBC 2011)*, Sep. 2011, pp. 4555–4559.

[10] T. E. Nygren, "Psychometric Properties of Subjective Workload Measurement Techniques: Implications for their Use in the Assessment of Perceived Mental Workload," *Human Factors: The Journal of the Human Factors and Ergonomics Society*, vol. 33, no. 1, pp. 17–33, 1991.

[11] J. Reason, "Human error: models and management," *BMJ: British Medical Journal*, vol. 320, no. 7237, p. 768, 2000.

[12] S. Serefoglou, W. Lauer, A. Perneczky, T. Lutze, and K. Radermacher, "Multimodal User Interface for a Semi-Robotic Visual Assistance System for Image Guided Neurosurgery," in *Proc. Computer Aided Radiology and Surgery, (CARS 2005)*, vol. 1281, 2005, pp. 624–629.

Pseudo-Haptic Feedback for Tissue Stiffness Simulation

Min Li, Maisarah Binti Ridzuan, Kaspar Althoefer
Department of Informatics
King's College London
London, UK
min.m.li@kcl.ac.uk; k.althoefer@kcl.ac.uk

Prokar Daspupta
MRC Centre for Transplantation, DTIMB and NIHR BRC
King's College London
London, UK

***Abstract*—This paper introduces a low-cost simulation technique for soft tissue stiffness and hard inclusions. Although without expensive haptic interfaces users receive only visual feedback (pseudo-haptics) when maneuvering an indenter avatar over the surface of a virtual soft tissue by means of an input device – a pressure-sensitive touchpad or tablet, the alterations to the indenter avatar behavior induced by the method creates the experience of actual interaction with a hard inclusion in the user's mind. The proposed method is experimentally evaluated for hard inclusions identification. It proves that this pseudo-haptic feedback method can be used to express haptic information in palpation.**

Keywords—haptic feedback; palpation; pseudo-haptic feedback; tumor identification

I. INTRODUCTION

Tissue stiffness distribution within an organ can be perceived through the application of appropriate forces to an organ and the observation of the resulting indentation. Simulating the function of haptic sensations resulting from palpations is beneficial for tissue abnormality identification in medical training. 3D haptic devices are commonly used for palpation simulation [1]. One drawback for those devices is that the costs are relatively high. Pseudo-haptic feedback creates an illusion of haptic feedback by visual display [2]. Haptic devices are not needed when pseudo-haptic feedback is applied. In our previous work, the pseudo-haptic feedback technique is applied to simulate soft tissue stiffness using a computer mouse [3]. Lateral reacting force of sliding behavior and normal reacting force of indenting behavior are simulated separately. In this paper, a pressure-sensitive touchpad is used as a motion input device that lateral force and normal force are simulated simultaneously.

II. METHODOLOGY

The relationship between the input device movement and the movement of the slave indenter avatar is introduced. The avatar display ratio is the relationship between the indenter avatar displacement distance (*d*) and the input device displacement distance (*D*) (*R=d/D*). Therefore, the movement speed of the indenter avatar can be reduced by changing the avatar display ratio when it is approaching a hard inclusion. The user can experience a corresponding resistance when the speed of indenter avatar is slower. If the user moves the input device towards a relative hard area on a certain distance (D), the indenter avatar display ratio will be modified to be smaller than the original ratio ($R_m<R_o$, R_m is the modified ratio and R_o is the original ratio), thus the modified avatar displacement distance dm will be smaller than the original indenter avatar displacement distance do ($d_m=R_m D$, $d_o=R_o D$), and a resistance to motion will be experienced compared with when the original indenter avatar display ratio is applied. Thus, virtual forces (*VF*) are perceived through visual perception along the movement direction. Rather than applied to the user's finger, virtual forces are directly exerted on the indenter avatar. In order to achieve position correspondence, the indenter avatar will move faster when moving away from the hard area until the position correspondence is reached. The frame diagram of the pseudo-haptic soft tissue stiffness simulation using a pressure-sensitive touchpad motion input device is shown in Fig. 1.

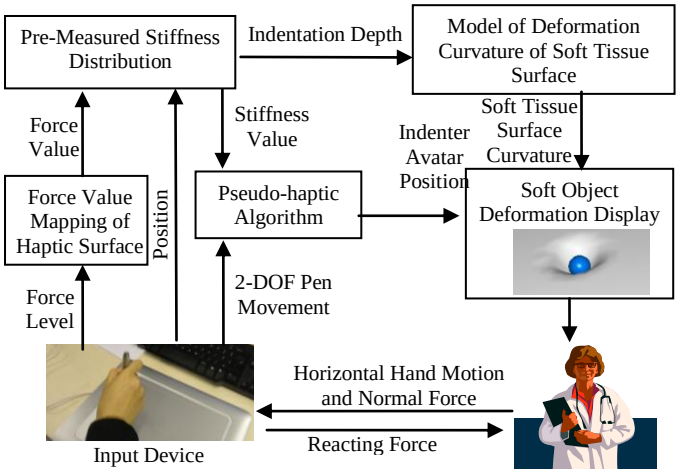

Fig. 1. The block scheme of the pseudo-haptic soft tissue stiffness simulation using a pressure-sensitive touchpad motion input device.

In this pseudo-haptic soft tissue stiffness simulation, deformation of the virtual soft tissue during indentation is displayed in real time using a geometrical deformable soft tissue model, which was established based on predefined finite element modeling considering the influence of the indenter diameter. The detail of this model is presented in [4]. If a node of the mesh is pressed by the indenter, the normal vertex of this node is redefined according to the depth of the indenter. At the

same time, the normal vertices of other nodes nearby on the mesh are affected by the indentation and are adapted according to the geometrical model to display the tissue displacement. If the indentation depth increases, the number of the affected nodes increases.

The stiffness distributions used in the simulation came from two soft silicone blocks with hard nodules embedded. The stiffness distribution of the two silicone blocks were obtained using a force-sensitive rolling probe, which can be attached to a rigid tool to scan the surface of a soft tissue to obtain its force distribution by concurrently measuring the tool-soft tissue interaction dynamics as it rolls over the surface of the soft tissue. The force distribution matrix can show the stiffness distribution of the soft tissue at a given indentation depth [5]. If the indentation depth is zero, the coordinates recorded would be the contour of the soft tissue. The stiffness distribution used in the pseudo-haptic soft tissue stiffness simulation comes from a silicone block. This silicone block was $120 \times 120 \times 25$ mm^3 with three spherical nodules embedded inside.

In order to validate the pseudo-haptic soft tissue stiffness simulation using a force-sensitive haptic surface, a user study was conducted. Twenty participants (all have engineering background, one subject is a surgeon, others had no palpation experience), participated in the empirical study. First, participants were also asked to do a practice run with known tumor locations. Then, participants were asked to manipulate the input device to palpate the virtual soft tissue and observe the change of the ratio between the indenter avatar displacement distance and the input device displacement distance. When they found hard inclusions, they recorded the positions of them. Time consumed was also recorded.

III. Results and Discussion

The smallest tumor C has a low detection rate which is 15%. The detection rate of nodule B is the highest (75%), followed by nodule A (65%); it is interesting to note that nodule B has a higher detection rate despite being smaller than nodule A. It implies that this method is more suitable for detecting middle sized nodules. Three participants (15%) detected all nodules while the same rate of participants detected no nodules at all. Eleven participants (55%) detected more than two tumors correctly. The detection rates for the three nodules are 65%, 75% and 15%. Total nodule identification (51.7%, SD= 31%) indicates that there is a high inter-individual variability of the performance. The average time is 248.9s.

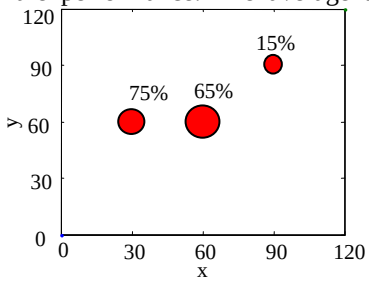

Fig. 2. Nodule identification results of pseudo-haptic feedback using touchpad as input device

This pseudo-haptic palpation simulation method produces visual and haptic information which are not spatially coincide with each other. During manipulation of a system by hands, haptic feedback is presented at user's hands. To improve the effectiveness of tissue stiffness and abnormality localisation, haptic and visual information should be presented at the same active point of interaction using direct touch interaction. Thus, to improve the performance at the next step, we propose to utilize direct touch which let user feel as though their finger is immersed in the screen to manipulate virtual tissue by using pressure-sensitive tablet. In contrast with available pseudo-haptic developments for palpation, this research is aimed to produce pseudo-haptic feedback with spatially coincide visual-haptic information, compact, mobile, wireless, and easy to manipulate for more effective interaction.

IV. Conclusion

This paper presented a novel method to apply pseudo-haptic feedback in soft tissue stiffness simulation for palpation by using an inexpensive 2D haptic surface. This method was evaluated for tumor localization. Analyzing the evaluation tests, we saw that participants were able to notice the stiffness differences among different areas. It proves that the pressure-sensitive touchpad can be used to express tissue stiffness haptic information during palpation simulation. In the future, a pressure-sensitive tablet will be used for a better immersive illusion through direct touch.

Acknowledgment

The work described in this paper is partially funded by the Seventh Framework Programme of the European Commission under grant agreement 287728 in the framework of EU project STIFF-FLOP, the China Scholarship Council, as well as by the National Institute for Health Research (NIHR) Biomedical Research Centre based at Guy's and St Thomas' NHS Foundation Trust and King's College London. The views expressed are those of the authors and not necessarily those of the NHS, the NIHR or the Department of Health.

References

[1] T. Endo, H. Kawasaki, T. Mouri, Y. Doi, T. Yoshida, Y. Ishigure, H. Shimomura, M. Matsumura, and K. Koketsu, "Five-fingered haptic interface robot: HIRO III," World Haptics 2009 Third Joint EuroHaptics conference and Symposium on Haptic Interfaces for Virtual Environment and Teleoperator Systems, vol. 4, no. 1, pp. 458–463, 2009.

[2] A. Lecuyer, S. Coquillart, A. Kheddar, P. Richard, and P. Coiffet, "Pseudo-haptic feedback: can isometric input devices simulate force feedback?," in Proceedings IEEE Virtual Reality 2000 (Cat. No.00CB37048), 2000, pp. 83–90.

[3] M. Li, H. Liu, L. D. Seneviratne, and K. Althoefer, "Tissue Stiffness Simulation and Abnormality Localization using Pseudo-Haptic Feedback," in IEEE international conference on robotics and Automation, 2012, pp. 5359–5364.

[4] M. Li, L. D. Seneviratne, P. Dasgupta, and K. A. Althoefer, "Virtual palpation system," in International Conference on Intelligent Robots and Systems workshop "Learning and Interaction in Haptic Robots", 2012.

[5] H. Liu, J. Li, X. Song, L. D. Seneviratne, and K. Althoefer, "Rolling Indentation Probe for Tissue Abnormality Identification During Minimally Invasive Surgery," IEEE Transactions on Robotics, vol. 27, no. 3, pp. 450–460, 2011.

Palpation Strategies for Artificial Soft Tissue Examination

Jelizaveta Konstantinova, Min Li, Kaspar Althoefer, Thrishantha Nanayakkara
Department of Informatics, Centre for Robotics Research
King's College London
London, United Kingdom
jelizaveta.zirjakova@kcl.ac.uk

Prokar Dasgupta
MRC Centre for Transplantation, DTIMB and NIHR BRC
King's College London
London, United Kingdom

***Abstract*—This paper presents studies developed to understand the need of the specific behavioral strategies during artificial tactile examination of soft tissues for robot-assisted minimally invasive surgery. Conventional manual palpation techniques are studied to understand the desired patterns that should be applied using intra-operative tactile probes. In addition the tele-manipulation studies are carried out. Our results demonstrate the importance of application of specific palpation behavior during artificial tactile examination.**

Keywords— Robot-Assisted Minimally Invasive Surgery, Medical Robotics, Palpation, Soft Tissue, Tele-manipulation

I. INTRODUCTION

Robot-assisted Minimally Invasive Surgery (RMIS) is an advanced medical procedure that allows reducing the recovery time and complications for patients during various types of surgical procedures [1]. The appearance of robotic surgery induced the rapid development of associated technologies, such as advanced interfaces and smart instruments [2], [3].

RMIS is performed via small trocar ports that do not allow surgeon to palpate organs, to understand the location of tumor, for instance. The representation of the surgical environment is typically represented with the help of high-quality spatial visualization (e.g. Da Vinci Surgical system), which cannot give a complete representation of soft tissue mechanical structure, such as stiffness. Therefore, a number of miniature tactile devices are developed to enable tele-manipulated palpation of the organs during surgical procedure [4–6]. Nevertheless, surgical tactile devices are not broadly used for RMIS yet. This happens mainly because the devices developed for surgical applications are required to be accurate and well tested. Consequently, the result of tactile examination should be efficient and reliable. However, non-linear mechanical properties of soft tissues and additional factors, such as the mobility of internal organs and the flows of body liquids lead to the complexity and uncertainty of the environment. Thus, the results of tactile examination can be subject to high variability of results.

In our studies, we propose that the result of tactile examination depends not only on the technical parameters of a device, but also on the environmental conditions. In order to take into account the above-mentioned factors and to improve the accuracy of the tactile examination, specific patterns can be used [7–10], similarly as it is done for the manual palpation. Therefore, we study the way people use manual palpation to detect hard nodules embedded in a softer material, which represents soft tissue. The aim of such studies is to understand salient features of manual palpation, as well as to understand the search patterns.

The second issue, concerning soft tissue tactile property measurement is the translation of the haptic feedback to the user. For this purpose, a number of tele-manipulation systems have been developed [11–13]. In this work, we use the system, presented in [14] to study the palpation behavior during tele-manipulated palpation of soft tissue. Thus, it is needed to understand, whether the application of the specific search pattern can enhance the performance of the tactile examination and to increase the detection rate of hard nodules.

II. MANUAL PALPATION TRAJECOTRY PATTERN

A. Studies on Manual Palpation

For the studies of manual palpation, twenty participants have been recruited [15]. Ten out of them had prior surgical or manual palpation experience.

During experimental evaluation of manual palpation, subjects were asked to palpate an artificial organ with embedded tumours. The relation of stiffness between soft tissue and abnormity is created according to typical conditions of cancer disease, as the abnormality is typically stiffer [16]. A silicone block with embedded hard nodules is used in our user study. To fabricate this silicone block, silicone gel (RTV6166, ratio of 4:6, viscosity of 900 mPa·s) was used. The hard nodules, of different diameters (6, 8 and 10 mm), were embedded at different depths from the surface of the silicone material. To create the nodules, a hard silicone compound (RTV615, ratio of 10:1, 4000 mPa·s viscosity) was used.

The experimental setup is shown in Fig.1. The trajectory of palpation was measured. The applied forces are recorded with six degree-of-freedom force/torque sensor MINI 40 (ATI Industrial Automation, normal force resolution 0.01 N). A Microsoft Kinect sensor (sample rate 30 fps, 640 × 480 pixel resolution) is used to track the spatial position of the hand using Microsoft Visual C++ OpenCV package. The position accuracy for the Kinect sensor was obtained experimentally for an average palpation velocity, and is 1-2 mm.

This work was supported by STIFF-FLOP project grant from the European Commission Seventh Framework Programme under agreement 287728 and National Institute for Health Research (NIHR) Biomedical Research Centre based at Guy's and St Thomas' NHS Foundation Trust and King's College London.

To understand the strategies used by subjects to get information about the properties of the embedded nodule, we examined the experiments of movement of free one-finger palpation.

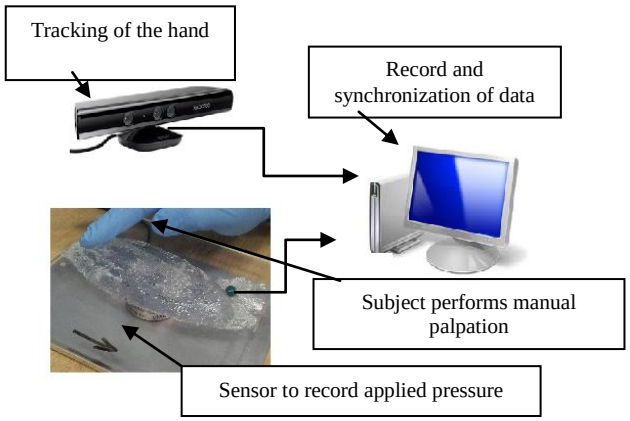

Figure 1. Schematic representation of the experimental setup

B. Result

Fig. 2 demonstrates the distribution of palpation velocity and applied finger pressure over the trajectory over a phantom organ. Both experts and novices have indicated the use of specially applied behavioural pattern to enhance the detection of hard nodules. The trajectories almost cover the entire surface of the artificial organ; circular movements can be observed in the vicinity of hard nodules.

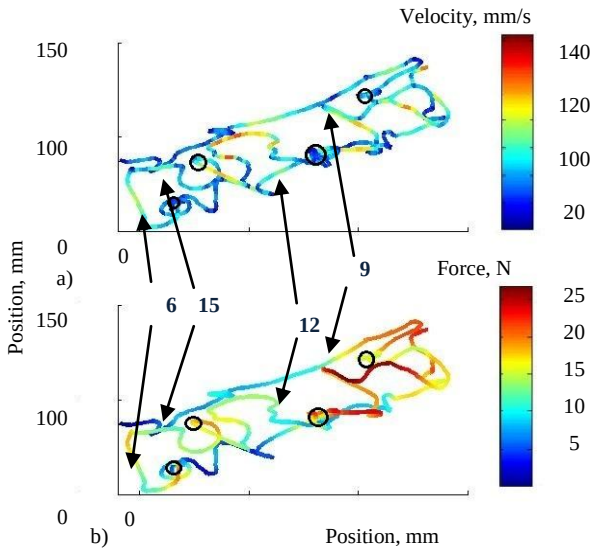

Figure 2. Representative example of palpation path over a phantom tissue with four embedded nodules (diameters in mm marked with arrows): a) modulation of velocity magnitude, b) modulation of applied finger pressure.

III. STUDIES ON PALPATION USING TELE-MANIPULATION

A. Tele-manipulation Setup and Test Protocol

The purpose of our studies is the application of artificial tactile sensors during RMIS. Therefore, as a next step, the tele-manipulation experiments were performed. To study the use of manual palpation strategies, which have been addressed in section II, during RMIS, the experimental tele-manipulation platform, shown in Fig. 3 is used. Soft tissue phantom is examined remotely with a tactile probe, and haptic and visual information about the stiffness is fed back to the human subject. This setup enables the possibility to study various strategies of soft tissue remote palpation or probing.

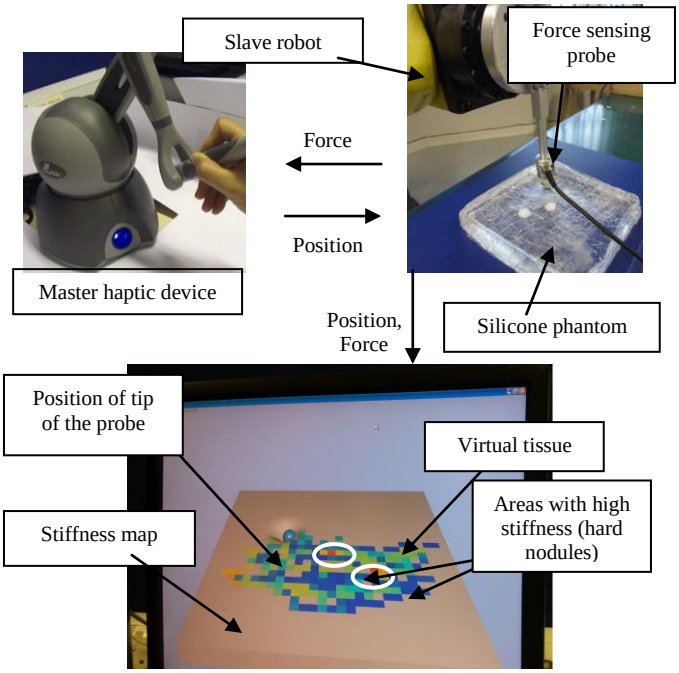

Figure 3. Tele-manipulation setup

B. Random palpation trajectory vs. manual palpation trajectory pattern

Subjects were asked to perform two tests [17]. Firstly, users were asked to palpate the artificial use random palpation behavior. Then, to understand the fidelity of manual palpation pattern during remote palpation, participants were asked to apply consequent scanning of the silicone combined with circular movements over possible locations of hard nodules [18]. This pattern is typically used for clinical breast examination.

A master haptic device (Phantom Omni, Sensable Technologies) is used to operate the probe, with 8 mm spherical indentation tip. A force and torque sensor NANO17 (ATI technologies) measures normal and tangential forces from the lubricated surface of the silicone phantom. A slave robot arm follows the defined trajectory, rolling the force-sensing probe over the phantom tissue. The accuracy of the position tracking for the tele-manipulation is 0.2 mm. The average delay for the position tracking is 0.25 sec with standard deviation of 0.04 sec.

A virtual tissue representation is displayed on a computer monitor. The position of the probe is displayed in the virtual environment in real time. The pointer (cursor) of the virtual model is moving according to the user-defined trajectory and reflects the position of the probe in real-time. The deformation of the tissue is shown on the virtual model according to the indentation depth. Stiffness distribution color map is created using force and indentation depth data, and areas of high

stiffness are shown with the high intensity color. The RGB color value reflects the value of stiffness (increasing from dark blue to red). The colors of the stiffness map are updating in realtime with regard to an updated range of magnitude of stiffness.

Subjects receive visual and haptic feedback in realtime during tele-manipulation. Haptic feedback is exerted via a haptic device (the master robot) in three dimensions. Tree-dimensional force feedback enables the display of not only normal force but also dragging forces (tangential direction).

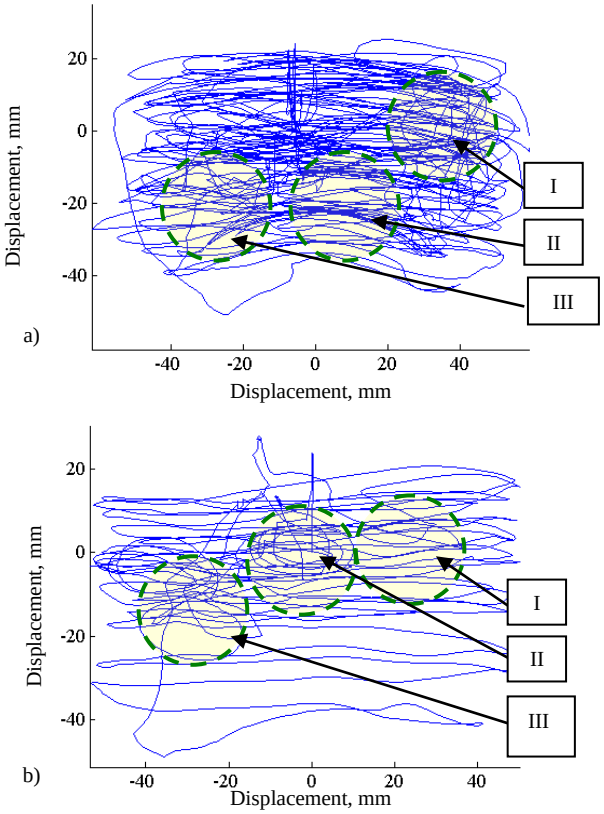

Figure 4. Trajectory of remote palpation for: a) unrestricted and unstructured user-defined movements – Test1, and b) pre-defined pattern – Test 2; the orientation of the silicone phantoms is different for two tests, the locations of hard nodules – I, II, III

A. *Results*

The trajectory of the movement for two trials using tele-manipulation was recorded and evaluated. Fig. 4 shows the sample trajectories of one subject performing two tests.

The results show, that 30% of subjects have used some palpation pattern during first trial (subjects were defining the palpation trajectory), such as intensive circular patterns in the vicinity of a hard nodule. For the second test, subjects were asked to apply the pre-defined pattern. The analysis of trajectory shows that all subjects were successful in that task, and all have applied the circular pattern for the possible locations of nodules along with the sequential scanning of the silicone phantom.

To evaluate the effectiveness of the second palpation test, the detection rate of hard nodules was evaluated. The overall result shows that the second test was more productive across all subjects, see Table I. Moreover, small nodules were detected more often for the second tests. Three-way analysis of variance showed the influence of trajectory pattern on the detection rate of hard nodules ($p < 0.001$). In addition, the time spent for the second test was significantly less ($p < 0.001$). All subjects have indicated that the use of special pattern improves the efficiency of examination.

TABLE I. DETECTION OF EMBEDDED NODULES

Nodule, diameter	**Detection rate for all tests, %**	
	Undefined pattern (Test 1)	***Defined pattern (Test 2)***
A, 10 mm	80%	100%
B, 8 mm	90%	90%
C, 6 mm	50%	80%
All together	73%	90%

IV. CONCLUSIONS

Our results have demonstrated the importance of specific behavioral pattern during remote soft tissue palpation. Therefore, the application and usage of artificial tactile devices can be improved. We propose that in order to get a better understanding about the optimal examination strategy, the interaction dynamics between soft tissue and a device should be studied. One needs to take into account not only the trajectory of examination, as it is shown here, but also the modulation of force and velocity of palpation. In addition, the unpublished work demonstrates the significance of the examination material. Therefore, we believe, that in order to introduce artificial remote palpation, there is a need for the development of behavioral control policies and algorithms.

ACKNOWLEDGMENT

The research has received funding from the European Commission's Seventh Framework Programme, project STIFF-FLOP (Grant No: 287728) and the National Institute for Health Research (NIHR) Biomedical Research Centre based at Guy's and St Thomas' NHS Foundation Trust and King's College London. The views expressed are those of the authors and not necessarily those of the NHS, the NIHR or the Department of Health.

REFERENCES

[1] D. B. Camarillo, T. M. Krummel, and J. K. Salisbury, "Robotic technology in surgery: past, present, and future.," *American journal of surgery*, vol. 188, no. 4A Suppl, p. 2S–15S, Oct. 2004.

[2] S. Schostek, M. O. Schurr, and G. F. Buess, "Review on aspects of artificial tactile feedback in laparoscopic surgery.," *Medical engineering & physics*, vol. 31, no. 8, pp. 887–98, Oct. 2009.

[3] P. Puangmali, K. Althoefer, L. D. Seneviratne, D. Murphy, and P. Dasgupta, "State-of-the-Art in Force and Tactile Sensing for Minimally Invasive Surgery," *IEEE Sensors Journal*, vol. 8, no. 4, pp. 371–381, Apr. 2008.

[4] J. W. Klaesner, P. K. Commean, M. K. Hastings, D. Zou, and M. J. Mueller, "Accuracy and Reliability Testing of a Portable Soft Tissue Indentor," *Rehabilitation*, vol. 9, no. 2, pp. 232–240, 2001.

[5] H. Leng and Y. Lin, "Development of a Novel Deformation-Based Tissue Softness Sensor," *Sensors (Peterborough, NH)*, vol. 9, no. 5, pp. 548–554, 2009.

[6] H. Liu, O. Elhage, P. Dasgupta, B. Challacombe, D. Murphy, L. Seneviratne, and K. Althoefer, "A haptic probe for soft tissue abnormality identification during minimally invasive surgery," in *Advances*, 2009, pp. 417–422.

[7] M. E. Murali and K. Crabtree, "Comparison of two breast self-examination palpation techniques.," *Cancer nursing*, vol. 15, no. 4, pp. 276–82, Aug. 1992.

[8] B. A. Hungerford, W. L. Gilleard, M. Moran, and C. Emmerson, "Evaluation of the ability of physical therapists to palpate intrapelvic motion with the stork test on the support side Research Report Evaluation of the Ability of Physical Therapists to Palpate Intrapelvic Motion With the Stork Test on the Support Side," *Physical Therapy*, vol. 87, no. 7, pp. 879–887, 2007.

[9] J. Konstantinova, M. Li, V. Aminzadeh, P. Dasgupta, K. Althoefer, and T. Nanayakkara, "Force-Velocity Modulation Strategies for Soft Tissue Examination," in *IEEE International conference on intelligent Robots and systems*, 2013 - to be published.

[10] P. Polygerinos, D. Zbyszewski, T. Schaeffter, R. Razavi, L. D. Seneviratne, and K. Althoefer, "MRI-compatible fiber-optic force sensors for catherisation procedures," *IEEE Sensors Journal*, vol. 10, no. 10, pp. 1598–1608, 2010.

[11] A. Talasaz, R. V Patel, and M. D. Naish, "Haptics-enabled Teleoperation for Robot-assisted Tumor Localization," *Robotics and Automation (ICRA), 2010 IEEE International Conference on*, pp. 5340–5345, 2010.

[12] H. Il Son, T. Bhattacharjee, and D. Y. Lee, "Estimation of environmental force for the haptic interface of robotic surgery," *The international journal of medical robotics and computer assisted surgerY*, vol. 6, no. May, pp. 221–230, 2010.

[13] T. Yamauchi, S. Okamoto, M. Konyo, Y. Hidaka, T. Maeno, and S. Tadokoro, "Real-time remote transmission of multiple tactile properties through master-slave robot system," in *2010 IEEE International Conference on Robotics and Automation*, 2010, pp. 1753–1760.

[14] M. Li, J. Konstantinova, V. Aminzadeh, L. D. Seneviratne, P. Dasgupta, and K. Althoefer, "Real-time Visual Stiffness Feedback for Soft Tissue Palpation in a Telemanipulation Environment," in *Hamlyn Simposium 2013*, 2013.

[15] [J. Konstantinova, M. Li, G. Mehra, P. Dasgupta, K. Althoefer, and T. Nanayakkara, "Characteristics of Manual Palpation to Localize Hard Nodules in Soft Tissues," *IEEE transactions on bio-medical engineering*, 2013 - submitted for publication.

[16] H. T. Krouskop TA, Wheeler TM, Kallel F, Garra BS, "Elastic moduli of breast and prostate tissue under compression," *Ultrasonic imaging*, vol. 20, pp. 260–274, 1998.

[17] J. Konstantinova, M. Li, V. Aminzadeh, K. Althoefer, P. Dasgupta, and T. Nanayakkara, "Evaluating Manual Palpation Trajectory Patterns in Tele-Manipulation for Soft Tissue Examination," in *IEEE Systems Men and Cybernetics*, 2013 - to be published.

[18] W. H. Goodson, "Clinical Breast Examination," *Topics in Primary Care Medicine*, vol. 164, no. 4, pp. 355–358, 1996.

Spatially distributed stiffness rendering system for handsfree palpation

Sergio Portolés Bert Willaert, Emmanuel Vander Poorten and Dominiek Reynaerts
Dept. of Mechanical Engineering, KU Leuven, 3001 Heverlee, Belgium
Email: sergio.portolesdiez at mech.kuleuven.be

***Abstract*—Robotic surgery is a relatively young field of research. The effectiveness of surgical robotic devices remains subject of debate. While the ergonomy of the employed interfaces is considered a strong point, the content and quality of the information that they feed back and present to its operator be it a surgeon or a trainee is still limited. Therefore a lot of research is being conducted in search for intuitive and effective interfaces. In this abstract a novel haptic interface for handsfree palpation is presented. The interface follows the principle of an encountered-type robot replicating more naturally the actual palpation procedure. The concept of this new development is presented. The control method to render spatially distributed kinaesthetic information is explained next. Experimental results show a proof-of-principle towards a more natural palpation.**

I. Introduction

Robotic surgery is an emerging technology stirring up lots of animosity into modern medicine. Robots can be seen performing tasks in orthopedic surgery, neurosurgery, gynecologic surgery, urology or cardiothoracic surgery. Some of the more popular platforms are e.g. the Magellan Robotic system of Hansen Medical, DLR's MiroSurge [1] or da Vinci® of Intuitive Surgical. While the the number of procedures suited for robotic assistance remains low, this number is increasing and robotic solutions are drawing more and more the attention of surgeons. One of the possibly most cited drawbacks of robotic surgery is the lack of haptic feedback. Haptic feedback is very much present in manual laparoscopic interventions [2] and its presence is shown to greatly improve the perfomance and reduce the learning curve [3], [4]. Haptic features can help to prevent collisions between instruments [5], but also for palpation, to diagnose and localize tissues, damaged cells or tumors; even if other methods exist (CT or USG), haptic feedbak remains essential [6].

In this abstract we present in section II the *haptic screen*, a novel haptic device that was developed to allow more natural haptic-feedback-enhanced palpation. A brief word about the control of this device is described in section III. Some first results are reported in section IV.

II. Design of a haptic screen

A novel approach to recreate natural palpation according to the encountered-type display principle [7]–[10] is presented here.

The haptic screen, a large area haptic display has following features: *a)* display renders spring-damping impedance *b)* encountered-type interaction allowing hands-free manipulation and *c)* haptics feedback derived form spring-damping virtual reality simulation.

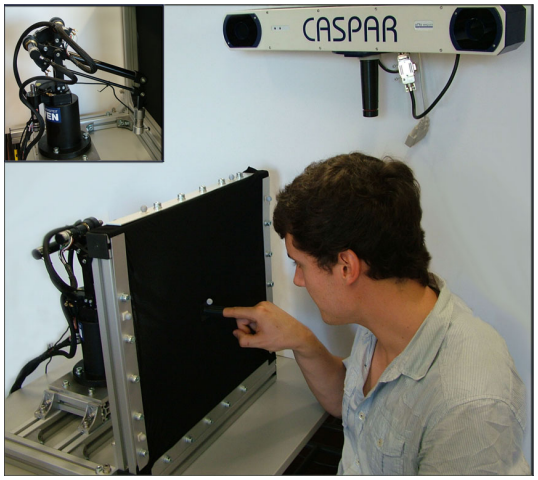

Fig. 1. Overview of the whole system

A. System overview and principle

The haptic screen consists of a membrane placed in front of the user representing a palpation plane with whom the user can interact (Figure 1). Additionally, the robotic system is equipped with a vision system that measures the relative position between the user's hand and the haptic surface. The hand pose is used to command the motion of an encountering haptic device behind the screen. An in-house developed 3 d.o.f. haptic device [11] was used for this purpose. While sitting in front of the haptic screen and moving his/her finger this device mirrors the hand motions. When the hand comes into contact with the screen, kinaestic feedback is rendered to the user, replicating natural palpation. The workflow of a palpation task can thus be divided into next steps:

1) a user takes place in front of the screen,
2) extends the arm approaching the screen, a.k.a. approaching stage.
3) the robot mirroring the user, waits at the surface.
4) user's finger enters into contact w. haptic surface.
5) applying pressure at the surface.
6) robot presents impedance mimicking virtual or remote tissue corresponding to that contact location / finger position.
7) user removes disengages.
8) new palpation cycle can start.

B. System components

To turn the robotic system into a handsfree palpation display, a tracking system and a tensioned membrane are employed. Below a brief explanation of these elements.

1) Tracking system: A tracking system is required to position and encounter the user's motion at the appropriate instant in time and the correct location. A Polaris® tracker from NDI was selected for this purpose. The tracking system reads in the position of reflective markers normally placed somewhere in the surgical theater. Here, a single marker was attached to the distal phalanx of the finger. For easy registration of the finger with respect to the haptic screen ${}^{marker}_{screen}\boldsymbol{p}$ additional markers were fixed upon the frame of the haptic screen.

2) Membrane as haptic surface: The haptic surface is approximated as a plane that represents the surface of the patient's organ to be examined. Here, a polyethylene fabric was selected and mechanically fixed to a vertical rame between user and robot. The membrane smoothens out the interaction creating the feeling of a continuous contact. It further adds to the overall safety. The membrane does introduce an additional impedance during in-contact motion, but this is assumed to be negligible within the range of the impedances rendered by the haptic device, as: $Z_{membrane} \ll Z_{HRI}, Z_{control}$.

III. Control for Haptic Rendering

A tracking controller and an impedance controller are used for respectively approaching phase and in-contact motion. The latter is described below in some detail.

A. Stiffness control

Figure2 shows an impedance controller with inner proportional force feedback loop, analysed in detail in [12], that was used to render a desired desired impedance Z_d to the user.

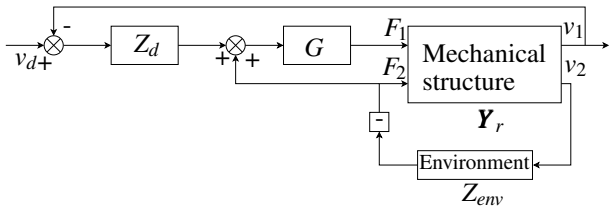

Fig. 2. Schema of the impedance controller

B. Kinaesthetic map

The desired impedance Z_d is selected as function of the position of the finger $Z_d = f({}^{marker}_{screen}\boldsymbol{p})$. The result is a distributed impedance map corresponding to the distributed impedance of an organ. High stiffness values are e.g. used to simulate nodules hidden underneath the surface.

IV. Experiments

Two tests were conducted to verify the device performance.

A. Map exploration

A map exploration experiment replicated a palpation procedure similar to the one applied during normal operation. Two nodules were positioned along a horizontal line of the haptic surface. A user follows the line applying pressure along it. The forces at the end-effector are recorded for any position of the finger. Fig. 3 shows the forces of the transducer, positions of the finger and desired stiffness in w_x direction. The graph shows nicely how forces increase when the desired stiffness grows and that often the amount of indentation reduces in such cases. Figure 4 shows the relation between force and position, the perceived stiffness, plotted against the desired stiffness. A certain mismatch at high values of stiffness can be observed, while low stiffnesses are rendered fairly well.

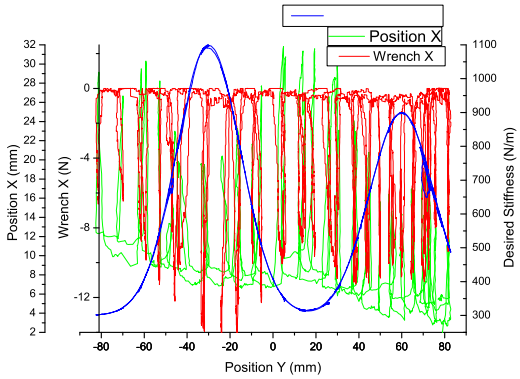

Fig. 3. Finger position, end-effector forces and desired stiffness are compared along the scanning line (z=0)

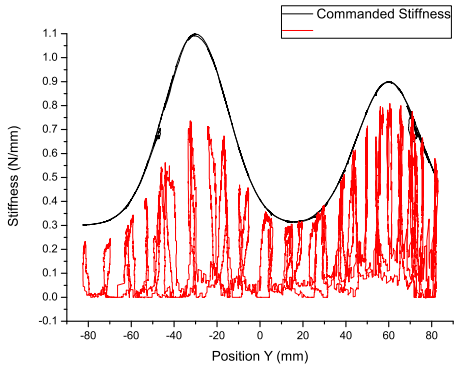

Fig. 4. Measured perceived stiffness is compared with the desired stiffness commanded by the kinaesthetic map

B. Perceptual tests

A user test was performed in the following conditions. Six right-handed users with ages comprised between 26 – 35 years old were asked to palpate the haptic surface. The users were told to find 3 hard nodules on 3 different maps using as much the time as they needed. A training phase preceded once for every user to get used to the system. The workflow was explained and two training maps were shown.

Once a user finds the centre of a nodule he/she is asked to hold the position and the examiner records it. After three guesses, the experiment finishes and the next map is loaded.

Figure 5 shows the locations of the centre of the nodules as indicated by the users. The kinaesthetic map is also depicted to see the accuracy of the user guesses. There is a good correspondence between indicated and rendered nodule locations. It should be noted that some users identified the same location twice (nodules with more than 6 marks).

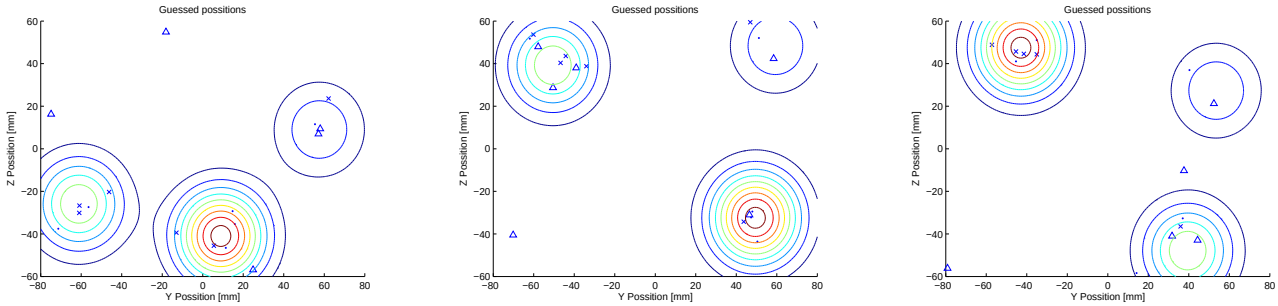

Fig. 5. Estimations of the position of the stiffness peaks made by the users. The level lines indicate the geometric place for iso-stiffness values.

V. Conclusions

In this abstract the proof of concept of a novel haptic interface to render large areas of kinaesthetic information for hands-free operation in encountered-type basis is presented. The proposed system consists of an interfacing membrane, a tracking sytem and an encountering mechanism. By releaving the need of continuously gripping the display, the minimum achievable impedance can go down to $Z_0 = 0$ increasing the Z-width of the device.

Experimental results show that stiffness can be represented with an encountered-type haptic interface. Nevertheless, there is still some mismatch on the fidelity of rigid walls as shown in the map exploration test. Other problems associated with such interface are the the lack of robustness of the current implementation and a low update rate of the tracking system. Some work on these points is planned for the future.

References

[1] U. Hagn, M. Nickl, S. Jörg, G. Passig, T. Bahls, A. Nothhelfer, F. Hacker, L. Le-Tien, A. Albu-Schäffer, R. Konietschke, M. Grebenstein, R. Warpup, R. Haslinger, M. Frommberger, and G. Hirzinger, "The dlr miro: a versatile lightweight robot for surgical applications," *Industrial Robot: An International Journal*, vol. 35, no. 4, pp. 324–336, 2008.

[2] O. Bholat, R. Haluck, W. Murray, P. Gorman, and T. Krummel, "Tactile feedback is present during minimally invasive surgery," *Journal of the American College of Surgeons*, vol. 189.4, pp. 349–355, 1999.

[3] A. M. Okamura, "Methods for haptic feedback in teleoperated robot-assisted surgery," *Industrial Robot*, vol. 31, no. 6, pp. 499–508, 2004.

[4] F. W. Mohr, V. Falk, A. Diegeler, T. Walther, J. F. Gummert, J. Bucerius, S. Jacobs, and R. Autschbach, "Computer-enhanced robotic cardiac surgery: Experience in 148 patients," *The Journal of Thoracic and Cardiovascular Surgery*, vol. 121, no. 5, pp. 842 – 853, 2001.

[5] N. Koliakos, G. Denaeyer, P. Willemsen, P. Schatteman, and A. Mottrie, "Failure of a robotic arm during da vinci prostatectomy: a case report," *Journal of Robotic Surgery*, vol. 2, pp. 95–96, 2008.

[6] I. Haberal, H. elik, H. Gmen, H. Akmansu, M. Yrk, and C. zeri, "Which is important in the evaluation of metastatic lymph nodes in head and neck cancer: palpation, ultrasonography, or computed tomography?" *Otolaryngology - Head and Neck Surgery*, vol. 130, no. 2, pp. 197 – 201, 2004.

[7] Y. Yokokohji, J. Kinoshita, and T. Yoshikawa, "Path planning for encountered-type haptic devices that render multiple objects in 3d space," in *Virtual Reality, 2001. Proceedings. IEEE*, 2001, pp. 271–278.

[8] R. Uesugi, K. Inoue, R. Sasama, T. Arai, and Y. Mae, "See-through sheet visual display for haptic device using flexible sheet," in *ICAT 2003*, December 2003, p. 6.

[9] T. Furukawa, K. Inoue, T. Takubo, and T. Arai, "Encountered-type visual haptic display using flexible sheet," in *Robotics and Automation, 2007 IEEE International Conference on*, 2007, pp. 479–484.

[10] W. McNeely, "Robotic graphics: a new approach to force feedback for virtual reality," in *Virtual Reality Annual International Symposium, 1993., 1993 IEEE*, sep 1993, pp. 336 –341.

[11] B. Willaert, B. Corteville, J. V. Vlem, K. Vanwynsberghe, D. Reynaerts, and H. V. Brussel, "A multi-purpose haptic device for research on physical human-robot interaction," in *13th International Conference on New Actuators*, Bremen, Germany, June 2012, pp. 530–533.

[12] B. Corteville, "Mechatronic design of high-force manipulators under interaction control," Ph.D. dissertation, KU Leuven, Augustus 2010.

Toward Remote Teleoperation with Eye and Hand: A First Experimental Study

Fabien Despinoy, Jonathan Leon-Torres, Marie-Aude Vitrani, and Benoît Herman

***Abstract*— Despite the continuous improvement of master interfaces, distant robot teleoperation remains a challenging task. In many applications, including robot-assisted single port laparoscopic surgery and NOTES, the operator has only an indirect vision of the remote environment, provided by a video camera usually mounted on the robot end-effector itself and displayed on a monitor. Driving such an *eye-in-hand* robot smoothly in real time is known to be difficult. Even a skilled user will likely generate a succession of independent translations and rotations punctuated by frequent stops, in order to keep the target inside the camera field of view. Since one can assume that she/he will look most of the time at the target on the video monitor, our idea is to gather additional information on the remote target with an eye-tracking device, and to use it to facilitate teleoperation. This paper introduces a novel remote teleoperation system that comprises such a device, as well as an 6-axis joystick. Several eye-hand couplings are compared in a first experimental trial. It is shown that the system is effective and intuitive.**

I. Context, Motivation, and Objectives

When operating an interactive robotic device in real time, both user and robot sensorimotor loops act in synergy to perform a desired task under the user's supervision. Implementation of such a system depends on the chosen interaction between user and robot. With most master-slave systems used for teleoperation and virtual reality, interaction is limited to the exchange of kinematic information (e.g. position and/or velocity) with or without haptic feedback, and the slave arm simply copies the operator's motion. In many applications where robotic arms operate in inaccessible locations (e.g. space, nuclear plants, or during minimally access surgery), the robotic end-effector and its environment are captured by a scene camera and displayed on a monitor in front of the operator. The da Vinci teleoperation system from Intuitive Surgical [1] and the DLR MiroSurge [2] are typical examples of such an *hand-in-eye* configuration in surgery, and are known to be easy to drive with their master arms.

This work was supported by Fondation Belge Contre le Cancer (Grant No. SCIE 2006/20), and by own funds from UCL, ISIR, and F.R.S.-FNRS.

F. Despinoy, J. Leon-Torres, and B. Herman are with the Center for Reserach in Energy and Mechatronics, Université catholique de Louvain, Louvain-la-Neuve, Belgium. J. Leon-Torres is also with Université Pierre et Marie Curie, Paris, France. B. Herman is also with Fonds de la Recherche Scientifique – FNRS benoit.herman@uclouvain.be.

F. Despinoy is now with the Laboratoire d'Informatique, de Robotique et de Microélectronique de Montpellier, Université Montpellier 2 – CNRS (UMR5506), Montpellier, France fabien.despinoy@lirmm.fr.

M.-A. Vitrani is with UPMC Univ. Paris 06, UMR 7222, ISIR, Paris, France marie-aude.vitrani@upmc.fr.

The ongoing trend to reduce invasiveness leads to the design of poly-articulated devices (e.g. iSnake form Imperial College [3]) or continuum robots using concentric tubes (e.g. robots from Dupont at Boston University [4] and Webster at Vanderbilt University [5]). When the camera is embedded in such a snake-like system, creating an *eye-in-hand* configuration as with a flexible endoscope, teleoperation difficulty can increase rapidly. Even a skilled user will not make the most of a 6-axis master interface that could normally induce a smooth and continuous motion. Instead, she/he will likely generate a succession of basic motions in Cartesian or even joint space, punctuated by frequent stops [6]. The main reason is that the target (e.g. tissue to grasp or to cut) must be kept inside the camera field of view during robot motion. A smoother motion would require to combine translations and rotations of the end-effector, with a ratio between linear and angular velocities that depends on the distance to the target, the latter being usually unknown.

The development of numerous eye- and gaze-tracking devices allows to add a new channel for human-robot interaction. Several systems have been developed for providing assistance to disabled people. In [7], authors present an actuated wheelchair with eye-control, using the eye as a computer mouse. The same idea is used in [8] to drive a mobile robot remotely. Yet, the gaze is generally not combined with any other interactive information. Furthermore, user needs to perform a specific eye gesture to send an order to the robot, using his/her eyes in an unnatural way. In this paper, we address the following question: Can natural gaze tracking help to teleoperate a robot? Interestingly, Pinpin *et al.* [9] predict the motion of a robot based on user's natural gaze. The main limitation of their setup is that gaze is only reliable for predicting which actions from a predefined list will occur. To overcome this predefined list, we propose to drive a robot using the user's eye movement, without any pattern recognition. Spindler and Chaumette already implemented a visual servoing of the orientation of a robot-mounted camera, using human eye-movement [10]. This device is however limited to a 2D task. We propose to extend this work to a general 3D task.

The paper introduces a novel teleoperation system that combines joystick and natural gaze inputs in several ways to teleoperate an *eye-in-hand* robot. Section II presents the robotic platform, and 3 control schemes are described in Section III. A first experimental performance assessment is then reported and discussed in Section IV.

II. Remote Teleoperation Platform

A proof-of-concept prototype was built around a 6 degrees-of-freedom (DOF) Adept Viper s650 robot with a MotionBlox 60R real-time controller, as depicted in Fig. 1. The teleoperation system comprises a webcam mounted on the robot end-effector to capture the task environment, a head-mounted eye-tracking camera (EYE-TRAC H6 from Applied Science Laboratories, Bedford, MA), a stand to prevent any head motion with respect to a monitor where the webcam images are displayed, and a 6-axis joystick (SpaceNavigator from 3Dconnexion, Waltham, MA).

The platform specificity lies in the original combination of control interfaces. The 6-axis joystick is used to drive the robot in a pose/velocity scheme: Robot linear and angular Cartesian velocities are linked to the joystick position and orientation imposed by the user's hand. An eye-tracker device is also used to record user's pupils movements and to compute gaze direction with respect to the monitor. These two interfaces can then be combined in several ways to control the robot more easily and efficiently.

III. Control Schemes with Eye and Hand Inputs

When performing a task on an object—directly by hand or with any teleoperation means—one usually looks at this object or point of interest (POI): The brush tip while painting, the nail when holding a hammer, or the blood vessel the surgeon wants to clip. This basic assumption lead us to use a gaze-tracking device as a supplement to a joystick or master arm so as to make teleoperation faster, smoother, and easier. Knowing *where on the monitor* the operator looks thanks to a gaze-tracker, a couple of end-effector motions can be automated, or information about robot-target distance or relative orientation can be deduced, even *without any image processing* of what is displayed. We designed and implemented 3 control schemes that use in different ways the 2D-coordinates of the focus point on the screen.

The two first possibilities are to maintain the target at the center of the screen, either by correcting automatically the end-effector orientation during a manual translation (*autonomous rotation*, see Fig. 2), or conversely, by shifting the robot when the user rotates it (*autonomous translation*). In these two similar scenarios, the user has to control only 4 DOF manually, the remaining two being handled by the controller thanks to the eye-tracker 2D signal. This signal can be seen as a measure of the on-screen distance between POI and monitor center. The control loop then simply tries to minimize this distance by using the 2 automatic rotational or translational DOF, respectively.

A third possibility is to estimate the distance between end-effector and target, so as to make the robot rotate around the target instead of around its end-effector. This can be achieved iteratively by measuring the user's eye motion induced by a robot displacement, in order to move the center of rotation from the end-effector to the target. In opposition to the first two above, this *distance estimation* control scheme does not induce any autonomous motion. All translations and rotations are then induced manually but the rotations are more natural. If this distance is underestimated, a manual rotation will induce a shift of the POI in the image in the opposite direction. Conversely, an overestimation of the distance will also translate the POI in the same direction. An iterative algorithm can use this error measured by the gaze-tracker to update the distance estimation.

All these modes, along with a fully manual mode without eye-tracking, were implemented on the robot controller. After initial calibration of the gaze direction with respect to the monitor center, signals form joystick and eye-tracker are acquired, filtered and scaled. They are then used and combined, depending on the scheme, to update the robot pose in real-time.

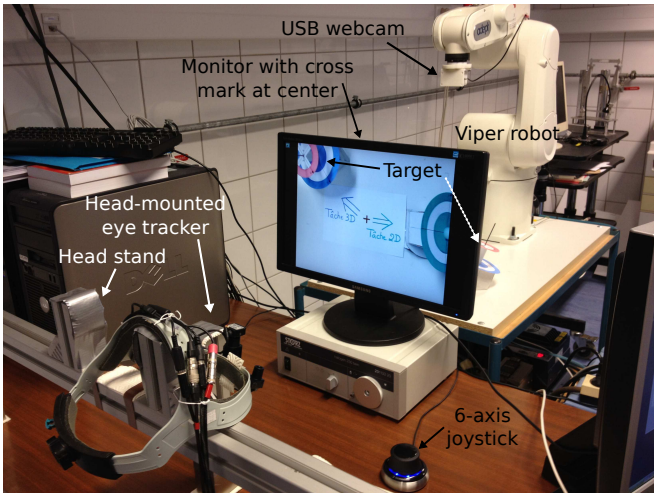

Fig. 1. Experimental setup built around the Viper robot.

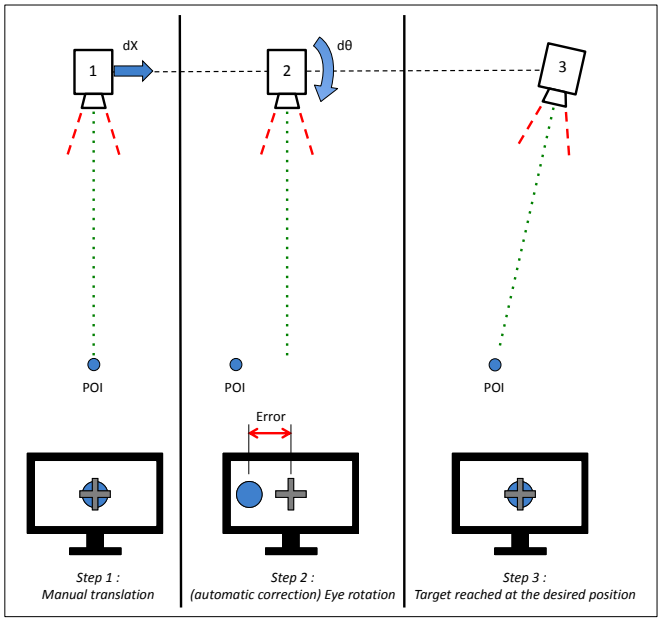

Fig. 2. Autonomous rotation to bring the target back to the center of the monitor after a manual translation.

IV. Performance Assessment

An experimental study was conducted in order to assess the feasibility and usability of the proposed teleoperation system, and to compare the performance of the proposed control schemes. This section describes the teleoperation task proposed, the metrics used for performance comparison, the experimental protocol and the results.

A. Teleoperation Task

A wide variety of tasks can be performed with a teleoperated robot, depending on the context and the tool held by the robot. However, most tasks can be divided in two phases, that can occur at the same time but are more frequently successive: First, the robot is driven to approach a target, and then an action is performed with the tool.

Since our teleoperation system only intends to increase the performance of robot motion, the task is a simple point-to-point displacement combined with an effector reorientation so as to reach a target under a prescribed pose. A specific target (see Fig 3) was designed to ensure that all 6 DOF must be used. It also gives to the operator visual clues on the position and orientation of the end-effector.

B. Metrics

Task duration is the main criterion to compare the schemes. Duration corresponds to the time elapsed between the first operator manual instruction with the joystick and the arrival next to the target. A tolerance zone was programmed to ensure the experiment stop and each linear or angular tolerance was tuned experimentally to define the task difficulty. Moreover, during the experiments, articular robot positions and input signals were also recorded. Graphical analysis of the kinematic data showed that the task could be decomposed into two successive phases: A first approach phase where the error decreases rapidly, followed by an adjustment phase where motions are much shorter and slower. It was then decided to compute the duration of these two phases for each trials, as secondary metrics.

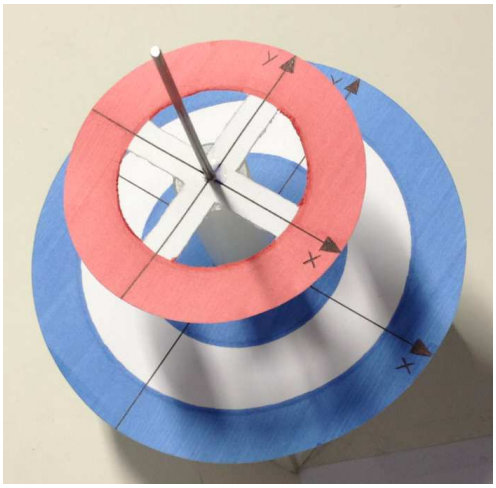

Fig. 3. Target that requires 6 DOF motions of the end-effector.

Subjects were also asked to estimate, on an integer scale from 0 to 10, the performance, precision and intuitiveness of each mode. Performance indicates speed perception to perform the task. Precision reflects the possibility to drive the robot exactly where the operator wants to. Finally, intuitiveness reveals the operator mental workload to control the system correctly.

C. Experimental Protocol

Six researchers from the CEREM were enrolled in the experimental campaign and repeated the same target-reaching task with the various control schemes, being asked to be as quick and precise as possible. Each subject started the protocol with the fully manual mode so as to learn to use the system. He/she repeated the task until the reach of a plateau on the learning curve fitted and refreshed after each trial. The last 3 trials (on the plateau) were taken into account for statistical analysis. Afterwards, the subject tried the 3 assisted modes in randomized order. For each assisted mode, 8 repetitions were performed. The 4 best out of the 5 last trials were taken for analysis.

D. Statistical Analysis

Data were analyzed using General Linear Model (GLM) with JMP 9.0.3 and SAS 9.3 statistical software. The mixed model contained the following effects: subject and control scheme, and the two-factors interaction. Control scheme was defined as fixed factor for the ANOVA (analysis of variance). Subject and its interaction with the fixed factor were defined as random. The model was solved using REML (Restricted Maximum Likelihood). The Tukey HSD test of multiple comparisons was used to compare modalities of significant factors.

E. Results

Figure 4 depicts the average value and standard deviation of approach, adjustment and total duration for all trials of all subjects, for each control mode. Standard deviation for each mode is similar, ensuring that the ANOVA can model the data properly. One can observe that the autonomous translation mode is the slowest, especially during the adjustment

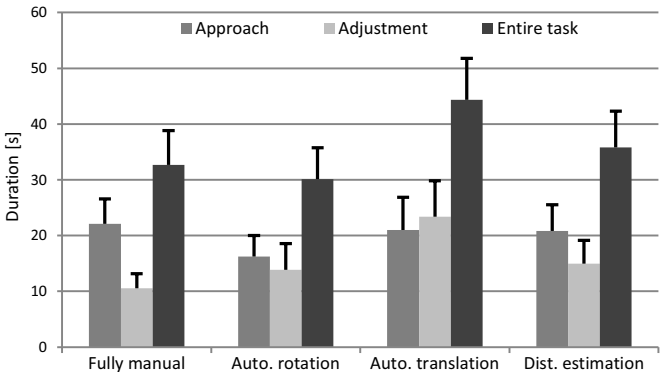

Fig. 4. Average value and standard deviation of task duration for all subjects and repetitions.

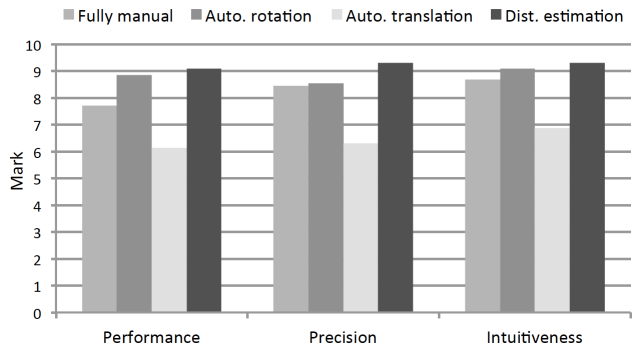

Fig. 5. Average value of subjective indicators normalized between subjects.

phase. This is confirmed by the statistical analysis, since this mode is significantly different from all others regarding the adjustment duration. For the approach duration, the only significant difference is between the fully manual (slowest) and the autonomous rotation (fastest). Finally, analysis of the overall task duration shows that the autonomous translation (slowest) is significantly different form the autonomous rotation (fastest).

Average values of subjective indicators are presented on Fig. 5, after normalization. It appears that the autonomous translation mode is believed to be the less efficient, precise and intuitive mode. In opposition, the distance estimation is perceived as the best mode, followed closely by the autonomous rotation mode.

F. Discussion

This first experimental session demonstrates the feasibility and efficiency of our teleoperation approach using eye and hand. Although the statistical analysis does not highlight many large differences, results are promising. In particular, it seems that the approach phase can be shortened with a gaze-tracker, since all 3 assisted modes are faster that the fully manual one. This might be thanks to the fact that, during large motions, it is easier to keep the target close to the center of the monitor with assistance.

However, during the adjustment phase, a fully manual control seems faster. Subjects declared that this was because it was difficult to keep the focus on the center of the target while perform fine adjustments, since several parts of the targets were to be used to check alignment. Therefore, autonomous motions were sometimes felt like a small disturbance during the final adjustment phase. This suggests that the eye-tracking system should be switched off after the initial approach phase.

Additionally, subjective indicators show the same trend than the objective measurements, with the autonomous translation mode that seems less efficient, precise and intuitive. This suggests to abandon this mode and to keep improving the two other assisted schemes.

V. Conclusion and Future Work

In this paper, we introduced an original system that uses both hand and eyes as master inputs to drive a robot in real time. Three control schemes were proposed that use the gaze information in different ways to reduce the number of DOF that must be driven with a joystick, or to facilitate rotation around the target. A first experimental session demonstrated that teleoperation with eye and hand is feasible and efficient for remote teleoperation with an *eye-in-hand* configuration.

An improved version of the system is currently being developed, using a 3D tracking system to allow head motion, in order to decrease mental and physical workload. As a consequence, this should probably increase the performance level of the whole system. In addition, the task difficulty should be adjusted, since duration decomposition showed that nearly half of the time was spent for small adjustments that might not be required in real applications. The system and control schemes should also be studied in case of a change of POI during the task, which is not unusual.

Acknowledgement

Authors would like to thank warmly all colleagues from the CEREM who took part in the experiments. Authors are also grateful to Catherine Rasse, from the Institute for Multi-disciplinary Research in Quantitative Modelling and Analysis (UCL), for her support and advices regarding experimental methodology and statistical analysis.

References

[1] G. H. Ballantyne and F. Moll, “The da Vinci telerobotic surgical system: The virtual operative field and telepresence surgery,” *Surgical Clinics of North America*, vol. 83, no. 6, pp. 1293–1304, Dec. 2003.

[2] U. Hagn, R. Konietschke, A. Tobergte, M. Nickl, S. Jrg, B. Kbler, G. Passig, M. Grger, F. Frhlich, U. Seibold, L. Le-Tien, A. Albu-Schffer, A. Nothhelfer, F. Hacker, M. Grebenstein, and G. Hirzinger, “DLR MiroSurge: A versatile system for research in endoscopic telesurgery,” *International Journal of Computer Assisted Radiology and Surgery*, vol. 5, no. 2, pp. 183–193, Mar. 2010.

[3] R. C. Newton, D. P. Noonan, V. Vitiello, J. Clark, C. J. Payne, J. Shang, M. Sodergren, A. Darzi, and G. Z. Yang, “Robot-assisted transvaginal peritoneoscopy using confocal endomicroscopy: A feasibility study in a porcine model,” *Surgical Endoscopy*, vol. 26, no. 9, pp. 2532–2540, Sep. 2012.

[4] P. E. Dupont, J. Lock, B. Itkowitz, and E. Butler, “Design and control of concentric-tube robots,” *IEEE Trans. Robot.*, vol. 26, no. 2, pp. 209–225, Apr. 2010.

[5] D. C. Rucker, B. A. Jones, and R. J. Webster, “A geometrically exact model for externally loaded concentric-tube continuum robots,” *IEEE Trans. Robot.*, vol. 26, no. 5, pp. 769–780, Oct. 2010.

[6] J. Cotti, A. Guillaume, N. Alahyane, D. Pelisson, and J. L. Vercher, “Adaptation of voluntary saccades, but not of reactive saccades, transfers to hand pointing movements,” *Journal of Neurophysiology*, vol. 98, pp. 602–612, 2007.

[7] R. Barea, L. Boquete, M. Mazo, and E. Lopez, “System for assisted mobility using eye movements based on electrooculography,” *IEEE Trans. Neural Syst. Rehabil. Eng.*, vol. 10, no. 4, pp. 209–218, Dec. 2002.

[8] H. O. Latif, N. Sherkat, and A. Lotfi, “Teleoperation through eye gaze (TeleGaze): A multimodal approach,” in *Proc. IEEE International Conference on Robotics and Biomimetics (ROBIO)*, Guilin, China, Dec. 19–23, 2009, pp. 711–716.

[9] L. K. Pinpin, R. S. Johansson, C. Laschi, and P. Dario, “Gaze interface: Utilizing human predictive gaze movements for controlling a hbs,” in *Proc. IEEE RAS & EMBS International Conference on Biomedical Robotics and Biomechatronics (BioRob)*, Scottsdale, AZ, Oct. 19–22, 2008, pp. 158–162.

[10] F. Spindler and F. Chaumette, “Gaze control using human eye movements,” in *Proc. IEEE International Conference on Robotics and Automation (ICRA)*, Albuquerque, NM, Apr. 20–25, 1997, pp. 2258–2263.

Modelling and Control Framework for Robotic Telesurgery

Sándor Jordán, Árpád Takács, Imre Rudas and Tamás Haidegger
Antal Bejczy Center for Intelligent Robotics
Óbuda University, Budapest, Hungary
{jorsa89, arpi.takacs}@gmail.com, {rudas, haidegger}@uni-obuda.hu

***Abstract*—Frequently encountered limitations of hardware and software systems regarding teleoperation capabilities include the incomplete modelling of robot dynamics, tool–tissue interaction, human–machine interfaces and the communication channel. Furthermore, the inherent latency of long-distance signal transmission may endanger the stability of a robot controller. All of these factors contribute to the very limited deployment of robotic telesurgery. This paper gives an overview of the challenges of establishing high fidelity telepresence systems for medical applications, and proposes development directions beyond the state of the art.**

Keywords—telesurgery; robot control system; latency

I. INTRODUCTION

Long-distance surgical procedures supported, or performed by robots would open up new frontiers in medical interventions. This was the initial idea behind the first concepts when they appeared at NASA in the early 1970s [1].While the concept of telesurgery in space never reached beyond simulations, by 2001, it was possible for the first time to perform surgery on the basis of ISBN-based intercontinental communication [2]. This proved that in urgent cases—in theory—doctors could reach out to patients hundreds or thousands of kilometres away. The interventions could be executed in places difficult to reach (remote rural areas) or dangerous for people (war zone). DARPA (the US Department of Defense) has sponsored various projects—most notably the TRAUMA POD—to develop a technology that supports injured soldiers on the battlefield without risking the Medical Doctor's life [3]. Nevertheless, the difference in the complexity between supporting a distant operation on Earth and one in space is huge. Human space exploration is unimaginable without full medical support (despite the recent announcements of plans from a Dutch consortium to initiate a one-way Mars mission [4]), yet it is impossible to send an entire medical crew with the spacecraft because of the high costs and the limited space. This severe constraint keeps the research open towards telesurgical solutions, since many of the possibly emerging problems could be solved with one surgical robot sent along the expedition. Thus, proper modelling and control of both master and slave side remains an important research topic [2]. Communication with the surgical crew on Earth creates further tasks to solve. Most of the problems are caused by signal latency, which get worse with the increase of the range of the mission. Some of the disturbing effects of a generally proposed teleoperational surgical robotic system can be reduced by well-chosen system architecture and control. Current options are investigated in this paper.

II. STATE OF THE ART

The best known surgical robot is the da Vinci Surgical System (Intuitive Surgical Inc., Sunnyvale, CA), functioning as a teleoperated manipulator. Over 2,800 da Vincis have been sold around the world to more than 2,000 hospitals [5]. Although the system is not used routinely for distant telesurgery as the master and the slave are just a few metres away from each other (due to the limitation of the custom-developed communication protocol), the potential has been there to make it work at a greater distance, and some limited experiments have been performed. DARPA presented collaborative telerobotic surgery with modified da Vinci consoles in 2005, being able to overtake the controller with another through the Internet [6]. The Canadian Surgical Technologies and Advanced Robotics (CSTAR, London, ON) used the core network of Bell Canada to test the telesurgery-enabled version of the da Vinci. Six successful telesurgical porcine pyeloplasty procedures were performed in Halifax, Nova Scotia—1,700 km away from London, ON[7].

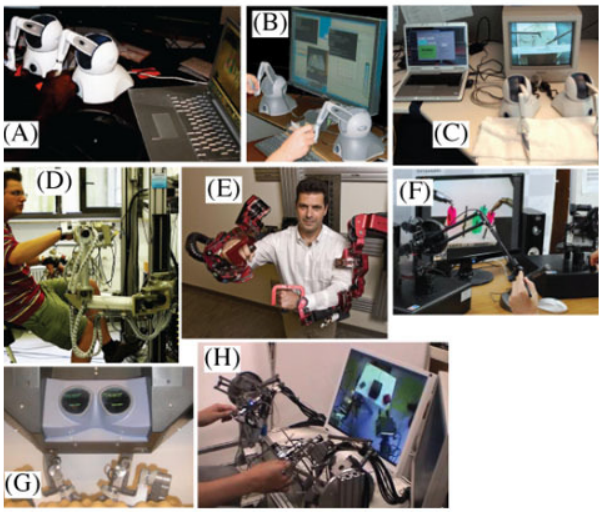

Fig. 1. Interconnected master devices of the 2009 world wide Plugfest event, demonstrating the capabilities of current telesurgical architectures [8].

An outstanding experiment of the domain was the Plugfest in 2009 (Fig. 1), when eight master devices were interconnected with six slave machines [8]. The custom-developed communication *Interoperable Teleoperation Protocol* (ITP)has been successfully used over 24 hours, supporting efficiently the simulated interventions (peg transfer task of the SAGES Fundamentals of Laparoscopic Surgery [9]). The reliability of the public Internet network has recently advanced to a stage where these experiments could safely be arranged. In the meanwhile, the newest data show that the Internet backbone infrastructure is getting overloaded, therefore the lags are increasing [10]. The security of the system should be developed in the future for the protection of the patients (in accordance with IEC 80001-1:2010). Nevertheless, surgeons will have to get prepared for the u se of these robots through special training courses, since the disturbing effect of latency also has to be learnt to tolerate and be compensated by the operator as much as possible.

III. TELEOPERATION SYSTEM COMPONENTS

Just as in the case of other teleoperational systems, surgical robots also have three major components from the modelling and control point of view: master device, slave device and the communication system. On the top of that, the tool–tissue interaction should also be assessed. The modelling of these components is indispensable in order to build a valid simulator for the whole system to observe and analyze certain control attributes and behaviours. These models should be validated independently first, and the modelling error should be examined in each case.

A. *Communication system*

The communication system includes the transmitter, the receiver and the communication medium. These, in total are responsible for the quality of the signals and the latency. The package loss is a generic phenomenon that is better handled by some protocols, such as the *User Datagram Protocol* (UDP) [11].

The communication delay must be kept at a low level, because human can only adapt to a limited amount of time delay, typically max 0.5 s. The first trans-Atlantic telesurgery was built on the *Zeus* robot (Computer Motion, Mountain View, CA) in 2001, where the mean signal delay was 155ms, which is easily adaptable by humans [12]. It was a 85ms lag in signal transmission, while the remaining 70 ms was the encoding and decoding time for the video. Depending on the level of latency, we can talk about three types of technologies:

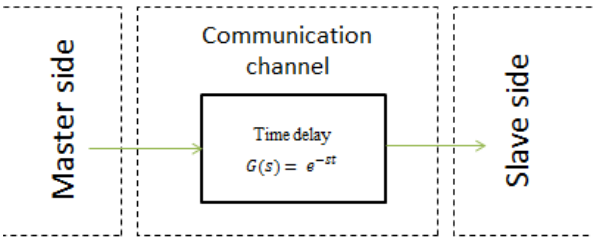

Fig. 2. Block diagram of the time delay model employed in telesurgery robot control.

- Telesurgery (max. 2s)
- Telementoring (max. 50–70s)
- Teleconsultancy (max. 15min)

The effect of time delay could be reduced with latency-tolerant control methods, thus larger distances can be bridged by these systems [12]. To achieve this, robust models of the system components are required. The complete architecture is proposed to be approximated with three models. The master includes the controller and the human operator, which is connected via a high-delay medium to the slave model that covers the intervening master arm. In the deriving cascade setup, the time delay can be partially alleviated using appropriate predictive controllers tuned to the master and slave systems [13].

The simplest possible way to model a T time delay element is described by the following formula [14]:

$$y(t) = u(t - T). \tag{1}$$

For the sake of simplicity, let the input be $u(t) = e^{st}$.Then, the output is given by the following formula:

$$y(t) = y_0 e^{st}. \tag{2}$$

Thus, (1) can be written as follows:

$$y(t) = y_0 s^{st} = e^{s(t-T)} = e^{-sT} \cdot e^{st} = e^{-sT} u(t) \tag{3}$$

The signal delay can be modelled by the $G(s) = e^{-st}$ transfer function, as it has been illustrated in Fig. 2.

B. *Master model*

The master side is where the "*human operator*" or the replacing automatic control device is located. Further, the surgical staff can be found here, providing the control signals for the actuators of the slave. A commonly used human model is the *crossover model* that was developed in the 1960s for fighter pilots 0. It is based on the highly non-linear and time-dependent response of the human body, but it is well-approximated by a quasi-linear model. The model complexity depends on the precision that the execution of the task requires, but the following form provides a reasonably good approximation:

$$H(s) = K_p \cdot \frac{\tau_L s+1}{\tau_I s+1} \cdot \left(\frac{e^{-\tau s}}{\tau_N s+1}\right), \tag{4}$$

where the bracketed term refers to the human physiological limitations. Accordingly, the term$e^{-\tau s}$refers to the signal

delay that occurs during human reaction. The term $\frac{1}{\tau_N s+1}$ represents the neuromuscular system delay.$K_p$is the static gain of the operator, $\frac{1}{\tau_I s+1}$ is the time delay section and the term $\tau_L s+1$ is the control time constant. The model is not extended to all the details of human attributes, such as the subject's motivation, expertise, but the effect of delay can be measured with it. Further, the distorting effects of tiredness, stress needs to be formulated within, adding the effect of time delay on the top. The human operator model proposed is shown in Fig. 3.

Another human operator model was introduced by Ornstein, which is slightly more complex, and it is also applicable for pursuit-type manual tracking tasks [15]:

$$H(s) = \frac{a_1 \cdot s + a_0}{b_2 \cdot s^2 + b_1 \cdot s + b_0} \cdot e^{-s\tau}, \qquad (5)$$

where a_1 arises from the velocity component and τ is the transport delay. The determination of the values of the coefficients was discussed in [15].

The number of parameters represented in the model can make it more sophisticated, allowing one to obtain a more accurate description of basic human behaviour. The neuromuscular limitations can be well-described by certain time delay elements and different dynamic response characteristics [17], while human sensing can be characterized by threshold elements. A variety of sensory input noise is modelled as a member of general signal noise, which can also be used in the modelling of vision. Introducing non-linearity will have similar effect, increasing the complexity.

One of the most applicable non-linear car driver models is the GM/UMTRI model, developed for General Motors. This is an extension of an older quasi-linear UMTRI driver model [18]. The block diagram of the model is shown in Fig.4. These models have been shown to represent the master–slave type telesurgery tasks [19].

IV. SLAVE MODEL

While not all of the latencies can be avoided, empowering the salve system with autonomous capabilities can also improve functionality and safety. Robust control methods may further reduce the effect of latency. Thus, better and more appropriate control for the presented tasks needs to be investigated. The slave robot's kinematic model is typically given to a fine level of details, enabling its integration into kinematic and dynamic models [20], [21].

It is most challenging to gain information about the interactions of the robot arm and the tissue. It is possible to gain this information if force feedback is provided, but among

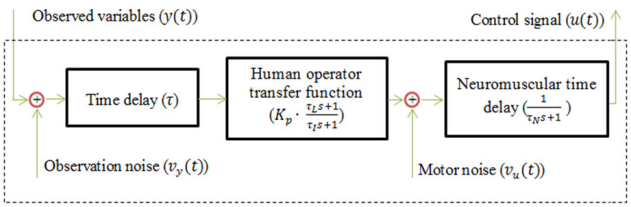

Fig.3. Multivariable, yet one value driven model of a human, operating as a controller.

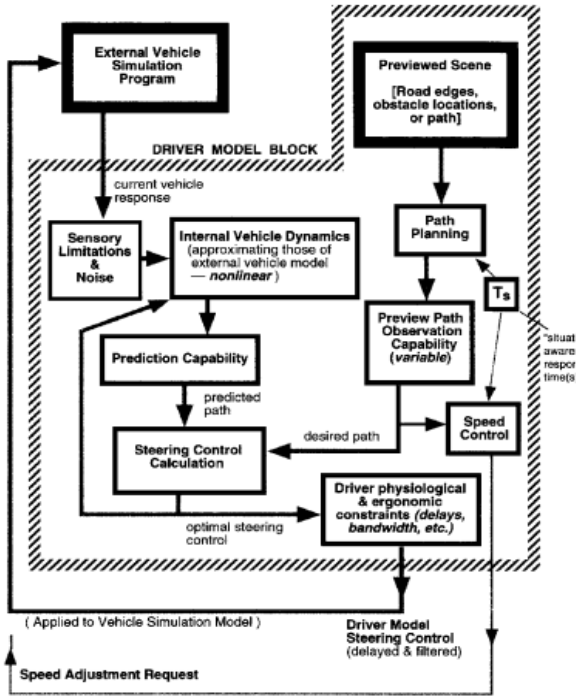

Fig.4. The GM/UMTRI non-linear car driver model, shown to be applicable to robotics surgery [18].

today's surgical robots, this option is not common [22]. Static models may be used instead of the dynamic models, since the effects on tissues are relatively small, due to the fact that current trends are focusing on minimal invasiveness.

Table I. summarizes the most important models used for tool–tissue interaction in surgical robotics, enlisting some of their basic properties. Depending on the surgical device and the complexity of the anatomy, different models are to be chosen.

When choosing a controller for the entire system, all the model parameters should be considered, and in order to increase the robustness, the overall complexity and rank of the models should be kept as low as reasonably possible [13].

V. DISCUSSION

Rapidly developing robotics technology and communication infrastructure boosts telesurgical applications. However, these concepts still need the right choice of models, considering accuracy, robustness and computational requirement. Separate models must be used for the master controller, the robotic arm, operating tool and the tissue itself, whereas the time delay and the lack of adequate feedback greatly affect the controller's performance. As described in this paper, it is typically possible to perform a task based on a simplified, or complex, non-linear models as well, but the increasing complexity and lower performance of the employed control system may not worth it after all.

ACKNOWLEDGMENT

The authors acknowledge the indispensable help of Levente Kovács (Óbuda University) and Radu-Emil Precup ("Politehnica" University of Timisoara) during the research.

Table I List and basic properties of the most commonly employed soft tissue models for robotic surgery applications.

Model number	Used for	Tissue model	Tool model	Feedback type	Sensors	Model complexity	Reference
1	Analyzing transparency under slave link and joint flexibility	Rigid	Linear elastic	Force feedback to user's hand	Position and velocity sensors at tool tip	Varying, from simple to moderate. Determined by the mechanical model of the tool.	Tavakoli*et al.* 2009 [25]
2	Medical training through simulation in virtual reality	Mesh based FEA model, using modal analysis / Real-time method of finite spheres	rigid	Force and torque feedback to user's hand, collision detection and detection of multiple tissue layers	Force and position sensors mounted on the tool, held by the user	The complexity is determined by the level of system reduction / Simple, with minimized computational effort	Basdogan *et al.* 2004 [26]
3	Detecting lumps in organ tissues (kidney, liver, heart)	7 different models, model validation on real tissues	rigid	No feedback to human user	1DoF force feedback from point-to-point palpation	Increased accuracy with model complexity	Yamamoto 2011 [27]
4	Detection of lumps in prostate tissues, definition of forbidden regions for patient-side manipulators	Manufactured artificial tissue based on existing commercially available artificial prostate	rigid	3D visual feedback generated with a stereo-vision system	Position, velocity and force sensors on slave manipulator	Hunt-Crossley, a complex but accurate model	Yamamoto *et al.* 2012 [28]

REFERENCES

[1] T. Haidegger, "Surgical Robot Prototyping—System Development, Assessment and Clearance," ch. 10 in T. Sobh and X. Xiong, Eds. *Prototyping of Robotic Systems: Applications of Design and Implementation* , IGI Book, Bridgeport, CT, pp. 288–326, 2012.

[2] T. Haidegger, J. Sándor and Z. Benyó, "Surgery in Space: the Future of Robotic Telesurgery," *Surgical Endoscopy*, vol. 25, issue: 3, pp. 681–690, 2011.

[3] P. Garcia, J. Rosen, C. Kapoor, M. Noakes, G. Elbert, M. Treat, T. Ganous, M. Hanson, J. Manak, C. Hasser, D. Rohler, and R. Satava, "Trauma pod: a semi-automated telerobotic surgical system," *J. of Medicine*, vol. 5, no. 2, pp. 136–146, 2009.

[4] Mars One press release: "78,000 sign up for one-way mission to Mars" http://mars-one.com; May 7, 2013.

[5] Intuitive Surgical. "Intuitive Surgical Earnings Conference Call". Available: http://edge.media-server.com/m/p/p8h59m89/lan/en, 2013.

[6] E. Flynn,"Telesurgery in the United States". *J. of Homeland Defense*, vol. 6, pp. 24–28, 2005.

[7] C. Nguan, B. Miller, R. Patel et al.,"Preclinical remote telesurgery trial of a da Vinci telesurgery prototype". *Intl. J. of Medical Robotics and Computer Assisted Surgery*, vol. 4, pp. 304–309, 2008.

[8] H. H. King, B. Hannaford, K.-W. Kwok, G.-Z. Yang, P. Griffiths, A. Okamura, et al., "Plugfest 2009: Global interoperability in Telerobotics and telemedicine". *In Proc. of IEEE Intl. Conf. on Robotics and Automation (ICRA)*, Anchorage, pp. 1733–1738, 2010.

[9] N. J. Soper, G. M. Fried, "The Fundamentals of Laparoscopic Surgery". *J. of Gastrointestinal Surgery*, vol. 12, no. 4, pp. 624–628, 2008.

[10] AT&T, "NGlobal Network Latency Averages". Available: ipnetwork.bgtmo.ip.att.net/pws/global_network_avgs.html, 2013.

[11] S. Butner and M. Ghodoussi, "Transforming a surgical robot for human telesurgery," *IEEE Trans. on Robotics and Automation*, vol. 19, no. 5, pp. 818–824, 2003.

[12] T. Haidegger, L. Kovács, R.-E. Precup, B. Benyó, Z. Benyó and S. Preitl, "Simulation and control for telerobots in space medicine," *Acta Astronautica*, vol. 81, issue: 1, pp. 390–402, 2012.

[13] R.-E. Precup, T. Haidegger, L. Kovács, A. S. Paul, S. Preitl and Z. Benyó, "Fuzzy Control Solution for Telesurgical Applications," *Applied and Computational Mathematics. An International Journal (ACM)*, vol. 11, no. 3, pp. 378–397, 2012.

[14] R. M. Murray, "Transfer functions". Course materials. Available: http://www.cds.caltech.edu/~murray/courses/cds101/fa04/caltech/am04_ch6-3nov04.pdf, 2004.

[15] D. L. Kleinman, S. Baron and W. H. Levison, "An optimal control model of human response part I: Theory and validation". *Automatica*, vol. 6, no. 3, pp. 357–369, 1970.

[16] G. N. Ornstein, "The automatic analog determination of human transfer function coefficients." *Medical Electronics and Biological Engineering*, vol. 1, no. 3, pp. 377–387, 1963.

[17] C. C. MacAdam, "Understanding and modeling the human driver". *Vehicle System Dynamics*, vol. 40, no. 1-3, pp. 101–134, 2003.

[18] C. C. MacAdam,: "Development of a Driver Model for Near/At-Limit Vehicle Handling", Technical report, UMTRI-2001-43. Sponsored by the General Motors Corporation, pp. 1–122, 2001.

[19] J. H. Chien, M. M. Tiwari, I. H. Suh, D. Oleynikov and K.-C. Siu, "Accuracy and speed trade-off in robot-assisted surgery," *Intl. J. of Medical Robotics Assisted Surgery*, vol. 6, no. 5, pp. 324–329, 2010.

[20] L. W. Sun, F. Van Meer, Y. Bailly and C. K. Yeung, "Design and development of a Da Vinci surgical system simulator," *In the IEEE Intl. Conf. on Mechatronics and Automation (ICMA)*, pp. 1050–1055, 2007.

[21] A. A. Syed, X. G. Duan, X. Kong, M. Li, Y. Wang, Q. Huang, "6-DOF Maxillofacial Surgical Robotic Manipulator Controlled By Haptic Device," In Proc. of the *9th Intl. Conf. on Ubiquitous Robots and Ambient Intelligence (URAI 2012)*, Daejeon, pp. 71–74, 2012.

[22] C. Liu, P. Moreira, N. Zemiti and P. Poignet, "3D Force Control for Robotic-Assisted Beating Heart Surgery Based on Viscoelastic Tissue Model", *Intl. Conf. of the IEEE Engineeringin Medicine and Biology Society (EMBC)*, Boston, pp. 7054–7058, 2011.

[23] S. Misra, K. T. Ramesh, and Allison M. Okamura, "Modeling of Tool-Tissue Interactions for Computer-Based Surgical Simulation: A Literature Review". *Presence: Teleoperators and Virtual Environments* vol. 17, no. 5, pp. 463–491, 2008.

[24] A. Bolopion and S. Régnier, "A Review of Haptic Feedback Teleoperation Systemsfor Micromanipulation and Microassembly", *IEEE Trans. on Automation Science and Engineering*, vol. 10, no. 3, pp. 496–502, 2013.

[25] M. Tavakoli and R. D. Howe, "Haptic Effects of Surgical Teleoperator Flexibility". *The International Journal of Robotics Research* vol. 28, no.10, pp. 1289–1302, 2009.

[26] C. Basdogan, S. De, J. Kim, M. Muniyandi, H. Kim and M. A. Srinavasan, "Haptics in Minimally Invasive Surgical Simulation and Training", *Haptic Rendering—Beyond Visual Computing*, March/April, pp. 56–64, 2004.

[27] T. Yamamoto, "Applying tissue models in teleoperated robot-assisted surgery", PhD dissertation, The Johns Hopkins University, Baltimore, Maryland, 2011.

[28] T. Yamamoto, N. Abolhassani S. Jung el at., "Augmented reality and haptic interfaces for robot-assisted surgery". *Intl. J. of Medical Robotics and Computer Assisted Surgery*; vol. 8, pp. 45–56, 2012.

3D vessel modeling for diagnosis and training

M. De Piccoli, F. Visentin, D. Zerbato, P. Fiorini
Department of Computer Science, University of Verona
Verona, Italy
Email: michela.depiccoli@univr.it

***Abstract*—Patient specific knowledge of hepatic segmental anatomy is essential to liver therapy and surgical planning. Contrast enhanced computed tomography (CT) is the predominant 3D imaging modality for non-invasive analysis due to its ability to highlight the intra-hepatic vascular network, and distinguish tumor from normal parenchyma. In this clinical context, computer-aided tools can assist diagnostic and therapeutic planning for liver diseases. This leads to a simple three-dimensional visualization of the organ, its vascular system, and the tumor position. The surgeon uses this information during the pre-operative phase to plan the operation. The purpose of this work is to pose the basics for the development of a semi-automated system for the realization of low-cost, deformable, patient-related organs (or part of them) to be used for pre-operative planning and surgical training.**

I. Introduction

A specific planning procedure for tumor resection is a real challenge in oncological liver surgery due to the enormous individual anatomical variability [1]. The liver has a complex internal anatomy consisting of three different vessel systems and the biliary ducts. This intricate three-dimensional configuration makes liver resections a challenging operation. A transection of any of these structures leaves a part of the liver without supply or drainage causing, in the worst case, the death of the patient. However, as introduced by Couinaud in [2], the liver is built on individual anatomical segments, which allow the surgeon to resect specific parts of the liver while maintaining intact its functionalities [3]. This schematic classification divides the liver into eight different segments according to the branching structure of the portal and the hepatic vein. It is a useful tool for surgeons since it allows a better understanding of the intervention environment.

Currently, in addition to the anatomical knowledge, various tools are available for planning a surgical operation. Surgeons can use 3D volumetric rendering (e.g. coming from CT) of the specific area or its physical realistic model that can be bought from synthetic organ manufacturer. The former is a promising tool since it allows a more direct comprehension of the organ's anatomy and so have a more clear planning ability. Despite this, commercially available synthetic organs do not always correctly represent the patient-specific anatomy. To improve surgeon's planning capability a more precise tool has to be produced.

In the following, the different stages for the realization of a low-cost patient-based 3D physical deformable models of the liver's vessel are presented. Figure 1 is depicted a schematic view of the process used. This model is a first step toward the realization of a full organ that can be used for diagnosis and training. The importance of these results can be identified in the reproducibility of the cast anatomical structures (also without the need for expensive 3D printers) and the possibility of having a more realistic surgical mock ups.

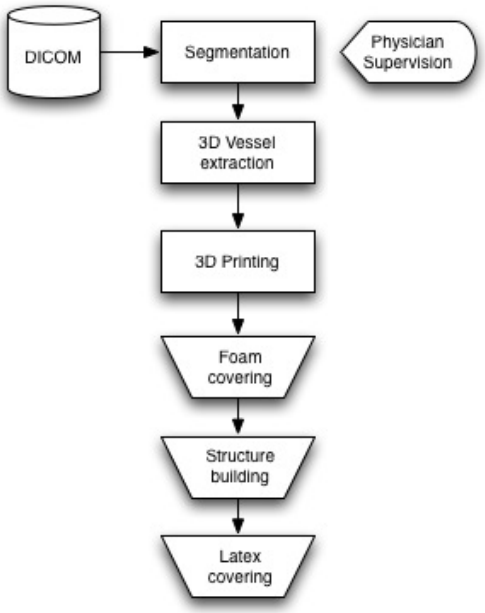

Fig. 1. A schematic view of the realization process. The rectangle shape indicate unsupervised automated action, while trapezoid ones are executed manually by a human operator.

II. Materials and Methods

For simplicity, we considered a non-pathological liver CT data from which we are interested to extract the vessel' structure. We performed a segmentation by applying a set custom-designed MeVisLab [4] block-functions. The first step consist in the identification of the vascular system (made both by vessels and arteries) with its branches. This was done manually by identifying some seed points for the region growing like algorithm. An experienced physician gives as input the few parameters that control the algorithm evolution and acts as a supervisor of the system (i.e. he/she validates the output of this phase). Figure 2 shows the results of the output of this phase.

The result is then used to create a virtual representations

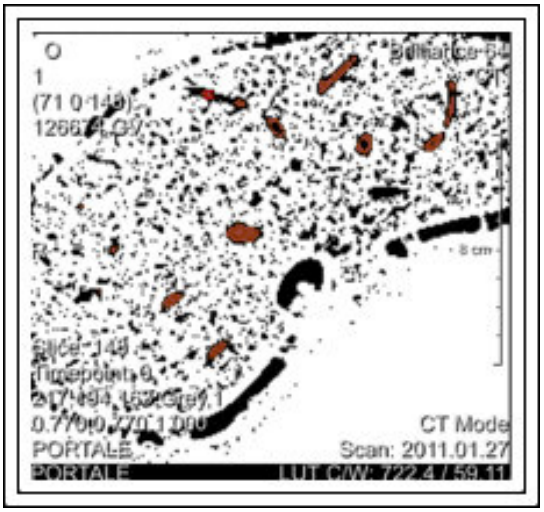

Fig. 2. Output of the region growing segmentation. In the figure the dark area is the liver profile, the red area identifies the vessels segmentation. The white is identify as image background and it is not taken into consideration during the analysis.

Fig. 3. The 3D visualization of the segmented vessels.

of patient anatomy (Fig. 3). It can be used to provide to the surgeon a immediate visualization of the liver's vessel structure. It can be further processed and can be directly used as input for any standard stereo-lithographic printer. This allow to obtain a patient-specific physical rigid model that can be used for planning the surgery. However, due to their stiff structure they can not be used during training. In fact, to effectively support training, the models have to reproduce the physical behavior of real vessels, and deform under the application of external forces given by surgical tools. Thus the synthetic organs should be built with soft materials.

The idea is to retrieve a modular structure from the rigid model previously made and then cover each section with foam rubber. This step allows to obtain a semi-rigid structure that can be placed in shape, with an adequate support system (e.g. metal wires placed within the structure), and permit a easier extraction once the covering material is dry. It is important to chose the most suitable material that will be used to obtain the final model. Among the available ones, we used Prochima's

Fig. 4. The casted model. A 3D latex model.

natural pre-vulcanized latex [5]. Due to the complexity of the structure of the liver's vessel tree (it branches along different planes), to prove the concept, we used a simplified version of it that includes only few branches.

III. Results

The results of the segmentation and 3D model extraction are encouraging. They have been validated by an expert radiologist and thus confirming the correctness of the process. The model obtained by following the presented procedure, although its simplicity, has given promising results. In figure 4 is presented a prototype of the simplified vascular system. The method used to cast the model and the material used have been demonstrated to be suitable to reproduce the structure of the vessels and to ensure their vascularity. Different physicians have considered useful having such model to be used in pre-operative phase, unlike this further analysis related to their usage have not yet been done.

IV. Conclusion and Future Works

Traditional surgical planning uses volumetric information stored in a stack of intensity-based images coming from computerized tomography (CT) or similar imaging methods. The surgeon then uses specific software that displays 2D slices of the volume leaving the surgeons in charges to build its own mental 3D model. This is a difficult task even for experienced surgeons. To help their mental process and to allow them to exhaustively explore the operational area, physical 3D patient-based model can be useful. In addition to this, the models can be used to train surgeons on peculiar situation.

In this paper we proposed a technique for fast prototyping of low-cost, patient-based 3D soft model that can be used during training and pre-operative planning. Starting from CT data, we segment and reconstruct a 3D volumetric model of the liver's vessel system. From that we build a modular structure and then produce a simplified deformable model.

As future work we are interested in considering the realization of the more complex model, i.e. the full liver's vessels tree. In order to archive this goal a (semi-)automatic method, that identify the branches of the vessel, is needed. Its output will help us in the realization process and allow us to produce a more realistic anatomic model.

ACKNOWLEDGMENT

The research leading to these results has received funding from the European Union Seventh Framework Programme (FP7/2007-2013) under grant agreement n°248960 (SAFROS).

REFERENCES

[1] L. S. Friedman, "Surgery in the patient with liver disease," *Trans American Clinical anf Climatological Association*, no. 121, pp. 192–205, 2010.
[2] C. Couinaud, *Le foie: études anatomiques et chirurgicales*. Masson & Cie, 1957.
[3] H. Bismuth, "Surgical anatomy and anatomical surgery of the liver," *World Journal of Surgery*, vol. 6, no. 1, pp. 3–9, 1982.
[4] "Mevislab homepage," http://www.mevislab.de, 2009.
[5] "Prochima homepage," http://www.prochima.com.

State of the art in 3D printing of compliant cardiovascular models: HeartPrint

Material characterization of HeartPrint models and comparison with arterial tissue properties

Katrien Baeck, Patricia Lopes, Peter Verschueren
Materialise NV
Leuven, Belgium
Katrien.Baeck@materialise.be

Giovanni Biglino, Claudio Capelli
Institute for Cardiovascular Science
University College London
London, UK

***Abstract* — Over the years, catheter-based interventions have gained popularity for the treatment of cardiovascular diseases and became daily practice. However, the errors in manual catheter-based interventions remain too high which motivates the use of precisely controlled robotic catheters. CASCADE, a recent EU-funded FP7 project has been set up to investigate autonomous catheter control for endovascular aortic valve replacement procedures. Robotic surgical skills will be learned and assessed on an artificial test-bed which should mimic the anatomy and behavior of the real vasculature. Therefore, this paper presents both the design and the material properties of the 3D printed compliant vascular model used in the test-bed setup. It was found that the HeartPrint™ flex 3D printing process was capable of creating flexible models with a Young's modulus and distensibility that are within the range of human arterial tissue properties. Thus besides the correct anatomical representation of the aorta, the designed model also mimics the material behavior of the real anatomy.**

Keywords—3D printing, cardiovascular, HeartPrint, material characterization

I. INTRODUCTION

Catheter procedures are amongst the most common medical interventions used to treat cardiovascular diseases. However, errors in manual catheter-based interventions remain too high in medical practice [1]. The use of precisely controlled robotic catheters can make an important contribution in this context. A new European research project ("CASCADE", Cognitive AutonomouS CAtheter operating in Dynamic Environments) has been set up in order to advance the treatment of cardiovascular diseases, by providing a new dexterous and intelligent (self-aware, self-exploring) robotic instrument, initially focusing on endovascular aortic valve replacement.

Robotic surgical skills will be learned and assessed on a representative artificial test-bed prior to transferring this to cadavers, animals, and ultimately to patients. The test-bed will further help in the development of techniques for real-time 3D reconstruction and finite element simulation of the vasculature, to investigate safe and reliable exploratory strategies and to validate procedure outcome in terms of successful procedure execution. This test-bed consists of a realistic cardiovascular system, i.e. the bench-top model, along with simple actuation systems to replicate physiological motion due to respiration and the cardiac cycle.

The focus of this paper will be on the design of the bench-top model and its material properties, which ought to be comparable to human artery mechanical properties.

II. MATERIALS AND METHOD

The bench-top model is a transparent, flexible model of the aorta, from the aortic valve to the common iliac artery, and includes the main side branches (Figure 1). Based on a CT scan, the Mimics Innovation Suite® (Materialise, Leuven, Belgium) was used to obtain the virtual 3D reconstructed aortic model and to prepare it in a printable format. Afterwards, the bench-top model is printed using the Materialise HeartPrint™ Flex technique which is capable of 3D printing the model directly from the virtual file. This 3D printing technique has several advantages compared to the traditional method for creating flexible models using the two-step approach of mold making and casting. It is less time consuming and it can go beyond the possibilities of molding for creating highly complex, patient-specific cardiovascular anatomies.

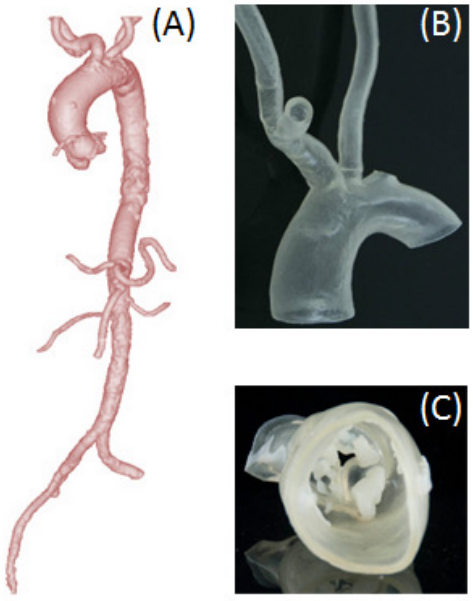

Figure 1: 3D design of the aortic bench-top model (A) and two printed segments of this model, including the aortic arch with carotids (B) as well as the valve with calcifications (C).

In order to verify whether the 3D printed aortic bench-top model mimics the behavior of the real vascular tissue, quantification of the material properties of this HeartPrint^{TM} flex model is necessary. Therefore, based on a set of tensile and compliance tests on small samples, the material properties of the model were defined and compared with human arterial tissue properties.

Five uniaxial tensile tests, as well as 15 compliance tests, were performed to identify the ultimate strength (σ_u, ε_u), Young's modulus (E) and distensibility (D) of the material. The shape and dimensions of the samples are shown in Figure 2. For the tensile test, samples are stretched at 1mm/s and the applied force with the corresponding extension are continuously recorded. For the compliance tests, variations in internal pressure were monitored during a gradual increase and decrease of the internal volume of the samples.

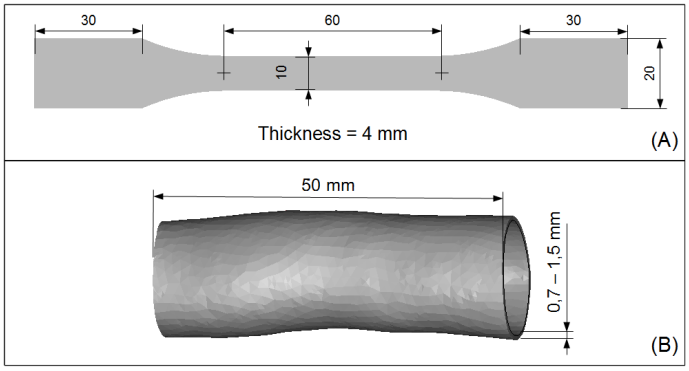

Figure 1: Schematic illustration of the samples for the uniaxial tensile test (A) and the compliance test (B). Dimensions are in mm.

III. RESULTS AND DISCUSSION

The results for the uniaxial tensile test are shown in Figure 3 with ultimate stress and strain values of 1.05 ± 0.17 MPa and 73.19 ± 6.52 % respectively. Since the stress-strain curve of this rubber-like material is highly non-linear, the Young's modulus is calculated for two different sections of the curve. A first value of E is calculated using the secant-method at the points of 5 and 25% strain resulting in an average value of E_1 = 0.91 ± 0.02 MPa. A second value of E is calculated at the point of maximum stress and has an average value of E_2 = 2.06 ± 0.23 MPa. Based on these results, it is observed that the HeartPrint^{TM} Flex samples exhibit a stiffness which is within the range of arterial tissue. Depending on the artery (e.g. aorta, carotids, coronaries) the stiffness can vary substantially, from 0.2 MPa up to about 9 MPa [2, 3].

The results for the compliance tests are shown in Figure 4, with the distensibility of the samples varying between 1.9 – 3.7 x10^{-3} mmHg^{-1} whereby a decrease in wall thickness of the samples corresponds with a decrease in distensibility. This range is comparable to the clinical range of distensibility values for various arteries, such as the ascending and descending aorta, carotid arteries and pulmonary arteries, as shown in Table 1.

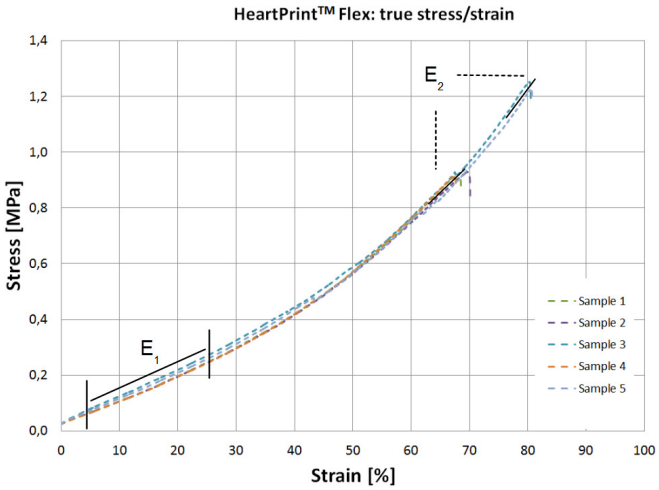

Figure 2: Stress-strain curves of the HeartPrint^{TM} Flex samples obtained during a uniaxial tensile test.

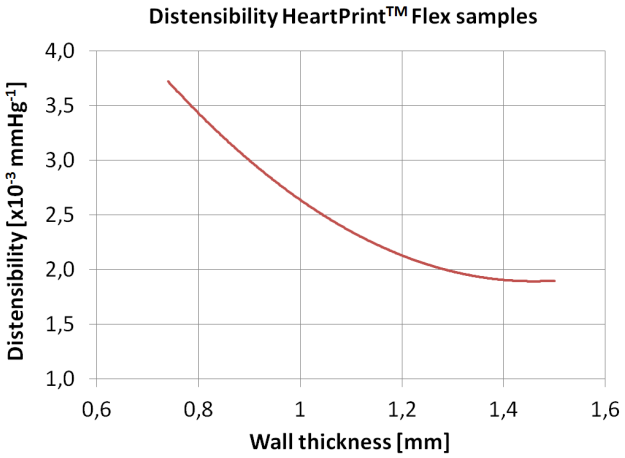

Figure 3: Distensibility of HeartPrintTM Flex samples with different wall thicknesses.

Table 1: Clinical range of distensibility values for arteries such as the ascending and descending aorta, carotids as well as pulmonary arteries, reported by various authors.

Study	Vessel	Distensibility [x10^{-3} mmHg^{-1}]
Chue et al. [4]	Aorta	Asc: 4.1 ± 2.1 Desc: 4.4 ± 1.7
Groenink et al. [5]	Aorta	Asc: 4.4 ± 2.2 Desc: 4.6 ± 1.5
Gan et al. [6]	Pulm. artery	4.6 ± 3.8
Lénárd et al. [7]	Carotid	3.8 ± 1.4 (static) 2.1 ± 0.9 (dynamic)

IV. CONCLUSION

The material properties of the bench-top model were determined and it was found that both Young's modulus and distensibility of the HeartPrint^{TM} Flex model are within the range of human arterial tissue properties. The designed model does therefore not only offer the correct geometry of the aorta,

but it also mimics the material behavior of the real anatomy. These features are needed for training, accurate modeling and validation of the robotic surgical skills, all developed within the framework of the CASCADE-project.

ACKNOWLEDGMENT

The research leading to these results has received funding from the European Union's 7th Framework Programme under EC-GA No. 601021 (CASCADE).

REFERENCES

[1] Kohn et al., To err is human: building a safer health system. National Academy Press, Washington, 2000.

[2] Khamdaeng et al., Arterial stiffness identification of the human carotid artery using the stress–strain relationship in vivo, Ultrasonics, 2012; 52 (3):402- 411.

[3] Duprey et al., In vitro characterisation of physiological and maximum elastic modulus of ascending thoracic aortic aneurysms using uniaxial tensile testing. Eur J Vasc Endovasc Surg. 2010; 39(6):700-7.

[4] Chue et al., Insights into differential regional aortic distensibility in early chronic kidney disease: a cardiac magnetic resonance study. Eur Heart J 2010; 31:143.

[5] Groenink et al., Biophysical properties of the normal-sized aorta in patients with Marfan syndrome: Evaluation with MR flow mapping. Radiology 2001;219:535

[6] Gan et al., Noninvasively assessed pulmonary stiffness predicts mortality in pulmonary arterial hypertension. Chest 2007; 132(6):1906–12.

[7] Lénárd et al., Static versus dynamic distensibility of the carotid artery in humans. J Vasc Res 2000; 37(2):103–11.

Biomechanical simulations, soft tissue phantoms and open data - validating and benchmarking systems for computer assisted minimally invasive surgery

S. Suwelack*, S. Röhl*, S. Bodenstedt*, D. Katic*, H. Kenngott†, B. Mueller-Stich†, A. Wekerle†, M. Wagner†, J. Wünscher†, R. Dillmann*, L. Maier-Hein‡ and S. Speidel*
*Institute for Anthropomatics, Karlsruhe Institute of Technology (KIT)
†Department for General, Visceral and Transplantation Surgery, University Heidelberg
‡ Junior group computer-assisted interventions, Div. of Medical and Biological Informatics, German Cancer Research Center (DKFZ)

***Abstract*—Determining the accuracy of computer assisted surgery (CAS) systems is challenging. This is in particular true in the realm of minimally invasive soft tissue interventions. Here, it is very complicated and sometimes even impossible to obtain reliable in vivo ground truth data. For this reason numerical simulations, organ phantoms and animal experiments are used as a means for validating the accuracy of CAS systems. In this paper, we discuss these common evaluation tools in the context of sensor data processing and registration techniques. Furthermore, we present solutions for mechanically accurate soft tissue phantoms and numerical validation tools for endoscopic surgery. It will become apparent that even when using these strategies the acquisition and processing of suitable evaluation data can be very time consuming. We will thus conclude with a discussion of the need for and core requirements of suitable open repositories for ground truth data.**

I. Introduction

The validation of accuracy is a very important step towards a thorough evaluation for computer assisted surgery systems [7]. It is especially important for algorithms, modules and systems that are in a research or prototype state. In order to provide navigational information to the surgeon CAS systems rely on suitable intraoperative sensors such as tracking systems, endoscopic video or ultrasound data. Typically, complex algorithms for sensor processing and registration techniques are used in order to align pre-operative planning data to the patient based on the sensor information. In this context, the first validations step is to assess the accuracy of each individual component before proceeding to validate the whole system. Validation data can be acquired *in silico*, *in vitro* or *in vivo* including numerical simulations, phantoms or clinical data sets [7].

Until now, numerical environments for *in silico* validation of sensor hardware and processing algorithms are usually restricted to simple synthetic data [5]. Even more elaborate approaches to sensor data simulation are often only used as a means for preliminary validation during development [14].

In contrast, phantom data is widely used for sensor processing validation. Models based on Poly(vinyl alcohol) (PVA-C) can reproduce both the sound and the mechanical properties of human tissue and are suitable for validating ultrasound-based techniques [17]. The properties of the material can be tuned by changing the exact composition of the material and the number of cycles of a freeze-thaw process that is applied during manufacturing. Sufficient experience in handling this substance is required in order to accurately adjust its properties. Silicon phantoms are often used in the context of endoscopic image processing. Examples include phantoms of the heart [13], [16] and the liver [12]. Different paints allow to emulate typical optical properties such as specular reflections. However, it is challenging to reproduce realistic texture patterns in this way.

Animal organs *in vitro* can also be used for accurate validation and benchmarking of image processing techniques in the context of endoscopic interventions [11]. Careful planning and time consuming post processing is required in order to obtain ground truth values using this approach.

For the validation of non-rigid registration techniques it is important to obtain a sufficient dense ground truth of the deformation field. This can be achieved by placing small marker balls inside a phantom [2]. Depending on the scenario, many marker balls are required for this purpose. Thus, it is important to set up the configuration in such a way that the processing of the ground truth data (segmentation, spatio-temporal registration) can be done (semi-)automatically. An important aspect in this application area is the accuracy of the phantom's mechanical behaviour. Kerdok et al. performed the first quantitative analysis by means of force measurements and finite element analysis of appropriate silicon material for simple shapes [9]. More recent results show how phantoms for complex organ geometries can be constructed that provide an adequate accuracy in terms of the mechanical properties [6].

For some interventions, intraoperative volumetric imaging such as cone-beam CT can be used to obtain ground truth data from animal experiments or potentially even during real interventions [4].

Due to advances in simulation technology, components for both real-time simulation of the mechanical behaviour of organs [3] and the accurate ultrasound sensor data are already available [10]. However, currently no system exists that can generate different sensor data and ground truth data for the validation of CAS systems.

In this paper we present ongoing work towards an *in silico* evaluation environment for computer assisted minimally

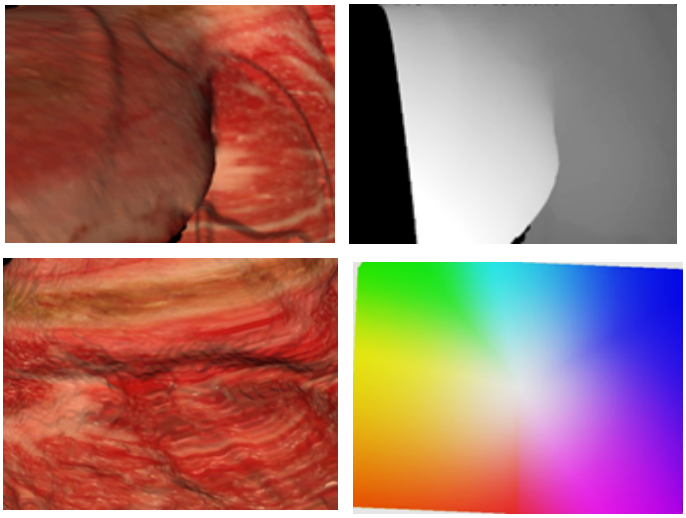

Fig. 1. For each video frame the disparity ground truth between the left and right image is computed (top). Furthermore, the displacement during camera motion or organ deformation is saved and displayed a color coded image (bottom).

invasive surgery. Furthermore, we show how mechanically accurate soft tissue phantoms can be built for validation purposes. Finally, we discuss how such tools and generated data can be made available in open databases.

II. IN SILICO EVALUTION SUITE

We are developing a simulation environment for validating components and systems for computer assisted minimally invasive surgery. The core module of the simulation is an accurate camera model. It can be parameterized to resemble the set-up typically found in different stereo endoscopes. By using realistic organ textures and appropriate lighting models, the optical properties commonly found in endoscopic image sequences (e.g. specular reflections) can be reproduced in sufficient detail for an accurate validation of image processing algorithms. Real-time finite element (FE) techniques are integrated into the model to allow for a realistic deformation of organs in the surgical scene.

The simulation suite generates all necessary ground truth data to validate many image processing (e.g. 3D-reconstructions) and non-rigid registration algorithms. Both the disparity map of the two stereo endoscopic images and the displacement for each pixel in the image over time can be accurately computed using a raycasting algorithm (Fig. 1). Additionally, the deformed organ meshes are saved along with important landmark positions for each timestep in order to evaluate registration results. The numerical simulation is especially useful to assess the sensitivity of algorithms to specific parameters (e.g. camera calibration, noise).

Currently, we are including more relevant sensor data into the simulation tool (e.g. tracking information). In this context we are developing a suitable data format that allows to easily save sensor and ground truth data and to feed the sensor data into the CAS system. Although the simulation runs in real-time, some components for generating and saving ground truth values (e.g. raycasting) do not achieve interactive rates. That's why we are including a tool that allows saving the user interaction (e.g. instrument and camera movement) in order to generate all accurate ground truth computations by re-running the simulation in a non-interactive mode.

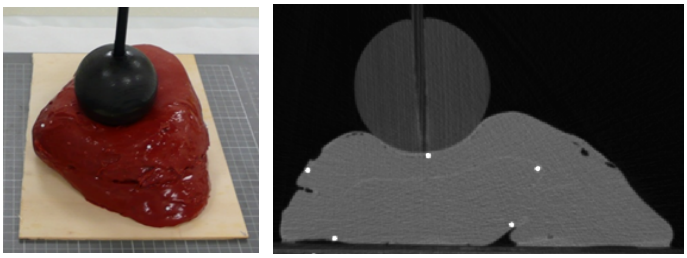

Fig. 2. Liver phantom is deformed in an indentation experiment (left). The deformation can be tracked in CT images using Teflon marker balls (right).

Fig. 3. Upper body phantom build from segmented CT images (left), endoscopic video frame featuring several silicone organs (middle) and corresponding 3D-reconstruction from stereo endoscopic data (right).

III. SOFT TISSUE PHANTOMS

In order to develop mechanically realistic silicon phantoms, we analyzed several different silicon types within an elastometer in order to obtain a database that contains exact material parameters for each silicone. As material models and parameterization for most organs are available in the literature, the database allows selecting suitable silicones for organ phantoms. We use a parameter optimization method on a FE model in order to accurately match different material models. However, silicon exhibits a much more linear behavior than human soft tissue. In order to mimic real tissue behavior over a larger deformation range, the phantoms are equipped with a stiff core and a softer outer region. The stiffness parameters (and thus corresponding silicon types) are again matched using non-linear optimization. More than 100 Teflon balls are inserted into each phantom in order to track the deformation in CT images (Fig. 2).

In order to build a model of the upper body, all major organs were segmented from CT images. A rigid outline of the body as well as bony structures were manufactured using rapid prototyping techniques (Fig, 3). Similarly, molds for each organ were built from the segmented images and silicone organs were cast from these molds. The resulting torso phantom allows simulating more complex deformation pattern and inter-organ interaction. All deformations can be easily tracked in CT images thanks to the markers in the silicone organs. The model thus serves as a very useful validation tool and even offers a cheap, reproducible and accurate alternative to animal experiments for many validation steps.

IV. Discussion

In this paper we presented recent advancements in numerical simulation and accurate organ phantom design for the validation of CAS systems in the realm of minimally invasive surgery. While both techniques have become important tools for CAS validation in the development stage, their design and application is non-trivial and time consuming. Furthermore, the execution and post processing of experimental results from phantom experiments requires not only the access to CT imaging hardware, but also manual effort (e.g. segmentation). Thus we are planning to release an open collection of numerical and experimental phantom data that include accurate ground truth information and are thus suited for accuracy validation.

Having common data sets does not only allow researchers to spend more time on development and less time on validation, but it also allows to benchmark algorithms against each other. In the realm of computer vision, the Middlebury datasets is widely used for that purpose [15]. Although there are few datasets for the validation of CAS components are available (e.g. the Hamlyn Centre endoscopic video datasets [16] and the 3D-IRCAD database [1]), it would be desirable to have a more extensive selection of data. In particular, it would be beneficial to establish a common repository that can serve not only as a central access point for data, but also for benchmark results. As the complexity of the data is growing (e.g. different types of temporally registered sensor data) it is especially important to develop standardized data formats and corresponding processing tools in order to make the data easily accessible.

Naturally, such a repository should not be limited to numerical or phantom data. In the context of image processing (e.g. instrument segmentation) *in vivo* sensor data is often used for qualitative evaluation. In some contexts, manually labeled image data can even serve as a reliable ground truth. Making these kinds of data freely available would significantly speed up the development for many research groups. This is even more true for algorithms that rely on machine learning approaches such as segmentation or situation recognition techniques [8]. In these applications, the acquisition and manual processing of suitable learning and test data often is the most time consuming part of development.

References

[1] 3Dircadb. 3d image reconstruction for comparison of algorithm database. http://www.ircad.fr/softwares/3Dircadb/3Dircadb.php?lng=en, June 2013.

[2] P. Dumpuri, L.W. Clements, B.M. Dawant, and M.I. Miga. Model-updated image-guided liver surgery: Preliminary results using surface characterization. *Progress in biophysics and molecular biology*, 103(2-3):197–207, 2010.

[3] F. Faure, C. Duriez, H. Delingette, J. Allard, B. Gilles, S. Marchesseau, H. Talbot, H. Courtecuisse, G. Bousquet, I. Peterlik, et al. Sofa: A multi-model framework for interactive physical simulation. *Soft Tissue Biomechanical Modeling for Computer Assisted Surgery*, pages 283–321, 2012.

[4] Marco Feuerstein, Thomas Mussack, Sandro Michael Heining, and Nassir Navab. Intraoperative laparoscope augmentation for port placement and resection planning in minimally invasive liver resection. *Medical Imaging, IEEE Transactions on*, 27(3):355–369, 2008.

[5] Mingxing Hu, Graeme Penney, Philip Edwards, Michael Figl, and David J Hawkes. 3d reconstruction of internal organ surfaces for minimal invasive surgery. In *Medical Image Computing and Computer-Assisted Intervention–MICCAI 2007*, pages 68–77. Springer, 2007.

[6] Nikolai Hungr, Jean-Alexandre Long, Vincent Beix, and Jocelyne Troccaz. A realistic deformable prostate phantom for multimodal imaging and needle-insertion procedures. *Medical Physics*, 39:2031, 2012.

[7] Pierre Jannin, Christophe Grova, and Calvin R Maurer Jr. Model for defining and reporting reference-based validation protocols in medical image processing. *International Journal of Computer Assisted Radiology and Surgery*, 1(2):63–73, 2006.

[8] Darko Katić, Anna-Laura Wekerle, Jochen Görtler, Patrick Spengler, Sebastian Bodenstedt, Sebastian Röhl, Stefan Suwelack, Hannes Götz Kenngott, Martin Wagner, Beat Peter Müller-Stich, et al. Context-aware augmented reality in laparoscopic surgery. *Computerized Medical Imaging and Graphics*, 2013.

[9] A.E. Kerdok, S.M. Cotin, M.P. Ottensmeyer, A.M. Galea, R.D. Howe, and S.L. Dawson. Truth cube: Establishing physical standards for soft tissue simulation. *Medical Image Analysis*, 7(3):283–291, 2003.

[10] Oliver Kutter, Ramtin Shams, and Nassir Navab. Visualization and gpu-accelerated simulation of medical ultrasound from ct images. *Computer methods and programs in biomedicine*, 94(3):250–266, 2009.

[11] L Maier-Hein, P Mountney, A Bartoli, H Elhawary, D Elson, A Groch, A Kolb, M Rodrigues, J Sorger, S Speidel, et al. Optical techniques for 3d surface reconstruction in computer-assisted laparoscopic surgery. *Medical Image Analysis*, 2013.

[12] David P Noonan, Peter Mountney, Daniel S Elson, Ara Darzi, and Guang-Zhong Yang. A stereoscopic fibroscope for camera motion and 3d depth recovery during minimally invasive surgery. In *Robotics and Automation, 2009. ICRA'09. IEEE International Conference on*, pages 4463–4468. IEEE, 2009.

[13] Rogério Richa, Philippe Poignet, and Chao Liu. Deformable motion tracking of the heart surface. In *Intelligent Robots and Systems, 2008. IROS 2008. IEEE/RSJ International Conference on*, pages 3997–4003. IEEE, 2008.

[14] S. Röhl, S. Bodenstedt, S. Suwelack, H. Kenngott, B. Mueller-Stich, R. Dillmann, and S. Speidel. Dense gpu-enhanced surface reconstruction from stereo endoscopic images for intraoperative registration. *Medical Physics*, 39(3):1632–45, 2012.

[15] Daniel Scharstein and Richard Szeliski. Middlebury stereo vision page. *Online at http://www. middlebury. edu/stereo*, 2002.

[16] Danail Stoyanov, Marco Visentini Scarzanella, Philip Pratt, and Guang-Zhong Yang. Real-time stereo reconstruction in robotically assisted minimally invasive surgery. In *Proceedings of the 13th international conference on Medical image computing and computer-assisted intervention: Part I*, pages 275–282. Springer-Verlag, 2010.

[17] KJM Surry, HJB Austin, A Fenster, and TM Peters. Poly (vinyl alcohol) cryogel phantoms for use in ultrasound and mr imaging. *Physics in medicine and biology*, 49(24):5529, 2004.

Accurate and Low Cost Training System for Robotic Surgery

Davide Zerbato, Luca Vezzaro, Lorenzo Grespan, Lorenza Gasperotti and Paolo Fiorini
Department of Computer Science
University of Verona
Verona, Italy
Email: davide.zerbato@univr.it

***Abstract*—Surgeons' training is mainly based on a Halstedian apprenticeship model whereby residents learn by directly assisting an experienced surgeon during the intervention and slowly increase their hands-on experience over time. Hands on training is indeed essential for effective training to robotic surgery, however the reservation of the robot for training represents an additional cost that hospitals can hardly afford . A possible solution to this problem is the use of simulators.**

Current surgical simulators have some severe limitations in the realism of the physics simulation provided and this reduces their effectiveness. Improving the realism of physics simulation is thus one of the ways to further increase cos/benefits ratio of simulators.

This paper describes Chiron, a new simulator for robotic surgery which is focused on providing realistic simulations and thus to increase the training outcome. The simulator currently provides more than twenty tasks, some are inspired by the tasks used in current training curricula whereas other have been developed to exploit the specific functionalities of the software and to evaluate users cognitive load. Thanks to the scripting language integrated into the software, it is possible to easily customize all the tasks and to quickly develop new ones following the requirements of several surgery specialization.

The simulator is currently being validated in different hospitals and training centers in Europe and USA.

Fig. 1. Examples of hardware configuration supported by the training system: in foreground a pair of Sensable Phantom Omni plus Zeiss Cinemizer glasses providing 3D vision and in background one Razer Hydra and standard 2D monitor.

I. Introduction

Surgeons training is mainly based on a Halstedian apprenticeship model [1] whereby residents learn by directly assisting an experienced surgeon during the intervention and slowly increase their hands-on experience over time. This approach is difficult to extend to robotic surgery, where only the surgeon (or at most one other person) can actually control the robot and have the stereoscopic view of the intervention area whereas assistants can only have an overall impression of the procedure flow. Hands on training is essential for effective training to robotic surgery, however the reservation of the robot for training represents an additional cost that hospitals can hardly afford [2].

A suitable solution to this problem is the use of simulations. Virtual simulations, in particular, are suited since in robotic surgery the surgeon interacts with the robot console, composed by haptic devices and monitors, which can be easily replicated with lower cost devices. Simulations should reproduce two important aspects of the intervention: the robot, with its kinematics and dynamics properties, and the patient, with anatomy, pathology and, possibly, physiology [3]. The reconstruction and the simulation of complex anatomical scenarios is still an open problem, both from the point of view of modeling but also for computation. Thus virtual simulations often focus on the development of basic skills [4] , which do not require high anatomical realism to be trained as they are more related to the dexterous use of the robot. Virtual simulators demonstrated to effectively support the acquisition of the basic skills required by minimally invasive surgery in a safer, less stressing and cheaper way. Real time data recording constitutes a relevant advantage provided by these tools and makes their application in training and evaluation extremely valuable and effective [5]. However, basic abilities only enable the surgeon to dexterously control the robot but they do not ensure that he/she can carry out a surgical procedure following the right steps, without harming the patient and effectively facing adverse events.

Surgical simulators available on the market [7], [6], [8] suffer from some severe limitations, such as objects intersection, extremely hard constraints between grabbed objects and robots. Moreover simulated surgical tools only reproduce the end part of the actual robot, without modeling the dynamics of the whole robot. These limitations reduce the usefulness of the simulation for procedural abilities. In fact, for a training tool to be effective, it is mandatory to ensure its realism both in terms of robot dexterity and physics realism. The absence of

physics realism in particular can lead the trainee to learn wrong maneuvers. If, for example, the interaction between a suture needle and the tissue being punctured is poorly modeled, the surgeon learns how to move the wrist of the robot, but cannot learn how to actually insert needles without damaging tissues. Another severe limitation of current simulators is their cost effectiveness. A single training station usually costs more than 60 thousand Euros, thus the cost of the training remains high even in presence of these simulators. Improving the realism of physics simulation is one of the ways to make simulators more useful to surgeons. This paper reports on Chiron, a system for robotic surgery training whose primary characteristic is the correctness of physics simulation.

II. Material and Methods

The goal of the work described in this paper is the development of a training system that ensures reduced costs and accuracy in the physics simulation. One of the requisites of the final system is the compatibility with different hardware configurations: this translates into the possibility to adapt it to existing hardware and to provide different levels of realism in the interface in accordance with user proficiency. In fact high realism may impede the learning process in novices because of the cognitive load.

On the software side, the training system must be based on free libraries, to ensure that the cost of the simulator is kept low. The developed simulation software is thus based on on the open source Bullet Physics library [9] and interfaces with many different hardware devices to provide input/output capabilities. The software has a modular architecture with four modules that handle: 1) physics, 2) graphics, 3) haptic devices and 4) logic.

The physics module is the core of the training system: it is in charge of the simulation of the physics phenomena (e.g. interactions between objects, friction, deformations, robot motion) and takes advantage of the functionalities provided by Bullet, i.e. collision detection, constraint solver, rigid body dynamics. The big limitation with Bullet is represented by its poor deformable models. As correctly modeling deformations is one of the key requirements to train surgeons to handle biological tissues and suture threads, Bullet has been extended with support to proprietary deformable models [10]. Thanks to this extension the training system is able to compute the internal strain due to deformations, which means that the simulation can handle tears and rupture of biologic tissues and thread but it can also keep track of the necrosis that is inflicted by user. This, in turns, results in more realistic training scenarios and in more complex and complete evaluation metrics.

The graphics module, instead, renders the interface and the scene to the user. The graphics module gets the description of the scene from the physics module and compute the graphics rendering, with the support for different kinds of stereoscopic visualization. This is required to reproduce the Da Vinci visual experience on different hardware configurations. The graphics module also handles the graphical user interface thus providing information and hints to the user during all the training curriculum.

The haptic module embeds all the routines that handle the input device and translate users movements into actions

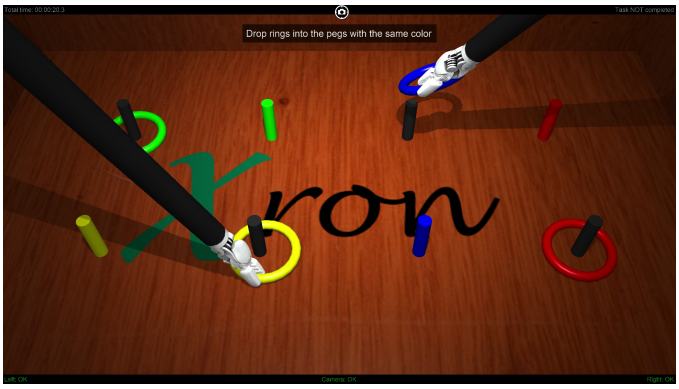

Fig. 2. One of the tasks currently supported by the simulator (Peg transfer) with step-by-step help message.

of the robot. This includes motion scaling, tremor filtering and the actual mapping of users motion into the frame of reference associated to the virtual endoscope. One key aspect of the haptic module is the support for different hardware configurations.

The last module of the training system is the logic module which is in charge of the logics of the training tasks. The training supervisor can, in fact, describe the task goals and the evolution of the environment by defining a finite state machine (FSM) that reacts to user inputs. In this way it is possible to keep track of user performance and errors in the execution of tasks and to generate hints to assist the surgeon during the training. The same scripting language that is used to define the FSM can be used online to customize many aspect of the training tasks or to insert adverse events in the simulation.

III. Results

The training system supports a wide range of hardware devices, thus providing scalable configurations and costs. The software runs on standard modern PCs with Windows 7 or 8 operating system. It supports many different input devices: from the low cost Hydra by Razer to Geomagic Touch, and from Omega by Force Dimension to Freedom 6/7s by MPB. When supported by the hardware device the system can also provide force feedback during the interaction with the virtual environment or to reproduce Da Vinci system behaviors. Thanks to its support to HDMI 1.4 3D rendering the software can take advantage of all the modern 3D monitors and head mounted displays to provide the same stereoscopic view that the surgeon experiences using the Da Vinci. However the simulator is also compatible with older hardware that use the side by side format to encode 3D rendering (see Figure 1).

Chiron currently provides more than twenty tasks, some are inspired by the tasks used in current training curricula (e.g. peg transfer, torn wire, bimanual pick and place - see Figure 2) whereas other have been developed from scratch to exploit the specific functionalities of the software and to evaluate users cognitive load (tasks inspired by Simon electronic game, tasks with random adverse events). It includes realistic anatomies and organs that can be obtained from CT or MRI segmentations with reduced efforts. This allows to reproduce specific anatomies or pathologies (see Figure 3).

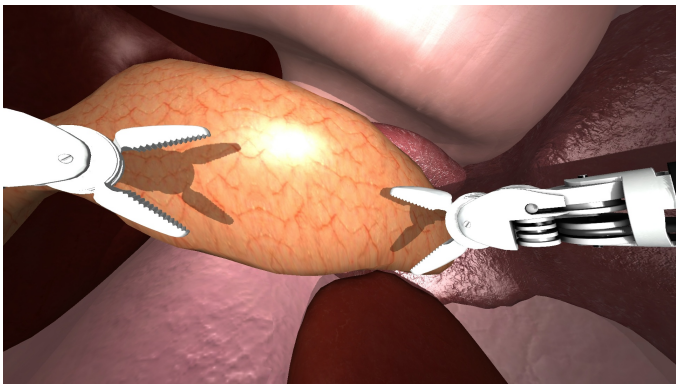

Fig. 3. Reconstruction of a pig abdomen with pancreas in foreground and stomach, liver, spleen and kidneys in background.

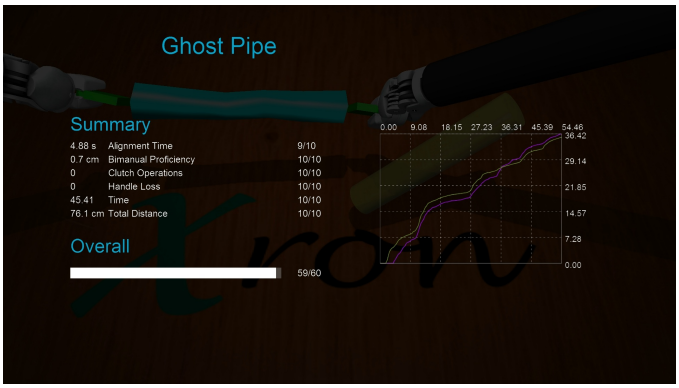

Fig. 4. Screenshot of the final score provided by the system. Along with the overall evaluation the user can understand where he/she can improve and has a graphical representation of the distance covered by each tool.

The scripting language integrated into the software allows to easily extend the training curriculum. In particular it supports the definition of the virtual environment, in terms of number, position and parameters of objects and organs in the scene. It allows determining the logic of the training task, through the design of the FSM that rules the evolution of the environment. Finally, it supports the definition of the metrics and the scoring system that evaluate trainee performances (Figure 4). This results in the possibility to quickly develop new tasks following the requirements of the target surgery specialization.

As a result of its flexibility, Chiron has been used in SAFROS European Project [11] in which it provided the virtual platform for an innovative training curriculum. In addition it is currently in use in several hospitals and training centers around Europe and USA. The validation of the system is ongoing[12]. The simulator is provided for free upon request to interested hospitals or institutions [13].

IV. Discussion and Future Work

The training system described in this paper combines the realism provided by physics engine and the flexibility of modular approach. In particular it features all the benefits of Bullet Physics plus the advantages of proprietary deformable models, and seamlessly interfaces with a number of input/output devices. It is currently being validated in different hospitals and training centers in EU and USA.

Using the same technology other training systems are currently under development, in particular, Chiron has been interfaced with two Simball 4D devices to obtain a laparoscopic surgery training system. A hysteroscopy simulator is also being developed.

Acknowledgment

The research leading to these results has received funding from the European Union Seventh Framework Programme (FP7/2007- 2013) under grant agreement n°248960 (SAFROS).

References

[1] W. Halsted, *The training of the surgeon*, Bulletin of the Johns Hopkins Hospital, 1904.

[2] W.R. Chitwood, L.W. Nifong, W.H. Chapman, J.E. Felger, B.M. Bailey, T. Ballint, K.G. Mendleson, V.B. Kim, J.A. Young and R.A. Albrecht, *Robotic surgical training in an academic institution*, Ann Surg, 234(4), 2001.

[3] S. Hariri, C. Rawn, S. Srivastava, P. Youngblood and A. Ladd, *Evaluation of a surgical t for learning clinical anatomy*, Medical Education. 38(8), p 896-902, 2004.

[4] C.D. Lallas, J.W. Davis and Members of the Society of Urologic Robotic Surgeons *Robotic Surgery Training with Commercially Available Simulation Systems in 2011: A Current Review and Practice Pattern Survey from the Society of Urologic Robotic Surgeons*, J. of Endourology 26 (3), 2012.

[5] K. Kunkler, *The role of medical simulation: an overview*, Int. J. of Medical Robotics and Computer Assisted Surgery 2(3), p 203-210, 2006.

[6] http://www.simulatedsurgicals.com/

[7] http://www.mimicsimulation.com/products/dv-trainer/

[8] http://www.simsurgery.com/robot.html

[9] http://bulletphysics.org/wordpress/

[10] D. Zerbato, D. Baschirotto, D. Baschirotto, D. Botturi and P. Fiorini, *GPU-based physical cut in interactive haptic simulations*, Int. J. of computer assisted radiology and surgery 6 (2), 265-27, 2011.

[11] http://www.safros.eu.

[12] J.A. Sańchez-Margallo, J.B. Pagador Carrasco, L.F. Sańchez Peralta, J.L. Moyano Cuevas, L. Gasperotti, D. Zerbato, L. Vezzaro, F.M. Sańchez-Margallo *A preliminary validation of the Xron surgical simulator for robotic surgery*, Accepted for Int, Conf. of the Society for Medical Innovation and Technology, 2013.

[13] http://metropolis.scienze.univr.it/xron/

Systems for handheld surgical robotics and man-machine OR teams

Auguste van Poelgeest, Dominik Kaltenbacher, Timo Cuntz, Christian Spindler, Arash Sanagoo,
Jonathan Schaechtele and Andreas Rothfuss
Project Group for Automation in Medicine and Biotechnology
Fraunhofer IPA, Mannheim, Germany
Email: auguste.van.poelgeest@ipa.fraunhofer.de

***Abstract*—Medical robotics is an expanding field of research with more certified products entering the market and more technologies being developed. Given the number of surgical specialties and procedures, there is no one solution that would suit all applications. This paper focuses on the requirements and the development of systems for novel techniques in visceral surgery. Here the aim is to design surgical instruments with greater flexibility and degrees of freedom that are still intuitive to use.**

I. Introduction

The use of robot assistance is an increasing market with a lot of growth potential [1]. The only commercially available telerobotic system, namely the da Vinci platform, is still limited with regards to the range of procedures that it can perform [2]. Within this limited range, the number of robotically assisted procedures is increasingly growing regardless of the lack of clinical advantages over manual laparoscopic surgery [3]. The advantages such as 3D visualisation, improved dexterity, surgeon ergonomics and elimination of the fulcrum effect [2] outweigh the disadvantages such as the high cost, bulky size, and lack of tactile feedback [2].

Besides the growth in robot assisted surgery, developments in surgical techniques focus on making minimally invasive surgery even less invasive. This is achieved by Laparoscopic Endoscopic Single Site (LESS) surgery whereby all the instruments and the camera are entered into the patient through a single trocar in the abdominal wall. Another method is to access the abdomen via the esophagus, the rectum or the vagina and inserting the instruments and camera via an incision in one of these structures. For LESS surgery there are a few commercial systems available and various systems being developed [4]. Similarly, there are systems for NOTES available or under development [4].

Technological solutions could bring robot assisted surgery together with techniques such as NOTES to enable the full potential of this novel technique [5]. For LESS surgery there is also a great potential for combination with robot assistance as shown, experimentally by [6]. In this study, customised da Vinci instruments were used to carry out a gall bladder removal. Although feasible, it was evident that the da Vinci system was not designed for such a procedure.

The next sections discuss the requirements of robot assistance systems for NOTES and LESS and proposes technologies and methods to develop solutions that meet these requirements.

II. Requirements

As [7] identified, the instruments need to be more flexible and have a much greater range of motion from the point where they enter the abdomen. Also the instruments should not protrude out of the access port in a straight line more or less parallel to the port, but articulate away from the trocar. Finally, it was argued that if the instruments had different lengths, they could operate in different planes thus avoiding collisions. To be able to carry out standard procedures, the forces that are transferred through the instrument should not differ from those measured during ”normal” laparoscopic procedures. This means that the small flexible instruments should be able to transfer forces of approximately 30N [8]. With these force magnitudes, it is important that the surgeon has some tactile feedback in the instrument handle. The lack of haptic feedback has been identified as a current weakness of robot assisted systems. Experimental work has shown that the precision and control of instruments and flexible endoscopes is vastly improved by this feedback [9], [10]. Finally, the whole system consisting of instruments and their holders, a camera and its holder and the user interface devices should be small and light, and ideally be hand-held.

III. Solutions

A novel system where a robot and a surgeon work together to carry out LESS or NOTES surgery requires a number of technological advances. The instruments need to be highly manoeuvrable, generate relatively large forces for their size and ideally have flexible supply lines. This has led to the development of small hydraulic actuators.

Prototypes of miniature hydraulic cylinders and pneumatic muscles, see figure 1, have been manufactured from off-the-shelf components. Both actuator types were tested to establish the maximum pressure they could withstand, their force generation capacity, stroke, and in case of the cylinder, friction. The hydraulic cylinder had a piston diameter of 2.7mm and was sealed with an o-ring. It withstood pressures up to 200

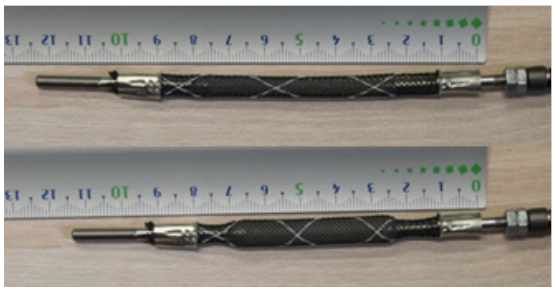

Fig. 1. Example of flexible, energy dense, pneumatic muscle actuator made from off-the-shelf components

Fig. 2. Parallel kinematic system for instruments and scopes

bar at which point a force of 94N was measured. The seal friction at this presssure was measured at 2N, which was lower than expected from an o-ring. The working fluid was medical white oil, which is the hydraulic fluid that is proposed for the novel instruments. The pneumatic muscle prototypes were tested with both air and water as their working fluid. They could not withstand high pressures such as the cylinder: the connection between the flexible tube and the pressure supply would start to look. Nevertheless, a muscle actuator with an inner tube diameter of 1.5mm and outer tube diameter of 2.5mm tested with water generated a force of 30N with a supply pressure of 9 bar. These results have indicated that hydraulic drives are appropriate for this application. Another advantage of hydraulics provides is that the supply pressure is a direct indicator of the force generated at the instrument tip. In other words, this type of actuation enables a simple and safe implementation of haptic feedback. Finally, for robotic applications, hydraulics also have the advantage that its dynamics are well understood as well as potential friction losses. This means that robot control systems can be developed rapidly and with a high level of certainty.

To hold and move instruments or cameras, a spherical parallel kinematic system has been developed, see figure 2. It is small for the range of motion it has, the parallel arms ensure increased robustness over a serial kinematic system and the pivot point of the instrument motion is mechanically defined. Its kinematic and dynamic characteristics are currently being analysed and the design is being optimised for a range of parameters. One of these parameters is the range of motion. Ideally, this is a large as possible inside the patient, but as small as possible outside the patient. Another parameter is the sensitivity and relative linearity between the motion of the drives and the motion of the instrument. Here the ideal case is that the drive requires a large displacement for the instrument to move by a small amount. The goal is to find the best compromise between these optimisation parameters, which can be conflicting.

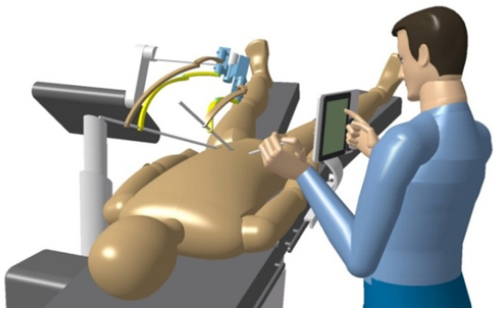

Fig. 3. Example of a Man-Machine Team

Once all the components have been characterised and optimised, the goal is to integrate them into a flexible surgical robotic assistance system. Starting with a typical laparoscopic intervention with 4 incisions, the parallel kinematic system is used to hold the endoscope and one rigid instrument while the surgeon holds the two other instruments. The challenge is to develop a user interaction method for handsfree control of the camera angle and rigid instrument orientation. The next step is combine the components to enable Single Port surgery. The two parallel assistive robots need to be dimensioned to ensure maximum motion while avoiding collisions. In this application, the surgeon will require flexible instruments to reach all structures. These are the flexible handheld instruments descibed previously with equiped mechatronic input devices. Figure 3 illustrates this vision.

IV. Conclusion

There is a great potential to develop technology for man-machine OR teams that have been designed to carry out novel operating techniques such as NOTES and LESS. This type of system has many requirements to meet, but they can be addressed by developing modular solutions for the instruments, the instrument manipulators and the user interfaces and all the other components. These modular solutions can finally be combined to form a flexible, small and lightweight, user-friendly assembly that can be used for routine as well as complex surgeries. Hydraulic actuators form part of this modular solution to provide more flexibility to the system, while meeting the force generation requirements. Parallel kinematic devices form the basis of the small and lightweight instrument manipulator modules. Both these modular systems have so far shown promising results.

V. Future Work

Once the modules for the instruments and their parallel robot manipulators are finished, the challenge is to ensure

their interaction with the user is intuitive. The first step is to establish what constitutes a good interface. For this purpose, computer models and real-time simulations will be used, so various input device prototypes can be tested rapidly without needing to adapt the instruments and their drives to all the different interfaces. The next step will be to integrate all the modules to demonstrate the feasibility of handheld mechatronic instrument systems and man-machine surgical teams.

ACKNOWLEDGMENT

The authors would like to thank the department of Baden Wuerttemberg for the financial support as well as the students that have contributed to the research.

REFERENCES

[1] Frost & Sullivan. (2013) Image-guided and robot-assisted surgery market in western europe: Market grows despite skepticism over proven advantages of robotics. [Online]. Available: http://www.frost.com/c/10024/sublib/display-report.do?id=M8BC-01-00-00-00

[2] H. W. Schreuder and R. H. Verheijen, "Robotic surgery," *BJOG: An International Journal of Obstetrics & Gynaecology*, vol. 116, no. 2, pp. 198–213, 2009.

[3] H. G. Kenngott, L. Fischer, F. Nickel, J. Rom, J. Rassweiler, and B. P. Müller-Stich, "Status of robotic assistance—a less traumatic and more accurate minimally invasive surgery?" *Langenbeck's Archives of Surgery*, vol. 397, no. 3, pp. 333–341, 2012.

[4] E. O. Olweny, S. L. Best, C. R. Tracy, and J. A. Cadeddu, "New technology and applied research: what the future holds for less and notes," *Archivos españoles de urología*, vol. 65, no. 3, pp. 434–443, 2012.

[5] D. Canes, A. C. Lehman, S. M. Farritor, D. Oleynikov, and M. M. Desai, "The future of notes instrumentation: Flexible robotics and in vivo minirobots," *Journal of endourology / Endourological Society*, vol. 23, no. 5, pp. 787–792, 2009.

[6] A. Balaphas, M. E. Hagen, N. C. Buchs, F. Pugin, F. Volonté, I. Inan, and P. Morel, "Robotic laparoendoscopy single site surgery: a transdisciplinary review," *The International Journal of Medical Robotics and Computer Assisted Surgery*, vol. 9, no. 1, pp. 1–11, 2013.

[7] J. R. Romanelli and D. B. Earle, "Single-port laparoscopic surgery: an overview," *Surgical Endoscopy*, vol. 23, no. 7, pp. 1419–1427, 2009.

[8] J. Rosen, B. Hannaford, C. Richards, and M. Sinanan, "Markov modeling of minimally invasive surgery based on tool/tissue interaction and force/torque signatures for evaluating surgical skills," *IEEE Transactions on Biomedical Engineering*, vol. 48, no. 5, pp. 579–591, 2001.

[9] R. Reilink, S. Stramigioli, A. M. Kappers, and S. Misra, "Evaluation of flexible endoscope steering using haptic guidance," *The International Journal of Medical Robotics and Computer Assisted Surgery*, vol. 7, no. 2, pp. 178–186, 2011.

[10] R. Reilink, A. M. L. Kappers, S. Stramigioli, and S. Misra, "Evaluation of robotically controlled advanced endoscopic instruments," *The International Journal of Medical Robotics and Computer Assisted Surgery*, p. n/a, 2013.

Low invasive therapy under robotic guidance in the vascular district: a case study

A computer-assisted robotic platform for soft-wired therapy of vascular obstructions

Selene Tognarelli, Piero Miloro, Antonella Verbeni, Marco Mura, Andrea Cafarelli, Gastone Ciuti, Paolo Dario, Arianna Menciassi*
The BioRobotics Institute, Scuola Superiore Sant'Anna (SSSA), Pontedera (PI), Italy
*corresponding author: a.menciassi@sssup.it

***Abstract*—Integration between surgery and robotics leads to new paradigms in clinical field. Innovative robotic solutions represent the enabling technology for highly targeted therapeutic actions, such as operating in the cardiovascular system. In this framework, the authors present a robotic platform for the treatment of vascular obstructions. It integrates a system for locomotion and navigation based on magnetic dragging and ultrasound tracking and a therapeutic module which involves mechanical attack to the obstruction by means of high intensity focused ultrasound. The system overview and the technical and theoretical instruments for developing the overall platform were illustrated; preliminary results, together with future planned works, are reported in order to demonstrate the feasibility of the proposed approach.**

Keywords—robotic magnetic guidance, cardiovascular therapy, robotic-assisted surgery, ultrasound-based tracking.

I. INTRODUCTION

In the last decade, surgery and robotics have reached a maturity which has allowed them to be safely translated in a new kind of operating room [1]. However, medical robotics is a young and relatively unexplored research field where the enabling technologies continue to evolve, leading to even new interventional scenarios. For instance, there has been a recent trend away from autonomous or semiautonomous surgical robots, toward synergistic manipulation and virtual fixtures [2]. Thus, the robot acts as a guidance tool, providing information to keep the surgeon on target, yet guaranteeing accurate tissue localization thanks to advanced imaging solutions.

Cardiovascular system offers a perfect room for such innovations. Different platforms and strategies are under development worldwide (e.g. [3]): robotic wireless or softly tethered approaches could answer the quest for miniaturization, and interesting devices have been already developed by exploiting the knowledge gained in different setting [4]. However, due to challenging environmental conditions (physiological flows and reduced length scales), transferring the same technologies into the vascular system is not straightforward. Moreover, locomotion and tracking into the vascular system are still ongoing research issues [5-7]. Finally, as regards therapeutic strategies, removing vascular obstructions is a dynamic field of research and different approaches have been proposed in the latest years [8]. Keeping in mind potentials, challenges and limitations of robotic approaches, we present here the system design and initial investigations of an innovative computer-assisted robotic platform for the treatment of vascular occlusions. The proposed platform integrates safe navigation solutions with advanced therapeutic strategies. More in details, the platform (Fig. 1) consists of two robotic arms, respectively holding an external permanent magnet (EPM) and an ultrasound (US) probe. The EPM drags an internal softly-tethered magnetic unit, while US provides the tracking of the device with the help of pre-operative imaging. A low level control ensures that the endovascular device is constantly in the US field of view and that the movement of the device is consistent with the desired path. Once the occlusion is reached, the device will be able to release micro-bubbles to facilitate lysis through an external high intensity focused US high intensity focused ultrasound (HIFU) transducer, which is expected to be integrated with the diagnostic/tracking probe. Micro-agents can be released from the magnetic device via the micro-tether, which will also act as a retrieval system for safety. It is worth remarking that the micro-tether will not have any structural function, thus preventing damage to the internal walls of the vessel and increasing system flexibility and steerability. Debris resulting from the action of US lysis should be smaller than red blood cells in order to be absorbed by the reticuloendothelial system; however, some large fragments can detach, thus causing risk of embolization. In our platform the fragments of blood clots, properly functionalized, will be collected and dragged to a safe area for further removal.

Based on the target pathologies and the actual capabilities of driving a softly-tethered magnetic device, the current platform will mainly address carotid arteries and vessels of the lower limbs.

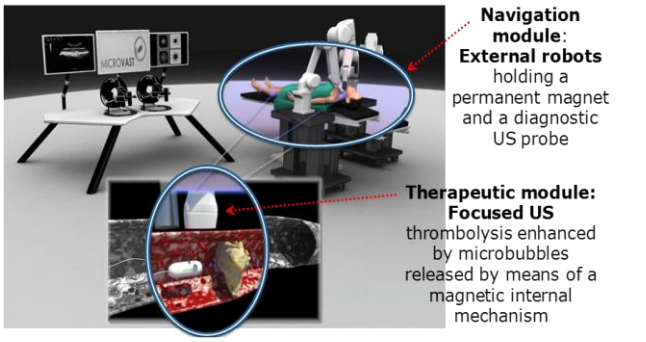

Fig. 1. Schematic representation of the computer-assisted robotic platform for softly-tethered therapy of vascular obstructions and operative modules.

This work is supported by Cassa di Risparmio di Pisa in the framework of MicroVAST (Microsystem for Vascular diagnostics and inTervention) project.

II. System Overview and Preliminary Results

In this section we discuss in details both the navigation and therapeutic modules of the proposed platform by highlighting the main features of the system and giving some preliminary results aiming to demonstrate the feasibility of the entire system.

A. Navigation module: locomotion and tracking

Combining the benefits of robot-aided magnetic navigation and US imaging, a methodology based on traditional Computer-Assisted Surgery (CAS) adapted to intravascular medical procedures has been developed for locomotion and tracking purposes. US-based intra-operative data, together with pre-operative lumen centerline reconstruction for optimal path definition, represent the navigation workflow for assisted or completely autonomous safe propulsion of an endoluminal device in cardiovascular procedures.

As schematically illustrated in Fig. 2, the robotic module for vascular navigation is composed by an EPM attached to the end-effector of a 6 Degrees of Freedom (DoFs) anthropomorphic robotic arm (RV-3SB, Mitsubishi Electric, Japan); a second anthropomorphic robotic arm with 6 DoFs (RV-6SL; Mitsubishi Electric) for holding and moving a US probe (CA430E; Esaote, Italy) for autonomous US-based servoing control; a human–machine interface (HMI) including an intuitive control peripheral; a softly-tethered endoluminal device with an internal permanent magnet (IPM). The interaction between the EPM and the IPM of the endovascular device is employed for propelling the softly-tethered endoluminal robot along the cardiovascular system while locomotion is supervised by the US-based methodology. In particular, an axially magnetized NdFeB N52 (remanence 1.48T) permanent magnet (KJ Magnetics, Jamison, USA) was selected as the EPM. It is 51mm in diameter, 25mm in thickness, and 0.4kg in weight. A rapid prototype miniaturized capsule (5mm in diameter, 10.6mm in length, and 0.75g in weight) equipped with a NdFeB N52 IPM, made up of 6 tablets, was developed as a first prototype for the vascular platform evaluation phase. Each tablet is axially magnetized; it has a diameter of 3.2mm and a thickness of 1.6mm [9]. The second robotic arm holds a US probe for a US-based control. The US probe is a convex array transducer with a working frequency between 3.5 and 5MHz and a radius of curvature of 40mm. With the aforementioned US system, an accuracy of about 0.2mm is derived by the entire acquisition and processing pipeline [10]. In case of assisted propulsion navigation modality, the operator can drive the system through a haptic input device (Phantom-Omni, Sensable Technologies, Wilmington, MA, USA) imposing motion commands to the robotic arm used for holding, moving, and orienting the EPM, while the second robot (holding the US probe) follows the motion of the endoluminal device for tracking purposes. In both the navigation modalities, the US-based tracking algorithm represents the navigation closed-loop control core for maintaining a reliable and effective magnetic link along the procedure. It consists of the tracking of the internal device by using a combination of features detection, optical flow and segmentation techniques. In particular, the algorithm segments the endoluminal device. On the segmented region of interest, the extraction of the object features and the knowledge of the

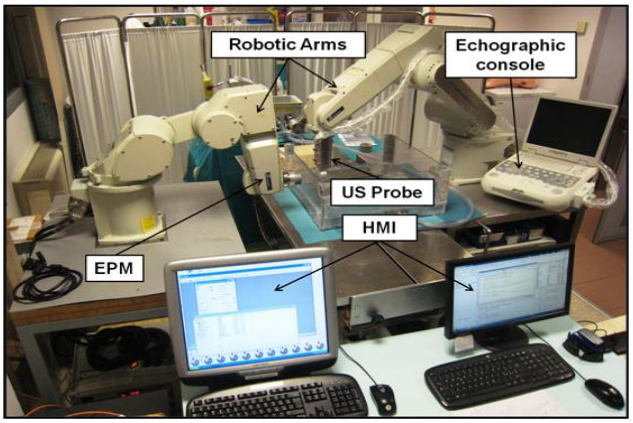

Fig. 2. Representation of the navigation module components.

intrinsic features dynamic state allow for the tracking of the object position and definition of the propulsion behavior. The US-based control loop is iterated until the end of the medical procedure in combination with the locomotion module for the cooperative control of the two robots. The two manipulators are moved together along the calculated pre-operative vascular path while a high-level algorithm calculates the endoluminal robot displacement and compares the device position with respect to an imposed action region centered in the US frame. If the endovascular device exceeds the imposed safe area, the procedure is retrieved in the previous state in order to maintain or to re-establish a reliable magnetic link.

Several preliminary trials were performed by dragging the magnetic capsule along an *in-vitro* vascular 3D mock-up by the dedicated software implementation, and tracking the endoluminal device by means of the US images mode control. The effectiveness of the magnetic dragging in well-defined operative conditions and the validation of the tracking of the device by the US-based algorithm have been assessed. The magnetic device was dragged by the EPM, in no-flow condition, with a velocity of 5mm/s and an average control loop time of 40ms, due to the US image acquisition frame rate. The tracking mode control algorithm enables a reliable trace of the endoscopic device and the accomplishment of the vascular task in the *in-vitro* conditions (Fig. 3).

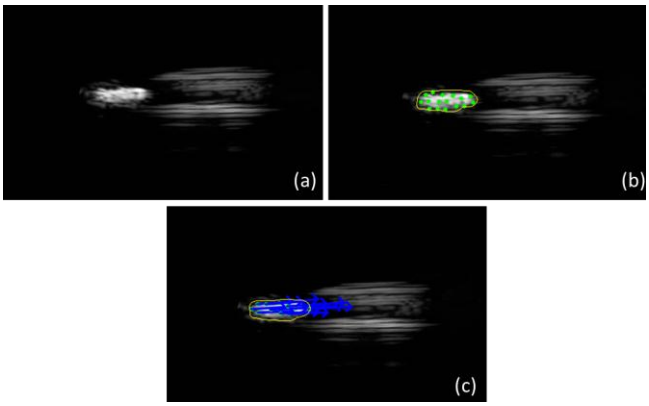

Fig. 3. US images of the tracking algorithm; the device at (a) $t=t_0$ and at (b) $t=t_0+\delta t$ is shown, where the detected features are represented in green while the segmented shape with the yellow line. The derived displacement of the selected features is visualized in (c) with blue arrows.

B. *Therapeutic module*

The aim of the therapeutic module is to remove vascular obstructions in order to restore physiological blood flow. Physical constraints of the environment and the required dimensions for magnetic locomotion make all those therapeutic strategies which demand bulky tools not suitable candidates. Considering the non-invasive, precise and fast dynamics of their action, external US are deemed to be an appropriate solution. The effectiveness of US in destroying thrombi has been demonstrated in several works (e.g. [11]) and important results have been achieved, mainly as an enhancement of chemical attack (by the addiction of thrombolytic drugs), both *in-vitro* and within some sound clinical trials [12]. However, limitations are related to the use of thrombolytic drugs, mainly due to their systemic effects. US thrombolysis without thrombolytic drugs has been proposed to overcome this limitation [13]. An in-house system has been developed to validate the therapeutic action of US in thrombolysis and to correlate the exposition dose to the generated effect. The system is able to map the US field generated by a commercial acoustic transducer. The acoustic field is generated by a HIFU transducer (Precision Acoustics, UK) with 1MHz center frequency, whose acoustic power can reach 85W in the focus; it is in series connected with a power amplifier (240L, Electronics & Innovation, USA) and a wave generator (33220A, Agilent Technologies, USA). A 0.2mm PVDF needle hydrophone (Precision Acoustics) is used to detect the pressure signal, transferred to an oscilloscope (InfiniiVision 7014A, Agilent Technologies, USA). The needle hydrophone is mounted on a 3 axis step-by-step motorized positioning frame (XXYZ BiSlide, Velmex) with a full range of approximately 500x1000x500mm^3 and a precision of 6µm. Wave generation, hydrophone position and signal acquisition are controlled and synchronized remotely by a home-made LabView (National Instruments, USA) interface. A 2D scan has been carried out by positioning the hydrophone parallel to the beam axis and measuring the pressure on an half-plane (axial-symmetry has been previously demonstrated by a 3D scan). This scan allows mapping the acoustic field around the focus in a y-x plane of 70x5mm with pitches of 0.5mm and 0.1mm respectively on beam axis and on its perpendicular direction. Data acquired are post-processed in MatLab (MathWorks, USA) environment. Electric signal is converted to pressure taking into account the hydrophone sensitivity at the center frequency. Results (Fig. 4) show the cigar-shape of the HIFU beam, with a focal length (-6dB) of 24.36mm and a focal diameter of 2.94mm. The scans are performed using low intensities (up to approx. 4W) in order to avoid to damage the hydrophone. For input power of 1W I_{SPTP} (Spatial Peak Time Peak Intensity) and I_{SATP} (Spatial Averaged Time Peak Intensity) are respectively 57.2W/cm^2 and 31.3W/cm^2.

Preliminary tests on porcine, human and fibrin clots have been carried out exploiting the presented setup. Human clots are obtained by collecting them into citrate vacutainers and then treating the blood with $CaCl_2$ and thrombin, while fibrin clots are obtained by simply mixing *in-vitro* fibrin and clotting factors. Porcine clots are obtained from spontaneous coagulation of fresh blood taken from local slaughterhouse; porcine clots have similar acoustic properties of human clots [14].

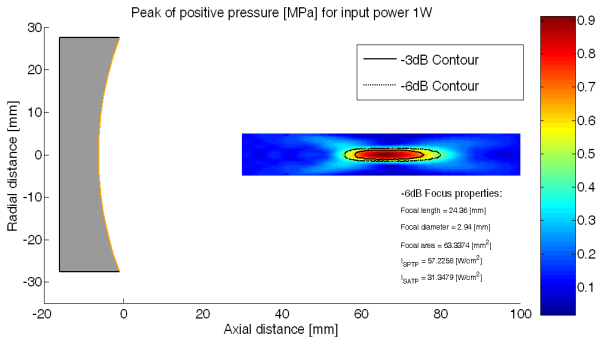

Fig. 4. Cigar-shape of the HIFU beam.

The different blood clots were placed in a low-density Polyethylene (LDPE) tube, with inner diameter of 7mm and thickness of 0.5mm. LDPE has been chosen because of its similar acoustic impedance with respect to water. A flow system has been included and all the experiments were carried out under a flow of water of 2ml/min. Acoustic parameters are reported in Table 1. They have been chosen basing on previous literature experiments [13] and on the specifications of the transducer. These parameters showed their efficacy in considerably reduce clot size in the proposed time. Fig. 5 shows the results in form of screenshots taken at 0s, 30s, 60s, 90s and 120s for human and porcine blood clots.

TABLE I. ACOUSTIC PARAMETERS FOR US THROMBOLYSIS TESTS

Frequency	Acoustic Power	Pulse Length	Duty Cycle	Treatment duration
1MHz	65W	450µs	10%	120s

Furthermore, physical mechanism on the basis of thrombus dissolution must be investigated in order to optimize the therapy, in particular for augmenting thrombolytic efficiency while avoiding damage to healthy tissues. Bioeffects of US include a plethora of phenomena, which usually contribute to the final result. Among these, thermal and cavitational effects are credited to play a major role. In US thrombolysis thermal damage is considered a drawback. However traditional methodologies for thermal measurement (i.e. thermocouples [15] or pulse-echo ultrasound [16]) are not applicable for the proposed experiments, so that qualitative assessment is commonly considered [13, 17].

In order to evaluate thermal effects, experiments have been carried out on porcine blood clots, shaped in order to fill the entire sample holder. Tests have been carried out keeping constant the quantity of energy delivered to the target, while varying the duty cycle from 0% (control) to 100% (continuous wave), and subsequently varying the duration of the treatment. Visual analysis and optical microscope (HiroxKH7700) zoom

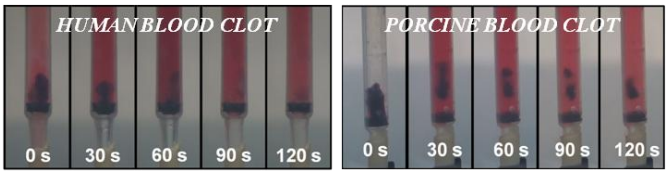

Fig. 5. Screenschoot of human and porcine thombi during US exposure.

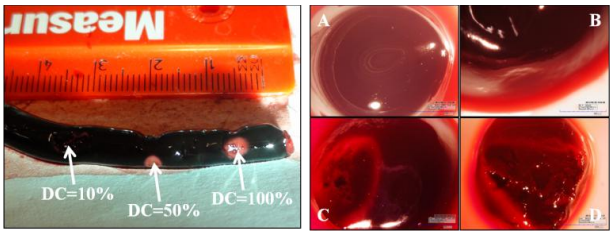

Fig. 6. Qualitative assessment of thermal damage, (left) treated porcine clot; (right) 0%(A), 10%(B), 50%(C), 100%(D) duty cycle treated section.

20x, (Fig. 6) show evidence of thermal damage for continuous and 50% duty cycle (DC) waves, while for the exploited parameters only evidence of surface erosion can be identified. Basing on these considerations, a passive cavitation detection (PCD) system has been implemented, in order to determine whether cavitational effects are present. As a matter of fact, by measuring the acoustic emission from oscillating/collapsing microbubbles, it is possible to determine and quantify the presence of cavitational effects.

III. Conclusions and Discussions

Frontier research in the management of vascular obstructions poses very challenging medical and technological problems and the quest for innovative strategies/platforms is continuously increasing. The here proposed platform includes some innovative solutions for navigation and therapy. Preliminary results show the feasibility of the proposed solution: the traditional CAS architecture was adapted to intravascular medical procedures and the feasibility of magnetic navigation and US tracking was assessed. Future works are planned for employing a 3D US system (in replacement to the 2D probe) for preoperative vascular tract reconstruction and intraoperative vessels registration and endoluminal probe tracking. The US thrombolysis setup demonstrates the ability to accurately map the acoustic field on the transducer axis and US thrombolysis efficacy was established. Future works aim at correlating the cavitational dose to thrombolytic efficiency: if this correlation exists, therapy could be optimized for enhancing cavitational effects.

New platforms such as the one proposed in this paper, which cannot exist without the fully exploitation of robotic strategies, will be developed over the next 10 years. The scenario including a multi-robotic platform paves the way for the reduction of invasiveness of surgical interventions and personalized medicine. The ideal and paradigmatic example of minimally invasive surgery (MIS) leads to the concept of therapy completely non-invasive, such as, for example, in focused ultrasound surgery (FUS), which involves the transmission of acoustic energy through the body from an external source. FUS is already used in several clinical applications, but it suffers from some drawbacks and limitations which narrow the applicability to non-moving and non-essential organs, mainly under guidance of magnetic resonance (MR). Developing an autonomous and human-supervised robotic platform to perform a completely non-invasive therapy by means of FUS will allow to overcome the current drawback of this technology. The robustness, safety, and accuracy of FUS procedures will be enhanced by exploiting robotic assistance, by using real-time therapy monitoring and self-learning procedures as closed-loop control. It is worthy to mention that this innovative application could be considered a step towards the real implementation of multifunctional and versatile robotic platforms for healthcare applications.

References

[1] R. Satava, Cybersurgery: Advanced Technologies for Surgical Practice, John Wiley & Sons, Inc.: New York, 1997.

[2] A. R. Beasley, Medical Robots: Current Systems and Research Directions, Journal of Robotics, vol. 2, pp. 1-14, 2012.

[3] S. Park and J. O. Park, "Frontier Research Program on Biomedical Microrobot for Intravascular Therapy," in Proc. 2nd IEEE Ras & Embs International Conf. on Biomedical Robotics and Biomechatronics, Scottsdale, 2008, pp. 360-365.

[4] G. Ciuti, A. Menciassi, and P. Dario, "Capsule Endoscopy: From Current Achievements to Open Challenges," IEEE Rev Biomed Eng, vol. 4, pp. 59-72, 2011.

[5] S. Martel, M. Mohammadi, O. Felfoul, Z. Lu, and P. Pouponneau, "Flagellated Magnetotactic Bacteria as Controlled MRI-trackable Propulsion and Steering Systems for Medical Nanorobots Operating in the Human Microvasculature," Int J Rob Res, vol. 28, pp. 571-582, Apr 2009.

[6] L. Arcese, A. Cherry, M. Fruchard, and A. Ferreira, "Optimal trajectory for a microrobot navigating in blood vessels," in Proc. Ann. International Conf. of the IEEE Engineering in Medicine and Biology Society, Buenos Aires, 2010, pp. 1950-1953.

[7] B. J. Nelson, I. K. Kaliakatsos, and J. J. Abbott, "Microrobots for Minimally Invasive Medicine," Annu Rev Biomed Eng, vol. 12, pp. 55-85, 2010.

[8] P. Miloro, E. Sinibaldi, A. Menciassi, and P. Dario, "Removing Vascular Obstructions: a challenge, yet of opportunity for interventional microdevices," Biomed Microdevices, vol. 14(3), pp. 511-32, 2012.

[9] S. Tognarelli, et al. " Magnetic propulsion and ultrasound tracking of endovascular devices", *J Robotic Surg* vol. 6, pp.5–12, 2012.

[10] P. Miloro, et al., " An innovative platform for treatment of vascular obstructions: system design and preliminary results ", EEE/RAS-EMBS International Conference on Biomedical Robotics and Biomechatronics (BioRob 2012), pp. 731-737, 2012.

[11] B. Petit, F. Yan, F. Tranquart, and E. Allemann, "Microbubbles and ultrasound-mediated thrombolysis: a review of recent in vitro studies," *J. Drug Deliv. Sci. Technol.*, vol. 22, pp. 381-392, 2012.

[12] E. Bor-Seng-Shu, R. D. Nogueira, E. G. Figueiredo, E. F. Evaristo, A. B. Conforto, and M. J. Teixeira, "Sonothrombolysis for acute ischemic stroke: a systematic review of randomized controlled trials," *Neurosurg. Focus*, vol. 32, 2012.

[13] U. Rosenschein, V. Furman, E. Kerner, I. Fabian, J. Bernheim, and Y. Eshel, "Ultrasound imaging-guided noninvasive ultrasound thrombolysis - Preclinical results," *Circulation*, vol. 102, pp. 238-245, 2000

[14] V. M. Nahirnyak, S. W. Yoon, and C. K. Holland, "Acousto-mechanical and thermal properties of clotted blood," *J Acoust Soc Am*, vol. 119, pp. 3766-3772, 2006.

[15] H. Morris, I. Rivens, A. Shaw, and G. ter Haar, "Investigation of the viscous heating artefact arising from the use of thermocouples in a focused ultrasound field," *Phys Med Biol*, vol. 53, pp. 4759-4776, 2008.

[16] C. Simon, P. VanBaren, and E. S. Ebbini, "Two-dimensional temperature estimation using diagnostic ultrasound," vol. 45, pp. 1088-1099, 1998.

[17] A. D. Maxwell, G. Owens, H. S. Gurm, K. Ives, D. D. Myers Jr, and Z. Xu, "Noninvasive Treatment of Deep Venous Thrombosis Using Pulsed Ultrasound Cavitation Therapy (Histotripsy) in a Porcine Model," *J Vasc Interv Radiol*, vol. 22, pp. 369-377, 2011.

Medrobotics FLEX System

Marco A. Zenati M.D., M.Sc., FETCS
Department of Cardiothoracic Surgery, BHS and Harvard Medical School
Boston, Massachusetts, USA Marco_Zenati@hms.harvard.edu

***Abstract*— Medrobotics' FLEX System is a novel endoscopic platform that has been successfully introduced in cardiovascular and more recently in oropharynx and hypopharynx procedures. Preliminary clinical experience shows promise as a surgical tool in head and neck oncology.**

Keywords—minimally invasive surgery; single port surgery; NOTES; surgery

I. INTRODUCTION

The Medrobotics' FLEX System™ (Medrobotics Inc., Raynham, MA, USA) is a highly articulated platform that features a multilink endoscope allowing minimally invasive procedures in target organs located deep within the body and otherwise difficult or previously impossible to reach through a single port. The FLEX system contains multiple open accessory channels to accept a variety of compatible flexible surgical and interventional instruments as well as on-board visualization. The platform is self-supported and enables physicians to drive and navigate through non-linear circuitous paths, and through a single access point into the body. The FLEX system's flexibility and motion is gained from its numerous mechanical linkages (>30) with two concentric mechanisms. Each mechanism can be placed into a rigid or flexible state. By employing a patented "follow-the-leader" movement strategy with these two alternate states (rigid or flexible), FLEX can be directed into any shape through the relative orientation of its linkages.

The multi-jointed FLEX System Scope component is disposable to ensure sterility, whereas the physician console and feeder unit are reusable. In addition to the core system there are a number of accessories: (i) a support stand, which attaches to the operating table and enables easy positioning of the Scope into the clinical site of interest; (ii) a camera system, incorporated into the distal tip, employs a near high-definition CMOS camera and LED lamps for high-quality visualization of the site of interest; and (iii) 3rd party hand-held compatible flexible instruments, allowing rotation and articulation, in addition to triangulation towards the site of interest. The surgeon retains tactile feedback from the instruments, enabling more efficient and safe retraction, dissection, and excision of tissue for the desired clinical application. A key distinguishing feature of the FLEX System Scope is that it contains multiple degrees of freedom distributed across its length and it is self-supporting. When compared to the 7 degrees of freedom of movement possible using the human arm, the FLEX's

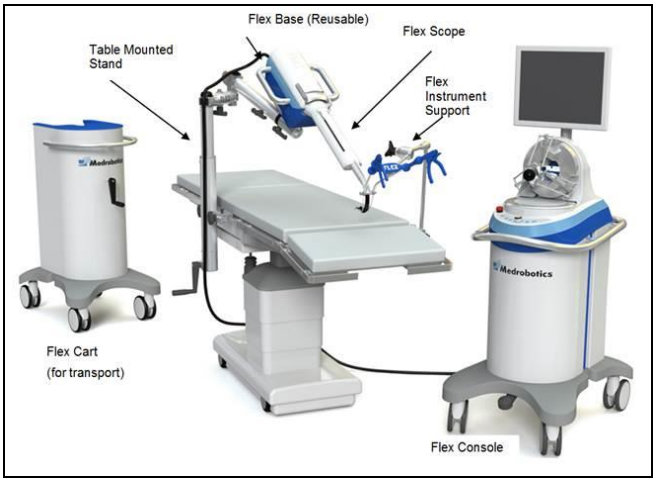

Figure 1. Medrobotics FLEX System

greater than 30 degrees of freedom enhance the physician's ability to access, visualize, and with 3rd party tool perform interventions in hard to reach anatomic targets. The FLEX system accepts an operator-defined input to generate a unique shape in 3D space. The FLEX can track along this curvilinear 3D path and return to points along the path or take a new shape as defined by the operator. One shape can be "remembered" at a time. This core property allows the FLEX to work outside the constraints of a natural lumen, such as the oropharynx, or on the surface of an organ, such as the heart. The FLEX's exact shape and location can remain static allowing it to hover in place without any tremor while delicate procedures are being performed at its distal end, and then automatically retract along the exact same path from where it came to protect the delicate anatomic structures and surrounding tissues from compression or friction damage. Additionally, the FLEX not only

supports its own weight but can support additional loads via instruments delivered through its channels for dissection or retraction. Conversely, the FLEX can become limp, allowing it to take the shape of the surrounding structures. In this state the FLEX will lie in a hand as a soft braided rope, which is an important safety feature.

II. Pre-clinical and Clinical Experience

A. Cardiovascular Applications

The first report of pre-clinical cardiac applications of the FLEX System prototype in a porcine preparation was published by Zenati and Choset in 2006 and referred to as the "CardioARM" system [1]. The first human use (FHU) trial of the clinical prototype of the FLEX System was initiated in February 2010 and successfully completed in June 2010 with a total of three patients having been enrolled [2]. The FHU procedures were all performed in Prague, Czech Republic with approval from the local Institutional Review Board by Drs Neuzil (cardiac electrophysiologist) and Czerny (cardiac surgeon). The physicians were able to perform all elements of the clinical protocol without incident and the cases were completed in less than 5 hours from initial access to skin closure per approved protocol. All patients were discharged home 1–2 days later without any adverse events reported. During these procedures, a J&J CARTO mapping and ablation catheter was used successfully through the FLEX's instrument channel. Up to 200 recordings from the patient's beating heart surface using the CARTO mapping electrodes demonstrated that the FLEX system could be safely manipulated within the pericardial space from a small single subxiphoid port and over the heart's ventricular surfaces in a human with no induced hemodynamic changes in the heart. The clinical prototype of the FLEX was also able to integrate well with high-tech imaging modalities frequently used by interventionalists, such as intracardiac echocardiography (ICE), fluoroscopy, electroanatomic mapping (CARTO), and direct endoscopic visualization.

The portfolio of cardiovascular diagnostic and therapeutic applications of the FLEX system include epicardial beating heart atrial and ventricular mapping and ablation, epicardial injections of stem cells or tissue-engineered scaffolds for regeneration, delivery of left atrial appendage closure devices, pacing leads, etc. [3]

B. Eye, Ear & Throat (ENT) Applications

Unhindered access to the laryngopharynx is best achieved with a flexible instrument that can be introduced through the oral cavity. Although the FLEX system was originally designed for cardiac procedures, the robot has 102 degree-of-freedom and a snakelike advancement mechanism capable of steering a nonlinear, self-supported path also in other organ spaces within the body. Accordingly the FLEX Scope was modified and transformed into the Medrobotics FLEX System, developed specifically for use in applications requiring nonlinear access such as transoral surgery [4]. This flexible platform drives a chip-on-tip endoscope through nonlinear pathways, and provides a platform for the delivery of compatible flexible instruments. In a recently published study, the utility of the Medrobotics FLEX System for visualization and access to areas normally difficult to reach within the laryngopharyngeal complex was demonstrated. Feasibility of access and visualization without the use of suspension laryngoscopy, which comes with its own associated risks and disadvantages including dental injury, lingual nerve injury, and additional operative time, was confirmed. The FLEX System was also found capable to act as an appropriate platform for 3rd party compatible instruments, allowing successful surgical resections in the upper aerodigestive site.

The most recent iteration of the Medrobotics FLEX System for ENT applications consists of 50 discrete linkages that are capable of rotating 13 degrees with respect to each other. The leading linkage, that is, the most distal linkage, is controlled by the surgeon. Using the joystick-like control handle, the leading linkage is pointed in the desired direction and advanced millimeters at a time along the directed vector. The remaining linkages of the flexible Scope are also advanced, following the precise pathway of the leading linkage in a ''follow- the-leader'' fashion. The leading linkage serves as the housing for important surgical hardware including a camera, LED lamps, lens washer, and two external accessory channels. The system's two-dimensional video is captured via a specialized ''chip-on-a-stick -type'' scope embedded in the distal end of the device, and thus the camera position and orientation corresponds to the controlled position of the distal linkage of the FLEX Scope. Fixed into this linkage, the camera can be moved from side to side, up and down, and the image rotated upon its axis. The camera can also be controlled to zoom digitally. The video is then relayed to a high-definition, two-dimensional video screen. Compatible flexible instruments can be inserted through the accessory channels for tissue manipulation. Instruments are passed through the accessory channels and are manipulated manually by the surgeon with two hands without requiring instrument crossing, thus preserving instinctively and natural control.

REFERENCES

[1] A. Degani, H Choset, A. Wolf, T. Ota, M.A. Zenati. Percutaneous intrapericardial interventions using a highly articulated robotic probe. *Proceedings, First IEEE/EBIB International Conference on Biomedical Robotics and Biomechatronics* (BioRob'06) Pisa, Italy 2006, pp. 7-12 DOI 10.1109/BIOROB.2006.1639051

[2] P. Neuzil, V. Reddy, M.A. Zenati, R. Kuenzler, O. Svanidze. Single port subxiphoid access epicardial ablation using a snake robotic system. *Proceedings, International Society for Minimally Invasive Cardiac Surgery* (ISMICS), 2010 Annual Meeting, Berlin, Germany, June 2010

[3] T. Ota, et al., A highly articulated robotic surgical system for minimally invasive surgery. *Annals of Thoracic Surgery* vol 87, pp.1253-1256, 2009

[4] P.J. Johnson, C.M. Rivera Serrano, et al. Demonstration of transoral surgery in cadaveric specimens with the Medrobotics Flex system. *Laryngoscope* 123:1168-1172, 2013.

Stiffness-controllable octopus-like robot arm for minimally invasive surgery

Allen Jiang, Emanuele Secco, Helge Wurdemann,
Thrishantha Nanayakkara, Kaspar Althoefer
Centre for Robotics Research
Department of Informatics
King's College London
London WC2R 2LS, UK
k.althoefer@kcl.ac.uk

Prokar Dasgupta
MRC Centre for Transplantation
NIHR Biomedical Research Centre
Guy's Hospital, King's College London
London SE1 9RT, UK

***Abstract* – We are presenting a new concept for a robot arm design that can change its structure from complete soft to stiff. The proposed system makes use of the principle of granular jamming: A granule-filled membrane is soft and flexible when the pressure inside the membrane is higher or equal to the outside pressure; however, lowering the pressure inside below the outside pressure jams granules into each other, hence, increasing the stiffness of the structure. Employing this principle, we create low cost, variable stiffness manipulation systems that have great application potential, as for example in the field of minimally invasive surgery. Employing granular jamming, our approach can be used to create controllable-stiffness tools covering the whole spectrum of current surgical manipulation devices – from laparoscopes (straight and rigid) to endoscopes (flexible and soft). Combining the granular jamming manipulation system with end effector tools such as a camera or a gripper, this overall system can fit through a Trocar port and bend around organs in a patient's abdominal cavity providing the surgeon with improved views or a retraction aid.**

Keywords—variable and controllable stiffness, granular jamming, soft robot manipulator, octopus-like, camera/retraction system.

I. INTRODUCTION

Successful and safe laparoscopic and endoscopic surgery is heavily dependent on its vision system, with the primary emphasis on the viewing angle and image stability [1]. Today's laparoscopic instruments are typically long, rigid tubes that have poor accessibility to target areas and often require a second surgeon to aid during the overall procedure. There is a noticeable trend towards natural orifice translumenal endoscopic surgery (NOTES); hence, a number of surgeons prefer flexible endoscopes over the traditional rigid laparoscopes for the operations to be conducted. However, these endoscopes were originally designed for intralumenal use, and tend to be application specific [1]. Thus, there is a technological and clinical need for small, flexible manipulation systems designed for NOTES and other minimally invasive surgical procedures, incorporating retractors, cameras and possibly other elements such as miniaturized force sensors [2].

Our approach – inspired by the biological counterpart: the octopus – aims to bridge these gaps. Our octopus-inspired manipulation device is a 10 mm diameter robot that can alter its body stiffness from being flexible to rigid via granular jamming. Most commonly seen in vacuum packed bags of rice or coffee, granular jamming is a phenomenon where a multitude of particles normally act like a fluid, but lock into a solid-like state when an external stress is applied [3],[4]. Thus, our device is naturally compliant and can be pushed into position by the surgeon's laparoscopic tools, then it can lock its current position when a differential between the internal and external pressure is applied; we achieve this by vacuuming the interior of the robot's membrane.

Fig. 1. An octopus entering a narrow opening.

Fig. 2. A schematic drawing of our low cost, granular jamming-based flexible laparaoscopic camera. Shown here its ability to access difficult areas, while occupying only 4 mm of trocar port space.

This variable stiffness mechanism not only provides the surgeon with a wide viewing angle and accessibility when the robot manipulator is flexible, but also a stable platform once stiffened [5]. Although it requires pneumatic tubing and a tether for video cables and possibly gripper actuation, the entire cable and tube bundle (for our robot that has a camera integrated) is only 4 mm in diameter. The design of the robot allows the manipulator to be deployed into the body cavity, thus only occupying 4 mm of trocar port space after initial insertion, a significant improvement over current endoscopes.

II. Methodology

The octopus-inspired robot manipulator, seen in Figs. 2 and 3, is 10 mm in diameter, composed of three 65 mm long segments filled with 1.5 mm diameter plastic spherical granules, and followed by a 4 mm tether. The outer membrane is made with a 0.12 mm thick PVC film. The section dividers are ABS plastic and were printed with a rapid prototyping machine. The tip camera is a 10 mm diameter CMOS sensor with a 640x480 resolution at 30 frames per second and was connected to a computer via USB. Vacuum pressure is achieved with a Mastercool 90066-2V-220 pump, and measured by a Honeywell 0-30 PSI absolute pressure sensor.

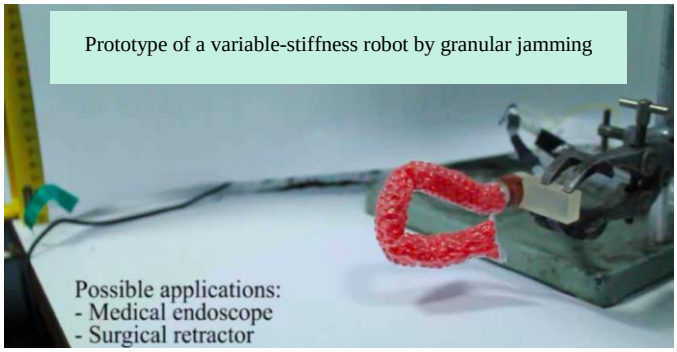

Fig. 3. Here, jamming the granules locks the manipulator into its rigid state, and holding a 180 degree bend. The flexibility and variable stiffness of the camera system allows surgeons to navigate to a area of interest and lock the camera or attached gripper in the position.

III. Experimental Results

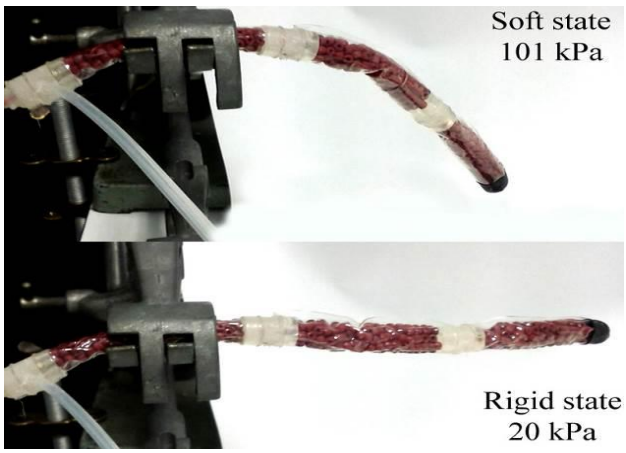

Fig. 4. The granular jamming manipulator bending due to weight when soft (top) vs holding a horizontal position when stiff (bottom).

Other researchers utilizing granular jamming have shown that ground coffee is the ideal granule type for jamming [6]. However, in medical applications, concerns for using organic materials in a surgical system lead to tests to examine if there is a plastic substitute. The synthetic substitute would need to match the stiffness of ground coffee and withstand an autoclave, the most common method of disinfection. We conducted a number of force tests. Our results show that, after deflected, one segment can exhibit 0.20 N of force at 101 kPa (soft state) and 0.42 N at 20 kPa (rigid state). Fig. 4 visually shows what these stiffness values represent: the varied ability to hold the manipulator system in a horizontal position. Thus, the rigidified octopus limb is a stable platform. Bending tests performed evaluating the performance profiles of ground coffee and plastic spheres for granular jamming show that a synthetic substitute achieves improved stiffness.

IV. Conclussions

This paper presents a new type of NOTES-orientated robotic manipulation system whose stiffness can be varied, and, is deployable and low cost. The total cost of the camera-equipped manipulator, excluding the vacuum pump, is approximately 20 GBP, 50 times less than traditional laparoscopes. Though some preliminary sterilization tests have been performed for the granules, they have not been done for the manipulator as a unit. Currently, the positioning of the camera can be done by the surgeon's laparoscopic tools, reducing the need for a "cameraman."

Future works will involve adding a high definition camera, increasing the stiffness range of the manipulator arm, adding an integrated actuation system, and testing it in-vivo. The integration of gripping mechanisms will be explored.

Acknowledgment

This work was funded in part by the Seventh Framework Programme of the European Commission under grant agreements 287728 in the framework of EU project STIFF-FLOP and 270138 in the framework of EU project DARWIN, as well as by the National Institute for Health Research (NIHR) Biomedical Research Centre based at Guy's and St Thomas' NHS Foundation Trust and King's College London.

References

[1] Chang, Victoria C., et al. "A Randomized Comparison of Laparoscopic, Flexible Endoscopic… Cameras..." Surgical innovation (2012).

[2] Polygerinos, P, Zbyszewski, D, Schaeffter, T, Razavi, R, Seneviratne, L.D, Althoefer, K, "MRI-compatible fiber-optic force sensors for catheterization procedures", IEEE Sensors Journal, **10**(10): 1598-1608, 2010.

[3] Liu, Andrea J., and Sidney R. Nagel. "Jamming is not just cool any more." Nature 396.6706 (1998): 21-22.

[4] Aste, Tomaso, and Denis Weaire. The Pursuit of Perfect Packing. New York: Taylor & Francis, 2008. Print.

[5] Loeve, Arjo, Paul Breedveld, and Jenny Dankelman. "Scopes too flexible... and too stiff." Pulse, IEEE 1.3 (2010): 26-41.

[6] Cheng, Nadia G., et al. "Design and Analysis of a Robust, Low-cost, Highly Articulated manipulator enabled by jamming of granular media." ICRA, 2012. IEEE, 2012.

A modular soft manipulator with variable stiffness

Tommaso Ranzani, Matteo Cianchetti, Giada Gerboni, Iris De Falco, Gianluigi Petroni, Arianna Menciassi
The BioRobotics Institute
Scuola Superiore Sant'Anna
Pontedera (PI), Italy
t.ranzani@sssup.it

***Abstract*— This paper presents the design of a single module composing a modular soft variable stiffness manipulator for minimal access surgery. The module exploits flexible fluidic actuation for obtaining multi directional bending and elongation capabilities. A novel flexible crimped braided sheath is introduced in order to increase the performances of the flexible actuator. Granular jamming based stiffening mechanism is used to tune the stiffness of the module. The fabrication of the module is described and the performances in terms of bending, elongation and stiffening are reported.**

Keywords— Surgical manipulator; soft manipulator; variable stiffness; minimally invasive surgery; flexible fluidic actuator; granular jamming; crimped braided structure

I. INTRODUCTION

Among the innovative tools for Minimally Invasive Surgery (MIS) [1] flexible tools represent a promising solution to overcome the limitations of current instrumentation [2]. Flexible endoscopes can be used for endoluminal and transluminal surgery since they allow reaching the surgical target from a remote insertion trocar or a natural orifice. However endoscopes may lack stability that rigid tools normally provide [3] and the achievable dexterity is still limited to the distal end.

Continuum manipulators consent to fully control their shape taking advantage of robotic technology, enabling the surgeon to perform challenging tasks not only in endoscopy but even in surgery, in a minimally invasive way [2]. Such systems are able to pass through obstructed and tortuous passages to reach the surgical target. Due to their unique features they have been proposed for different body districts like abdomen [4], heart [5], throat [6] and brain [7]. The aforementioned systems are mainly externally actuated and generally have an underactuated structure with a compliant backbone [8], which often results in low stiffness at the end effector. The lack of possibility to control the stiffness of the structure may limit the performances and the possible tasks achievable by such highly dexterous structures as shown in [8]. Various stiffening mechanisms for medical instruments have been developed in literature and have been extensively reviewed in [3]. For continuum like structures different rigidity control strategies have been applied such as phase change polymers [9], interlocking fibers [10], granular [12] or layer jamming [13] and systems based on cable tensioning [14]. Most of them can provide an on/off behavior with the exception of cable tensioning that by the way may suffer of backlashes and requires powerful actuators located in a proximal position. Layer and granular jamming seem promising technologies since they can provide tunable stiffness and still can be integrated in continuum like structures.

The work described in this paper is supported by the STIFF-FLOP project grant from the European Communities Seventh Framework Programme under grant agreement 287728.

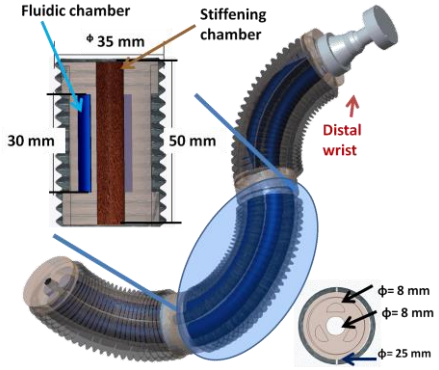

Fig. 1. Achitecture of the STIFF-FLOP arm and dimensions of a single module. On the left inset section of the single module, on the right inset cross section of the module.

Biological manipulators, such as the octopus arm and the elephant trunk, are considered an interesting source of inspiration, because they can manipulate objects while controlling the stiffness of selected body parts and being inherently compliant when interacting with objects [15]. Several soft manipulators were developed trying to emulate the capability that biological manipulators [16][17][18] have in manipulating objects while controlling their stiffness [15]. Soft robots present distributed deformation with theoretically an infinite number of degrees of freedom (DoF) and generate little resistance to compressive forces and thus easily conform to obstacles. In addition, they can squeeze through openings smaller than their nominal dimensions [19]. In this paper a variable stiffness soft manipulator for MIS is presented. Due to its soft structure it is able to elongate, squeeze and reach high bending angles. A stiffness mechanism based on granular jamming was integrated in the manipulator in order to be able to control its stiffness.

II. ARCHITECTURE OF THE MANIPULATOR AND DESIGN OF A SINGLE MODULE

The envisaged architecture is shown in Fig. 1. The manipulator will be composed of multiple modules, e.g. three modules, each of them capable of bending in all directions, elongating and stiffening independently. On the tip, a wrist will provide

the necessary dexterity for orienting a surgical tool. The wrist is under development and will not be described in this paper.

In this paper the design and characterization of one single module is presented. The module of the manipulator is basically composed of a silicone cylinder. Inside this cylinder there are three equally spaced semi-cylindrical chambers in radial arrangement (the fluidic actuators) and another one centrally placed (for the stiffening mechanism) as shown in Fig.1.

A. *Actuation system*

Flexible fluidic actuators technology was exploited for moving the module. The use of such technology is facilitated by the available literature in terms of modeling [21][22] and application cases [23]. Optimal geometries for this specific system are under investigation, previous works comparing several cross section designs [24] concluded that the key factor is to find a trade-off between the thickness of the separation wall among the chambers and their diameter.

The dimensions of the module and the embedded chambers are reported in Fig. 1. The inflation of one chamber causes a small bending coupled with an outward expansion in the radial direction (Fig. 2). In order to constrain the lateral deformation maximizing the bending, a crimped braided sheath (like those used in McKibben actuators) is used around the module (Fig. 2, right). The sheath is fixed at the ends of the module and due to the crimped structure it allows high deformations of the module without affecting its flexibility. Since three chambers are embedded in the module bending in all directions is possible, actuating them both singularly or in combination. Elongation can be obtained by inflating all the three chambers at the same time with the same pressure.

B. *Stiffening system*

For stiffness modulation, a granular jamming solution is used. The effectiveness of this strategy on soft robots has been already demonstrated in [20], [25], [12], [26]. One of the main advantages of this technology is that it is highly deformable in the unjammed state and undergoes to a drastic stiffness increase in the jammed condition. In our application coffee powder was used as granular material and latex as containing membrane. Jamming is induced by increasing density in the flexible membrane due to the applied vacuum. By controlling the vacuum level the stiffness can be tuned. The stiffening chamber is placed in the central cannel of the module (Fig. 1).

Figure 2. Effect of 0.32 bar pressure on a single fluidic chamber.

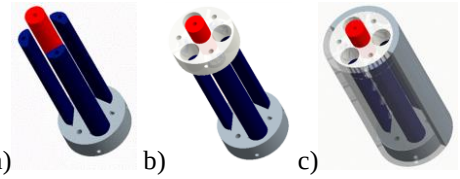

a) b) c)

Figure 3. Assembling of the mold for the silicone cylinder hosting the three fluidic chambers and the central stiffening channel.

III. FABRICATION

The flexible fluidic actuator is fabricated by pouring silicone (Ecoflex™ 0050 – Smooth on Inc.) in an aluminum mold. As shown in Fig. 3a, the three chambers mold and the stiffening chamber mold are fixed to a base by screws and aligned on the top with alignment grooves (Fig. 3b). Two semi-cylindrical shells close the mold (Fig. 3c) and silicone is cast inside. After complete curing the two bases are removed and silicone is again cast to create a layer on top for closing the chambers. On one side three screws are left screwed in the fluidic chambers mold in order to keep a free channel for leaving space to insert the pipes.

The external crimped sheath is realized starting from an off-the-shelf flexible braided sheath (RS Components) with a maximum reachable inner diameter of 33 mm. The sheath is fitted in an aluminum cylinder 20 mm in diameter and compressed until the development of the crimped structure. The obtained shape was thermally fixed by heating the sheath at 400°C with a heat gun for a few minutes. The sheath is then fixed at the two bases of the elastomeric module with silicone.

The stiffening chamber is fabricated by filling 5 g of coffee powder in a latex membrane. It is then inserted in the central channel of the flexible fluidic actuator and fixed on top of it using silicone glue.

IV. EXPERIMENTAL CHARACTERIZATION OF A SINGLE MODULE

Pressurizing the three embedded fluidic chambers, bending in all directions and elongation can be obtained. Three pressure regulator valves (series K8P, E.V.P. systems) enable the modulation of the air pressure in each chamber. Pneumatic supply is provided by a compressor (Compact 106, Fiac Air-Compressors). Vacuum for stiffness modulation is generated by a vacuum pump (LB.4, D.V.P. vacuum technology). A 5 µm filter (MC104-D10, E.V.P. systems) was used to prevent particles to enter into the pump. A vacuum reducer with pneumatic regulation (110130, E.V.P. systems) was used in combination with a pressure regulator valve (series K8P, E.V.P. systems) powered by the compressor in order to control the vacuum level in the stiffening chamber. The output pressure of the four pressure regulator valves is measured with four analog outputs (voltage) by using an acquisition board (USB NI6363 DAQmx). A LabView interface was set up for controlling input pressures in the fluidic chambers and the vacuum level in the stiffening chamber.

Bending and elongation performances of the module were characterized by inflating the fluidic chambers singularly, in pairs and all at the same time. The applied pressures ranged from 0 to 0.65 bar, with a step of 0.05 bar, and each test was repeated three times. At each step the bending angle was estimated from a static picture elaborated in MatLab. In the case of three fluidic chambers activation, elongation is obtained and the length variation was measured.

The force developed by the single module was measured by fixing a load cell (ATI Mini45) on the top of the module and

actuating one fluidic chamber with a pressure ranging from 0 to 0.8 bar in isometric conditions (inset of Fig. 6). The same test was performed actuating two and three fluidic chambers.

The rigidity variation, due to the vacuuming of the stiffening chamber, was measured by imposing different displacements at the tip of the module in different configurations of it, by using a 6 DoF industrial robot (RV-6SL, Mitsubishi) with a load cell (ATI Mini45) mounted on its end effector. Three conditions were tested: a) base condition (no actuation), Fig. 7a; b) 90 deg bending condition, lateral displacement of 16.5 mm along the *-y* direction, Fig. 7b; c) 90 deg bending condition displacement of 8 mm on the upper base (*-z* direction), Fig. 7c. The tests were carried out both at atmospheric pressure and at the 1.5 psi vacuum pressure. Each test was repeated three times. Forces necessary for the above displacements were recorded.

V. Results and Discussion

In Fig. 4 the bending angle as a function of the input pressure is presented. For low pressures the increase in the bending angle is low since the expanded chamber is starting to interact with the braided sheath. At higher pressure the interaction becomes more effective due to the volume increase leading to a considerable improve in bending. Beyond 0.55 bar the bending capability seems to reach saturation since the portion of the braided sheath, located externally along the bending plane, reaches its maximum elongation capability and starts limiting the achievable angle. Bending angles of up to 120 deg were measured. When the two chambers are actuated simultaneously a similar behavior is shown, but the saturation occurs at lower angles since the simultaneous activation of the two chambers causes a faster saturation of the available volume. In this case, the reachable bending angle is lower (80 deg) but the bending radius is bigger.

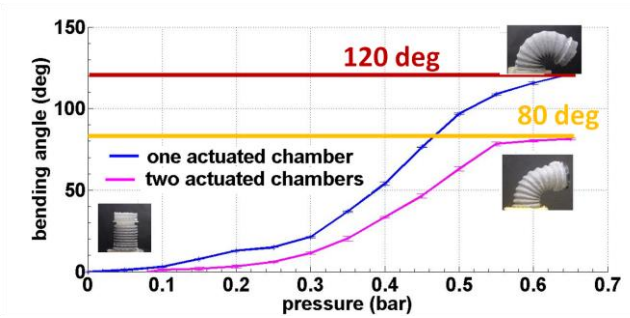

Figure 4. Bending capability of the single module under the action of increasing pressure.

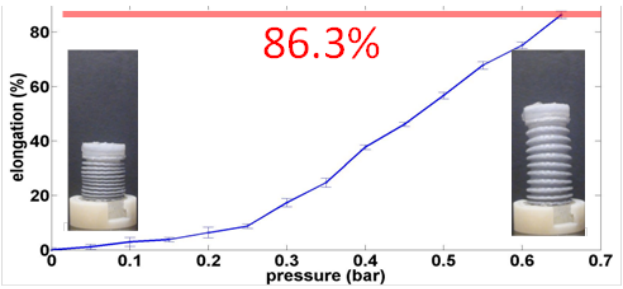

Figure 5. Elongation capability of the module under the action of increasing pressure applied simultaneously to all the chambers (values on *x* axis refer to the pressure of every single chamber).

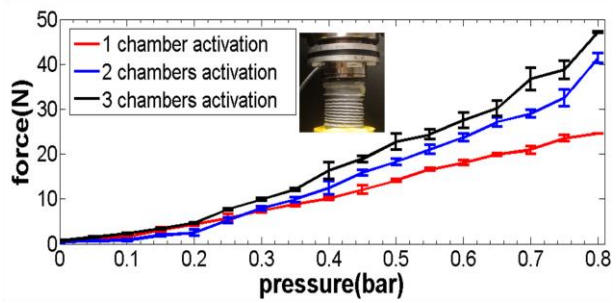

Figure 6. Isometric force developed by the module.

Elongation (Fig. 5) was obtained by activating the three chambers simultaneously: with an activation pressure of 0.65 bar in each chamber, a final length of 83.3 mm was measured, corresponding to an elongation of 86.3%.

The force developed by a single module in isometric conditions and activating different chambers is reported in Fig. 6. One single chamber is able to generate 24.6 N increasing almost linearly respect to the input pressure. In the case of two and three chambers activated the force reaches 41.4 N and 47.1 N respectively.

The activation of the stiffening chamber demonstrated the possibility to change the rigidity of the module. The first test carried out on the module at base condition (Fig. 7a) shows a consistent increase of the module stiffness when the stiffening chamber is vacuumed (36%). In the second test with the 90 deg bending condition, the stiffening demonstrated to be less performing as expected since the internal channel is deformed together with the module and its cross section is reduced (Fig. 7b, c). In *y* direction the maximum stiffness increase is equal to 12.4%, and in *z* direction it is 17.2%. For low imposed displacements the plots in Fig. 7 show a similar trend resulting from the compression of the external silicone part of the module. After a few millimeters of displacement, the resistant force contribution of the central stiffening chamber starts to predominate and the force needed to deform the module increases. In Fig. 7c this phenomenon is not present since the displacement is applied directly to the stiffening channel.

The results underlined that it is not possible to generate a complete shape locking of the module. However, a remarkable increase of the stiffness in the different configurations was demonstrated, leading to an improvement of the stability of the robot during the surgical operation, and enabling to comply with the surgical environment.

VI. Conclusion

In this paper the concept design of a new modular manipulator for MIS has been presented. One single module composing such manipulator was fabricated and characterized. The single module successfully combines omnidirectional bending, elongation capability, and selective stiffness changing. In addition, since the module does not contain any rigid components, it can be squeezed by the user for fitting it into smaller diameter holes.

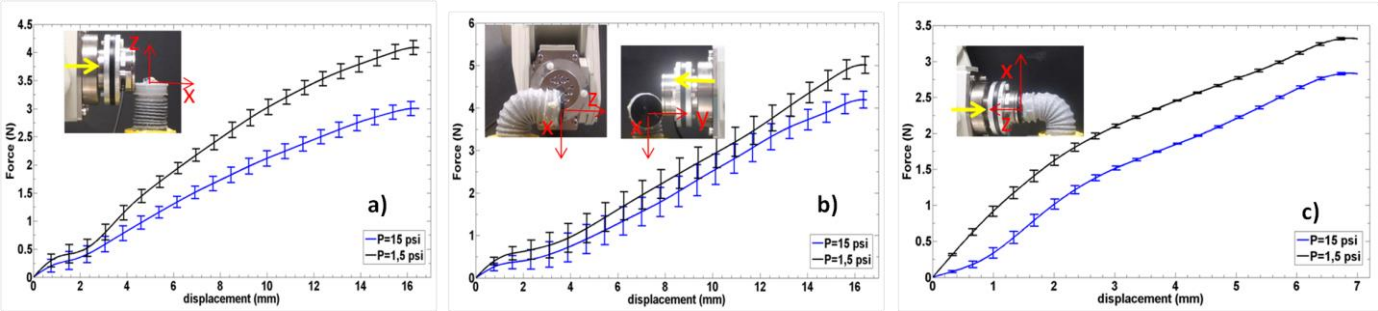

Figure 7. Stiffening variation tests: the module has been tested in base condition (a) 90 deg bending position along y (b) and z (c) direction.

VII. Acknowledgment

The authors would like to thank the STIFF-FLOP consortium for the useful suggestions and discussions related to the design of the surgical module.

References

[1] V. Vitiello, S. Lee, T. Cundy, G. Yang, "Emerging Robotic Platforms for Minimally Invasive Surgery", IEEE Rev Biomed Eng. 2012.

[2] L. Vyas, D. Aquino, C.-H. Kuo, J. S Dai, P. Dasgupta, "FLEXIBLE ROBOTICS", BJU International 107, 2011, pp.187-189.

[3] A. Loeve, P. Breedveld, and J. Dankelman, "Scopes too flexible...and too stiff," Pulse, IEEE, vol. 1, no. 3, 2010, pp. 26 –41.

[4] A. Bajo, R. E. Goldman, W. Long; D. Fowler, N. Simaan, "Integration and preliminary evaluation of an Insertable Robotic Effectors Platform for Single Port Access Surgery," Robotics and Automation (ICRA), 2012 IEEE International Conference on , pp.3381,3387

[5] A. Degani, H. Choset, B. Zubiate, T. Ota, M. Zenati, "Highly Articulated Robotic Probe for Minimally Invasive Surgery," IEEE International Conference EMBS, pp.3273-3276, 2008.

[6] N. Simaan, et al. "Design and integration of a telerobotic system for minimally invasive surgery of the throat." The International journal of robotics research 28.9 (2009): 1134-1153.

[7] P. J. Swaney et al "Minimally-Invasive Intracerebral Hemorrhage Removal Using An Active Cannula" 2013 IEEE International Conference on Robotics and Automation (ICRA), 2013

[8] I.Gravagne, I.Walker, "Manipulability, force, and compliance analysis for planar continuum manipulators," IEEE Trans. Robot. Autom., vol. 18, no. 3, pp. 263–273, Jun. 2002.

[9] AJ Loeve, JH Bosma, P Breedveld, D Dodou, J. Dankelman "Polymer rigidity control for endoscopic shaft-guide 'Plastolock' a feasibility study". Trans. ASME—J. Med. Dev 2010

[10] M. S. Moses, M. D. M. Kutzer, H. Ma, M. Armand, "A Continuum Manipulator Made of Interlocking Fibers" 2013 IEEE International Conference on Robotics and Automation (ICRA), 2013

[11] G. Salvietti, D. Prattichizzo, M. Niccolini, T. Ranzani, A. Menciassi "A task priority approach for modular robots in minimally invasive surgery" ICRA 2012 workshop: Modular Surgical Robotics: how can we make it possible?

[12] A. Loeve, O. S. van de Ven, J. G. Vogel, P. Breedveld, J. Dankelman. "Vacuum packed particles as flexible endoscope guides with controllable rigidity". Granular matter 2010: 543-554.

[13] Y.-J. Kim, S. Cheng, S. Kim, K. Iagnemma, "A Novel Layer Jamming Mechanism With Tunable Stiffness Capability for Minimally Invasive Surgery," Robotics, IEEE Transactions on , vol.PP, no.99, pp.1,12, 0

[14] T. M. Huh, Y-J Park, K-J Cho, "Design and analysis of a stiffness adjustable structure using an endoskeleton" International Journal of Precision Engineering and Manufacturing, 2012, Vol. 13, Issue 7, pp 1255-1258

[15] K. K. Smith and W. M. Kier "Trunks, tongues, and tentacles: Moving with skeletons of muscle", American Scientist 77 (1), 1989, pp. 28–35.

[16] W. McMahan, et al "Field trials and testing of the OctArm continuum manipulator", Robotics and Automation, Proceedings IEEE International Conference on , 2006, pp. 2336–2341.

[17] C. Laschi, et al "A Soft Robot Arm Inspired by the Octopus", Advanced Robotics (Special Issue on Soft Robotics), 26 (7) pp. 709-727, 2012.

[18] V. Ramses Martinez, et al "Robotic Tentacles with Three-Dimensional Mobility Based on Flexible Elastomers", Advanced Materials, vol. 25, issue 2, 2013, pp 205–212.

[19] D. Trivedi, C. D. Rahn, W. M. Kier, I. D. Walker, (2008). Soft robotics: Biological inspiration, state of the art, and future research. Applied Bionics and Biomechanics, 5(3), 99-117.

[20] N. G. Cheng, et al "Design and Analysis of a Robust, Low-cost, Highly Articulated manipulator enabled by jamming of granular media", Robotics and Automation (ICRA), IEEE International Conference on , 2012, pp.4328–4333.

[21] R. J. Webster III and B.A. Jones, "Design and Kinematic Modeling of Constant Curvature Continuum Robots: A Review" *The International Journal of Robotics Research*, 2010.

[22] K. Suzumori, S. Iikura, H. Tanaka, "Flexible microactuator for miniature robots", Micro Electro Mechanical Systems, MEMS '91, Proceedings. An Investigation of Micro Structures, Sensors, Actuators, Machines and Robots. IEEE , vol., no., pp.204-209, 1991.

[23] A. D. Greef, P. Lambert and A. Delchambre, "Towards flexible medical instruments: Review of flexible fluidic actuators" Precision Engineering, 33, pp. 311 – 321, 2009.

[24] K. Suzumori, T. Maeda, H. Watanabe and T. Hisada, "Fiberless Flexible Microactuator Designed by Finite-Element Method" *IEEE/ASME transactions on mechatronics*, vol. 2, no. 4, pp 281-296, 1997.

[25] E. Steltz, A. Mozeika, J. Rembisz, N. Corson, H.M. Jaeger,"Jamming as an Enabling Technology for Soft Robotics," *2010 SPIE Conf. on Electroactive Polymer Actuators and Devices*, San Diego, CA, 2010.

[26] A. Jiang, A. Ataollahi, K. Althoefer, P Dasgupta, T. Nanayakkara, "A Variable Stiffness Joint by Granular Jamming" Proceedings of the ASME 2012 International Design Engineering Technical Conferences & Computers and Information in Engineering Conference IDETC/CIE 2012.

Electromagnetic design for capsule endoscope navigation: a preliminary study

A cost effective and minimally invasive capsule endoscopy strategy

Gioia Lucarini[1], Alessandro Tozzi[2], Carlo Bruni[3], Alessio Vallesi[3], Elena Gaggini[1], Gastone Ciuti[1], Arianna Menciassi[1]*

[1]The BioRobotics Institute, Scuola Superiore Sant'Anna, Pontedera (PI), Italy
[2] U.O. Gastroenterologia ed Endoscopia Digestiva, Ospedale San Giuseppe, ASL11 Empoli (FI), Italy
[3] Special Electronic Design S.r.l, R&D Division, Certaldo (FI), Italy
*corresponding author: a.menciassi@sssup.it

***Abstract*— The gastrointestinal tract is home to some of the most deadly human diseases. Problems are related to the difficulty of accessing it for diagnosis or intervention and concomitant patient discomfort. Flexible endoscopy has established itself as the method of choice with high diagnostic accuracy, but there remain several technical limitations and the procedure is poorly tolerated by patients. The use of magnetic fields to control and steer endoscopic capsules is increasing in minimally invasive surgical applications. In fact, magnetic coupling is one of the few physical phenomena capable of transmitting motion beyond a physical barrier and allowing for a compact design of the "slave" device. In this framework, the authors present a preliminary study for the design of a magnetic coupling for magnetic endoscopic capsules considering an electromagnetic approach within the EU SUPCAM project. In particular the target was to maximize the magnetic interaction forces and torques induced by the external electromagnetic source on the endoscopic capsule embedding an internal permanent magnet, still complying with the limitations imposed by the specific applicative scenario.**

Keywords—gastrointestinal endoscopy, magnetic medical devices, electromagnets design, robotic magnetic guidance.

I. INTRODUCTION

Today, colonoscopy and gastroscopy with flexible endoscopes are the standard examination procedure for the gastrointestinal tract (GI). These techniques are fairly reliable and provide high-resolution images stream that enable accurate diagnosis. However, these techniques entail also several drawbacks [1]. First, the physician needs much practice to acquire the necessary dexterity to manipulate the endoscope. Second, movements done by the endoscope inside the body are frequently painful and traumatic and poorly tolerated by patient. Wireless capsule endoscopy (WCE) has become a useful diagnostic tool that enables clinicians to study the GI tract and reduce patient discomfort since its introduction in clinical practice in 2001 [2]. It consists of a small capsule with an embedded camera that is swallowed by the patient and transmits its images towards a storage device outside the body. Several companies produce "smart camera pills", but they still have two major limitations. As an intrinsic limitation, WCE does not allow the operator to control the navigation and the capsule proceeds by means of visceral peristalsis and gravity. This makes the trajectory of the capsule purely uncontrollable and unplanned, so that some portions of the GI surface are unlikely to be visualized. Another drawback of WCE is represented by the fact that, if areas of clinical interests are identified, the endoscopist cannot manoeuvre the capsule locally (back and forth, right and left) for detailed inspections. Therefore, solving the manoeuvring problem might significantly enhance the accuracy of the endoscopic investigation with an expected improvement of diagnostic efficacy. The use of magnetic-based systems for actuation and localization of endoscopic capsules in the GI tract has become an active area of research and it represents a good approach to solve the problem of control [3]. Magnetic forces and torques provide an efficient actuation solution whenever traditional motors cannot be integrated in medical devices for powering and size constraint [4-6]. Two different approaches, that can be used to generate magnetic forces and torques for achieving the magnetic control of a magnetic capsule, are the use of one or more permanent magnets [4, 5] or electromagnets [6]. Nevertheless, despite the growing scientific interest in magnetically controllable WCE, no effective systems with straightforward clinical applicability have been yet demonstrated. This is ascribable to a lack of reliable magnetic coupling between magnetic capsule and external magnetic source and to the difficulty to fine localize and control locomotion by means of magnetic fields. A significant example of magnetic capsule locomotion and orientation was pursued within the VECTOR project [7] that brought to the development of three endoscopic magnetic actuated capsules (Fig. 1).

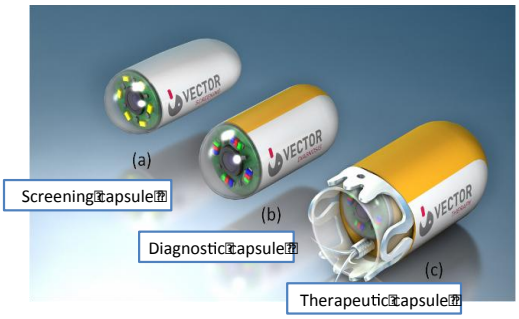

Fig. 1. VECTOR project capsule concepts, *i.e.* (a) screening, (b) diagnostic and (c) therapeutic capsule.

In this paper, the authors investigated and preliminary designed the magnetic coupling for magnetic WCE considering an

The research leading to these results has received funding from the European Union Seventh Framework Programme (FP7/2007-2013) under Grant Agreement No. 315378 (FP7-SME-2012-315378) – SUPCAM project.

electromagnetic approach within the SUPCAM project [8]. In particular, starting from the background and knowledge of permanent magnets design, maturated within the VECTOR project, the target was to maximize the magnetic interaction forces and torques induced by the external electromagnetic controllable source on the endoscopic capsule with an internal permanent magnet, still complying with the limitations imposed by the environment.

II. Magnetic Locomotion for Magnetic WCE

A magnetic capsule will experience both a torque and a force within an external induced magnetic field with flux density B (T). The magnetic torque τ (Nm) can be expressed as [9]:

$$\tau = VM \times B = V \begin{bmatrix} M_x B_x \\ M_y B_y \\ M_z B_z \end{bmatrix} \quad (1)$$

where V (m^3) and M (A/m) are the volume and the magnetization of the object, respectively. This torque tends to align the magnetization of the magnetic capsule to the applied external magnetic field. The magnetic force F (N) on the magnetic capsule is represented by:

$$F = V \nabla BM = V \begin{bmatrix} M_x \frac{\partial B_x}{\partial x} + M_y \frac{\partial B_y}{\partial x} + M_z \frac{\partial B_z}{\partial x} \\ M_x \frac{\partial B_x}{\partial y} + M_y \frac{\partial B_y}{\partial y} + M_z \frac{\partial B_z}{\partial y} \\ M_x \frac{\partial B_x}{\partial z} + M_y \frac{\partial B_y}{\partial z} + M_z \frac{\partial B_z}{\partial z} \end{bmatrix} \quad (2)$$

Equations (1) and (2) are based on the assumption that the magnetic capsule is small compared to the spatial changes of the applied external magnetic field's flux density B. Under this assumption, B can be considered fairly uniform within the capsule. Hence, assuming that the capsule has spatially homogeneous magnetic properties, B represents the value of the applied magnetic field's flux density in the centre of mass of the object. These torques and forces can be generated by using either permanent magnets or electromagnets. Both approaches have advantages and disadvantages to control the locomotion of a magnetic capsule. Although the first approach represents a cheap and flexible solution, adequate navigation accuracies are very difficult to achieve due to the impossibility to modulate the generated field. Since permanent magnets generate fixed magnetic fields, both precision and accuracy depend on their fine motion. The second strategy, employed within the SUPCAM project, can lead to a higher navigation precision, fine control of produced magnetic fields and consequently definition of specific forces that can be obtained by modulating the intensity of the current flowing through the electromagnet itself. Moreover, the safety of the patient and physician is increased because the magnetic coupling can be reduced or, in the case, turned off by switching off the remote power supply. However, cumbersome electromagnetic coils and high currents may be required in order to generate adequate magnetic fields and unwanted heating should also be considered.

III. Requirements and Scenario for Magnetic WCE

The SUPCAM endoscopic platform will allow performing an endoluminal medical examination through an external control magnetic system with a compact and simple manipulation structure, inexpensive, and usable in normal outpatient setting, able to ensure an accurate diagnosis of the colonic mucosa. Therefore, within the design phase of an external electromagnet, representing the locomotion external source, compactness has to be considered; the electromagnet has to be adapted to be transported and easily controlled by the physician for generating a proper link with the endoscopic device. In particular, suitable forces and torques for navigation and visualization against a high frictional deformable environment have to be generated in a narrow range of distance between the external magnet and the endoscopic device due to the abdominal thickness. Moreover, for a fine control of pitch (visualization of upper and lower wall of the colonic lumen) and yaw (visualization of right and left wall of the colonic lumen) orientations of the capsule (range of around ± 90°) specific magnetic torques have to be exerted on the capsule system.

In this framework, to perform an effective and reliable magnetic locomotion capsule endoscopy, a modular solution was investigated: it consists in the use of a cylindrical-shape electromagnet supported by a 5 degrees-of-freedom (DoFs - 3 for translation and 2 for the electromagnet orientation) manipulator for gravity compensation and accurate remote or local control (Fig. 2a). The electromagnet will be employed in two different configurations: for an initial attraction phase of the capsule (configuration C1 in Fig. 2b - magnetization direction perpendicular to the abdominal wall) and for a locomotion and orientation phase (configuration C2 in Fig. 2c - magnetization direction parallel to the abdominal wall). For a geometric distribution of magnetic field vectors, the configuration C1, reported in Fig. 2b, allows (with the same amount of current) for a higher magnetic gradient along the attraction axis, pointing to the capsule and perpendicular to the patient abdomen, with respect to the configuration C2 in Fig. 2c. However, in configuration C1, it is not possible the yaw DoF because of the axial symmetry of the electromagnet. Therefore, the configuration C1 has to be considered only in the use at the beginning of the procedure for capturing the capsule (a target distance of 100 mm was considered for the magnetic design) but not for the locomotion and the continuous inspection of the colon. Once attracted, a ±90° pitch rotation of the electromagnet (with the magnetization direction parallel to the abdominal wall) can allow for the shift to the configuration C2, resulting in a closer capsule-electromagnet control and thus preserving for a lower amount of current needed for capsule attraction and then locomotion and orientation. In configuration C2, due to the occurred attraction of the capsule from the bottom of the colonic tract, a reduction of about 20 mm (half of the average diameter of the colonic district, resulting in a target distance of 80 mm) in the distance between the electromagnet and capsule can be considered, as a specific design hypothesis. In this configuration, the current provided to the electromagnet is sufficient to maintain the attraction of the capsule for locomotion (in C2 the capsule reaches the centre of the electromagnet for orientation purposes). In the next sections the design and the definition of the electromagnetic specifications

for the magnetic locomotion of the SUPCAM capsule are investigated and presented in details.

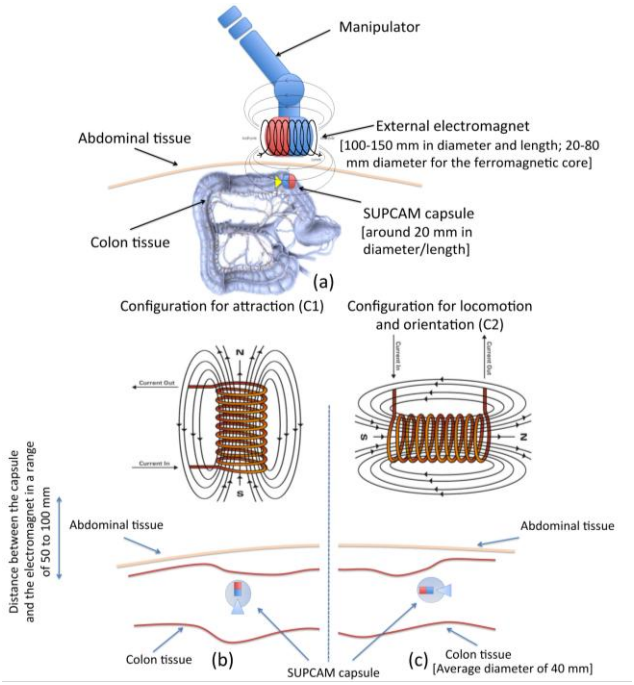

Fig. 2. (a) Schematic representation of the navigation SUPCAM platform, and (b) attraction and (c) locomotion and orientation configurations of the electromagnet.

IV. ENDOSCOPIC CAPSULE

The SUPCAM endoscopic capsule integrates a permanent magnet to achieve a magnetic control for locomotion and orientation, in the interaction with the external electromagnetic source. Considering that the dimensions of the internal magnet have to be compatible with the space constraints and other embedded components (*e.g.*, battery, electronics boards, telemetry, camera, etc.), and considering the required DoFs for a diagnostic system, a cylindrical-shaped axially magnetized permanent magnet with a volume of at least $4x10^{-7}$ m^3 was preliminary selected to be incorporated into the capsule. A neodymium magnet (NdFeB, N52, magnetization equal to 1.48 T) was chosen because neodymium magnets are the strongest types of permanent magnets available and it allows reducing dimensions and/or current of the electromagnet. A rough yet conservative weight prediction for such a device may be two times the PillCam weight (around 4 g), considered a golden standard for capsule endoscopy. Considering all these issues, the targeting magnetic link should be able to navigate a device having a weight of at least 8 g in terms of attraction (at least 78.4 mN that the electromagnet must exert on the wireless device in both the configurations), dragging forces and magnetic torques for orientation. Fig. 3 reports a schematic representation of the attraction and locomotion forces relevant in the configuration C1 and C2, respectively. The equilibrium of the acting forces for allowing attraction and locomotion of the SUPCAM capsule are also reported and they were considered, subsequently, in the electromagnetic design.

V. MAGNETIC CONTROL BY USING AN ELECTROMAGNET

In this approach, the endoscopic capsule is controlled by an external magnetic source consisting of an electromagnet. The electromagnetic source is moved, supported by a robotic manipulator, by the physician in order to achieve high accuracy and reliability. With regards to the SUPCAM capsule conservative weight prediction and basing on Eq. (2), the electromagnet should produce a magnetic field gradient of at least 0.17 T/m at a distance of 100 mm in the case of the configuration C1 and 80 mm for configuration C2. In this framework, the electromagnetic system design entails sophisticated analysis and definitions of physical qualities resulting in a substantial trade-off in the parameters selection (*e.g.*, power, current, resistance and dimensions of copper wire, and number of turns). The aforementioned parameters, strictly depend on each other and system design constraints, have to be preliminary fixed with regards to the operating conditions in order to derive the electromagnetic source system performance. The magnetic field gradient is proportional to the total number of winding (N_{tot}), and it is represented by the formula:

$$\nabla B \approx \frac{N_{tot} I}{\phi^2} \qquad (3)$$

where I (A) is the current and ϕ (m) the copper wire diameter. N_{tot} can be derived by the following equation that reports also the dependence between the system design parameters:

$$\frac{\pi\varphi^2}{h} N_{tot}^2 + 2r_{\min} N_{tot} - \frac{P\pi\phi^2}{4I^2\rho} = 0 \qquad (4)$$

where P (W) represents the power, h (m) the height of the electromagnetic system, r_{min} (m) the inner hole radius, and ρ (A/m) the resistivity parameter of copper. An important parameter that was considered in the electromagnet design is represented by the maximum current density, defined as a vector whose magnitude is the electric current per cross-sectional area. In electrical wiring, the maximum current density can vary from $4Amm^{-2}$ for a wire with no air circulation around it, to $6Amm^{-2}$ for a wire in free air.

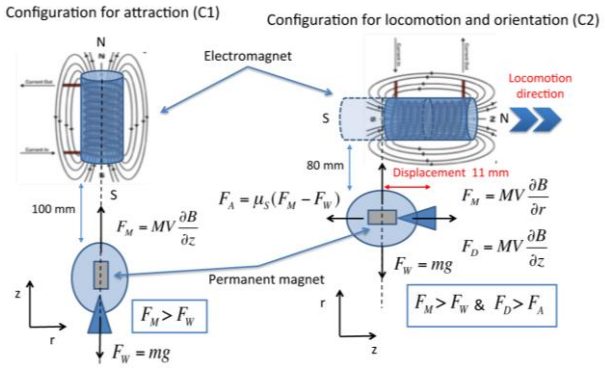

Fig. 3. Schematic representation of the attraction and locomotion forces in the configuration C1 and C2, respectively. μ_S is the static friction coefficient, F_A the friction force, F_M the magnetic attraction force, F_W the weight force and F_D the locomotion force.

For compact designs, such as windings of transformers or electromagnets, a current density value in the range of 2 to 3

Amm^{-2} is recommended; higher current density can be allowed for a short time or with the combination of a properly designed cooling system. The aforementioned formulas were exploited for the design of the electromagnet and a FEM analysis (with COMSOL Multiphysics Inc.) was performed to evaluate the magnetic field gradient (Fig. 4). In particular, based on Eq. (3) and Eq. (4), a cylindrical shaped electromagnet, 150 mm in diameter and 150 mm in length, with a copper wire section of 8.4 mm^2 (920 total windings) and an internal ferromagnetic core of 20 mm in diameter (weight of around 15 Kg) was selected as a compatible and suitable candidate for the magnetic control of the SUPCAM capsule.

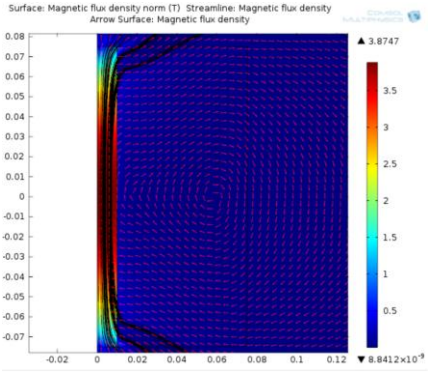

Fig. 4. 2D FEM simulation of the electromagnetic system by COMSOL.

Required magnetic forces and torques for managing the medical procedure in the applicative scenario can be generated by the electromagnetic system in order to guarantee the navigation of the SUPCAM capsule. Specific minimum electrical and physical requirements for the electromagnet are reported in Table I.

	Current (A)	Current density (A/mm^2)	Force (mN)	Distance (mm)
Attraction - C1	12.4	1.36	78.4	100
Attraction - C2	36.2	3.97	78.4	80
Locomotion - C2	37.6	4.12	85.1	80

Table I. Minimum electrical and physical requirements in terms of current, current density, force at the distances for the configurations C1 and C2.

A higher current of at least 36.2 A (current density of 3.97 A/mm^2) has to be imposed for maintaining the capsule attracted once the electromagnet is rotated of ± 90° (pitch angle) switching from the configuration C1 to the configuration C2 due to the different magnetic field profile in the operating space. In the configuration C2, a current of 37.6 A (resulting in a dragging force of 85.1 mN) has to be supplied for locomoting the capsule, displacing the electromagnet along the lumen locomotion direction half of the capsule diameter (11 mm) from the capsule itself. The current value was figured out taking into consideration the possibility to face an opposite sliding frictional force (equal to 78.1 mN) with a conservative static frictional coefficient of 1. Finally, the electromagnet in the configuration C2 allows, with a current of 36.2 A at a distance of 80 mm, a considerable magnetic torque in the order of 5 Nmm for pitch and yaw capsule orientation. These values are much larger than the system inertial momentum, therefore the dynamics of orientation could be neglected and the capsule is aligned nearly instantaneously with the magnetic field of the electromagnet.

VI. Discussion and Conclusion

Starting from the knowledge of permanent magnetic design in GI procedures maturated within the EU VECTOR project, a preliminary magnetic design of an electromagnetic system was performed for locomotion and orientation of an endoscopic capsule for diagnostic procedures in the colonic district. Target magnetic attraction/locomotion forces and magnetic torques were derived for the electromagnetic source design in order to guarantee a reliable navigation of the colonoscopic capsule. The presented electromagnetic design will bring to the development of a physical electromagnetic source; the data obtained in the modelling process will be evaluated by a direct field measurement analysis exploiting a magnetic field measuring probe for evaluating the correctness of the design model. Then, tests will be performed with the developed electromagnetic source with the SUPCAM capsule in *in-vitro* and *ex-vivo* conditions in order to evaluate the magnetic navigation principle and test the electromagnetic system in the project framework. Tests will also guarantee the potential tuning of the system and the need of a cooling system will be evaluated with regards to the real operating condition and required forces for navigation (especially for configuration C2). Due to the high weight of the electromagnetic system (around 15 Kg), a 5 DoFs robotic manipulator will be designed for holding and accurately moving the electromagnetic source by the physician. The use of a controllable manipulator and the possibility to tune the supplied currents in the electromagnetic system will bring to the implementation of an accurate navigation strategy of the SUPCAM capsule, in combination with the knowledge of the position of the device thanks to the development of a localization system [10].

Acknowledgment

The authors would like to acknowledge VECTOR FP6 European project EU/IST-2006-033970 and the partners of the SUPCAM FP7 European project FP7-SME-2012-315378.

References

[1] G. Ciuti, A. Menciassi, and P. Dario, "Capsule endoscopy: from current achievements to open challenges," Biomedical Engineering, IEEE Reviews in, vol. 4, pp. 59-72, 2011.

[2] G. Iddan, G. Meron, A. Glukhovsky, and P. Swain, "Wireless capsule endoscopy," Nature, vol. 405, p. 417, 2000.

[3] F. Carpi, "Magnetic capsule endoscopy: the future is around the corner," Expert review of medical devices, vol. 7, pp. 161-164, 2010.

[4] F. Carpi and C. Pappone, "Magnetic maneuvering of endoscopic capsules by means of a robotic navigation system," Biomedical Engineering, IEEE Transactions on, vol. 56, pp. 1482-1490, 2009.

[5] G. Ciuti, P. Valdastri, A. Menciassi, and P. Dario, "Robotic magnetic steering and locomotion of capsule endoscope for diagnostic and surgical endoluminal procedures," Robotica, vol. 28, p. 199, 2010.

[6] M. Sendoh, K. Ishiyama, and K.-I. Arai, "Fabrication of magnetic actuator for use in a capsule endoscope," Magnetics, IEEE Transactions on, vol. 39, pp. 3232-3234, 2003.

[7] VECTOR Project website: http://www.vector-project.com/.

[8] SUPCAM Project website: http://www.supcam.eu/.

[9] E.P. Furlani, "Permanent magnet and electromechanical devices," Academic Press, 2001.

[10] M. Salerno et al., "Magnetic and inertial sensor fusion for the localization endoluminal diagnostic devices," Int. J. Comput. Assist. Radiol. Surgery (CARS), vol. 7, no. S1, pp. 229–235, 2012.

Control of meso-robots for endoluminal surgery

Alonso SÁNCHEZ, Chao LIU, Nabil ZEMITI, Etienne DOMBRE, Philippe POIGNET
Montpellier, France
{sanchezsec, liu, zemiti, dombre, poignet} @ lirmm.fr

***Abstract*— This work deals with the design, the implementation and the experimental validation of a force-reflecting teleoperation architecture for robotic assisted endoluminal surgery. On that account, a meso-scale surgical robot was used as target device to be teleoperated. This meso-robot was developed during the ARAKNES (Array of Robots Augmenting the Kinematics of Endoluminal Surgery) FP7 project, in which the key idea consisted on transferring the robotic degrees of freedom that are required for surgery inside the peritoneal cavity.**

Keywords—safety; design framework; adaptive control; dual-quaternion; bilateral teleoperation; surgical robotics; endoluminal surgery

I. INTRODUCTION

In order to build the desired teleoperation architecture, several works were carried out:

1. First, the specifics of designing surgical robots were investigated in order to propose a systematic design framework for surgical robotic components that could facilitate the technology transfer from research centers to the operating room.
2. Second, by applying the proposed framework, a generic real-time software architecture for surgical robots was proposed and implemented. This software architecture serves as support for the global teleoperation architecture.
3. Third, the latter teleoperation architecture was developed. This architecture uses adaptive control techniques in which:

   A) An active state observer (AOB) is employed. Moreover, the original Kalman equations (proper of the AOB) were revised and reformulated in order to approximate a Markov chain Monte-Carlo method that allows to better consider, in real-time, nonlinear uncertainties and disturbances that affect the meso-robotic system.

   B) A realistic viscoelastic Kelvin-Boltzmann soft-tissue environment model is also used.

   C) All fundamental (robot) control equations are formulated and performed in the dual-quaternion domain. To that end, one of the first dual quaternion based control toolboxes was implemented.

Such combination of tools and techniques, allowed to demonstrate improved performance of the system with respect to previous works in the field. In this context, two teleoperation schemes of types ``position--position'' and ``position--force'' were proposed in order to fulfill the specific hardware requirements of ARAKNES. Both schemes were analysed in terms of their transparency and stability, i.e. the two parameters that allow quantifying the performance of teleoperated systems.

In addition, having implemented a stable real-time teleoperation control system (and the associated control toolboxes) allowed in turn to study the effects of scaling the positions and the forces, which are respectively commanded and felt by the surgeon. These effects were examined from the point of view of the surgeon's performance and also of the teleopoeration system's performance. In both cases, improvements were observed and it was additionally shown that the availability of online estimated environment's parameters could be exploited to offer surgeons new assistance capabilities that facilitate tasks such as detection of contact and/or discrimination of tissues.

Finally, the possibility of performing wireless control of surgical robots was also explored and experimentally demonstrated. The purpose of this latter study was to increase the mobility of the meso-robot and, possibly, to improve its mechanical performance and/or degree of miniaturization.

REFERENCES

[1] L.A. Sanchez, P. Poignet, E. Dombre, A. Menciassi, and P. Dario. “A design framework for safe surgical robots: case of the ARAKNES control architecture”. Submitted upon invitation to the Journal of Robotics and Autonomous Systems, special issue on Intelligent Autonomous Systems. Lee, S., Lee, J.M. and Menegatti, E., editors. Elseiver, 2013b

[2] L.A. Sanchez, M.Q. Le, K. Rabenorosoa, C. Liu, N. Zemiti, P. Poignet, E. Dombre, A. Menci- assi, and P. Dario. “A case study of safety in the design of surgical robots: The ARAKNES platform”. In Sukhan Lee, Hyungsuck Cho, Kwang-Joon Yoon, and Jangmyung Lee, edi- tors, Intelligent Autonomous Systems, volume 194 of Advances in Intelligent Systems and Computing, pages 121–130. Springer, 2013aJ. Clerk Maxwell, A Treatise on Electricity and Magnetism, 3rd ed., vol. 2. Oxford: Clarendon, 1892, pp.68-73.

Magnetic Control of Potential Microrobotic Drug Delivery Systems

Islam S. M. Khalil*, Veronika Magdanz†, Samuel Sanchez†, Oliver G. Schmidt†‡,
Leon Abelmann*♭ and Sarthak Misra*
*University of Twente, Enschede, The Netherlands
†Institute for Integrative Nanosciences, IFW Dresden, Germany
‡Material Systems for Nanoelectronics, University of Technology Chemnitz, Germany

***Abstract*—Development of targeted drug delivery systems using magnetic microrobots increases the therapeutic indices of drugs. These systems have to be incorporated with precise motion controllers. We demonstrate closed-loop motion control of microrobots under the influence of controlled magnetic fields. Point-to-point motion control of a cluster of iron oxide nanoparticles (diameter of 250 nm) is achieved by pulling the cluster towards a reference position using magnetic field gradients. Magnetotactic bacterium (MTB) is controlled by orienting the magnetic fields towards a reference position. MTB with membrane length of 5 μm moves towards the reference position using the propulsion force generated by its flagella. Similarly, self-propelled microjet with length of 50 μm is controlled by directing the microjet towards a reference position by external magnetic torque. The microjet moves along the field lines using the thrust force generated by the ejecting oxygen bubbles from one of its ends. Our control system positions the cluster of nanoparticles, an MTB and a microjet at an average velocity of 190 μm/s, 28 μm/s, 90 μm/s and within an average region-of-convergence of 132 μm, 40 μm, 235 μm, respectively. Further, we achieve point-to-point closed-loop motion control of microparticles in the three-dimensional space, at an average speed of 198 μm/s, and maximum root mean square position tracking error of 104 μm.**

I. INTRODUCTION

Magnetic microrobots have the potential to deliver concentrated pharmaceutical agents to diseased cells to avoid the negative side-effects associated with chemotherapeutical treatment [1], [2]. Many researchers proposed the utilization of biodegradable magnetic nanoparticles [3], [4], magnetotactic bacteria [5], artificial swimmers [6], and self-propelled microjets [7], [8] to execute limited tasks, such as targeted drug delivery [9], microassembly [10], and microactuation [11]. Realization of a reliable drug targeting system necessitates the development of precise closed-loop motion control systems. Kummer *et al.* developed and utilized a 5 degree-of-freedom magnetic system to puncture a blood vessel of a chorioallantoic membrane of a chicken embryo using a magnetic agent (two cubes with edge length of 800 μm) with permanent magnetization [12]. Magnetic control of a single paramagnetic microparticle in the presence of static and dynamic obstacles was presented by Khalil *et al.* [13]. Martel *et al.* demonstrated the effectiveness of a swarm of magnetotactic bacteria in the execution of a manipulation task of microobjects under the influence of the controlled magnetic fields [14]. Microassembly of microobjects using a cluster of microparticles (with average diameter of 100 μm) and a magnetic-based manipulation system has been shown by Khalil *et al*. [15]. These magnetic systems can be used for targeted drug delivery by the incorporation of a clinical imaging modality, such as magnetic resonance imaging or ultrasound systems.

In this work, we present point-to-point motion control of a cluster of iron oxide microparticles and nanoparticles,

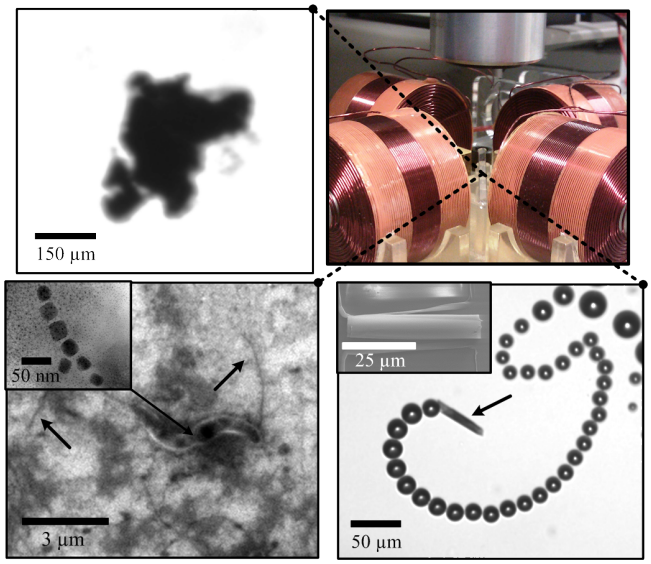

Fig. 1. Magnetic system for the point-to-point motion control of a cluster of iron oxide nanoparticles, magnetotactic bacterium (MTB) and a self-propelled microjet under the influence of the magnetic fields. The upper left image shows a cluster of nanoparticles. Motion of this cluster is achieved by the magnetic field gradients. The bottom left Scanning Electron Microscopy (SEM) image shows the membrane of an MTB (*Magnetospirillum magneticum* AMB-1), and its flagella, indicated by the black arrows. Motion of the MTB is due to the flagella and the external magnetic fields. The inset shows a Transmission Electron Microscopy image of the magnetite nanocrystals enveloped in the membrane of the MTB. The bottom right image shows a microjet moving under the influence of the external magnetic fields and its self-propulsion force. This propulsion force is generated by ejecting oxygen bubbles from one end of the microjet. The inset shows a SEM image of a microjet fixed to its substrate.

*Islam S. M. Khalil and Sarthak Misra are affiliated with MIRA–Institute for Biomedical Technology and Technical Medicine, University of Twente.
♭Leon Abelmann is affiliated with MESA+ Institute for Nanotechnology, University of Twente.

†Veronika Magdanz, Samuel Sanchez and Oliver G. Schmidt thank the Volkswagen Foundation (# 86 362). Samuel Sanchez thanks the European Research Council (ERC) for Starting Grant "Lab-in-a-tube and Nanorobotics biosensors".

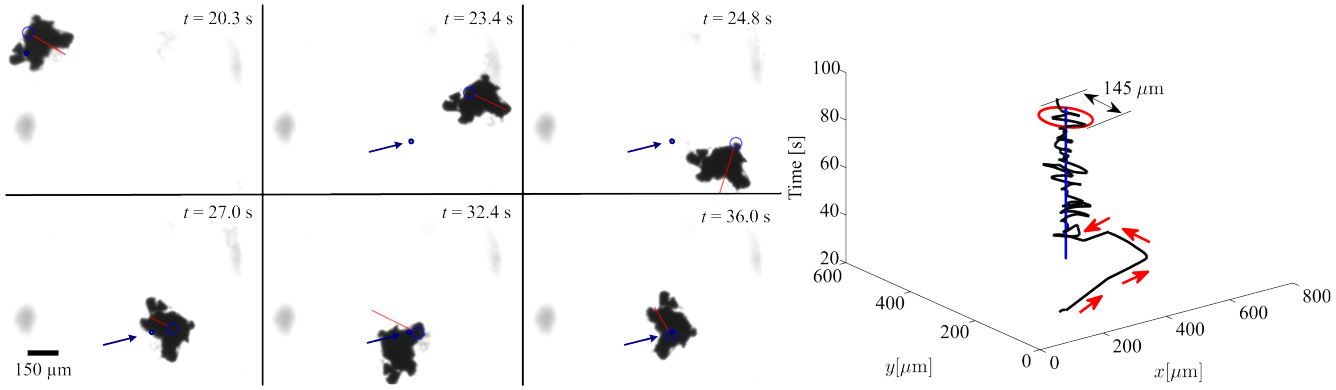

Fig. 2. Closed-loop motion control of a cluster of iron oxide nanoparticles (45-00-252 Micromod Partikeltechnologie GmbH, Rostock-Warnemuende, Germany) under the influence of the controlled magnetic fields. The cluster moves towards the reference position (small blue circle) by the magnetic field gradient generated using control law (3). In this representative experiment, the cluster moves at an average velocity of 195 μm/s, and is positioned by the closed-loop control system within a region-of-convergence of 145 μm in diameter. The entries of each of the diagonal matrices ($\mathbf{K}_\mathrm{p}$ and $\mathbf{K}_\mathrm{d}$) are 0.1 s^{-2} and 0.5 s^{-1}, respectively. The large blue circle is assigned by our feature tracking software [13] and represents the position of the cluster, whereas the red line represents its velocity vector. The blue arrows indicate the reference position. The solid blue line in the right image represents the reference position.

magnetotactic bacteria, and self-propelled microjets (Fig. 1) using a closed-loop motion control system. This control system is based on the characterization of the magnetic dipole moment of the aforementioned magnetic objects. Motion control of the microparticles and nanoparticles is achieved by controlling the gradients of the magnetic fields to pull the nanoparticles towards a reference position, whereas magnetotactic bacteria and microjets are controlled by orienting the fields towards a reference position. Magnetotactic bacteria and microjets move along the magnetic field lines using their self-propulsion forces that are generated by the helical flagella and the ejecting oxygen bubbles, respectively.

II. CONTROL SYSTEM DESIGN

In our work, iron oxide nanoparticles, magnetotactic bacteria and self-propelled microjets move in water, growth medium and hydrogen peroxide solution, respectively. Their motion is also guided using external magnetic fields. Therefore, these magnetic objects experience viscous drag forces and torques, and magnetic forces and torques. Details regarding the modeling of these magnetic objects is provided by Khalil *et al*. [16]. Our 2D- and 3D-magnetic system [13], [21] is used to generate controlled magnetic fields to realize the point-to-point motion control.

Our magnetic system consists of n-electromagnets. The magnetic field $(\mathbf{B}_i(\mathbf{P}))$ is linearly proportional to the applied current (I_i) at the ith electromagnet. Therefore, the magnetic fields at point $(\mathbf{P})$ is given by [12]

$$\mathbf{B}(\mathbf{P}) = \sum_{i=1}^{n} \mathbf{B}_i(\mathbf{P}) = \sum_{i=1}^{n} \widetilde{\mathbf{B}}_i(\mathbf{P}) I_i = \widetilde{\mathbf{B}}(\mathbf{P})\mathbf{I}, \qquad (1)$$

where $\widetilde{\mathbf{B}}(\mathbf{P}) \in \mathbb{R}^{3\times n}$ is a matrix which depends on the position at which the magnetic field is evaluated, and $\mathbf{I} \in \mathbb{R}^{n\times 1}$ is a vector of the applied current. The magnetic field due to each electromagnet is related to the current input by $\widetilde{\mathbf{B}}_i(\mathbf{P})$. Substituting (1) in the magnetic force equation $(\mathbf{F}(\mathbf{P}) = \nabla(\mathbf{m}(\mathbf{P}) \cdot \mathbf{B}(\mathbf{P})))$, where $\mathbf{F}(\mathbf{P}) \in \mathbb{R}^{3\times 1}$, $\mathbf{m}(\mathbf{P}) \in \mathbb{R}^{3\times 1}$ and $\mathbf{B}(\mathbf{P}) \in \mathbb{R}^{3\times 1}$ are the magnetic force, induced magnetic dipole moment of the magnetic objects and the magnetic field at point $(\mathbf{P} \in \mathbb{R}^{3\times 1})$, respectively, yields the following magnetic force-current map:

$$\mathbf{F}(\mathbf{P}) = (\mathbf{m}(\mathbf{P}) \cdot \nabla)\widetilde{\mathbf{B}}(\mathbf{P})\mathbf{I} = \mathbf{\Lambda}(\mathbf{m}, \mathbf{P})\mathbf{I}. \qquad (2)$$

In (2), $\mathbf{\Lambda}(\mathbf{m}, \mathbf{P}) \in \mathbb{R}^{3\times n}$ is the actuation matrix which maps the input current to the magnetic force [12]. Further, we devise the following proportional-derivative control law [15]

$$\mathbf{F}_\mathrm{des}(\mathbf{P}) = \mathbf{K}_\mathrm{p}\mathbf{e} + \mathbf{K}_\mathrm{d}\dot{\mathbf{e}}. \qquad (3)$$

where $\mathbf{F}_\mathrm{des}(\mathbf{P})$ is the controlled magnetic force which can be realized using (2) through the pseudoinverse of the actuation matrix, and by setting $\mathbf{F}_\mathrm{des}(\mathbf{P}) = \mathbf{F}(\mathbf{P})$. Further, $\mathbf{e}$ and $\dot{\mathbf{e}}$ are the position and velocity tracking errors, respectively, and are given by

$$\mathbf{e} = \mathbf{P}_\mathrm{ref} - \mathbf{P} \quad \text{and} \quad \dot{\mathbf{e}} = \dot{\mathbf{P}}_\mathrm{ref} - \dot{\mathbf{P}}, \qquad (4)$$

where $\mathbf{P}_\mathrm{ref}$ and $\dot{\mathbf{P}}_\mathrm{ref}$ are the reference position and velocity, respectively. Finally, in (3), $\mathbf{K}_\mathrm{p}$ and $\mathbf{K}_\mathrm{d}$ are diagonal positive-definite gain matrices. In order to implement the control law (3), the pseudoinverse of the actuation matrix $(\mathbf{\Lambda}(\mathbf{m}, \mathbf{P}))$ is calculated based on the magnetic dipole moment and position of the magnetic object [20].

III. EXPERIMENTAL RESULTS

Motion control experiments are done using a magnetic system, shown in Fig. 1. This system consists of four orthogonally oriented air-core electromagnets (n=4). These electromagnets can surround a reservoir, a capillary tube and a petri dish to incubate water, growth media and hydrogen peroxide solution for the cluster of nanoparticles, MTB and microjets, respectively. Our closed-loop control system allows for the positioning of the magnetic objects within the vicinity of a reference position. Fig. 2 shows a representative closed-loop motion control result of the cluster. We observe that the cluster is positioned at an average velocity of 195 μm/s and within a region-of-convergence (ROC) of 145 μm. Magnetotactic bacteria (strain *Magnetospirillum magneticum* AMB-1) are controlled inside a capillary tube with inner thickness and width of 0.2 mm and 2 mm, respectively. Our closed-loop control system positions an MTB at an average velocity of 19 μm/s and within a ROC of

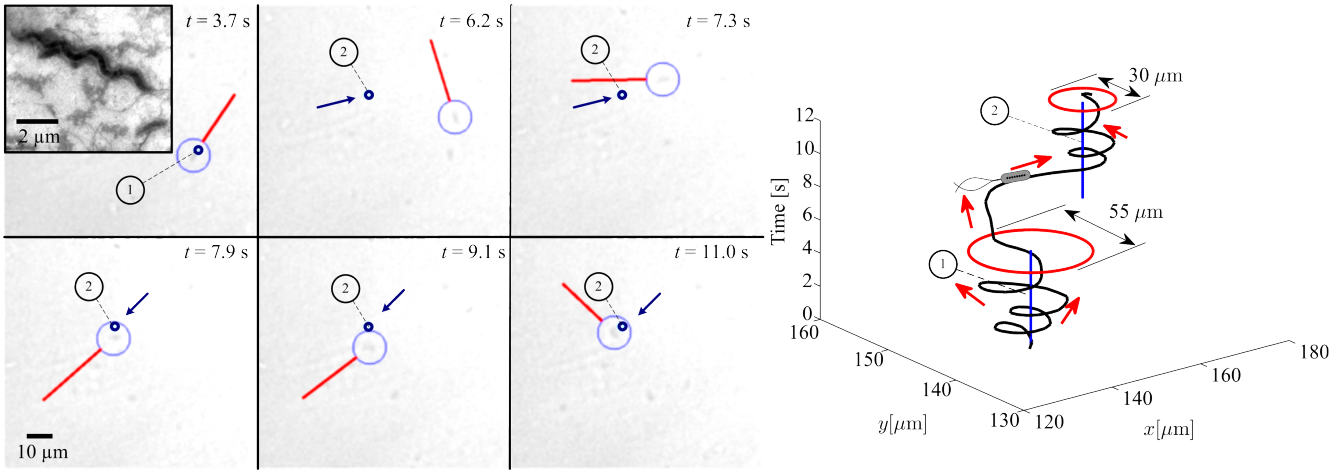

Fig. 3. Closed-loop motion control of a magnetotactic bacterium (MTB), strain *Magnetospirillum magneticum* AMB-1, under the influence of the controlled magnetic fields. An MTB moves towards the reference positions (small blue circles) along the magnetic field lines generated using the control law (3). MTB moves using its helical flagella. In this representative experiment, an MTB moves at an average velocity of 19 μm/s, and is positioned within the vicinity of two reference positions (represented by the solid blue lines in the right image). The closed-loop control system achieves a region-of-convergence of 55 μm and 30 μm in diameter for the first and second reference positions, respectively. The entries of the diagonal matrices ($\mathbf{K}_\mathrm{p}$ and $\mathbf{K}_\mathrm{d}$) are 15 s^{-2} and 15.5 s^{-1}, respectively. The large blue circle is assigned by our feature tracking software [13] and represents the position of the MTB, whereas the red line represents its velocity vector. The inset shows a Scanning Electron Microscopy image of the spiral membrane of the MTB.

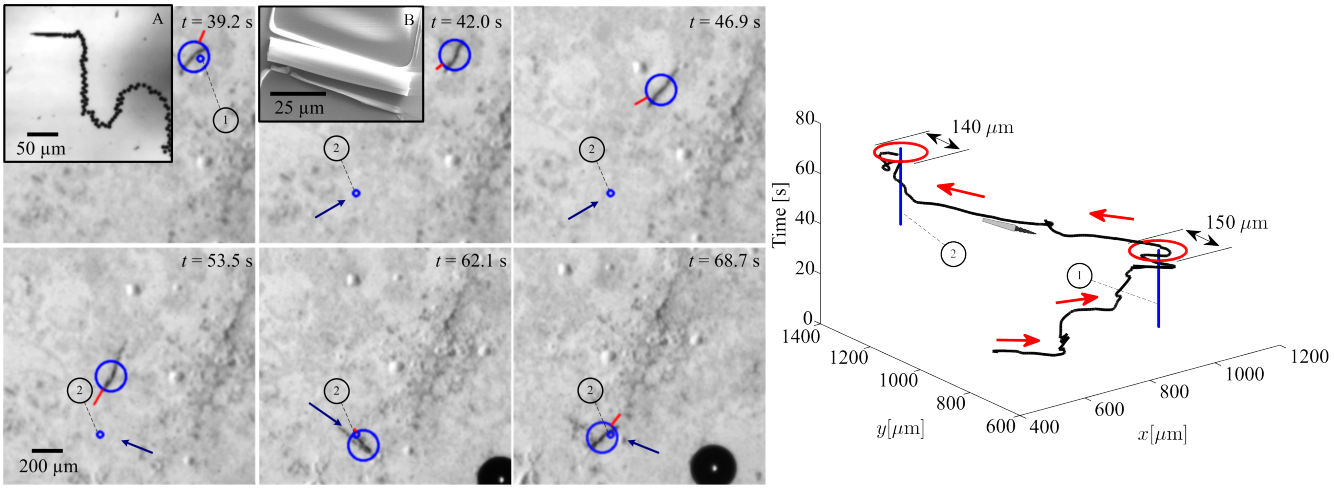

Fig. 4. Closed-loop motion control of a self-propelled microjet under the influence of the controlled magnetic fields. The microjet moves towards the reference positions (small blue circles) along the magnetic field lines generated using the control law (3). The microjet moves along the field lines using the propulsion force generated by the ejecting oxygen bubbles from its end. In this representative experiment, the microjet moves at an average velocity of 62 μm/s, and is positioned within the vicinity of two reference positions (represented by the solid blue lines in the right image). The closed-loop control system achieves a region-of-convergence of 150 μm and 140 μm in diameter for the first and second reference positions, respectively. The entries of the diagonal matrices ($\mathbf{K}_\mathrm{p}$ and $\mathbf{K}_\mathrm{d}$) are 15 s^{-2} and 5 s^{-1}, respectively. This experiment is done using 1 ml of hydrogen peroxide solution and Triton X at concentrations of 5% and 5%, respectively. The catalytic reaction is observed after the addition of 100 μl of hydrogen peroxide solution at concentration of 15%. Inset A shows the ejecting oxygen bubbles from one end of the microjet. Inset B shows a Scanning Electron Microscopy image of a microjet fixed to its substrate. The large blue circle is assigned by our feature tracking software [13] and represents the position of the microjet, whereas the red line represents its velocity vector.

55 μm and 30 μm for the first and second reference positions, respectively (Fig. 3). Control of the microjet is done using 1 ml of hydrogen peroxide solution and Triton X at concentrations of 5% and 5%, respectively. Our control system positions the microjet at an average velocity of 62 μm/s and within a ROC of 150 μm and 140 μm for the first and second reference positions, respectively (Fig. 4). All experiments are repeated 10 times, and we observe consistent results. Further, a minimum input control system is implemented on a three-dimensional (3D) electromagnetic setup, and we observe an average speed and the maximum root mean square (RMS) position tracking errors of the controlled microparticle to be 198 μm/s and 104 μm, respectively. The comparison with a proportional-integral (PI) control system shows that the minimum input control achieves 11% decrease in the current input.

IV. CONCLUSIONS AND FUTURE WORK

Point-to-point motion control of magnetic objects is demonstrated using a magnetic-based proportional-derivative control system. A cluster of iron oxide nanoparticles is positioned within the vicinity of a reference position (average ROC is 132 μm) at an average velocity of 190 μm/s ($\sim$2 body length

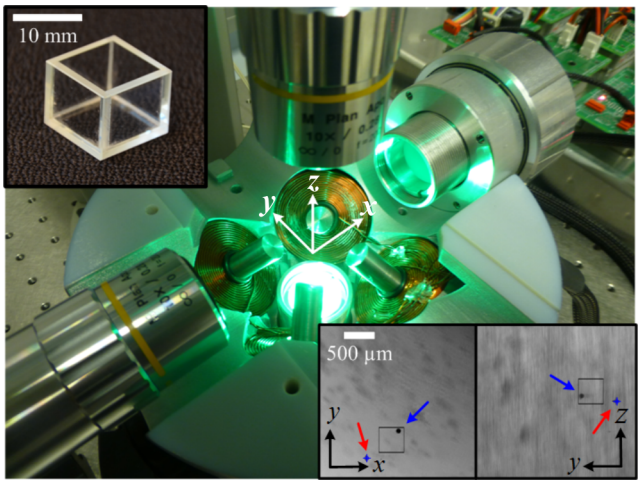

Fig. 5. Magnetic system for the closed-loop motion control of paramagnetic microparticles (PLAParticles-M-redF-plain from Micromod Partikeltechnologie GmbH, Rostock-Warnemuende, Germany) in three-dimensional (3D) space. The magnetic system consists of 8 iron-core electromagnets that surrounds a water reservoir, shown at the upper-left inset. The workspace of the magnetic system is $10\times10\times10$ mm^3. Our magnetic system provides autofocusing of the microparticles using two microscopic vision systems mounted on two linear motion stages (not shown). The magnetic system consists of upper and lower orthogonal sets of electromagnets. In the lower set, the electromagnets have 45 degrees orientation with respect to each other and with respect to the horizonal plane. In the upper set (not shown), electromagnets have 45 degrees and 90 degrees orientation with respect to the horizontal plane and the lower set, respectively. The bottom-right inset shows a microparticle, with an average diameter of 100 μm, moving towards a reference position in 3D space under the influence of the controlled magnetic fields generated using the minimum input control. The black box is assigned using our feature tracking software, whereas the blue and red arrows indicate the microparticle and the reference position, respectively [21].

per second) under the influence of the controlled magnetic field gradients. Self-propelled MTB and microjets are controlled at an average velocity of 28 μm/s and 90 μm/s ($\sim$5 and $\sim$2 body length per second), and positioned within an average ROC of 40 μm and 235 μm, respectively. Further, we investigate a magnetic-based minimum input control system to position paramagnetic microparticles in 3D space. The minimum input control system achieves point-to-point motion control, while minimizing the current at each of the electromagnets of a magnetic system. The closed-loop control characteristics of the magnetic-based minimum input control are compared to the characteristics of a PI controller.

As part of future work, our magnetic system will be integrated with an ultrasound-based imaging modality. In addition, our magnetic system will be redesigned to control magnetic objects in the three-dimensional space with varying fluid flow.

REFERENCES

[1] J. Wang and W. Gao, "Nano/microscale motors: biomedical opportunities and challenges," *ACS Nano*, vol. 6, no. 7, pp. 5745-5751, July 2012.

[2] B. J. Nelson, I. K. Kaliakatsos, and J. J. Abbott, "Microrobots for minimally invasive medicine," *Annual Review of Biomedical Engineering*, vol. 12, pp. 55-85, April 2010.

[3] R. Sinha, G. J. Kim, S. Nie, and D. M. Shin, "Nanotechnology in cancer therapeutics: bioconjugated nanoparticles for drug delivery," *Molecular Cancer Therapeutics*, Vol. 5, no. 8, pp. 1909-1917, August 2006.

[4] A. S. Lubbe, C. Bergemann, J. Brock, and D. G. McClure, "Physiological aspects in magnetic drug-targeting," *Journal of Magnetism and Magnetic Materials*, Vol. 194, no. 1-3, pp. 149-155, April 1999.

[5] S. Martel, M. Mohammadi, O. Felfoul, Z. Lu, and P. Pouponneau, "Flagellated magnetotactic bacteria as controlled MRI-trackable propulsion and steering systems for medical nanorobots operating in the human microvasculature," *International Journal of Robotics Research*, vol. 28, no. 4, pp. 571-582, April 2009.

[6] R. Dreyfus, J. Baudry, M. L. Roper, M. Fermigier, H. A. Stone, and J. Bibette, "Microscopic artificial swimmers," *Nature*, vol. 437, no. 6, pp. 862-865, October 2005.

[7] Y. F. Mei, G. Huang, A. A. Solovev, E. B. Urena, I. Monch, F. Ding, T. Reindl, R. K. Y. Fu, P. K. Chu, and O. G. Schmidt, "Versatile approach for integrative and functionalized tubes by strain engineering of nanomembranes on polymers," *Advanced Materials*, vol. 20, no. 21, pp. 4085-4090, November 2008.

[8] A. A. Solovev, Y. F. Mei, E. B. Urena, G. Huang, and O. G. Schmidt, "Catalytic microtubular jet engines self-propelled by accumulated gas bubbles," *Small*, vol. 5, no. 14, pp. 1688-1692, July 2009.

[9] Q. A. Pankhurst, J. Connolly, S. K. Jones, and J. Dobson, "Applications of magnetic nanoparticles in biomedicine," *Journal of Physics*, Vol. 36, no. 13, pp.167-181, July 2003.

[10] S. Martel, "Controlled bacterial micro-actuation," in *Proceedings of the International Conference on Microtechnologies in Medicine and Biology*, pp. 89-92, Okinawa, Japan, May 2006.

[11] S. Sanchez, A. A. Solovev, S. Schulze, and O. G. Schmidt, "Controlled manipulation of multiple cells using catalytic microbots," *Chemical Communication*, vol. 47, pp. 698-700, November 2010.

[12] M. P. Kummer, J. J. Abbott, B. E. Kartochvil, R. Borer, A. Sengul, and B. J. Nelson, "OctoMag: an electromagnetic system for 5-DOF wireless micromanipulation," *IEEE Transactions on Robotics*, vol. 26, no. 6, pp. 1006-1017, December 2010.

[13] I. S. M. Khalil, J. D. Keuning, L. Abelmann, and S. Misra, "Wireless magnetic-based control of paramagnetic microparticles," in *Proceedings of the IEEE RAS/EMBS International Conference on Biomedical Robotics and Biomechatronics (BioRob)*, pp. 460-466, Rome, Italy, June 2012.

[14] S. Martel and M. Mohammadi, "Using a swarm of self-propelled natural microrobots in the form of flagellated bacteria to perform complex micro-assembly tasks," in *Proceedings of the IEEE International Conference on Robotics and Automation (ICRA)*, pp. 500-505, Alaska, USA, May 2010.

[15] I. S. M. Khalil, F. van den Brink, O. S. Sukas, and S. Misra, "Microassembly using a cluster of paramagnetic microparticles," in *Proceedings of the IEEE International Conference on Robotics and Automation (ICRA)*, pp. 5507-5512, Karlsruhe, Germany, May 2013.

[16] I. S. M. Khalil, V. Magdanz, S. Sanchez, O. G. Schmidt, L. Abelmann, and S. Misra, "Magnetic control of potential microrobotic drug delivery systems: nanoparticles, magnetotactic bacteria and self-propelled microjets," in *Proceedings of the IEEE Engineering in Medicine and Biology Society (EMBC)*, pp. 5299-5302, Osaka, Japan, July 2013.

[17] Y. F. Mei, A. A. Solovev, S. Sanchez, and O. G. Schmidt, "Rolled-up nanotech on polymers: from basic perception to self-propelled catalytic microengines," *Chemical Society Review*, vol. 40, no. 5, pp. 2109-2119, May 2011.

[18] H. C. Berg, "Random walks in biology," *Princeton University Press*, Princeton, New Jersey, 1993.

[19] Y. R. Chemla, H. L. Grossman, T. S. Lee, J. Clarke, M. Adamkiewicz, and B. B. Buchanan, "A new study of bacterial motion: superconducting quantum interference device microscopy of magnetotactic bacteria," *Biophysical Journal*, vol. 76, pp. 3323-3330, June 1999.

[20] I. S. M. Khalil, M. P. Pichel, L. Abelmann, and S. Misra, "Closed-loop control of magnetotactic bacteria," *International Journal of Robotics Research*, vol. 32, no. 6, pp. 636-668, May 2013.

[21] I. S. M. Khalil, R. M. P. Metz, B. A. Reefman, and S. Misra, "Optimal motion control of paramagnetic microparticles in three-dimensional space," in *Proceedings of the IEEE International Conference of Robotics and Systems (IROS)*, Tokyo, Japan, November 2013. In Press.

System integration: A comparison of the SCATh and the CASCADE system architecture

Vincent Meiser
Zurich University of Applied Sciences
Institute of Mechatronic Systems
Winterthur, Switzerland
Email: vincent.meiser@zhaw.ch

Dejan Šeatović
Zurich University of Applied Sciences
Institute of Mechatronic Systems
Winterthur, Switzerland
Email: dejan.seatovic@zhaw.ch

***Abstract*—With a focus toward system architecture, the SCATh and CASCADE platforms are outlined and a comparison is drawn to show the characteristics of the medical platforms and their differences. In the field of system integration, the architecture is a very basic element of a new system design and development. In the prior project, SCATh, a Windows-based non-real time capable architecture was used. A hard real-time application set will be implemented in CASCADE using ready-to-use frameworks; Robot Operating System (ROS) and Open Robot Control Software (OROCOS) to achieve an accelerated development process. To illustrate the differences between the platforms, their development environment with regard to hard- and software is presented. The crucial elements of the system design, amongst others the multi-tier architecture, are revealed and the consequences for the development process are shown.**

I. Introduction

A European Union research project *Smart Catheterization* (SCATh) [1] was carried out over the last 3 years. Its subject was research on and development of a catheter guidance system for surgical interventions. A challenging aspect was the system integration of multiple, partly independent system components into one operational platform, whereby inhomogeneous software engineering skills and experiences turned out to be major hurdles for a fluent development process. A recently started project named *Cognitive AutonomouS CAtheter operating in Dynamic Environments* (CASCADE) [2] deals with a similar subject, but it is more focused on robotic than medical developments. The task of system integration is even more important in CASCADE, since the expected outcome of the project is an operational prototype. Hence the SCATh platform is presented here mainly with regard to the system architecture to serve as example and to offer background information for prospective developments. A comparison to the CASCADE architecture as currently planned is drawn.

II. SCATh platform

The SCATh platform was meant to serve as an integration framework for the different components developed by each project partner. A straightforward and small-scale environment was one of the targets during architecture design and implementation, to supervise and maintain the development progress of the project without increasing complexity of the development process itself. Hard real-time capabilities were limited to an additional device, a *National Instruments* (NI) real-time target, which was in charge of controlling the catheter and the sensors attached to it.

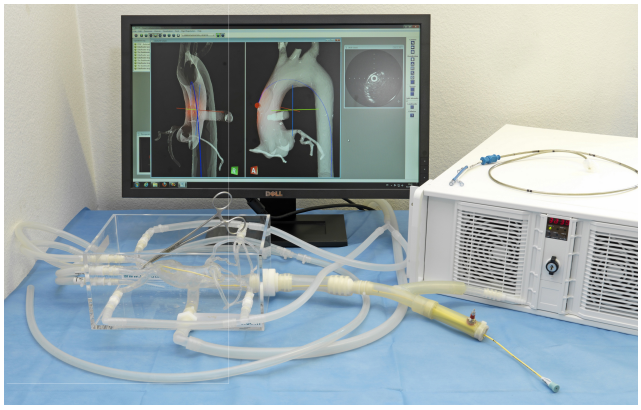

Fig. 1: Basic SCATh Platform Setup

A. Development environment

The target operating system (OS) for the SCATh platform is Windows 7, hence Visual Studio is defined as the integrated development environment (IDE). Several external libraries are integrated into the SCATh application for mathematical calculations, visualization and network communication. The programming language is C++ and Compute Unified Device Architecture (CUDA).

On the hardware side, the SCATh platform consists of an industrial PC for high performance computing (HPC) with sufficient RAM size (24 GB). The HPC is extended with an NVIDIA Tesla card, which adds additional data processing capability with the use of a General Purpose Graphics Processing Unit (GP-GPU). In SCATh this additional computation unit is used for Finite Element Modelling (FEM). The high-performance computer is also called Execution Environment Computer (EEC). The NI real-time target represents the second hardware component. A *LabView* application was implemented to forward measurement data provided by catheter sensors to the EEC.

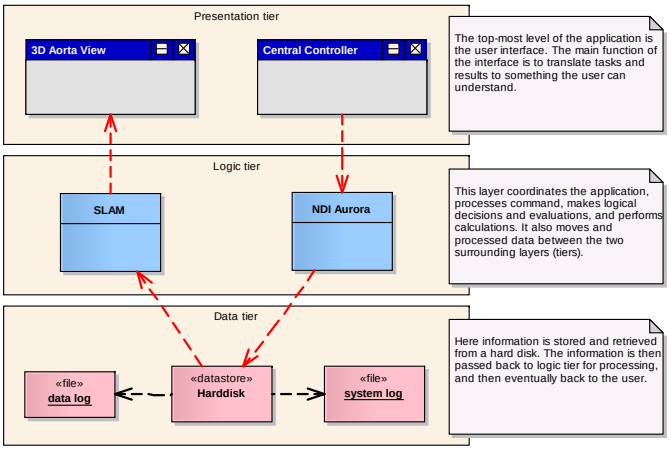

Fig. 2: Three-tier Architecture with Presentation, Application (Logic) and Data tier

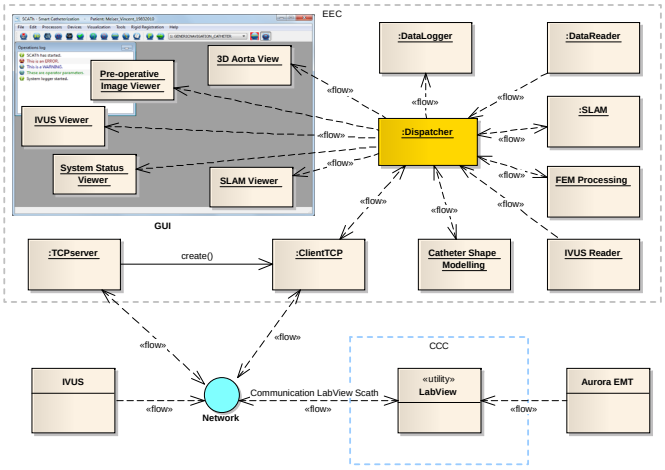

Fig. 3: Data Flow within SCATh Platform

B. System architecture

The SCATh system architecture consists of state-of-the-art software components, an abstract interface pattern as well as a provider-subscriber pattern [3], [4]. The design is based upon a three-tier architecture consisting of a data tier (data model), an application tier (logic) and a presentation tier (GUI). The three-tier architecture gathers logically separated parts of the software and minimises their dependencies. Fig. 2 displays a three-tier architecture.

The pattern of providing information to an arbitrary amount of subscribers is shown in Fig. 3. A *Dispatcher* instance controls all data transfer going throughout the SCATh platform. Subscribers such as *3D Aorta View*, *SLAM* or *FEM Processing* can subscribe for specific data types to receive them or can produce data and send it to the Dispatcher. This forwards the data to all components according to the subcriptions.

The most challenging part of the framework design is to provide a flexible architecture that is able to survive significant requirement changes. This goal has been fully achieved since requirement changes do not or only mariginally affect the system and framework architecture. This way, basic constraints for a robust system, reliability and stability, can be assured.

C. Outcome and experiences

The described SCATh platform provides a user friendly and flexible software framework, which is used by all project partners. It is designed to integrate a wide range of position, force and vision sensors with minimal implementation time. All partners used the framework for design and implementation of their own components. Integration of third-party libraries and components is mostly effortless. Therefore, the project schedule was not affected by late requests for additional components. The key to success of the SCATh platform lies in the approximately uniform level of understanding of essential parts of the framework, which means similar level of knowledge in areas of software engineering, implementation, etc. The usability study of the final SCATh platform in a clinical environment was successfully performed.

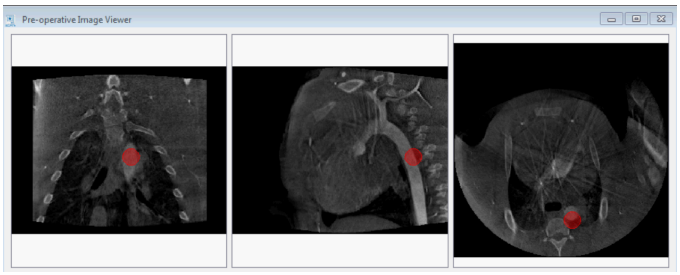

Fig. 4: SCATh Pre-operative Image Viewer, realized using *GDCM* library to cut slices from CT/MR: In automatic mode the viewer shows the appropriate slices of the CT/MR volume at actual catheter tip position.

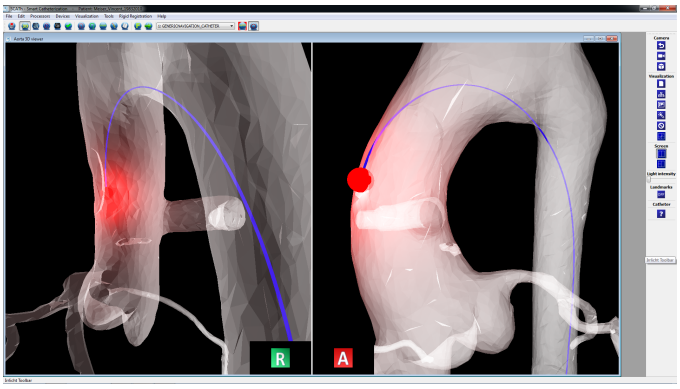

Fig. 5: SCATh three-dimensional Aorta Viewer, realized using *Irrlicht* graphics engine: The viewer displays a 3D model of a human aorta. If the catheter tip is approaching to a safety critical volume, a colored signal is sent to the operator.

Fig. 4 and Fig. 5 depict two graphical elements of the SCATh platform, which will be transfered to the CASCADE project to the greatest extent. This will be issued in the second part of this paper when it comes to the description of the platform's differences.

III. CASCADE SYSTEM ARCHITECTURE

The following section provides an outlook on the architecture planned for the CASCADE project. For multiple reasons, in particular the real-time capabilities, the architecture of CASCADE is distinctly different to the SCATh architecture. The software and hardware needed by the CASCADE system should be as flexible as possible without impinging on the project goals and targets. Therefore all system parts are encapsulated into modules (components). Components are completely independent applications, they only depend on a minimum set of other modules. It is possible to build and maintain a variety of configurations of the CASCADE system which consist of a complete set or subset of the available modules. The modules can be defined as components for example, as described in [5], [6]. The advantage of component-oriented programming is that every component is reusable and self-contained. Components are based strictly on a producer-consumer pattern, where the interface represents the one and (usually) only dependency between two different components.

A. Hard real-time constraints

Since CASCADE has strong hard real-time constraints such as catheter control and safety components, the platform requires a real-time capable operating system. Linux itself does not offer real-time capabilities, but if it is combined with a real-time patch, e.g. Xenomai, Linux OS can serve as a real-time system. Furthermore, only a few of the CASCADE components have hard real-time constraints, others are of soft real-time or non real-time type. A challenging task is the synchronization of these components without computing performance loss and real-time constraints violation. Both aspects increase the complexity of the system and its architecture, and prolong the first development phase of setting up the development environment. For better understanding, the environment is explained subsequently in the system design (section III-B).

The development of software frameworks for surgical robotics is a topical subject in several other research projects. Amongst others, the *EuRoSurge* project aims at developing a conceptual integration platform for Computer and Robot Aided Surgery (CRAS) [7].

B. System design

The CASCADE platform, which is under continuous development over the duration of the project, is facing several challenges. For example, the reliable communication between and coordination of a large number of distributed components and hard real-time constraints upon the execution of several components. Here, the ROS and OROCOS robotic frameworks (Meta Operating Systems) come into the picture. The CASCADE platform will be built on top of these frameworks and make use of their functionality whenever it makes sense and simplifies the development process. Considering modularity, independence, robustness and ease of development, a component-based architecture is chosen as the architecture under development. Components or nodes are separate processes that ideally only fulfill one single isolated task.

The system design is based upon a three-tier architecture as already described in section II-B. Individual CASCADE components are allocated to one particular tier. This enables a clear and logical separation of system parts, which simplifies the development process and encapsulates independent parts. The system design is displayed in Fig. 6.

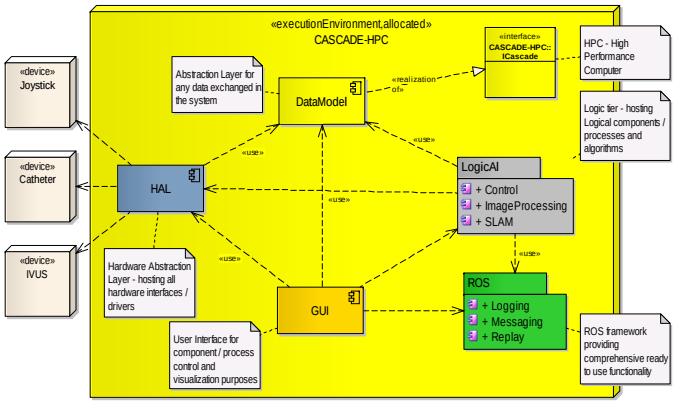

Fig. 6: CASCADE System Design

The data model defines the interface between the different components. Any data exchange within the platform will be performed in accordance to this interface. Since it is planned to use the ROS messaging system, the data model will implement functionality (create ROS messages, etc.) to use the ROS framework. Data exchanged between components within the CASCADE interface can range from position coordinates and force values all the way up to imaging data. The data model represents a single interface for the CASCADE platform. There is no other component that provides interface functionality.

The logic tier contains the processing logic of the components. As mentioned earlier, this layer is meant to be independent from other shared libraries. The logic tier provides processing components based on the interface defined by the DataModel.

The GUI represents the user interface and provides a visualization front end for the operator (surgeon). It is a layer on top of the DataModel and the Logic layer, which are hidden from the user. The GUI operates in detached mode; it fulfills no real-time constraints and is designed for user interaction, with sufficient performance for user-friendly operability.

As can be seen in Fig. 6, the logic tier and the GUI are dependent on the ROS framework. Especially within these tiers, the ROS functionality (messaging system, logging, replay, etc.) as well as the OROCOS functionality (hard real-time task definition and execution) is used. Furthermore, the architecture foresees a pre-definition of all system components considering their real-time characteristics and needs by the system integrator. The partners responsible for one or multiple components can start their development upon these pre-defined parts. This reduces the need for high-level understanding of certain frameworks and so decreases the development time. Prior to this component definition, the requirements of all system parts and subsequently the specification are essential steps in the development process.

TABLE I: Development Environment - Software

Project	*SCATh*	*CASCADE*
OS	Windows XP	Linux (Ubuntu LTS 12.04)
IDE	Visual Studio	Eclipse
Programming language	C++, CUDA	C++, CUDA
Compiler	MVC++	g++
Libraries	Irrlicht, OpenCV Qt, GDCM	OpenCV, rviz Qt, any graphics engine
Frameworks		ROS, OROCOS Xenomai RT-kernel

TABLE II: Development Environment - Hardware

Project	*SCATh*	*CASCADE*
Devices	High-performance computer/IPC	High-performance computer/IPC
	NI real-time target (PXI)	NI real-time target (PXI/cRIO)
	Epiphan VGA2Ethernet frame grabber	opt: Epiphan VGA2Ethernet frame grabber
		FPGA, ...
Internal memory	24 GB	24..64 GB
Graphics card	NVIDIA Tesla C2075	NVIDIA Tesla C2075, ...
Communication	Ethernet	EtherCAT, ...

C. Development environment

The development environment is distinctly different from the one in SCATh. A hard real-time capable OS was chosen to fulfill the constraints. The ROS framework is used for messaging, logging and replay, and the OROCOS connected to the Xenomai RT-kernel will provide hard real-time task definition and execution. A listing of software elements is given in Table I.

With the change of OS, the external libraries (Qt, OpenCV, GDCM, etc.) have also become partly obsolete. To use SCATh components as the *Pre-operative Image Viewer* and the *3D Aorta View* in the new CASCADE platform, larger modifications are necessary. On the other hand, this enables a review and improvement step on the way to a highly stable and robust CASCADE platform. To complete the development environment used in the SCATh and the CASCADE project, a listing of hardware equipment is given in Table II. The hardware components are mostly similar except for the real-time specific system parts, EtherCAT, FPGAs, etc. The purchase of hardware is still pending. To fulfill all real-time constraints and run the appropriate components within one system, it might be necessary to use a high-end HPC, such as Intel i7-39xx, Xeon E3-xxxx or E5-xxxx, combined with sufficient RAM size.

IV. Conclusion

Although the SCATh and CASCADE system architectures have several similarities, there are distinct differences between the platforms (architectures). The basic elements of a component-based system built upon a three-tier architecture are similar. However, the SCATh platform was developed in a Windows environment without hard real-time capabilities (except for the LabView part), whereas the CASCADE platform is designed to completely fulfill the given hard real-time constraints. Due to this fact, the CASCADE architecture is fundamentally different and more complex than that of SCATh. The platform development effort with regard to the architecture will be much higher, since more frameworks and external libraries will be integrated to one system. Once this first hurdle is overcome and the basic system setup is complete, a well-defined and structured architecture will be available for the given tasks to move towards project targets.

References

[1] "SCATh smart catheterization, the SCATh project," http://www.scath.net/, July 2013. [Online]. Available: http://www.scath.net/

[2] "CASCADE cognitive autonomous catheter operating in dynamic environments, the CASCADE project," http://www.cascade-fp7.eu/, July 2013. [Online]. Available: http://www.cascade-fp7.eu/

[3] E. Gamma, R. Helm, R. Johnson, and J. Vlissides, *Design patterns: elements of reusable object-oriented software*. Addison-Wesley Professional, 1995.

[4] H. Gomaa, *Software modeling and design : UML, use cases, patterns, and software architectures*. Cambridge University Press, 2011.

[5] "Nodes - ros wiki, [online]. available: http://www.ros.org/wiki/nodes, [accessed: 23-may-2013]." [Online]. Available: http://www.ros.org/wiki/Nodes/

[6] K. Andy Ju An Wang, *Component-Oriented Programming*. John Wiley & Sons, Inc. All rigths reserved, 2005.

[7] P. Fiorini, "Linking patient safety and automation in robotic surgery: the eurosurge project," in *ICRA2012 Workshop Modular Surgical Robotics: how can we make it possible?* Altair Robotics Laboratory, Department of Computer Science, University of Verona, Italy, 2012.

Nomenclature

ROS	Robot Operating System
OROCOS	Open Robot Control Software
SCATh	Smart Catheterization
CASCADE	Cognitive AutonomouS CAtheter operating in Dynamic Environments
OS	Operating System
HPC	High Performance Computing
GP-GPU	General Purpose Graphics Processing Unit
FEM	Finite Element Modelling
EEC	Execution Environment Computer

Minimally invasive, robot assisted cochlear implantation

Stefan Weber, Brett Bell, Nicolas Gerber, Tom Williamson
ARTORG Center
University of Bern
Bern, Switzerland

Peter Brett, Xinli Du
Brunel Institute for Bioengineering
Brunel University
London, UK

Marco Caversaccio
Department of ENT, Head and Neck Surgery
Bern University Hospital
Bern, Switzerland

David Proops, Chris Coulson, Andrew Reid
Department of Otolaryngology
Queen Elizabeth Hospital
Birmingham, UK

Cochlear implants allow the restoration of hearing function in patients with severe to profound sensorineural hearing loss through the direct stimulation of the auditory nerve by an electrode array inserted into the inner ear. Typically, access to the cochlea is gained through the performance of a mastoidectomy, which involves the removal of a large portion of the mastoid bone, allowing the surgeon to visualize and protect vital structures within the mastoid during milling. Once access to the cochlea has been achieved, the surgeon may insert the electrode through the round window, or alternatively through an artificial access called a cochleostomy. Recent advances in image guided robotics have allowed dramatic changes in the performance of both stages of this procedure. Recent work at the University of Bern has seen the realization of a robotic system designed specifically for minimally invasive cochlear implantation. The system enables significantly reduced invasiveness by removing the need for a mastoidectomy, replacing this with a direct tunnel approach known as direct cochlear access (DCA). Meanwhile, work at Brunel University has focused on improving the safety and accuracy of inner ear access through the cochleostomy. This work describes both of these systems individually and discusses the implications and opportunities associated with the combination of these devices.

Keywords—cochleostomy; robotics; image guidance; cochlear implant; direct cochlear access

I. INTRODUCTION

A. Minimally Invasive Cochlear Access

Direct cochlear access (DCA) is a minimally invasive method for accessing the inner ear. It involves the drilling of a trajectory directly from the surface of the temporal bone to the cochlea, thereby circumventing the need for a mastoidectomy. The mastoidectomy, which represents the current state of the art for inner ear access, comprises the milling of a large cavity in the mastoid region of the temporal bone, allowing the surgeon to visualize and protect vital structures while gaining access to the cochlea. The realization of a minimally invasive approach is of particular interest considering the diameter of a cochlear implant electrode (typically less than 1.5 mm) when compared to the size of the cavity created during the mastoidectomy. Typically, a DCA trajectory will pass from the mastoid through the facial recess (formed by the divergence of the facial nerve and chorda tympani) to the round window. While the size of the cavity created by drilling (tunnel diameter 1.5 – 2 mm) is more appropriate considering the size of the electrode to be placed, the anatomy of the facial recess significantly limits the area in which a trajectory can be drilled. It also leads to substantial accuracy constraints: in order to avoid damaging the facial nerve or other anatomy when passing blindly through the facial recess the surgeon must be confident in the position of the drill relative to vital anatomy. A significant body of research exists on DCA, with a number of groups evaluating a number of different approaches including standard navigation [1-3], patient specific templates [4-6] and robotics [7-13].

B. Robot Assisted Cochleostomy

The cochleostomy is a key component in many cochlear implantation procedures. The technique involves the penetration of the outer bone tissue of the cochlea in order to expose the scala in preparation for insertion of a cochlear electrode array. Surgical performance of a cochleostomy presents a number of challenges: conventionally the process is completed manually using a hand held drill while working under a microscope. The cochlear is accessed either from the promontory exposed through the ear canal or from its basal turn through a mastoidectomy. In either approach it is necessary to reach the desired position at the cochlea with precision to drill the access, minimize trauma caused by mechanical disturbance and avoid overrun into the scala and subsequent perforation of the fragile endosteal membrane. By avoiding penetration of the endosteum, debris produced when drilling the access hole can be removed and sterile conditions preserved. Furthermore, accurate cochleostomy placement can have profound effects on the intra-cochlear anatomy post insertion, with incorrect placement potentially leading to damage of the basilar membrane or other structures upon insertion [14].

II. Materials and Methods

A. Minimally invasive cochlear access

A robotic system, shown in Figure 1, was designed specifically for minimally invasive cochlear implantation procedures. The lightweight (5.5 kg), 5 degree of freedom robotic arm can be mounted directly to the side rails of a standard OR table with a dedicated robot mount, which includes a non-invasive patient fixation mechanism for minimization of patient movement. A force torque sensor is fitted at the robot wrist, enabling haptic control, semi-automatic registration and measurement of drilling process variables.

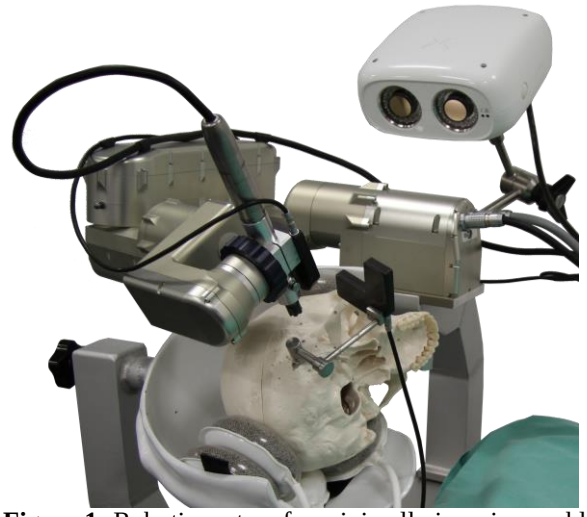

Figure 1: Robotic system for minimally invasive cochlear implantation.

A commercially available high accuracy tracking system (CamBar B1, Axios3d, Germany) is integrated into the robot control software; the tracking system is used in combination with custom active tracking markers for visual servoing control. Finally, custom drilling tools and a self-developed drill hand piece provide increased accuracy through reduced tool bending (increased tool stiffness) and reduced backlash. The safety of the robotic procedure is ensured through the integration of additional sensor sources, including position information obtained from the correlation of drilling force and mastoid density, and functional information through integrated facial nerve monitoring.

The system also includes a dedicated planning software, which guides the surgeon through each of the steps required to plan a minimally invasive CI procedure. Fiducial screws and important anatomical structures are segmented by the user with the aid automatic and semi-automatic segmentation tools [15]. Once the structures have been defined, the surgeon can then plan a trajectory which avoids these.

Assessment of the feasibility of minimally invasive cochlear implantation was completed in an in-vitro cadaver study, described in detail in [16]. A total of eight temporal bone specimens underwent the full proposed clinical workflow as well as an additional post-operative evaluation step. The accuracy of the robotic system was assessed through the co-registration of pre- and post-operative images; the drilled tunnel was segmented and compared to the planned position of the tunnel at the entrance position on the mastoid and at the planned target position. Additionally, the time required for the completion of each step was recorded. Note that the target in all eight cases was the round window; no cochleostomy was completed.

B. Robot Assisted Cochleostomy

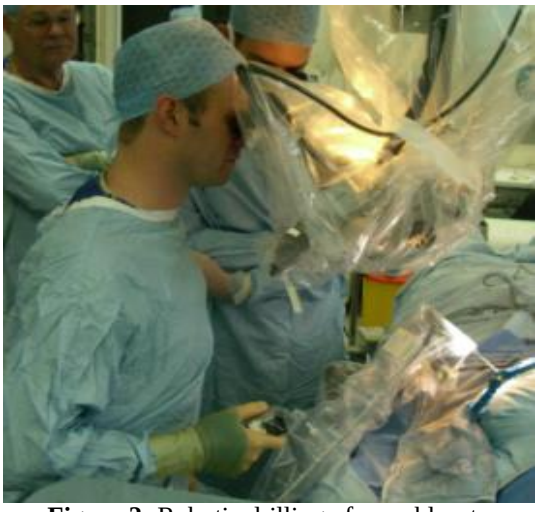

Figure 2: Robotic drilling of a cochleostomy.

A system with the ability to discriminate tissue and changes in tissue composition ahead on the drilling trajectory was developed for the completion of cochleostomy procedures [17]. The system consists of linear and rotational drives to feed and rotate standard surgical burrs. This system is then attached to a flex lock arm, permitting free movement and stabilization of the drill. The burr is advanced onto the surface of the cochlea and the autonomous process of breaking through the bone tissue to expose the endosteum through a window of specific diameter begins. The drilling is entirely controlled through a hardwired control unit with the surgeon retaining executive control. Autonomous perception of critical phenomena and structures is completed using the coupled force and torque drilling transients in real-time (Figure 2). This enables automated selection of appropriate control strategies to achieve a precise and consistent result with respect to the flexible tissues. The most important responsibility of the system is to prepare the window on the endosteum without penetration.

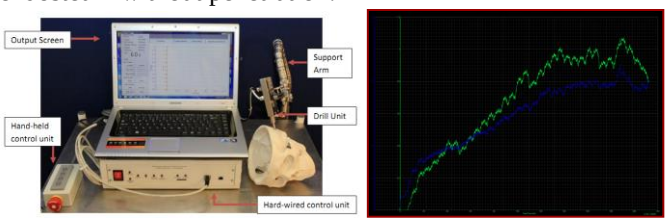

Figure 3: The micro-drilling system for controlling exposure of the endosteum without penetration uses force and torque transients to discriminate the state of tissue-tool interaction.

The controller analyses the force and torque imparted onto the drill bit in real time (Figure 3) to discriminate the state of the

tissue-tool point interaction from which actuation strategies are selected.

The robotic tool was comprehensively tested in pre-clinical porcine and cadaver studies, as well as being used in the operating theater for the performance of sensor guided cochleostomy.

III. RESULTS

A. *Minimally invasive cochlear access*

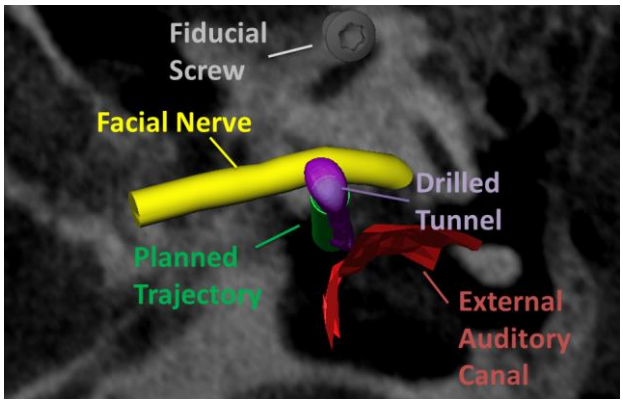

Figure 4: Post-operative analysis of drilling accuracy.

The robotic system allowed minimally invasive inner ear access without damage to surrounding anatomy in all cases. An accuracy of 0.08 ± 0.05 mm was observed at the surface of the mastoid; an accuracy of 0.15 ± 0.08 mm was observed at the planned target. Full electrode insertion through the round window approach was achieved in seven of eight cases: in a single case two electrode pairs remained outside of the cochlea. The setup of the robotic system took on average 7.1 minutes; positioning of the patient and fixation of the reference tracking marker an average of 4.6 minutes; patient to image registration approximately 3 minutes. The drilling, performed in 3 stages, required an average of 6 minutes to complete. The total procedure took, on average, approximately 21 minutes. Anatomy segmentation and trajectory planning was completed in less than 20 minutes in all cases.

B. *Robot Assisted Cochleostomy*

The system allows information about the state of the drilling process to be extracted from observed force and torque data; subsequently drill breakthrough can be predicted and controlled, minimizing trauma to the inner ear. Laboratory investigations confirmed robustness of the techniques to different angles of incidence with tissue interfaces (Figure 5) and tissue thickness [18].

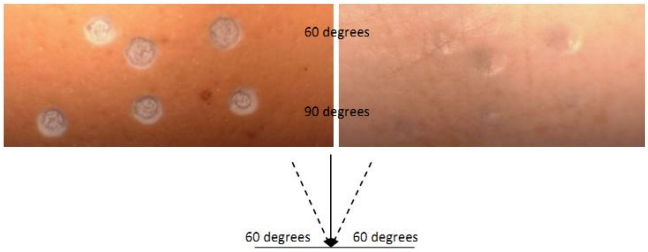

Figure 5: Robustness to angle of incidence of drilling trajectory (bone tissue and membrane aspects)

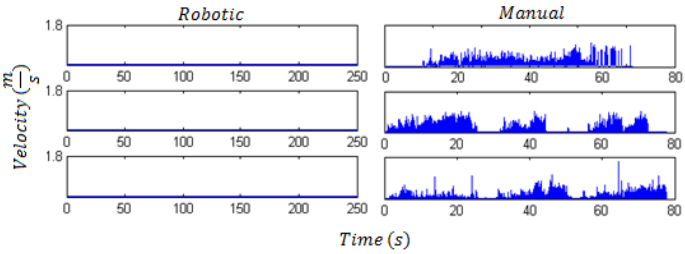

Figure 6: Intra-cochlear disturbance amplitude: robotic and manual drilling

Laser vibrometric measurements during cochleostomy demonstrated that the robotic approach produced only 1% of the peak disturbance amplitude of manual drilling (Figure 6) [19]. It was also shown that cochleostomies were uniform and that the endosteum remained intact. The results indicate that using the robotic drill reduces trauma within the cochlea and that the approach for detection is robust and consistent when subjected to a wide variation of operating and tissue conditions.

IV. DISCUSSION

Comprehensive pre-clinical validation of the image guided robotic system for minimally invasive cochlear access has established an overall accuracy sufficient for the safe completion of the procedure. In addition to being highly accurate, the system has been designed with eventual clinical integration in mind. Additionally, novel safety features based on alternative sensor sources provide an additional level of safety on top of the high accuracy workflow. The autonomous system for cochleostomy is able to penetrate the cochlear while leaving the endosteal membrane intact, thus maintaining sterility and avoiding the influx of debris. A decrease in complications, as well as increased retention of residual hearing, is expected as a result of this approach compared with conventional methods

Recent debate about the best route for cochlear electrode insertion (round window or cochleostomy) stems mostly from the desire for clinicians to retain residual hearing loss by minimizing intra-cochlear damage during the insertion process. Most literature advocates a round window approach when possible due to the increased trauma associated with the manual drilling process [20-23]. The robotic systems described within have proven successful in allowing both minimally invasive access to the cochlea and trauma free cochleostomy for electrode insertion. The combination of these two complimentary approaches will allow safe and reliable execution of the cochleostomy procedure, as well as highly accurate placement of the cochleostomy site, potentially leading to decreased trauma during insertion and increased retention of residual hearing.

REFERENCES

[1] J. Schipper, A. Aschendorff, I. Arapakis, T. Klenzner, C. B. Teszler, G. J. Ridder, and R. Laszig, "Navigation as a quality management tool in cochlear implant surgery.," *The Journal of laryngology and otology*, vol. 118, no. 10, pp. 764–70, Oct. 2004.

[2] R. F. Labadie, P. Chodhury, E. Cetinkaya, R. Balachandran, D. S. Haynes, M. R. Fenlon, A. S. Jusczyzck, and J. M. Fitzpatrick, "Minimally invasive, image-guided, facial-recess approach to the middle ear: demonstration of the concept of percutaneous cochlear access in vitro.," *Otology & neurotology : official publication of the American*

Otological Society, American Neurotology Society [and] European Academy of Otology and Neurotology, vol. 26, no. 4, pp. 557–62, Jul. 2005.

[3] O. Majdani, S. H. Bartling, M. Leinung, T. Stöver, M. Lenarz, C. Dullin, and T. Lenarz, "[Image-guided minimal-invasive cochlear implantation--experiments on cadavers].," *Laryngo- rhino- otologie*, vol. 87, no. 1, pp. 18–22, Jan. 2008.

[4] R. F. Labadie, J. Mitchell, R. Balachandran, and J. M. Fitzpatrick, "Customized, rapid-production microstereotactic table for surgical targeting: description of concept and in vitro validation.," *International journal of computer assisted radiology and surgery*, vol. 4, no. 3, pp. 273–80, May 2009.

[5] R. Balachandran, J. E. Mitchell, G. Blachon, J. H. Noble, B. M. Dawant, J. M. Fitzpatrick, and R. F. Labadie, "Percutaneous cochlear implant drilling via customized frames: an in vitro study.," *Otolaryngology--head and neck surgery : official journal of American Academy of Otolaryngology-Head and Neck Surgery*, vol. 142, no. 3, pp. 421–6, Mar. 2010.

[6] R. F. Labadie, R. Balachandran, J. E. Mitchell, J. H. Noble, O. Majdani, D. S. Haynes, M. L. Bennett, B. M. Dawant, and J. M. Fitzpatrick, "Clinical validation study of percutaneous cochlear access using patient-customized microstereotactic frames.," *Otology & neurotology : official publication of the American Otological Society, American Neurotology Society [and] European Academy of Otology and Neurotology*, vol. 31, no. 1, pp. 94–9, Jan. 2010.

[7] C. J. Coulson, A. P. Reid, D. W. Proops, and P. N. Brett, "ENT challenges at the small scale.," The international journal of medical robotics + computer assisted surgery : MRCAS, vol. 3, no. 2, pp. 91–6, Jun. 2007.

[8] H. Eilers, S. Baron, T. Ortmaier, and B. Heimann, "Navigated , robot assisted drilling of a minimally invasive cochlear access," *Communication*, no. April, 2009.

[9] S. Baron, H. Eilers, B. Munske, J. L. Toennies, R. Balachandran, R. F. Labadie, T. Ortmaier, and R. J. Webster, "Percutaneous inner-ear access via an image-guided industrial robot system," *Proceedings of the Institution of Mechanical Engineers, Part H: Journal of Engineering in Medicine*, vol. 224, no. 5, pp. 633–649, May 2010.

[10] T. Klenzner, C. C. Ngan, F. B. Knapp, H. Knoop, J. Kromeier, A. Aschendorff, E. Papastathopoulos, J. Raczkowsky, H. Wörn, and J. Schipper, "New strategies for high precision surgery of the temporal bone using a robotic approach for cochlear implantation.," *European archives of oto-rhino-laryngology : official journal of the European Federation of Oto-Rhino-Laryngological Societies (EUFOS) : affiliated with the German Society for Oto-Rhino-Laryngology - Head and Neck Surgery*, vol. 266, no. 7, pp. 955–60, Jul. 2009.

[11] L. B. Kratchman, G. S. Blachon, T. J. Withrow, R. Balachandran, R. F. Labadie, and R. J. Webster, "Design of a bone-attached parallel robot for percutaneous cochlear implantation.," *IEEE transactions on bio-medical engineering*, vol. 58, no. 10, pp. 2904–10, Oct. 2011.

[12] J.-P. Kobler, J. Kotlarski, J. Oltjen, S. Baron, and T. Ortmaier, "Design and analysis of a head-mounted parallel kinematic device for skull surgery.," *International journal of computer assisted radiology and surgery*, vol. 7, no. 1, pp. 137–49, Jan. 2012.

[13] B. Bell, C. Stieger, N. Gerber, A. Arnold, C. Nauer, V. Hamacher, M. Kompis, L. Nolte, M. Caversaccio, and S. Weber, "A self-developed and constructed robot for minimally invasive cochlear implantation.," *Acta oto-laryngologica*, pp. 1–6, Mar. 2012.

[14] R.J. Briggs, M. Tykocinski, K. Stidham, J.B. Roberson, "Cochleostomy site: implications for electrode placement and hearing preservation.," *Acta Oto-Laryngologica*, 2005 Aug;125(8):870-6.

[15] N. Gerber, B. Bell, M. Kompis, C. Stieger, M. Caversaccio, S. Weber, "A software tool for preoperative planning of implantable hearing devices.," *International journal of computer assisted radiology and surgery*, vol. 7, no. 1, pp. 134-35, Jan. 2012.

[16] B. Bell, N. Gerber, T. Williamson, K. A. Gavaghan, W. Wimmer, M. Caversaccio, and S. Weber, "In Vitro Accuracy Evaluation of Image-Guided Robot System for Direct Cochlear Access," Otology & Neurotology, in print, 2013.

[17] R. Taylor, X. Du, D. Proops, A. Reid, C. Coulson, and P.N. Brett, "A sensory-guided surgical micro-drill", *Proc IMechE, Part C, Journal of Mechanical Engineering Science*, July 1, 2010, vol. 224, no. 7, pp. 1531-1537

[18] X. Du, M.Z. Assadi, P.N. Brett, J. Dolton, D. Proops, and C. Coulson, "Robustness analysis of a smart surgical drill for cochleostomy", *Int J Medical Robotics and Computer Assisted Surgery*, 2013 Mar, vol. 9, no. 1, pp. 119-26.

[19] C. Coulson, M.Z. Assadi, X. Du, P.N. Brett, and D.Proops, "Smart micro-drill for cochleostomy formation: A comparison of cochlear disturbances with manual drilling and a human trial", *Cochlear Implants International*, 2013 Mar, vol. 14, no. 2, pp. 98-106

[20] S. Havenith, M.J Lammers, R.A. Tange, F. Trabalzini, A. Della Volpe, G.J. van der Heijden, W. Grolman, "Hearing preservation surgery: cochleostomy or round window approach? A systematic review.," *Otology & Neurotology*, 2013 Jun;34(4):667-74

[21] R.J. Briggs, M. Tykocinski, J. Xu, F. Risi, M. Svehla, R. Cowan, T. Stover, P. Erfurt, T. Lenarz, "Comparison of round window and cochleostomy approaches with a prototype hearing preservation electrode.," *Audiology & Neuro-otology*, 2006;11 Suppl 1:42-8.

[22] C. Richard, J.N. Fayad, J. Doherty, F.H. Linthicum Jr., "Round window versus cochleostomy technique in cochlear implantation: histologic findings.," *Otology & Neurotology*, 2012 Sep;33(7):1181-7

[23] D.A. Gudis, M. Montes, D.C. Bigelow, M.J. Ruckenstein, "The round window: is it the "cochleostomy" of choice? Experience in 130 consecutive cochlear implants.," *Otology & Neurotology*, 2012 Dec;33(9):1497-501

The µRALP Project: New Technologies and Systems for Robot-Assisted Laser Phonomicrosurgery

Leonardo S. Mattos and Nicolas Andreff

***Abstract*—This presentation will summarize the objectives, challenges, activities and targets of the EU project µRALP, which is dedicated to the creation of a new class of robot-assisted surgical system for laser phonomicrosurgeries.**

I. Introduction

Lasers form an increasingly common tool for precision treatment of pathological conditions on delicate and vital human organs. Laser phonomicrosurgery, which is a suite of complex otolaryngological surgical techniques for the treatment of minute abnormalities in the larynx, is one such example. However, laser aiming control for this procedure relies completely on the dexterity of surgeons, who must operate through a microscope and deal with its associated poor ergonomics, and this can have a strong impact on the quality of the procedures. In addition, the laser beam is directed from a comparatively large range (400mm), resulting in accuracy and consistency problems, and requiring extensive surgeon training.

In this multidisciplinary project a redesign of this surgical setup is proposed to create an advanced augmented micro-surgical system through research and development of real-time cancer tissue imaging, surgeon-machine interfaces, assistive teleoperation, intelligent (cognitive) safety systems, and augmented-reality. Furthermore, research and development of new endoscopic tools and precision micro-robotic end effectors will allow relocating the laser actuator closer to the surgical site (Fig. 1). This is expected to allow unprecedented levels of accessibility and precision, while the surgeon will benefit from a more ergonomic, information-rich, and assistive environment.

The outcomes of the project will be improved quality, safety, and effectiveness in laser phonomicrosurgery, enabling total tumor removal with minimal damage to healthy tissue. The research efforts herein will generate new knowledge in the design and control of medical micro-mechatronic devices; cancer tissue imaging; assistive teleoperation in surgery; physician-robot interfaces; and cognitive computer vision. These technological advances will pave the way towards new and safer minimally invasive laser microsurgeries, leading to a significantly enhanced capacity for cancer treatment in general.

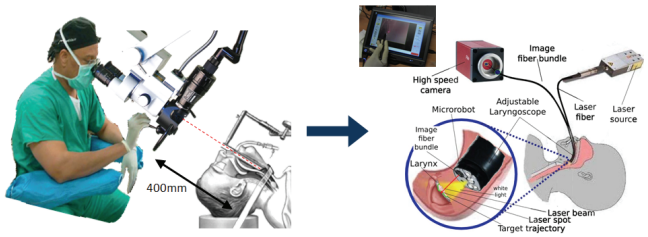

Fig. 1. The µRALP concept: from the gold-standard robot-assisted open-air laser phonomicrosurgery (left) towards safe, accurate and ergonomic endoscopic micro-robot-assisted laser phonomicrosurgery with fluorescence-based cancer detection (right).

II. Project Activities

Initially the project focused at the definition of specifications and guidelines for the final prototype, which was done extensive collaboration with the partner surgeons. This process resulted in a translation of medical needs and constraints to concrete technical specifications, a process that also assisted by the collection and distribution of multimedia data related to laser phonomicrosurgery cases.

Early developments within the project also included the design of experiments and definition of metrics to be used for the evaluation of currently available commercial devices and µRALP prototypes. These have already allowed randomized comparative trials to be performed, generating quantitative and qualitative data related to the precision, usability, and ergonomics of early system prototypes (Fig. 2, left).

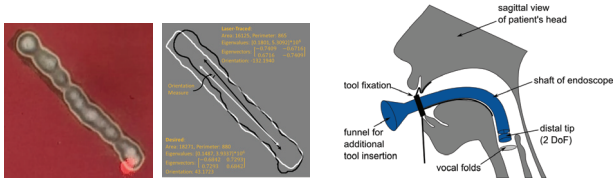

Fig. 2. Representative trial sample and extracted performance metrics (left). Schematic view of the endoscopic system fixed to the patient's mouth utilizing a retractor (right).

Based on the specification and guidelines, the µRALP consortium has been focusing most of its efforts on research, design and development of the constituent new technologies needed to achieved the envisioned robot-assisted system prototype. These include:

- Design of an endoscope body (Fig. 2, right) to bring all the µRALP components (and functionalities) into patient's larynx without stretching his/her neck to painful positions (as it is the case in the current gold-standard practice);
- Design of a hyperspectral optical system to gather fluorescence signal emitted by the cancerous cells, which is compatible with endoscopy (Fig. 3, left);
- Design of an out-of-plane micromanipulator with parallel kinematics, fitting in a 1cm^3 volume and able to scan the vocal fold at a 2cm distance (instead of 400 cm in the current gold-standard system);
- Design of a multi-view high-speed white-light imaging system, to allow for high-speed recording (and slow-motion

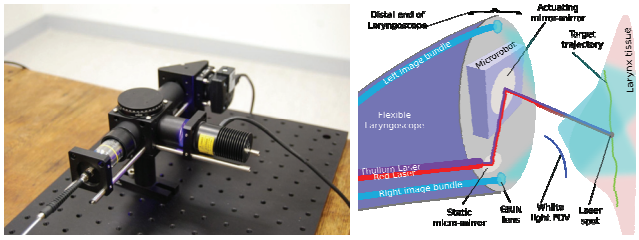

Fig. 3. Optical device for bundle-based fluoroscopy (left). Schematic view of the stereoscopic high-speed imaging system (right).

replay) of the procedure, as well as the real-time tracking and control of the laser motion (Fig. 3, right).

Systems integration has been a concern and a focus of R&D efforts from the beginning of the project. This has been identified as a critical factor for success since different partners are developing different hardware and software parts of the final µRALP system. Furthermore, the criticality of the application requires high safety and robustness. These concerns have lead to the adoption of the Robot Operating System (ROS) as the underlying software structure for inter-process communications and system control. In addition, real-time supervisory hardware is being developed for guaranteeing proper system operation and overall safety.

Interfaces between the surgeon and the µRALP system are also being developed, including a Virtual Scalpel that allows the surgeon to ergonomically define the path to be followed by the laser on the vocal fold (Fig. 4). The use of augmented reality is part of this effort, with the aim of providing relevant and useful information directly on the surgeon's field of view.

Finally, a cognitive supervisory system is being developed to model, supervise and control the laser power in order to avoid carbonization of the tissues and improve surgical quality.

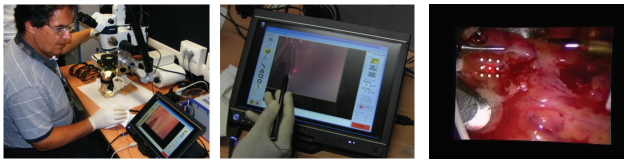

Fig. 4. Early ex-vivo trials of the virtual scalpel system for laser phonomicrosurgery performed at the IIT by a surgeon from UNIGE (left and center). 3D tissue deformation tracking based on SSD and rank transformation of stereo pair (right, image source: Hamlyn Centre, UK).

III. Main Results

Main results achieved by the research consortium during its first project year are summarized in the following list:

• Virtual Scalpel was designed, implemented and tested at a hospital setting. It was found very intuitive and easy to use by surgeons. Comparative trials showed 50% increase in precision with the new system, and the system usability analysis demonstrated an increase in the SUS score from 68% to 84%.

• Augmented reality stereoscopic feedback to the surgeon was developed with superimposition of (simulated) fluorescence data to video images, taking into account tissue deformation.

• An optical bench was designed, assembled and tested which demonstrates the feasibility of observing endoscopically the fluorescence of cancerous cells through an optical fiber bundle.

• A preliminary design of a 3D micro-manipulator with high range of motion and high dynamics was proposed, with innovative technological solutions.

• A novel high-speed vision-based control algorithm (and associated hardware) was derived for the accurate control of the laser spot on the vocal fold, based on an elegant use of multiview geometry.

• The preliminary design of an endoscope to support and position the µRALP technologies in close vicinity to the surgical site has been finalized, implemented and tested in a realistic human mannequin.

• Preliminary trials on ex-vivo swine larynxes were performed to assess the accuracy of preliminary prototypes including the Virtual Scalpel and visual servoing control.

IV. Expected Final Results and Impact

At the end of the project, significant scientific and technological advances are expected in:

• Surgeon-Robot Interfaces: A new and safer surgical setup offering higher usability, ergonomics and allowing better performance will be provided to the surgeon thanks to the use of new interface technologies and cognitive approaches.

• Spatial Micro-Mechanisms: A methodology for designing out-of-plane micro-fabricated mechanisms, with high range of motion and piezoelectric actuation, will be proposed.

• Medical Robot Design: The project will contribute to creating novel concepts for biocompatible, patient-friendly and surgeon-acceptable medical robots, with increased autonomy for realizing more complex tasks.

• Hyperspectral Fluorescence-based Cancer Detection: Appropriate exploitation of optics will allow for efficient diagnosis and accurate localization of tumors.

• Surgical practice: Laser phonomicrosurgery will require less training than currently, with less surgeon fatigue and better patient benefits.

Acknowledgement

The µRALP consortium involves the following institutions: Istituto Italiano di Tecnologia (Genoa, Italy), Institut FEMTO-ST (Besançon, France), Leibniz Universität Hannover (Germany), Università degli Studi di Genova (Italy), Centre Hospitalo-Universitaire (Besançon, France).

The project is funded by the European Union Seventh Framework Programme FP7/2007-2013 – Challenge 2 – Cognitive Systems, Interaction, Robotics – under grant agreement µRALP - n°288233.

Project website: www.microralp.eu

Mapping Tactile Information of a Soft Manipulator to a Haptic Sleeve in RMIS

Helge A Wurdemann, Emanuele Lindo Secco,
Thrishantha Nanayakkara, Kaspar Althoefer
Department of Informatics, King's College London
Centre for Robotics Research (CoRe)
Strand, London WC2R 2LS, UK
k.althoefer@kcl.ac.uk

Krzysztof Lis, Lukasz Mucha,
Kamil Rohr, Zbigniew Nawrat
Foundation of Cardiac Surgery Development
Zabrze, Poland
nawrat@frk.pl

I. Introduction

In Robot-assisted Minimally Invasive Surgery (RMIS), robotic tools enter the body through narrow openings and manipulate soft organs that can move, deform, or change in stiffness. The traditional robotic manipulation concepts that rely on fixed stiffness distributions, such as the da Vinci Robotic System, have limitations on these laparoscopic and robot-assisted surgical procedures due to restricted access through Trocar ports, lack of haptic feedback [1], and difficulties with rigid robot tools operating inside a confined space filled with organs [2]; the use of such systems can, in extreme cases, lead to harmful tissue tears [3-4]. Along the way, the solid structure of the laparoscopic instrument attached to the robotic arms and their external articulation make it problematic to change surgical targets inside the abdomen.

In this paper, we will present a novel approach to overcome the disadvantage of lack of haptic feedback in RMIS. Current work at King's also addresses the problem of rigid robot systems, and, with this in mind, we have developed a soft and stiffness-controllable MIS robot device allowing for more complex operations to be conducted inside a patient [5]. The work described here focuses on acquiring haptics information from tactile sensors attached to the MIS robot arm. Whilst our approach is generic and also applicable to rigid manipulators, here, we describe how tactile information from a stretchable tactile sensor sleeve of a soft manipulator is mapped to a haptic sleeve worn by a surgeon while operating with the manipulator. This paper will focus on the complete system (Section II): the stretchable tactile sensor sleeve (Section III), the wearable pneumatic haptic sleeve (Section IV) and the communication architecture between the two devices (Section V).

The presented system will be developed using the soft modular manipulator inspired by the octopus morphology for RMIS by Cianchetti et al. [5]. This research is part of the EU FP7 project STIFF-FLOP (STIFFness controllable Flexible and Learnable manipulator for surgical OPerations). The manipulator is a novel cylinder-shaped device which is manufactured from EcoFlex 00-50 silicone and covered by an off-the-shelf flexible braided sheath. This structural design allows omnidirectional bending, elongation capability and selective stiffness changing when pneumatically actuated via integrated chambers within the cylinder. The device has an overall length of 50 mm and an outer diameter of 35 mm with an elongation capability of up to 85%.

The research leading to these results has received funding from the European Community's Seventh Framework Programme (FP7-ICT-2011-7) under grant agreement n° 287728 – STIFF-FLOP. The research was also partially supported by the National Institute for Health Research (NIHR) Biomedical Research Centre based at Guy's and St Thomas' NHS Foundation Trust and King's College London.

This Publication reflects only the author's views and the European Community, NHS, the NIHR or the Department of Health is not liable for any use that may be made of the information contained.

II. System Overview and Objective

The conceptual system is shown in Figure 1. The tactile sensor sleeve and wearable haptic device are connected to a data acquisition module. Via a bridge, both components are linked to a ROS PC. An implemented system map processes data from the tactile sensors and actuate elements of a pneumatic haptic sleeve.

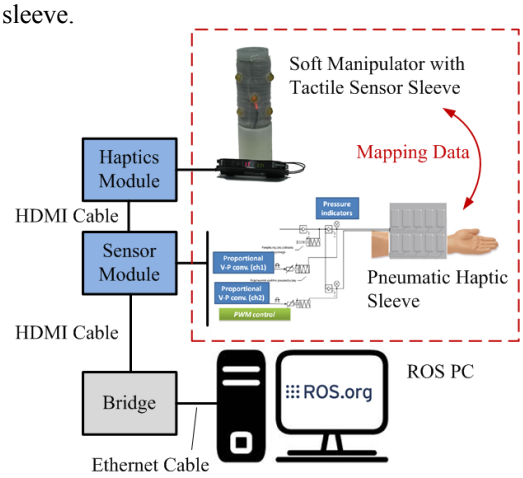

Fig. 1. ROS Interface of the Tactile Sensor and the Pneumatic Haptic Sleeve

The objective is to investigate how to best map the transferred information so that the surgeon obtains the most beneficial feedback. Hence, the received feedback should be useful for the surgeon and not distract or even obstruct him or her during an operation. An overview about the sensor and haptic sleeve is given in the next sections.

III. Tactile Sensor Sleeve Design

To develop a novel design and structure, the following two functional requirements are considered for the proposed tactile sensor sleeve:

1. The STIFF-FLOP robotic soft manipulator enters the body through narrow openings. This RMIS tool is able to squeeze, stiffen and elongate. Sensory data of a single sensor should not be affected by these features.
2. For RMIS, the tactile sensor array will need to be designed so that it can be miniaturized.

The design of the tactile sensor sleeve is described in the following subsections.

A. Individual Sensing Elements

The single tactile sensors use light intensity modulated fibre optics based on a prismatic tip [6]. The tip is cut at 45° angle in order to provide an internal reflection of 90° [7]. The sensor base has a 10 mm diameter and 1 mm thickness and is manufactured using a rapid prototyping machine (Project HD-3000 Plus, 3D Systems). The base embeds a 1 mm optical fibre. A flexible hemi-spherical dome of 8 mm diameter and 4 mm height (thickness: 1 mm) is mounted on the base. The emitted light is reflected on a 2 mm diameter mirror inside the dome which is manufactured of EcoFlex 00-50 silicone.

B. Tactile Sensing Integration into Stretchable Sleeve

In order to distribute the sensor elements along the manipulator, a sleeve has been designed (see Figure 2).

Fig. 2. (a) CAD Drawing and (b) Prototype of the Sensor Sleeve with Multiple Tactile Sensor Elements

The single sensors are placed into equally allocated holes along a silicon sleeve. In order to fit the stretchable sleeve to this manipulator, the silicone mould has a 30 mm diameter and 45 mm length. The optical fibres are winded along the braided sheath to feed forward necessary fibre length in case of elongation.

IV. Wearable Pneumatic Haptic Sleeves

A pneumatic actuated haptic sleeve is conceived around the end-user's forearm. It is based on a set of small chambers that are filled with air causing local pressure.

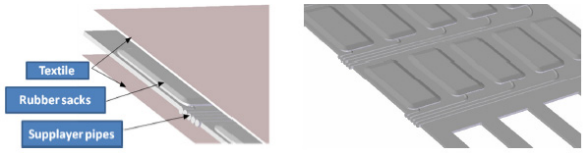

Fig. 3. Concept of the Proposed Haptic Sleeve

FigureFig. 3 shows the matrix of 4×5 pneumatic selectors having a dimension of 55×30 mm each, where applied pressure and sensitivity of human forearm affect the technical capability of sleeve to transfer the feeling of a force feedback to the end-user.

V. Intuitive Haptic Feedback Mapping

When the surgeon operates and navigates the soft and flexible tool inside the human body, interactions between the manipulator and tissue/organs occur. In general, continuous minor physical contact which is unavoidable appears. This kind of sensing information is not relevant to the surgeon as it is classified as not harmful to any surrounding tissue. Feeding back this data might result in a distraction and cause complications because the clinician is unable to concentrate on the surgical procedure.

Thus, possible scenarios and interrelated sensing information will be categorised and classified in order to support the surgeon while he/she is performing the procedure with the aim of preventing possible inappropriate movements. This data will then be translated into actuation modes of the pneumatic haptic sleeve. Rather using a linear transformation, the aim is to convert tactile sensor signals into substantial haptic feedback which make the surgeon intuitively reacting in the appropriate way to reconfigure the manipulator.

VI. Conclusions and Future Work

This paper introduces a new approach to feed back tactile information in RMIS to the surgeon's forearm. A tactile sensor sleeve for flexible and soft snake-like manipulators is presented. A control strategy will interpret the signals and feed useful and intuitive feedback by using a haptic device which is a wearable pneumatic actuated sleeve.

The implementation of this system will allow us to study how much feedback is beneficial for surgeons and when haptic feedback becomes more distractive than beneficial.

References

[1] A.M. Okamura, "Haptic feedback in robot-assisted minimally invasive surgery.," Current Opinion in Urology, vol. 19, no. 1, pp. 102–107, 2009.

[2] G. Dogangil, B.L. Davies, and F. Rodriguez y Baena, "A review of medical robotics for minimally invasive soft tissue surgery", Proceedings of the Institution of Mechanical Engineers, Part H: Journal of Engineering in Medicine, 224: 653-679, 2010.

[3] H.A. Wurdemann, A. Jiang, T. Nanayakkara, L.D. Seneviratne, K.Althoefer, "Variable Stiffness Controllable and Learnable Manipulator for MIS, Workshop: Modular Surgical Robotics: how can we make it possible?", IEEE International Conference on Robotics and Automation (ICRA), 2012.

[4] M. Li, H. Liu, J. Li, L. D. Seneviratne, and K. Althoefer, "Tissue stiffness simulation and abnormality localization using pseudo-haptic feedback," in IEEE International Conference on Robotics and Automation, pp. 5359–5364, 2012.

[5] M. Cianchetti, T. Ranzani, Member, G. Gerboni, I. de Falco, C. Laschi, A. Menciassi, "STIFF-FLOP Surgical Manipulator: mechanical design and experimental characterization of the single module" IEEE Conference on Intelligent Robots and Systems (IROS), 2013.

[6] P. Puangmali, K. Althoefer, L.D. Seneviratne, "Mathematical Modeling of Intensity-Modulated Bent-Tip Optical Fiber Displacement Sensors," IEEE Transactions on Instrumentation and Measurement, vol.59, no.2, pp.283, 2010.

[7] A. Ataollahi, P. Polygerinos, P. Puangmali, L.D. Seneviratne, K. Althoefer, "Tactile sensor array using prismatic-tip optical fibers for dexterous robotic hands", IEEE/RSJ International Conference on Intelligent Robots and Systems (IROS), pp. 910,915, 2010.

Communication and Teamwork Failure as a Barrier to Robotic Surgical Safety

Marco A. Zenati M.D., M.Sc., FETCS, Jason K. Maron, M.S.
MRCAS Lab, Department of Cardiothoracic Surgery, BHS and Harvard Medical School
Boston, Massachusetts, USA Contact: Marco_Zenati@hms.harvard.edu

Abstract— Robotic surgery is a high-consequence activity that heavily depends on optimal communication and teamwork. We discuss the current understanding of the role of communication and errors in high-risk surgery, with particular emphasis on conventional and robotic-assisted cardiac surgery.

Keywords— ***robotic cardiac surgery; minimally invasive surgery; communication breakdown; metacognition; teamwork; surgery***

I. INTRODUCTION

High-technology medicine, such as robotic cardiac surgery [1], is a complex socio-technical system in which performance depends on individual technical and organizational factors and their interactions; consequently, efforts to improve surgical quality have recently shifted from the individual to the team. In addition, awareness of surgical team quality and its impact on operating room efficiency has considerably increased over the last decade. The difficulty level of team communication increases as the number of health care providers involved with patient care increases and measures to reinforce the quality of communication among team members have been recommended. Unfortunately, team communication failures are widespread in the cardiovascular operating room and result in poor operative performance and unintended injury to patients [2-3]. These communication failures have been shown to be observable, classifiable and predictable. Yet, translation of this knowledge regarding human performance into practical tools for quality and safety improvement has been limited.

II. TEAM COMMUNICATION EFFECTIVENESS AND SURGICAL OUTCOMES

Effective teamwork and communication have long been identified as key drivers of quality and safety in many high-risk, high-reliability fields (e.g. aviation, military, etc) and team-based healthcare is no exception. The U.S. Joint Commission on Healthcare Quality and Safety has identified "communication" as the #1 root cause of reported sentinel surgical adverse events in a 10-year period starting in 1995. Adverse events related to surgery account for two thirds of hospital complications, with 75% of errors occurring inside the operating room. Surgical errors cannot be understood separately from the actions of the members of the surgical team: Wiegmann and associates reported that teamwork-related factors alone accounted for roughly 45% of the variance in the errors committed by surgeons during cardiac cases [4]. Teamwork issues involve cases of: (a) mis-communication, (b) lack of coordination, (c) failures in monitoring, and (d) lack of team familiarity. Poor team communication has been linked to poor surgical outcomes in studies from both the United States and Europe [5]. Gawande reported on the dangers of incomplete, nonexistent or erroneous communication in the operating room and found that they were causal factors in 43% of injuries made during surgery [6]. Reports of positive communication with the attending surgeon ($r=-0.38$, $p<0.01$) or resident surgeon ($r=-0.25$, $p=0.08$) from surgical staff have significant negative correlation with the observed/expected surgical morbidity ratio.

The specialty field of cardiac surgery, traditional or robotic-assisted, is a dangerous and complex area of medicine with significant morbidity and mortality. In recent years, cardiac surgery has experienced a growing complexity of its case mix due to increasing patients' age, co-morbidities and the introduction of advanced robotic technologies [7]. In this setting, achievement and maintenance of excellence is becoming more challenging. Despite a significant improvement of mortality and avoidable complication rates, Wiegmann found that cardiac surgeons make on average 3.5 errors per hour [4]. El-Bardissi studied 31 cardiac surgical cases at the Mayo Clinic and observed a strong correlation ($r=0.67$; $p<0.001$) between the occurrence of technical errors and teamwork failures,

with the majority (51%) of teamwork failures affecting surgeon-technical team interactions [8]. Gurses and associates recently performed a multisite study on patient safety hazards in the cardiovascular operating room and reported, among other significant findings, that cardiac surgeons often did not use names when giving orders, causing confusion between anesthesia and perfusion teams regarding the intended receiver of the order; in addition, recommended communication practices (i.e. repeat backs, callouts, confirmation, structured communication techniques) were rarely used [3].These authors concluded that communication-related hazards (defined as anything that has the potential to cause a preventable adverse patient safety event) are prevalent in the cardiovascular operating room resulting in widespread and substantial risk to patient safety**.**

Surgical safety should not be assessed exclusively in terms of "hard" clinical outcomes (e.g. death, myocardial infarction, bleeding, etc.): in fact, good outcomes may emerge from unsafe processes (that may result in a bad outcome in other situations). A recent study by Dierks and associates, indentified events in the operating room that compromised safety but had gone unnoticed by the providers involved because the outcome was favorable ("outcome bias" in clinical care) [Dierks unpublished 2013]. A more useful terminology for classifying adverse events distinguishes between: (1) System Vulnerability, as the exposure to or opportunity for adverse events; (2) Safety-Compromising Events ("near-misses"), as a variation in the expected course of care that has a negative effect on patient safety and puts the patient at risk for a measurable adverse change in patient status; (3) Adverse Event, a safety-compromising event that progresses to a measurable adverse change in patient status; (4) Contributing factor, conditions or properties that increase the vulnerability of the system, therefore increasing the chance of an adverse event; (5) Compensatory factor, conditions or properties that decrease the vulnerability of the system or reduce the severity of an adverse event.

Team communication in the operating room has been shown to reflect cognitive non-technical skills like situation awareness (SA). SA is defined as "the perception of the elements in the environment within a volume of time and space, the comprehension of their meaning, and the projection of their status in the near future". As such, SA is one of an array of 'non-technical' or 'behavioral' skills along with decision making, teamwork and leadership. SA is particularly crucial in cardiac surgery, as situational awareness underpins the ability to make appropriate decisions, communicate the correct information at the right time (e.g. between surgeon and perfusionist) and lead other team members successfully. Good SA can also make a critical difference in task effectiveness by reducing individual errors, improving shared mental models, and enabling team members to capture errors before they adversely affect outcomes [3]. This can make teamwork more successful and rewarding for participants, and safer for patients.

Unfortunately, adverse event analyses in healthcare often reveal failures in SA and diagnostic skills which lead to technical errors. The paradox is that these skills are usually only trained and assessed informally in healthcare. Recently, and in line with other high risk/ high reliability industries such as nuclear power and civil aviation, behavior rating systems for healthcare professionals have been developed for use in real and simulated healthcare learning environments such as NOTSS for surgeons, ANTS for anesthesiologists , SPLINTS for scrub technicians and a more recently developed marker system for emergency physicians [8-10]. These systems all include specific detail regarding SA and provide an opportunity to assess communication behaviors which underlie cognition in terms of ability to: (i) gather, (ii) understand, and (iii) project and anticipate future states. These frameworks allow clinicians and researchers to reflect on these skills in action, intervene to provide learners with strategies to improve their awareness, and recognize situation awareness states of others.

Team situational awareness (TSA) can be measured in terms of situation-related communications events (i.e. speech events that require timely coordination among two or more team members). Effective, closed-loop communication involves the following sequence of actions: (1) sender initiates message; (2) receiver accepts message and provides feedback that it was received; and (3) sender double checks to ensure that message was received as intended. This type of communication has a built-in check to ensure that not only does the communication get to the required person, but that the intended message sent was the same one received. When multiple sources of information as well as multiple recipients are present, such as in the operating room, closed-loop communication can differentiate between effective and ineffective teams.

The communication loop construct (i.e. the full cycle of information flow between the participants in the sequence) was used by Parush and associates to assess susceptibility to communication breakdown: based on their analysis, communication loops that are open, non-directed or with delayed closure, are susceptible to the risk of information loss [11]. These communication loops were quantitatively related to communication indicators of TSA such as questions, replies, and announcements and conceptually should be predictive of delays and efficiency in the operating room.

Translating these principles into modern surgical practice has been accomplished via medical simulation and team training. Yet despite the adoption of non-technical skills training warranting a Class I/B recommendation from Wahr and associates (on the American College of Cardiology Foundation and American Heart Association scale), measurement of how to precisely tailor best practices and sustain a safety culture incorporating values elicited from these skills is not awarded the same confidence [12]. This is partly due to the inherent difficulty of such measurement, but also because the positive transient effects of an experimental intervention tend to wane. Such diminishment is a consequence of the human practitioner. An automated decision-support system, or robot, might be less prone to deprioritize a recommendation or decision rule on grounds of indifference and inconvenience.

III. Situation Awareness with SurGIcal Robots

A critical non-technical skill in Cardiac Surgery is Situation Awareness (SA) [8]. Information sources that allow optimal SA are primarily visual (e.g. adequate surgical exposure of the operating field, visual access to monitors) and acoustic (ability to hear and discriminate critical verbal utterances from other team members). Surgery is a hand-busy, eye-busy activity and the eye gaze of the surgeon is generally focused on the operating field. In case of robotic cardiac surgery, the visual field is even more restricted to the endoscope and can be temporarily compromised by blood splattering on the lens. In addition, the master console of the DaVinci robotic system is located several feet away from the operating table and, even with the aid of a microphone, verbal communication is more difficult than during conventional open cardiac surgery. We conclude that SA is commonly severely compromised during robotic cardiac surgery.

Blum & associates have described a method for phase recognition of procedures using equipment utilization as inputs to predictive hidden Markov models (HMM) [15]; such systems may augment team communication during robotic cardiac surgery when team SA is diminished.

IV. Conclusion

Current research on the breakdown of surgical teams' communication and coordination during surgery indicates an unmet need for systematic acquisition of communication data in a measurable and quantifiable manner as a first step in order to ultimately provide patient safety solutions. To increase the capture of information in the operating room and to enhance SA, Guerlain and associates proposed the introduction of a "black box" recorder, similar to those used in the aviation industry, to assess individual and/or team events for quality improvement [16]. Such technology may help collect the complex data generated in the operating room and identify and understand the human behaviors that occur in the operating room and their relationship to patient safety events. However, none of these concepts has been translated and validated in the cardiovascular operating room. Successful translation of these concepts may improve safety and eliminate a barrier to the adoption of high-technology medicine such as robotic cardiac surgery.

References

[1] M.A. Zenati. Robotic cardiac surgery. *Cardiology in Review* 9:287-294, 2001.

[2] K. Catchpole, D. Wiegmann. Understanding safety and performance in the cardiac operating room; from "sharp end" to "blunt end". *BMJ Qual Saf* 21:807-809, 2012.

[3] A.P. Gurses, G. Kim, E.A. Martinez, J. Marsteller, L. Bauer, L.H. Lubornski, P.J. Pronovost, D. Thompson. Identifying and categorizing patient safety hazards in cardiovascular operating rooms using an interdisciplinary approach: a multisite study. *BMJ Qual Saf* 21:810-818, 2012.

[4] D.A. Wiegmann, A.W. ElBardissi, J.A. Dearan, et al. Disruptions in surgical flow and their relationship to surgical errors: an exploratory investigation. *Surgery* 142:658–65, 2007.

[5] M.R. de Leval, J. Carthey, D.J. Wright, et al. Human factors and cardiac surgery: a multicenter study. *J Thorac Cardiovasc Surg* 119:661-672, 2000

[6] A.A. Gawande, M.J. Zinner, D.T. Studdert, T.A. Brennan. Analysis of errors reported by surgeons at three teaching hospitals. *Surgery* 133:614-621, 2003.

[7] D. Wiedemann, N. Bonaros, T. Schachner. Surgical problems and complex procedures: Issues for operative time in robotic totally endoscopic coronary artery bypass grafting. J *Thorac Cardiovasc Surg* 143:639-407, 2012.

[8] Yule, S., Flin, R., Paterson-Brown, S., Maran, N., & Rowley, D. (2006). Development of a rating system for surgeons' non-technical

skills. Medical education, 40(11), 1098-1104.

[9] Fletcher, G., Flin, R., McGeorge, P., Glavin, R., Maran, N., & Patey, R. (2003). Anaesthetists' Non-Technical Skills (ANTS): evaluation of a behavioural marker system†. *British Journal of Anaesthesia*, *90*(5), 580-588.

[10] Mitchell, L., Flin, R., Yule, S., Mitchell, J., Coutts, K., & Youngson, G. (2012). Evaluation of the scrub practitioners' list of intraoperative non-technical skills (SPLINTS) system. *International journal of nursing studies*, *49*(2), 201-211.

[11] Parush, A., Kramer, C., Foster-Hunt, T., Momtahan, K., Hunter, A., & Sohmer, B. (2011). Communication and team situation awareness in the OR: Implications for augmentative information display. *Journal of biomedical informatics*, *44*(3), 477-485.

[12] Wahr, J.A., Prager, R.L., Abernathy III, J.H., et. al. (2013) Patient Safety in the Cardiac Operating Room: Human Factors and Teamwork: A Scientific Statement from the American Heart Association

[13] Leven, J., Burschka, D., Kumar, R., Zhang, G., Blumenkranz, S., Dai, X. D.& Taylor, R. H. (2005). DaVinci canvas: a telerobotic surgical system with integrated, robot-assisted, laparoscopic ultrasound capability. In *Medical Image Computing and Computer-Assisted Intervention–MICCAI 2005* (pp. 811-818). Springer Berlin Heidelberg.

[14] Kraft, B. M., Jäger, C., Kraft, K., Leibl, B. J., & Bittner, R. (2004). The AESOP robot system in laparoscopic surgery: Increased risk or advantage for surgeon and patient?. *Surgical Endoscopy And Other Interventional Techniques*, *18*(8), 1216-1223.

[15] Blum, T., Padoy, N., Feußner, H., & Navab, N. (2008). Workflow mining for visualization and analysis of surgeries. *International journal of computer assisted radiology and surgery*, *3*(5), 379-386.

[16] Guerlain, Stephanie, et al. "Assessing team performance in the operating room: development and use of a "black-box" recorder and other tools for the intraoperative environment." *Journal of the American College of Surgeons* 200.1: 29-37, 2005.

The ACROBOT technology: a model for robotic surgery?

Brian Davies,
Advanced Robotics, Istituto Italiano di Tecnologia, via Morego, 30, 16163 Genova
b.davies@imperial.ac.uk

***Abstract*—**the ACROBOT robot for orthopedic surgery is a rare example of a commercial surgical robot which utilizes 3D reconstruction, motion compensation, virtual guidance and haptic feedback. It has been used clinically for minimally invasive Uni-condylar surgery with excellent results. It uses a powered 3 axes robot together with a 2 axes passive orientation device. The system is trolley mounted and designed to fix to the operating room table. The patient motion is tracked using a mechanical arm that updates the plan in real-time. It is suggested that this type of hands-on robot, in which the robot actively constrains the surgeon to an accurate and safe region, is a possible model for other medical robotic systems.

Keywords*—*robotic surgery; orthopedics; ACROBOT; hands-on; Active Constraints.

I. Introduction

The Author started working on an orthopedic surgical robot for replacing hip & knee joints in 1991. This was just after clinical trials on the author's Prostate robot PROBOT [1], when an Orthopedic Surgeon, Prof. Justin Cobb, approached the author saying it must be easier to machine bone as, unlike the prostate, it did not change shape when cut. It was clear from clinical experience with the Probot that surgeons had been trained to have their hands on the patient and so an autonomous system such as the Probot was not appropriate. For this reason a hands-on robot was devised in which the surgeon was directly involved with the robot in a synergistic way [2]. As part of a hands-on robot, the surgeon holds a force control lever at the end of the robot arm next to the cutter. In this way the surgeon can feel forces applied by the robot and at the same time the robot can physically constrain the surgeon to a safe region avoiding cutting critical areas such as ligaments. The robot also enabled minimally invasive surgery, in which a minimal amount of bone stock is precisely removed, enabling small prostheses such as uni-condylar knee replacements, difficult to implement conventionally, to be used instead of much larger total knee prostheses. The system uses a pre-operative 3D CT scan and is a rare example of a commercial surgical robot which utilizes 3D reconstruction, motion compensation, virtual guidance and haptic feedback.

II. THE ACROBOT SYSTEM TECHNOLOGY

A. The Robot and its Control.

The term ACROBOT stands for Active Constraint ROBOT. An Active Constraint describes an approach in which the surgeon is Actively Constrained from damaging critical tissue, such as ligaments, that must be preserved [3],[4]. The constraint prevents the surgeon moving a cutter into a no-go area such as the forbidden zone in Fig. 1, whilst always allowing motion in the central safe zone. As the cutter moves towards the forbidden zone, in the near-boundary area, the force is gradually increased to push the cutter back to the central region or allow it to move tangentially around the periphery.

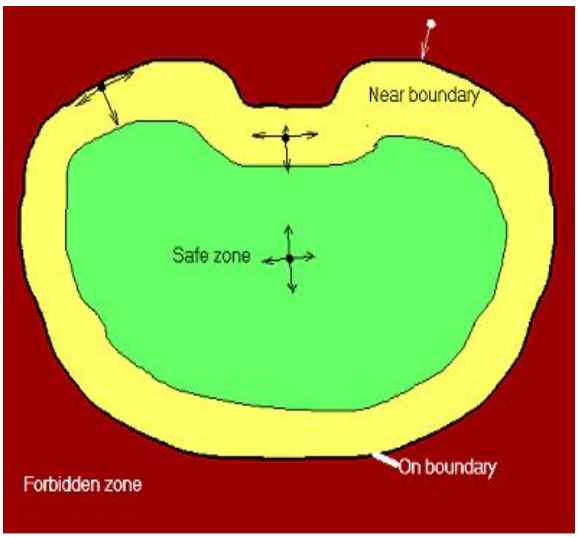

Fig. 1. The Active Constraint concept.

For the robot, 3 motions were powered by DC motors and low friction recirculating ball-screws. For the surgeon to be able to feel the forces applied by the robot in the hands-on mode, the motions need to be even and low impedance, so that the pitch, yaw and in-out motions all have even and low resistance and so there is no tendency for one axis to move preferentially. This was aided by ensuring all 3 axes intersected at a common point. This resulted in sufficient sensitivity that even without the use of a force sensor to amplify forces, the surgeon could feel when cutting a hard piece of bone and slow down or take a lighter cut. This synergy, in which the robot provided constraint and accuracy whist the surgeon was in direct control, proved to be attractive to surgeons.

Originally the robot was mounted on a robotic system which acted as a gross-positioner that was locked off for safety when the small active robot was in the right position and orientation. However, it was found from experience that this large and costly form of gross-positioner was not needed as the cutting forces were light and it was found possible to place the small active robot on a trolley that could be locked to the operating table. Patient motion monitoring was also provided using a mechanical "Microscribe" arm, the tip of which was lightly pinned to the patient's bone [5]. The 6 axes Microscribe arm

was passively actuated and had encoders at all joints and a sufficient update-rate that it could monitor patient motion and change the plan and the cutting constraints in real time to maintain the required cutting accuracy. This avoided the need adopted in early versions for locking down the patient and treating like a traditional CNC machining process. The small active robot utilized 3 powered axes (pitch, yaw and in/out) to provide location whilst the orientation had a passive linkage that carried the cutter on the end of the arm. This provides a low-cost small robotic system that is light and easy to use.

Fig. 2. The 5 axes trolley mounted robot with patient motion monitoring using a mechanical "Microscribe" arm.

3 axes (pitch, yaw and in/out) are powered, whilst the orientation device that carries the cutter on the end of the arm, is passive and configured to have a common centre of rotation at the centre of the ball cutter as shown in Fig. 3.

B. Planning System.

In order to fully utilize the potential accuracy of a robot, a planning system is required. This was based on a 3D CT scan of the patient leg to provide an accurate model on which to pre-operatively plan the procedure. A 3D image of the bones is provide that can be scaled, rotated to view from any direction and has variable transparency to show *quasi* x-ray views. Onto this the appropriate size and type of prosthesis can be overlaid and positioned until the desired amount of resection and alignment is achieved. A minimally invasive uni-condylar knee procedure was undertaken in which, instead of a total knee replacement (TKR), only one of the condyles is

Fig. 3. The passive orientation device showing the common center of rotation at the centre of the cutting ball.

resurfaced using a prosthesis [6]. This requires a minimal removal of bone stock compared to TKR, and is a more challenging procedure conventionally, but is made simpler by the use of the robot.

C. Registration

At the start of the operative procedure, it is necessary to register the patient data and pre-operative plan to the current location of the patient and robot. This can be a major source of inaccuracy in the overall procedure. A modified form of Iterative Closest Point (ICP) algorithm was used. To minimize the time and help accuracy this was "bounded" by using the hip centre as a location. To locate this, the robot tip was connected to a pin located in the distal femur and the leg rotated through small angular excursions whilst the robot encoders collected the motion data to extrapolate the hip centre location and correlate with that found in the whole leg CT scan. A 1mm dia probe was then mounted on the cutter drive and used to touch onto the bone surface of the distal femur at a number of locations through a small skin access slit in the femur. This produces a cloud of points on the surface of the femur which can then be correlated with the surface obtained from the pre-operative CT image. The process is repeated separately for the proximal tibia. Both femur and tibia are separately monitored for leg motion throughout the

procedure by a single pin attached to the tip of the Microscribe arm. A 10 mm dia ball-ended cutter is used whilst the cutting process is observed on a computer display, since the cutter is out of sight down a small slit inside the skin. The display shows the cutting process as the bone is machined. When the desired level of cut is achieved, the screen color at that location turns green. The tibia is usually machined before the femur to allow more easy access to cut the rear of the femur.

III. DISCUSSION

Some systems e.g. Robodoc [7], are autonomous and once positioned at the site the sequence of cuts is automatic with no further involvement in the process from the surgeon than to hold an emergency off button. However, the author feels that a hands-on approach is more acceptable to the surgeon in which the surgeon is in direct control of the robot tool and initiates the sequence of cuts whilst monitoring progress. The use of Active Constraints also ensures that the robot provides accuracy and constraint, thus enhancing safety. However, it is also possible to have some autonomous processes in such a hands-on system, e.g., a small number of roughing cuts or repetitive motions that would otherwise tire the surgeon.

Whilst some orthopaedic robot systems target total hip or total knee replacement, it can be argued that these are procedures that the surgeon conventionally finds easy to do and the results are usually acceptable since the prostheses are said to be designed to be forgiving of placement error. For this reason, the author feels that minimally invasive procedures, such as uni-condylar knee replacement, are a better area for robotics since they are more challenging conventionally.

In order to ensure that the uni-condylar knee replacement procedure was correctly carried out, a small prospective randomized trial of around 30 patients was carried out to compare the robot results with those conventionally [2]. To ensure a similar process, both conventional and robotic patients had a pre-operative CT scan and a plan of what was to be attempted. Post operatively, all patients received a CT scan to compare achieved with planned results. All robotic patients were shown to have mechanical alignment of femur and tibia within 2 degrees, whilst of the conventional patients only 40% were within 2 degrees although the surgeons were all experienced in this conventional approach. The planning system was found to be of benefit, even by the conventional surgeons who had not previously used one.

IV. CONCLUSIONS

A robotic system for orthopaedic surgery joint replacement has been developed and tried clinically. The concept of Active Constraint robotic control has also seen application in a number of surgical robotic systems, including that of the EU project uRALP. The system uses a pre-operative 3D CT scan and is a rare example of a commercial surgical robot which utilizes 3D reconstruction, motion compensation, virtual guidance and haptic feedback. After 8 years of research at Imperial College London, the Acrobot Company was set up in 1999 to exploit this work and a cost effective surgical robotic system was produced commercially based on a trolley mounted robot arm carrying a high speed cutting burr. The Acrobot Company was acquired in 2010 by the Stanmore Implants Worldwide Ltd (SIW) [8]. Development of the system continued and a patient-specific uni-condylar prosthesis was realized that benefitted from the use of a robot to generate complex but accurate bone cuts [9]. SIW sold the Acrobot system to the American company MAKO in 2013 [10]. However, the author is of the opinion that this type of hands-on robot, in which the robot actively constrains the surgeon to an accurate and safe region, is a possible model for other medical robotic systems.

V. ACKNOWLEDGMENTS

The research leading to these results has received funding in part from the European Union Seventh Framework Program FP7=2007-2013 – Challenge 2 – Cognitive Systems, Interaction, Robotics – under grant agreement uRALP N°288233.

VI. REFERENCES

[1]. B. L. Davies, R. D. Hibberd, M. J. Coptcoat, and J. E. A. Wickham, “A surgeon robot prostatectomy - a laboratory evaluation," Journal of Medical Engineering and Technology, vol. 13, no. 6, pp. 273-277, 1989.

[2]. J. Cobb, J. Henckel, P. Gomes, S. Harris, M. Jakopec, F. Rodriguez, A. Barrett, and B.L. Davies, “Hands-on robotic uni-compartmental knee replacement”. J. Bone J Surg. Br., 88, pp. 188–197, 2006.

[3]. B.L. Davies, M. Jakopec, S. J. Harris, F. Rodriguez y Baena, A. Barrett, A. Evangelidis, P. Gomes, J. Henckel, and J. Cobb, “Active-constraint robotics for surgery," Proceedings of the IEEE, vol. 94, no. 9, pp. 1696-1704, 2006.

[4]. S. C. Ho, B. L. Davies, R. D. Hibberd, and J. Cobb, “Robotic knee surgery – implicit force control strategy with active motion constraint," in European Robotics and Intelligent Systems Conference (EURISCON), vol. 3, 1994.

[5]. Microscribe.(2013) http://www.3d-microscribe.com/

[6]. J. Cobb, J. Henckel, F. Rodriguez, and B.L. Davies, “Accuracy improves outcome in knee arthroplasty: five-year results of a prospective randomised controlled trial of robotic uni-compartmental knee replacement”. In proc. of the IMechE Conference on Knee arthroplasty 2009: from early intervention to revision, London, pp. 210–213, 2009.

[7]. Robodoc.(2013) www.robodoc.com

[8]. SIW (2013) www.stanmoreimplants.com

[9]. A Barrett, B Andrews and J Cobb. “Accuracy of Truly Patient-Specific UKA Procedures Using Sculptor RGA”, Bone Joint J, vol. 95-B no. SUPP 15 11, 2013.

[10]. Mako (2013). www.**mako**surgical.com

ACTIVE: Active Constraints Technologies for Ill defined and Volatile Environments

Giancarlo Ferrigno
Department of Electronics, Information and Bioengineering
Politecnico di Milano
Milan, Italy
giancarlo.ferrigno@polimi.it

***Abstract*—The ACTIVE project exploits ICT and other engineering methods and technologies for the design and development of an integrated redundant robotic platform for neurosurgery. A light and agile redundant robotic cell with 20 degrees-of-freedom (DoFs) and an advanced processing unit for pre- and intra-operative control will operate both autonomously and cooperatively with surgical staff on the brain. As the patient will not be considered rigidly fixed to the operating table and/or to the robot, the system will push the boundaries of the state of the art in the fields of robotics and control for the accuracy and bandwidth required by the challenging and complex surgical scenario.**

Two cooperating robots will interact with the brain that will deform for the tool contact, blood pressure, breathing and deliquoration. Human factors are considered by allowing easy interaction with the users through a novel haptic interface for tele-manipulation and by a collaborative control mode ("hands-on"). Active constraints will limit and direct tool tip position, force and speed preventing damage to eloquent areas, defined on realistic tissue models updated on-the-field through sensors information. The active constraints will be updated (displaced) in real time in response to the feedback from tool-tissue interactions and any additional constraints arising from a complex shared workspace. The overarching control architecture of ACTIVE will negotiate the requirements and references of the two slave robots.

The operative room represents the epitome of a dynamic and unstructured volatile environment, crowded with people and instruments. The workspace will thus be monitored by environmental cameras, and machine learning techniques will be used for the safe workspace sharing. Cognitive skills will help to identify the target location in the brain and constrain robotic motions by means of on-field observations.

Framework for Managing Cognitive Load in a Data-Rich Robotic Operating Room

Jason K. Maron, MS, Marco A. Zenati, MD, M.Sc. (Hon.), FETCS
MRCAS Lab, Department of Cardiothoracic Surgery, BHS and Harvard Medical School
Boston, MA, USA Contact: jason.maron@va.gov

***Abstract*—Complete autonomy of robots and information technology in the operating room may one day be possible, such that decision support systems give way to decision surrogate systems. A binary of 'control' and 'slave' defines the current relationship between human surgical teams and medical robotics. Yet recognition of our own limitations motivates the development of these technological platforms. Endowed with a modicum of sensory faculties, humans bootstrap their sensitivity to data by enlisting the services of machines. However, in spite of our drive for information in surgery, we often struggle to design work-systems that simultaneously increase situation awareness and limit exposure to extraneous data. Cognitive overload continues to be problematic in spite of attempts to refine and simplify surgical intervention. It is therefore incumbent upon designers to stratify information pathways that alleviate the cognitive burdens stunting pragmatic decision-making in the operating room. We have proposed a framework for this endeavor.**

Keywords—robotic surgery, patient safety, sociotechnical system, industrial engineering, cognitive overload, design, optimization

Glossary of Key Terms

$t = time$
$k = signal\ source$
$x = sense\ type$
$i = surgical\ task\ (technical\ or\ non-technical)$
$j = sociotechnical\ agent\ (man\ or\ machine)$
$a_{k,x,i,t} = amount\ of\ attention\ invested\ to\ signal$
$l_{j,t} = naturally\ discarded\ cognitive\ load$
$r_{k,x,j,t} = rate\ of\ return\ (signal\ to\ cognitive\ load)$
$CL_{j,t} = individual\ cognitive\ load$
$\mathcal{E}\left[U\left(CL_{i,j,t}\right)\right] = expected\ utility\ of\ information\ load$
$K_{j,t} = \{k_1, \dots, k_N\} = signals\ currently\ observable$
$\underline{K}_{j,t} = \left\{\underline{k}_1, \dots, \underline{k}_{\notin}\right\} = signals\ currently\ not\ observed$
$\overline{K}_{j,t} = \left\{k_1, \dots, k_{N-n}, \underline{k}_1{}', \dots, \underline{k}_{\notin}{}'\right\} mixture\ of\ signal\ types$

I. Introduction

Mitigating and averting cognitive overload is a systems design problem. Unlike when a consumer firmly accepts a product's pros and cons after purchase, surgeons should not have to settle for the ostensible limitations of the cognitive sociotechnical system in the operating room (OR). The system is a product in its own right, with features that are complex and dynamic as is most healthcare delivery [1]. For our purposes the sociotechnical system is comprised of any agent that can share information in the OR—simply put, man and machine.

One utility of a machine is determined by what data it can detect and how well it communicates that data with other entities when they need it the most. From a reductionist perspective, each human is a set of sensory systems with cognitive capacity—a machine of sorts. Electronic devices, robots and other technologies can have sensitivities to data imperceptible to humans, but without sufficient programming the richness of the data economy can overwhelm the humans for which it is intended, or potentially even be squandered by them. While technological barriers currently prohibit perfect synergy between humans and robots, another rate limiting step exists—work. Surgical staff have multiple responsibilities that they must juggle during the course of an operation. These duties are inconsistent across professional boundaries, are not ubiquitous over different timeframes, nor does each task share the same priority [2].

If one clinician is enduring cognitive overload we must consider prioritizing the sources and means of delivering information [3-5], determining the triviality of certain data in the moment, transmitting the right data to avoid additional overload, reconfiguring data so that all mission-critical information can be *chunked* [5-6].

Eliminating cognitive overload in the operating room means marshaling information flow. In order to accomplish this undertaking we must have a good estimation of what the current intraoperative phase is, which data is most clinically important and who is focused on that data. Information theory lends itself to assessing the data volume and uncertainty [7], however we must synthesize this backbone with concepts from psychology and design to repurpose the data for easier detection, articulation and processing.

II. Cognitive Load Theory and Surgery

A human's ability to establish and sustain an appropriate level of situation awareness in an environment depends upon the individual's working memory capacity [8]. This capacity is limited by intrinsic cognitive load and diminishes with larger exposure to external stimuli [4]. Consequently attentiveness to new data, synthesis of old and current information and

articulation of relevant concepts in a timely manner are compromised. Inability to communicate new ideas, request for confirmation or deliver an appropriate response in the OR can cause discrepancies in the collective understanding of surgical stage and protocol [9]. Such divergence can have a malignant effect on intra/inter-team coordination.

Studying working memory capacity and cognitive loads has been attempted in many psychological experiments [10]. Computer simulations have been developed to estimate related metrics in response to different didactic tools and changing environments [11]. Even measures for comparing the similarities between dynamic mental models have been considered [12]. A formal scale, the NASA-TLX index has been used to disavow the notion of "sterile-cockpit" in cardiac surgery because of the variances in cognitive load experienced by different members of the clinical team over intraoperative phases [13].

The input gateways to the human brain are the senses and each individual has finite thresholds for sensory load [14]. As each stimulus signals the brain, the working memory capacity is apt to decrease, though not always [4]. The information that humans absorb in the operating room comes primarily from four senses—sight, audition, tactition and proprioception. Gatekeeping data is profoundly important, or else information overload will ensue.

The emergence of technologies that collect data from eye gaze, electric signals in the brain, heart rate, pressure, sweat etc. during activity elucidate upon the duress endured, mechanisms activated and allow for more complete models of cognition [15]. Leveraging these innovations in the operating room can have an acute effect on gauging how prone a clinician might be to committing an error. Furthermore if latent cognitive loads inhibit rational decision making and group engagement, then accurate and quick detection of reduced working memory capacity could allow an intelligent system to preempt dialogues before information is left unconsidered.

III. System Design

Unlike with conventional design theory, when the sensory mechanisms of humans do not satisfy all of the operational needs there is little opportunity to augment their range of sensitivity or add another sensory organ in real-time. Humans are the way they are: a completed package, fallible and require help.

An ideal design demands that at a given time each functional need is performed by a single component, which prevents undue coupling [16]. Surgical staff are often forced to meet multiple needs simultaneously and their sensory processing systems are being innervated by more than one stimulus at a given time. Resource competition theory of cognition intimates that in spite of sufficient resources of neurons to handle various sensory inputs at a given time, the human brain is wired such that perception of external data creates a hegemonic conflict for the same neural networks [17]. Ability to use a sense for perceiving task performance appears to be coupled with both the concomitant tasks and other senses being activated. Therefore a smart distribution and partitioning of the sociotechnical product is needed for improving work efficiency from a human perspective [18].

IV. Template Optimization Problem

Dynamic portfolio analysis

The first step in our solution method is to optimally distribute intraoperative information to clinicians given their current sensory loads and task-related needs. This means that their cognitive load must be held below a certain threshold and the utility of the information provided to them maximized. Such a process is akin to managing an investment portfolio across different time frames [19]. In this step, the market is constrained to one person and information resources are shuffled to various senses. This is iterated for each person and we first create a map of best information dispersion for each individual to best accomplish the goals set out for them.

Some key assumptions we have made are:

- the activity of all four senses in question can be measured in real-time
- a probabalisitc model can be constructed to demonstrate the likelihood of sensory occupation with a task
- cognitive load, sensory and working memory can be quantified and approximate overload thresholds defined
- the relationship between specific task perfomance and outcomes measures is known

Each team member has a task-specific cognitive load measured at every time step, Eqn (1). Cognitive loads for each successive time step are determined by the previous cognitive load, an estimate reduction in load caused by limitations in human working memory, the sensory attention dedicated to a given signal and rates of cognitive load return for each sensory commitment. Rates of return, $a_{k,x,i,t}$, act as discriminating multiplicative factors because investment in one sense likely influences how much mental stores can be devoted to a different sense or signal.

$$CL_{i,j,t+1} = \left(CL_{i,j,t-1} - l_{i,j,t}\right) + \sum_{x=1}^{4} \sum_{\substack{k'=2 \\ k' \neq k}}^{N} \sum_{k=1}^{N-1} \left(r_{k',x,j,t} - r_{k,x,j,t}\right) a_{k,x,i,t} \quad (1)$$

We have written step one of our method as a discounted dynamic programming problem with two objective functions [19]. The first, $\mathbb{O}_1$, imposes a limit on the cognitive load customized to each human agent at a given time. $\mathbb{O}_2$ dictates that the utility of the limited cognitive load must be maximized depending on the goal (or goals) of the human operator.

$$\mathbb{O}_1 \rightarrow CL_{j,t} \leq L_{j,t} \quad (2a)$$

$$\mathbb{O}_2 \rightarrow max\{\mathcal{E}[U(CL_{j,t})]\} \quad (2b)$$

A weighted multivariable utility optimization [20] will most likely be required because staff typically are concerned with patient safety, stability and resource utilization among a litany of other factors.

Asset selling

Ultimately however we are not striving to optimize the performance of individual agents autonomously, but to create a global system optimum for the OR so that all of the desired outcomes are achieved. The second step of our conceptual method is to expand the sensory marketplace to include all individuals, and eventually technologies. Similar to the financial analogy described above, information can be used as a currency whose value depends on how much utility it confers to the user [19]. If a global optimum can be achieved through exchange of information (or in this situation engineering the likelihood of an agent receiving that information) then these data assets should be traded fluidly.

Instead of moderating which information types are appropriate for just one person to complete a set of tasks with given priority, the second step allows for data carrying a semantic and clinically-relevant property to be distributed among agents in the OR sociotechnical system. For example, let us assume that there are two clinicians (j=1,2) in the operating room each able to observe one information bearing signal apiece, k_1 and k_2. Due to physical partitions in the OR both clinicians are obstructed from observing the other signal. According to this definition, $K_{1,t}=\{k_1\}=\underline{K}_{2,t}$ and $K_{2,t}=\{k_2\}=\underline{K}_{1,t}$. However, should the utility of receiving information conveyed by k_1 be more valuable than k_2 to j=2 at a given instance, then j=2 can "sell off" or discard k_2 so that he can be delivered k_1. This is not to say that we are censoring signals altogether, but rather limiting their exposure to those who might want or need them more. This is analogous to resituating a left-handed person to the left-end of a rectangular dinner table if they are bumping arms with their neighbor or offering a sign-linguist for the hearing impaired.

The decision rule for a next-state oriented scope is elementary.

$$if \quad \max_{K_{j,t}}\{\mathcal{E}[U(CL_{i,j,t+1})]\} \geq \max_{K_{j,t}}\{\mathcal{E}[U(CL_{i,j,t+1})]\} \qquad (3)$$

$$then \text{ "sell" } \{k_{N-n+1}, \dots, k_N\}, \text{"purchase" } \{\underline{k}_1', \dots, \underline{k}_{\varphi}'\} \; after \; t$$

$$otherwise \; keep \; K_{j,t} = \{k_1, \dots, k_N\} \; for \; t+1$$

However, what if we want to maintain a certain level of observable signal stability such that immediate information needs are trumped by routing policies that will likely yield more longitudinal efficiency and success? In such a case we would expand the horizon limits of our time frame [19].

V. Applications in the Robotic Operating Room

Present Day

Although Wadhera and associates measured disparities in cognitive loads between teams during intraoperative phases, there is no implication that manufacturing differentials in cognitive load alone enables sufficient situation awareness and application of other non-technical skills by less affected teams [13]. This level of assessment must be done for each clinician. Nonetheless, teams' interdependent workflows during surgery mandate essential communications of data which inform the decision to safely proceed with the next task [9].

Inclusion of a control-slave medical robot, like the da Vinci (Intuitiv Surgical, Inc, Mountain View, CA) into the milieu of the OR has the potential to exacerbate information communication dilemmas because of the physical disconnect between surgeon and other clinicians, limiting the sensory parity [2,21]. While some ORs are retrofitted with microphone systems that amplify voices to be fed through room or robot-control speakers, the ability to detect change and make inferences based upon directed or incidental observations is severely compromised. Thus, improving the mechanism for hearing communications does not rectify the issue of knowing when to elicit the correct information, but instead serves as a specious solution. Attentional blindness to these external events may in fact diminish a surgeon's external sensory or cognitive load, but the positional change from the table to the robot controller forces a surgeon to exert more effort in constructing and updating a mental model of team dynamics [3]. Working with robot in the OR introduces this complication as an unacceptable backslider.

Near Future

Having the ability to quantify cognitive load can be instrumental in eliminating denial as a deterrent from seeking help. Psychologically, some surgeons might be conditioned to believing that asking for assistance is tantamount to conceding their own shortcomings [22]. After hours of operation and the need to manage (or be observant of) many facets of care coordination, both physical and mental fatigue become salient obstacles to prudent decision-making. In a high-consequence environment like the OR, the perceived need to preserve ego and reputation should be relegated in priority compared with the overarching goal of providing therapeutic intervention for patients. If a personal cognitive load threshold is met, then the system could cue the OR suite manager of a need for relief.

From a robotics perspective, this same recognition could signal an array of "on-call" systems to gradually assume many of the menial or peripheral responsibilities (physical or supervisory) so that the surgeon can remain fully concentrated on the technical craft. In such a fashion, humans are not relinquishing control of the operating room to automation *per se*, but instead allow their confidence in cognitive surveillance to maintain continuity. What was once known as computer supported collaborative work could be afforded a new moniker—cognition attentive robotic assistance (CARA). Automobiles now have the ability to prompt steering correction for the drowsy driver and mobile phones adjust their setting when attention is diverted away from the screens. Because of these advancements, applications to the manipulation of robotic instruments appear tractable. Although some pundits will undoubtedly remark that human control in the surgical domain must remain sacrosanct, hopefully this serves as an acceptable compromise.

Distant Future

Looking more towards the distant horizon we can conceive a future where the cognitive loads experienced by surgical staff do not just prompt the OR information technology network to algorithmically rearticulate information or activate robotic "auto-pilot" features, but to dictate the physical and functional identities of machines themselves.

As morphogenic robots mature conceptually [23] and become actively integrated into the conversation of appropriate functionality in the OR, we envision that information "shunting" will also play a key role in determining what structural adaptations have a high-degree of fitness in an evolving environment.

VI. Conclusion

In assessing the novelty of this method, we do recognize that others have embraced a similar approach [24-25]. However these formulations are within a different context, use different inputs and have dissimilar time constraints. It should be noted that our method remains a kernel of an idea rather than an empirically validated approach. Nevertheless we feel strongly that measurement of cognitive and sensory loads for the reconstruction and rearticulating of information signals in the OR has significant potential to push the envelope of surgical patient safety innovation.

The objective is thus to alleviate cognitive overload by entrusting a larger cognitive network to remediate individual oversights and misinterpretations of information. However competent a surgical worker may be, he or she can only metabolize a limited amount of information while performing clinical task-work. Crafting a system that ensures clinicians' working memory can be strictly geared towards recalling medical training, past scenarios, previous patient status and developing case strategies instead of being inundated with superfluous information should be the underlying motivation. By our hypothesis, this will reduce the amount of preventable errors [26].

Constant fluctuation of task performance is not appropriate for people in a live OR. Some consistency must remain. Therefore the time intervals for measuring sensory loads and estimating informational utility require litigious selection. Custom, training deficits, dependence on protocol and human fallibility would most likely prohibit safe execution of tasks in a constantly changing environment. However, each moment of time provides a glimpse into how the sociotechnical system is structured and thus we can provide snapshots of potential improvements. Humans and technology should work collaboratively where the shortcomings of one can be compensated for by the other's abilities. Should the extant agents not complement each other perfectly, then that is evidence for an innovative need.

References

[1] Plsek, Paul. "Redesigning health care with insights from the science of complex adaptive systems." *Crossing the quality chasm: A new health system for the 21st century* (2001): 309-322.

[2] Carroll, John M., et al. "Notification and awareness: synchronizing task-oriented collaborative activity." *International Journal of Human-Computer Studies* 58.5 (2003): 605-632.

[3] Langley, Pat, John E. Laird, and Seth Rogers. "Cognitive architectures: Research issues and challenges." *Cognitive Systems Research* 10.2 (2009): 141-160.

[4] Van Merrienboer, Jeroen JG, and John Sweller. "Cognitive load theory and complex learning: Recent developments and future directions." *Educational psychology review* 17.2 (2005): 147-177.

[5] Cowan, Nelson, et al. "On the capacity of attention: Its estimation and its role in working memory and cognitive aptitudes." *Cognitive psychology* 51.1 (2005): 42-100.

[6] Miller, George A. "The magical number seven, plus or minus two: some limits on our capacity for processing information." *Psychological review* 63.2 (1956): 81.

[7] Shannon, C.E., Weaver, W., *The Mathematical Theory of Communication* (1949) University of Ilinois Press, Urbana

[8] Endsley, Mica R. "Toward a theory of situation awareness in dynamic systems." *Human Factors: The Journal of the Human Factors and Ergonomics Society* 37.1 (1995): 32-64.

[9] Yule, S., et al. "Development of a rating system for surgeons' non-technical skills." *Medical education* 40.11 (2006): 1098-1104.

[10] DeLeeuw, Krista E., and Richard E. Mayer. "A comparison of three measures of cognitive load: Evidence for separable measures of intrinsic, extraneous, and germane load." *Journal of Educational Psychology* 100.1 (2008): 223.

[11] Sawicka, Agata. "Dynamics of cognitive load theory: A model-based approach."*Computers in human behavior* 24.3 (2008): 1041-1066.

[12] Schaffernicht, Martin, and Stefan N. Groesser. "A comprehensive method for comparing mental models of dynamic systems." *European Journal of Operational Research* 210.1 (2011): 57-67.

[13] Wadhera, Rishi K., et al. "Is the "sterile cockpit" concept applicable to cardiovascular surgery critical intervals or critical events? The impact of protocol-driven communication during cardiopulmonary bypass." *The Journal of Thoracic and Cardiovascular Surgery* 139.2 (2010): 312-319.

[14] Lavie, Nilli, and Jan W. De Fockert. "Contrasting effects of sensory limits and capacity limits in visual selective attention." *Perception & Psychophysics* 65.2 (2003): 202-212.

[15] Vogel-Walcutt, Jennifer, and Julian Abich. "Using neurophysiological data to inform feedback timing: a pilot study." *Foundations of Augmented Cognition. Directing the Future of Adaptive Systems*. Springer Berlin Heidelberg, 2011. 265-274.

[16] Suh, Nam P. "Axiomatic design theory for systems." *Research in engineering design* 10.4 (1998): 189-209.

[17] Scalf, Paige E., et al. "Competition explains limited attention and perceptual resources: implications for perceptual load and dilution theories." *Frontiers in psychology* 4 (2013).

[18] Braha, Dan. "Partitioning tasks to product development teams." *Proceedings of ICAD*. 2002.

[19] Bertsekas, Dimitri P., and Dimitri P. Bertsekas. *Dynamic programming and optimal control*. Vol. 1. No. 2. Belmont: Athena Scientific, 1995.

[20] Tan, Weiping, et al. "Multiobjective Optimization in Multifunction Multicapability System Development Planning." 1-16.

[21] Goodwin, Dawn. "Upsetting the Order of Teamwork: IsThe Same Way Every Time'a Good Aspiration?." *Sociology* 41.2 (2007): 259-275.

[22] Wetzel, Cordula M., et al. "The effects of stress on surgical performance." *The American journal of surgery* 191.1 (2006): 5-10.

[23] Jin, Yaochu, and Yan Meng. "Morphogenetic robotics: An emerging new field in developmental robotics." *Systems, Man, and Cybernetics, Part C: Applications and Reviews, IEEE Transactions on* 41.2 (2011): 145-160.

[24] Yassine, Ali A., Ramavarapu S. Sreenivas, and Jian Zhu. "Managing the exchange of information in product development." *European Journal of Operational Research* 184.1 (2008): 311-326.

[25] Hou, Ming, et al. "Optimizing Operator–Agent Interaction in Intelligent Adaptive Interface Design: A Conceptual Framework." *Systems, Man, and Cybernetics, Part C: Applications and Reviews, IEEE Transactions on* 41.2 (2011): 161-178.

[26] Zegers, Marieke, et al. "The incidence, root-causes, and outcomes of adverse events in surgical units: implication for potential prevention strategies." *Patient Saf Surg* 5 (2011): 13.

EuRoSurge Workflow: From ontology to surgical task execution

E. De Momi, R. Perrone
Politecnico di Milano,
Milano Italy
Email: elena.demomi@polimi.it
roberta.perrone@mail.polimi.it

L. Schreiter, J. Raczkowsky
Karlsruhe Institute of Technology
Karlsruhe, Germany
Email: luzie.schreiter@kit.edu
joerg.raczkowsky@kit.edu

F. Boriero, M. Capiluppi, P. Fiorini
Università di Verona
Verona, Italy
Email: fabrizio.boriero@univr.it
marta.capiluppi@univr.it
paolo.fiorini@univr.it

***Abstract*—We present a workflow for design, deployment and verification of surgical robotic tasks. The workflow starts from the population of ontologies at two levels: task description and components specification. The ontologies are based on the technical and medical knowledge of the surgical task to be performed with a robot. From the ontologies, it is possible to design a model of the components and a finite state machine that represents the evolution of the task. This machine is verified using formal tools to avoid risks and preserve safety. Moreover a benchmarking phase assures the reliability of the components interaction. This workflow is applied to a simple case study.**

I. Introduction

The objective of the Coordination and Support Action *European Robotic Surgery* (EuRoSurge, FP7-ICT-2011-7) is to identify a methodology that is suitable for the integration of the research and manufacturing competences available in Europe in the two key areas of robotics and cognitive sciences, leading to easier product development and integration, standard settings, simpler technology transfer, and clearer identification of non-technical roadblocks. To this end, EuRoSurge aims at producing a reference workflow for the design, deployment and verification of a surgical robotic system.

In the preliminary part of the workflow an ontological modeling is used as knowledge base repository. Ontology is, by definition, a specification of a conceptualization [1]. The subject of ontology is the study of the categories of things that exist or may exist in some domain knowledge. Thus, a rigorous and exhaustive description of a specific domain is inside the ontology, and with the term domain, an area of knowledge, like for example the healthcare field, is meant [2]. An ontology is made of classes, individuals that populate classes, and properties that can link two different classes or can extend the meaning of a class. In medicine, ontologies have found large use because of problems of interoperability due to different nationalities and extraction of surgeons. Moreover, it is important to have a description of the medical knowledge that is understandable and processable by both men and machines. Medical ontologies like GALEN [3], SNOMED CT [4] and UMLS [5] are used as support for the healthcare practice from doctors, nurses, auxiliaries and also for the patients themselves. Ontologies can be used to formalize the workflow of a surgical procedure.

In our workflow, we use two different ontologies, with two different levels of granularity:

- The first ontology, named *TaskOntology*, will describe the considered task. It contains concepts related to all the possible states, transitions and commands that the component can assume. It could also contain information about the level of risk associated to the use of a component and related safety issues.
- The second ontology, named *ComponentOntology*, describes the set of components that participate to the scenario. All the components will be described by a set of property like inputs, outputs and specifications.

To control the surgical robotic system, we use a component-based software architecture [7] [8]. This software engineering technique suits our goal because it allows, thanks to its characteristics, to change the topology of the connections between the various software modules that implement the required functionalities. Currently, the most popular component-based robotic architectures are two: ROS and OROCOS. ROS [9] is a project created at Stanford (CA, USA) and mainly maintained by Willow Garage, broadly used in robotics communities. OROCOS [10] is another well known and used framework developed by the University of Leuven (BELGIUM).

The main feature of the surgical robotic context is the *heterogeneous* and *distributed* nature of the devices composing the setup. Indeed, the devices used in a teleoperation task [11] are spacially distributed and need to exchange a stream of real-time data. OROCOS has been chosen because, besides allowing the execution and transmission of real-time data [12], it integrates a finite state machine in each component to control its behaviour. This characteristic is of basic importance because it allows the designer to exploit reusability and modularity, e.g by changing the connections between the components without stopping or recompiling the software modules.

In order to design the software components corresponding to *ComponentOntology*, we need to find a tool that translates the ontological description into a coded model described by component name, input/output ports and type of data processed. Since we use the OROCOS architecture, we considered the two following tools: BRIDE[13]/VARP [14] and the script

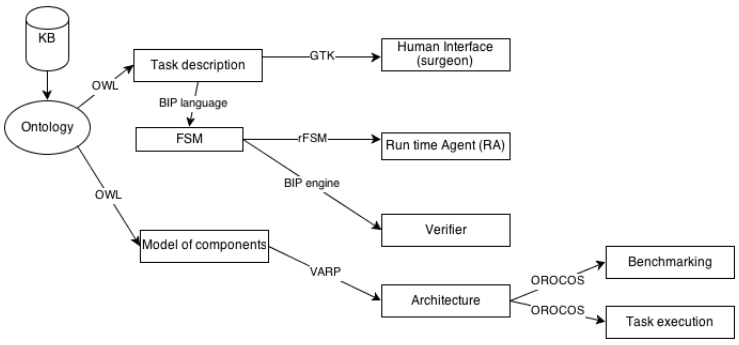

Fig. 1. The Eurosurge workflow. KB is the Knowledge Base repository, FSM is the Finite State Machine.

"orocreate-pkg" that is present in the OROCOS Toolchain. The idea is to start from a description ontology in OWL format [15], and automatically generate the code that could be integrated into the global architecture.

Once the components have been created and the functionalities implemented, it is necessary to coordinate them in order to follow the desired plan. For this purpose a deployer based on Lua [16] is used, an interpreted language used for the creation, the configuration and the implementation of the components.

In addition to the deployment and with the help of Lua, a finite state machine (FSM) can be used to describe and perform the operation task following a pre-defined plan. Indeed the FSM represents the evolution of the system to obtain the desired goal. It can also represent safety specifications and possible reconfiguration actions. A tool called RFSM described in [17] is used for designing such machine.

As for the components implementation, from the ontology description we can automatically generate a file readable by the RFSM toolbox. For its creation we used already existing ontologies exploiting available and reliable knowledge, like the suggested upper merged ontology (SUMO, [6]), that consists of general terms that can be used to connect and define our more specific terms. The final result is a running architecture generated by the two ontologies connected together: the $TaskOntology$ and the $ComponentOntology$. This is possible because concepts belonging to the two ontologies just explained can be linked, e.g concepts of the task ontology could have a relation with concepts of the component ontology.

Since the EuRoSurge project is interested in cognitive systems, the benchmarking phase afford tasks that cover the flexibility and autonomy of the aspired systems in order to respect the modularity. As explained above, one property of the reference architecture is the reusability: the components are created and should be used 'as they are', in different surgical-robotic contexts. For this reason a benchmark in the Eurosurge Project aims at comparing a similar component under the same conditions (task). The BRICS Project has launched three categories of metrics: cost, utility and reliability [18]. These metrics helped us in defining meaningful measurements based on a case study proposed in next section.

Formal methods tools, which help during the design phase to model synthesis of correct-by-construction systems, have been applied to high-level robot behaviours [20]. The aim of the verification phase is to verify the properties of modularity (two similar components with different characteristics but the same aim) and safety (ensuring that the system still performs in a region of safety) for the whole setup in a real-time environment. As we have figured out in [19] the technical aspect of safety is quite important in the area of robotic surgery. To respect the property of safety, the reliability metric of 'mission success' will represent in our case the accuracy property. To respect the modularity aspect, we are focusing on the BIP Framework. BIP is a component based framework for implementing embedded real-time systems in the area of robotics [21], [22] and [23]. We are especially interested in proving that our system is deadlock free, which means that in every reachable state a transition can still be activated. A derivative performance index of the first requirement is to prove reachability property. Hence, with the support of BIP, we are able to verify that the given finite state machine operates in a region of safety.

The above described workflow is presented in Fig. 1.

II. Case Study

We consider a manipulator moving freely in a room. The end effector of the manipulator has to reach a target, that might be a tissue in a surgical context. The position of the end effector in the task space is computed with a tracker, called Tracker 1. Since it is subject to faults, a second tracker (Tracker 2) is used as a backup. The setup is represented in Fig. 2, where a Staubli Puma 260 manipulator is used: it is controlled by a Galil 4080 control board and tracked using Naturalpoint Optitrack (Altair robotic laboratory setup) for Tracker 1 and ClaronTech Microtracker 2 for Tracker 2.

We use the *ComponentOntology* to describe particular instances, or classes, of components, thus the functional, physical and measurement aspects. In our scenario, we have four different components: *Robot, Supervisor, Tracker 1* and *Tracker 2*. Every component can have a label, some specific properties and ports. Ports can be input or output and, for every port, the type of data in input/output (e.g. integer, floating etc.) is defined, as shown in Fig. 3.

Fig. 2. Setup of the case study. T1 (Tracker 1) and T2 (Tracker 2) are represented by the circles: blue for T1 and red for T2.

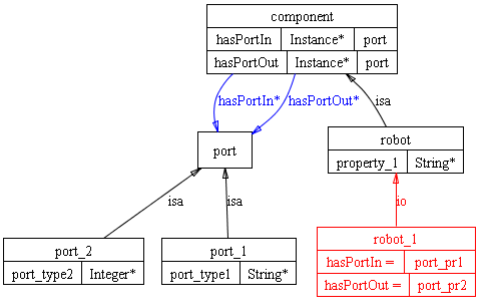

Fig. 3. Ontological description of a component. The component class is characterized by two properties that define the port of input and output. The component class is connected to the port class. In the figure the component class has an instance, which is a robot, that inherit all the properties of being a component.

The finite state machine (FSM) describing the operation plan is designed starting from the ontology that describes the surgical robotic task. For our case study, in the *TaskOntology* there are classes like: *State*, *Event* and *Transition*. The *State* class is populated with concepts like: *Init*, *Ready*, *DoTask*, *T1down* and *Goal*. The *Transition* class is populated with all the possible transitions that the robot can perform. Moreover, the *Transition* class will be characterized by two properties that states the starting state and the ending state of a specific transition.

Once the *TaskOntology* has described the finite state machine for our case study (Fig. 4), the verification phase implements it with BIP. A pseudo code of the finite state machine of Fig. 4 is given in Fig. 5: the events, states and transitions are described within commands **events, states, behaviour** respectively. The reader can see that the translation from the FSM to BIP code is straightforward. Here we added an event called e_μ representing the internal event moving the system from its initial state *Init* to the *Ready* state. This event is automatically generated by the FSM, but it has to be made explicit in the code. One of the most important problems to face is to check if the created FSM based on the ontology is deadlock free and if the states are in a valid order, via the reachability check. If and only if the verification is correct, the workflow can go on to the execution, which means that

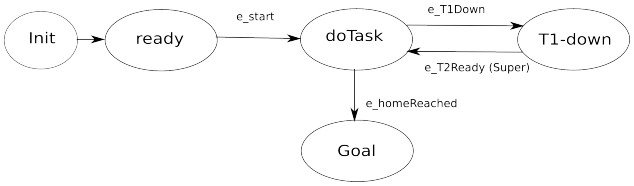

Fig. 4. Finite state machine of the case study

an automatic translation from the BIP language to RFSM is implemented and can be used for the execution of the task. We ran this check and verified that every state of the finite state machine in Fig. 4 is reachable using the BIP tools.

events e_μ(), e_start(), e_T1down(), e_T2ready(),
e_homeReached() , e_end()
states Init, Ready, DoTask, T1down, Goal
behaviour
initial to Init
on e_μ from Init to Ready
on e_start from Ready to DoTask
on e_homeReached from DoTask to Goal
on e_T1down from DoTask to T1down
on e_T2ready from T1down to doTask
on e_end from Goal to Goal

Fig. 5. BIP code of the case study.

Next step of the EuRoSurge workflow is the execution of the surgical task as shown in Fig. 6. In our simple case study, the robot performs a pre-planned trajectory. Tracker 1 calculates the position of the robot and sends it to the Supervisor component. If the error between the position calculated from the kinematics of the robot and the tracker measure is higher than a predefined threshold, the Supervisor will raise an event to the Run Time Agent (RTA). Notice that we are not interested in the algorithm used to choose the above mentioned threshold, since we are not discussing here the methods for fault detection. A simple study of the performance of Tracker 1 can lead to determine the right threshold to detect the fault

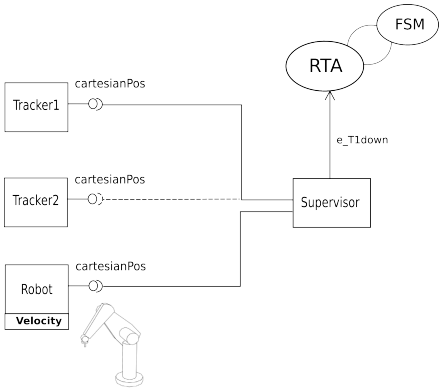

Fig. 6. Task execution of the case study: FSM is finite state machine, RTA is the Run-Time Agent.

and use residuals methods. In this case, the RTA will use this event to update the finite state machine that will return the new status of the surgical plan. The consequence is that the RTA will close the connection between Tracker 1 and the Supervisor and create a new connection between Tracker 2 and the Supervisor. As final result, in case of error, the second tracker automatically replaces the first one, allowing the continuation of the task. The RTA is the global coordinator that knows the described surgical task given by the FSM, controls the components, changes the architecture topology and verifies the desired properties using events exchanged with the supervisor.

The proposed benchmark starts by moving the robot with different estimated velocities from a starting point to an apriori defined target point, e.g. a point in the skin of a patient in case of a needle insertion operation. The benchmark takes place before the real surgical intervention will be done. The architecture provides a component, called *Reporter*, which is able to log all the required data for the benchmark. To estimate the accuracy of each tracker, the error between the given position of the robot and the given position of the trackers will be logged. The error value represents a comparative value for the accuracy of both tracking systems. The outcome of the benchmark phase depends strongly on the implementation and the environment. Hence the benchmark is performed with both trackers at the same time and the trajectory used is the same as in the surgical intervention scenario. Moreover, the collected data has been used in Matlab to calculate the error and to visualize the different error values depending on the defined velocities.

III. Conclusions

EuRoSurge workflow aims at giving guidelines for the design, implementation and verification of a surgical robotic system. In our workflow we started with an ontology describing both components and the surgical task, based on medical and technical knowledge. From this description, we model the components using a software (BRIDE/VARP, OROCOS) that translates the ontology written in OWL. The ongoing work aims at obtaining this translation automatically. The ontology provides the basis to design a finite state machine representing the evolution of the surgical task. It is necessary to involve the medical and technical experts to make this step. Indeed, the experts will help the designer to decide what parts of the ontology have to be used to design the specifications related to the specific instance of the surgical task. We are working on this cognitive aspect. Moreover, the verification procedure requires an automatic translation of the finite state machine from BIP to RFSM to design the run-time agent. Finally, a future extension of the workflow will include a human interface that should allow the surgeon to understand the level of risk it might take in performing specific actions. This interface will take into account the evolution of the system specified in the finite state machine and the task ontology. To this end, a level of risk has to be defined and an index needs to be agreed between the designer and the surgeon.

References

[1] T. Gruber, "What is an ontology," *Encyclopedia of Database Systems*, vol. 1, 2008.

[2] J. F. Sowa, "Ontology, metadata, and semiotics," in *Conceptual structures: Logical, linguistic, and computational issues*. Springer, 2000, pp. 55–81.

[3] A. L. Rector, J. E. Rogers, and P. Pole, "The galen high level ontology," *Studies in health technology and informatics*, pp. 174–178, 1996.

[4] L. Bos *et al.*, "Snomed-ct: The advanced terminology and coding system for ehealth," *Medical And Care Compunetics 3*, vol. 121, p. 279, 2006.

[5] O. Bodenreider, "The unified medical language system (umls): integrating biomedical terminology," *Nucleic acids research*, vol. 32, no. suppl 1, pp. D267–D270, 2004.

[6] I. Niles and A. Pease, "Towards a standard upper ontology," in *Proceedings of the international conference on Formal Ontology in Information Systems-Volume 2001*. ACM, 2001, pp. 2–9.

[7] D. Brugali and P. Scandurra, "Component-based robotic engineering (part i)[tutorial]," *Robotics & Automation Magazine, IEEE*, vol. 16, no. 4, pp. 84–96, 2009.

[8] D. Brugali and A. Shakhimardanov, "Component-based robotic engineering (part ii)," *Robotics & Automation Magazine, IEEE*, vol. 17, no. 1, pp. 100–112, 2010.

[9] M. Quigley, K. Conley, B. Gerkey, J. Faust, T. Foote, J. Leibs, R. Wheeler, and A. Y. Ng, "Ros: an open-source robot operating system," in *ICRA workshop on open source software*, vol. 3, no. 3.2, 2009.

[10] H. Bruyninckx, "Open robot control software: the orocos project," in *Robotics and Automation, 2001. Proceedings 2001 ICRA. IEEE International Conference on*, vol. 3. IEEE, 2001, pp. 2523–2528.

[11] B. Hannaford and P. Fiorini, "A detailed model of bi-lateral teleoperation," in *Proceedings of the IEEE international conference on systems, man and cybernetics*, vol. 1, 1988, pp. 117–121.

[12] H. Bruyninckx, P. Soetens, and B. Koninckx, "The real-time motion control core of the orocos project," in *Robotics and Automation, 2003. Proceedings. ICRA'03. IEEE International Conference on*, vol. 2. IEEE, 2003, pp. 2766–2771.

[13] H. Bruyninckx, M. Klotzbücher, N. Hochgeschwender, G. Kraetzschmar, L. Gherardi, and D. Brugali, "The brics component model: a model-based development paradigm for complex robotics software systems," in *Proceedings of the 28th Annual ACM Symposium on Applied Computing*. ACM, 2013, pp. 1758–1764.

[14] L. Gherardi, "Variability modeling and resolution in component-based robotics systems," Ph.D. dissertation, Katholieke Universiteit Leuven, Belgium, 2013.

[15] D. L. McGuinness, F. Van Harmelen *et al.*, "Owl web ontology language overview," *W3C recommendation*, vol. 10, no. 2004-03, p. 10, 2004.

[16] M. Klotzbücher, P. Soetens, and H. Bruyninckx, "Orocos rtt-lua: an execution environment for building real-time robotic domain specific languages," in *International Workshop on Dynamic languages for RObotic and Sensors*, 2010, pp. 284–289.

[17] M. Klotzbuecher and H. Bruyninckx, "Hard real-time control and coordination of robot tasks using lua," in *Proceedings of the Thirteenth Real-Time Linux Workshop*, 2011, pp. 37–43.

[18] W. Nowak, Z. Zakharov, S. Blumenthal, and P. E., "Delivarable 3.1: Benchmarking for mobile manipulation and robust obstacle avoidance and navigation," 2010.

[19] M. Capiluppi, L. Schreiter, P. Fiorini, J. Raczkowsky, and H. Woern, "A fault analysis procedure for surgical robotic systems," in *Hamlyn Symposium on Medical Robotics 2013*, 2013.

[20] ——, "Modeling and verification of a robotic surgical system using hybrid input/output automata," in *press European Control Conference, Zurich*, 2013.

[21] T. Abdellatif, S. Bensalem, J. Combaz, L. De Silva, and F. Ingrand, "Rigorous design of robot software: A formal component-based approach," *Robotics and Autonomous Systems*, 2012.

[22] S. Bensalem, L. de Silva, F. Ingrand, and R. Yan, "A verifiable and correct-by-construction controller for robot functional levels," *Journal of Software Engineering for Robotics*, vol. 1, no. 2, pp. 1–19, 2011.

[23] A. Basu, M. Bozga, and J. Sifakis, "Modeling heterogeneous real-time components in bip," in *Software Engineering and Formal Methods, 2006. SEFM 2006. Fourth IEEE International Conference on*. Ieee, 2006, pp. 3–12.

Learning Catheter-Aorta Interaction Model Using Joint Probability Densities

Yohannes Kassahun, Bingbin Yu
University of Bremen
Faculty 3 - Mathematics and Computer Science
Mary-Somerville-Str. 9, D-28359 Bremen, Germany
Email: kassahun@informatik.uni-bremen.de

Emmanuel Vander Poorten
University of Leuven
Dept. of mechanical engineering, division PMA
Celestijnenlaan 300B, B-3001 Heverlee, Belgium

I. Abstract

Catheter based diagnosis and therapy of cardiovascular diseases is becoming more popular these days. Often the vasculature is being accessed from a less invasive location remote to the cardiac region. For transfemoral approaches of TAVI procedures the vasculature is for example accessed through a cannula inserted into the patient's groin and then moved gently up to the heart [1]. Due to the complex and deformable nature of both the vasculature and the catheter, the overall controllability of the catheter itself is low in such a case. Tissue damage, dissection or perforation of the vessel and even of the heart cannot be ruled out [2], [3], [4]. The Cognitive AutonomouS CAtheter operating in Dynamic Environments (CASCADE) [5], a recent EU-funded FP7 project, investigates autonomous catheter control and explores machine learning techniques to learn the input-output behavior of the catheter inside vessels of artificial mock-ups. The results from this study should enhance the understanding, the control of catheter motion and interaction patterns also during real interventions.

Before learning to control a catheter, different ways of learning the interaction model of the catheter with the aorta should be investigated. These will help to transfer the learned model from the mock-up to the real world in the long run. Since it is not always possible to guarantee safety when applying learning methods, it is important to first investigate different ways of learning the catheter-aorta interaction model and evaluate their failure modes.

II. Experimental Setup

A two dimensional mock-up of the aorta was constructed; the mock-up together with an RFA ablation catheter (EndoSense SA) is shown in Figure 1. An exact replica of this exact mock-up is distributed among the partners of the CASCADE project so that algorithms can be shared freely. In addition to this, partners can compare their results or even reproduce results of other partners. The mock-up of the aorta is a rigid body, which is a very simple model of the aorta. Since the mock-up is a rigid body, the properties of the catheter-aorta interaction will mainly depend on the catheter. As a sensor a camera was used. The camera looks straight down to the plane in which the aorta is lying. It is a high-resolution network camera (AXIS 215 PTZ). The PTZ network camera provides pan, tilt and zoom functions, enabling wide area coverage and easy manipulation through

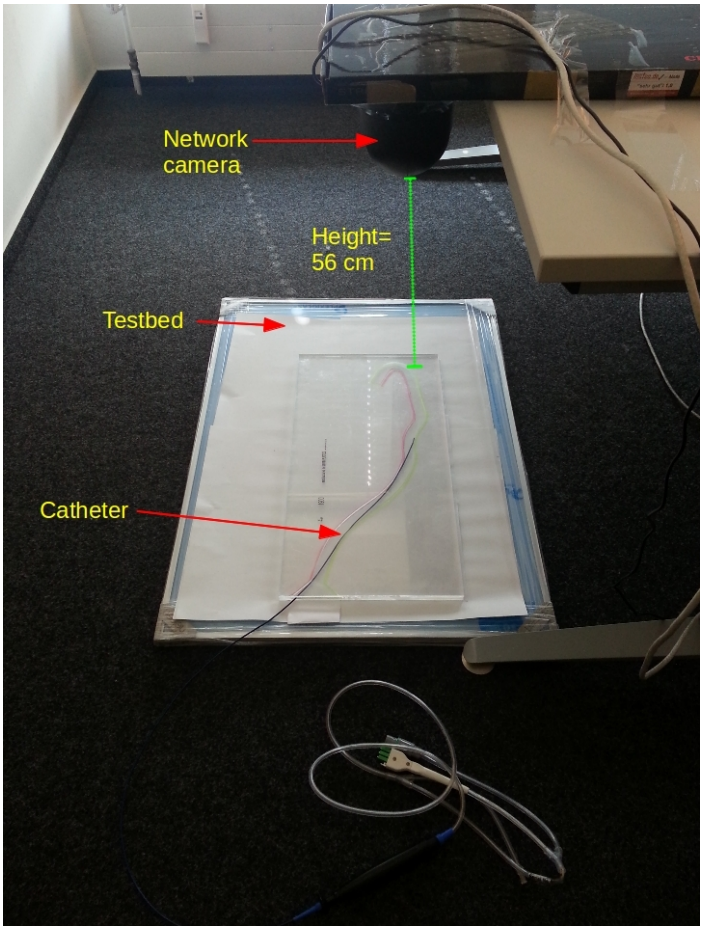

Fig. 1. The experimental setup. In the picture the mock-up, a commercial catheter and a camera used to measure the catheter are shown.

web browsers. The camera is mounted directly above the testbed at a height of 56 centimeters. The resolution of the video image is 704×576 pixels for the 4CIF format. The upper and lower boundaries of the aorta in the testbed are colored in pink and yellow, respectively. This marking simplifies the identification by image processing. Figure 2 shows the catheter and the mock-up as seen from the camera perspective. From the camera image, the following parameters are extracted: (1) the shape of the catheter, (2) the contact points where the catheter touches the boundaries of the aorta in different

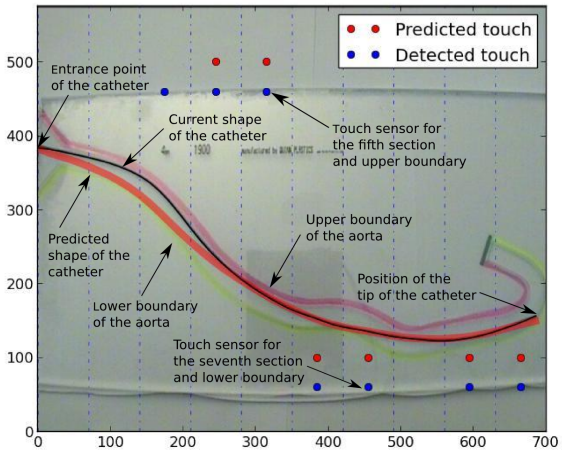

Fig. 2. The mock-up and the catheter as seen from the camera perspective. The different parameters that are used for modeling the catheter-aorta interaction are shown. The numbers on the horizontal and vertical axes show the pixel coordinates in the image. The dotted vertical lines in the image show the boundaries of the different sections. The red dots above and below the aorta show the state of the touch sensors.

sections, (3) the entrance point of the catheter and (4) the tip of the catheter. For the purpose of extracting the parameters listed above, we used an OpenCV implementation programmed in the Python programming language[6].

III. Method

In this paper we present a catheter-aorta interaction modeling using joint probability densities [7]. For modeling training data is collected using the above-mentioned camera setup. The training data is gathered by applying different manipulation acts on the catheter (mainly pushing the catheter into and pulling the catheter out of the mock-up). Each entry in the training data has five components. The first component is a vector of contact points of different sections of the catheter for the upper boundary of the aorta $\boldsymbol{t}_u$. The second component is a vector of contact points of different sections of the catheter for the lower boundary of the aorta $\boldsymbol{t}_l$. The dimension of the vectors for the touch sensors of the upper and lower boundaries of the aorta is equal to the number of sections. For this experiment the aorta was subdivided into ten sections. Figure 2 shows dotted vertical lines representing the boundaries of the different sections. The third component is a vector of coefficients of a function $\boldsymbol{\alpha}$ used to represent the shape of the catheter. In this work, we used B-splines of third order to approximate the shape of the catheter. The number of coefficients for approximating the shape of the catheter is 34, which corresponds to 30 splines. The fourth and fifth components represent the Cartesian coordinates (expressed in pixels) of the entrance point of the catheter $\boldsymbol{p}_e$ and the tip of the catheter $\boldsymbol{p}_t$, respectively. During training the joint probability distribution

$$p(\boldsymbol{t}_u, \boldsymbol{t}_l, \boldsymbol{\alpha}, \boldsymbol{p}_e, \boldsymbol{p}_t), \tag{1}$$

is learned and during testing from the joint probability distribution

$$\mathbb{E}\left[\boldsymbol{\alpha} | \boldsymbol{p}_e, \boldsymbol{p}_t\right], \tag{2}$$

is calculated, where $\mathbb{E}$ stands for expected value. Expression (2) gives the estimate of the current shape of the catheter given $\boldsymbol{p}_e$ and $\boldsymbol{p}_t$ by generating the shape of the catheter from the coefficients $\boldsymbol{\alpha}$. In reality $\boldsymbol{p}_e$ is more or less known and $\boldsymbol{p}_t$ could be e.g. acquired from an electromagnetic sensor embedded in the catheter tip. Here, this sensor is simulated through our camera measurements. Note that the model (1) implicitly incorporates the geometry of the vessel. For different vessel geometries this model thus needs to be updated. Now, the state of the touch sensors can then be estimated using

$$\mathbb{E}\left[\boldsymbol{t}_u, \boldsymbol{t}_l | \boldsymbol{p}_e, \boldsymbol{p}_t\right], \tag{3}$$

which can also be calculated from expression (1). If the shape of the catheter is known, then the state of the touch sensors can be estimated using

$$\mathbb{E}\left[\boldsymbol{t}_u, \boldsymbol{t}_l | \boldsymbol{\alpha}, \boldsymbol{p}_e, \boldsymbol{p}_t\right]. \tag{4}$$

To calculate analytically the quantities given by expressions (2), (3) and (4), we used a mixture of Gaussians for modeling the joint probability distribution given by expression (1). Mixture of Gaussians are discussed at length in the book by Mclachlan and Peel [8].

IV. Results

After training the catheter-aorta interaction model, the model is evaluated for its prediction capabilities for the shape of the catheter and the states of touch sensors for all sections of the aorta and for the upper and lower boundaries of the aorta. The evaluation is performed on a novel dataset, which is not included in the training set. Figure 3 shows the prediction performance of the model in predicting the shape of the catheter using expression (2) and the state of the touch sensors for the upper and lower boundaries of the aorta for some of the positions of the tip of the catheter using expression (3). As can be seen from these results, the model is able to predict

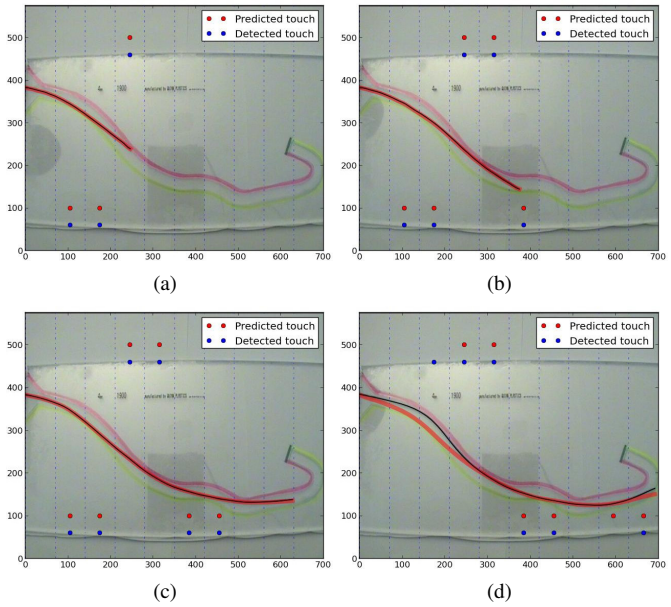

Fig. 3. The predictions of the shape of the catheter and the state of the touch sensors for the upper and lower boundaries of the aorta.

the shape of the catheter and the state of the touch sensors in the different sections of the catheter.

In the following we examine the prediction given by expression (4) more closely since in reality the shape of the catheter can be extracted from electromagnetic sensors embedded along the catheter, or from fluoroscopic images. During testing, for each section i we counted the number of times a touch sensor corresponding to section i and the upper boundary detects touch, $\#T_{ui}$, and the number of times a touch sensor corresponding to section i and the lower boundary detects touch, $\#T_{li}$. We calculated the true positive rates TPR_{ui} and TPR_{li} for the upper and lower boundaries and for section i using

$$TPR_{ui} = \frac{\#\left((\text{prediction}_{ui}\text{= touch}) \wedge (\text{sensor}_{ui}\text{ = touch})\right)}{\#T_{ui}}, \tag{5}$$

$$TPR_{li} = \frac{\#\left((\text{prediction}_{li}\text{= touch}) \wedge (\text{sensor}_{li}\text{ = touch})\right)}{\#T_{li}}. \tag{6}$$

Similarly, we counted the number of times a touch sensor corresponding to section i and the upper boundary detects no touch, $\#NT_{ui}$, and the number of times a touch sensor corresponding to section i and the lower boundary detects no touch, $\#NT_{li}$. We then calculated true negative rates TNR_{ui} and TNR_{li} for the upper and lower boundaries and for section i using

$$TNR_{ui} = \frac{\#((\text{prediction}_{ui}\text{=no touch}) \wedge (\text{sensor}_{ui}\text{ =no touch}))}{\#NT_{ui}}, \tag{7}$$

$$TNR_{li} = \frac{\#((\text{prediction}_{li}\text{=no touch}) \wedge (\text{sensor}_{li}\text{ =no touch}))}{\#NT_{li}}. \tag{8}$$

Then we calculated the harmonic mean accuracy (HMACC) for section i and the upper and lower boundaries using

$$\text{HMACC}_{ui} = \frac{2(TPR_{ui}\,TNR_{ui})}{TPR_{ui} + TNR_{ui}}, \tag{9}$$

$$\text{HMACC}_{li} = \frac{2(TPR_{li}\,TNR_{li})}{TPR_{li} + TNR_{li}}. \tag{10}$$

The values for the HMACC lie between zero and one. A higher value of HMACC means a better prediction accuracy. Standard accuracy measures for section i and the upper and lower boundaries given by

$$\text{Accuracy}_{ui} = \frac{TPR_{ui}\#T_{ui} + TNR_{ui}\#NT_{ui}}{\#T_{ui} + \#NT_{ui}}, \tag{11}$$

$$\text{Accuracy}_{li} = \frac{TPR_{li}\#T_{li} + TNR_{li}\#NT_{li}}{\#T_{li} + \#NT_{li}} \tag{12}$$

are also calculated. If the number of touches detected by the touch sensor for section i and a boundary is different from the number of no touches, then the HMACC gives high values for models predicting well both the touch and non touches. If a model predicts correctly all the non touches but predicts incorrectly all of the touches, it gets an HMACC value of 0. However, the same model might get a high value of accuracy. This is evident from the HMACC and accuracy values for section $S6$ of the upper boundary shown in Figure 4. As can be seen from the figure, the model detects the states of the touch sensors most of the times correctly. In the future, the deformable and variable nature of the vessel will need to be addressed.

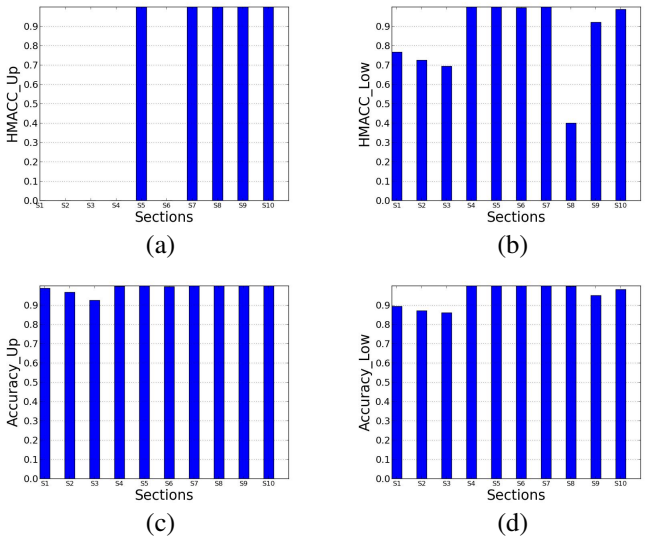

Fig. 4. The harmonic mean values and accuracies for each section and for the upper (a) & (c) and lower (b) & (c) boundaries of the aorta, respectively.

REFERENCES

[1] W. Gaasch and R. D'Agostino, "Transcatheter aortic valve implantation: The transfemoral versus the transapical approach." *Ann Cardiothorac Surg*, pp. 200–205, 2012.

[2] T. Kono, H. Kitahara, M. Sakaguchi, and J. Amano, "Cardiac rupture after catheter ablation procedure." *The Annals of Thoracic Surgery*, vol. 80, no. 1, pp. 326–327, 2005. [Online]. Available: http://www.ncbi.nlm.nih.gov/pubmed/15975397

[3] R. Tilz, K. Chun, A. Metzner, A. Burchard, E. Wissner, B. Koektuerk, M. Konstantinidou, D. Nuyens, T. De Potter, K. Neven, A. Furnkranz, F. Ouyang, and B. Schmidt, "Unexpected high incidence of esophageal injury following pulmonary vein isolation using robotic navigation," *Journal of Cardiovascular Electrophysiology*, vol. 21, no. 8, pp. 853–858, August 2010.

[4] A. Aminian, J. Lalmand, and B. El Nakadi, "Perforation of the descending thoracic aorta during transcatheter aortic valve implantation (tavi): An unexpected and dramatic procedural complication," *Catheterization and Cardiovascular Interventions*, vol. 77, no. 7, pp. 1076–1078, 2011.

[5] "Cognitive AutonomouS CAtheter operating in Dynamic Environments (CASCADE)," http://www.cascade-fp7.eu/, [Online; accessed August 30 2013].

[6] G. Bradski, "The OpenCV Library," *Dr. Dobb's Journal of Software Tools*, 2000.

[7] M. Edgington, Y. Kassahun, and F. Kirchner, "Using joint probability densities for simultaneous learning of forward and inverse models," in *IEEE IROS International Workshop on Evolutionary and Reinforcement Learning for Autonomous Robot Systems*, N. T. Siebel and J. Pauli, Eds., 10 2009, pp. 19–22.

[8] G. Mclachlan and D. Peel, *Finite Mixture Models*, 1st ed., ser. Wiley Series in Probability and Statistics. Wiley-Interscience, 2000.

Artificial Cognitive Supervision during Robot-Assisted Laser Surgery

Loris Fichera, Diego Pardo and Leonardo S. Mattos
Department of Advanced Robotics - Istituto Italiano di Tecnologia
Via Morego 30, 16163 Genova, Italy
Email: {loris.fichera, diego.pardo, leonardo.demattos}@iit.it

***Abstract*—This abstract focuses on the role of artificial cognition in the context of robot-assisted laser microsurgery. The issues related to the use of a laser as surgical tool are identified and contrasted against the possibilities offered by a cognitive system. The concept and progress in the development of a cognitive supervisory system for laser microsurgery are presented. This system is intended to supervise laser-tissue interactions occurring during surgery, controlling the incision process and generating alarms when potentially dangerous situations are detected.**

I. Introduction

Applications of cognitive systems in robotics vary widely. By definition, these systems exhibit a set of properties [1] that are desirable when tackling problems that require high-level reasoning capabilities i.e., similar to those of humans. Examples of such problems include planning and executing actions in real-world environments, dealing with high-dimensional or uncertain information and coping with situations that were not considered or cannot be taken for granted at design time.

Surgical robotics constitute a promising field of application for cognitive systems. Recent trends in this area point towards the development of special-purpose robots [2] to attain surgical procedures that would be difficult or impossible otherwise. The purpose of developing robots for surgery is to provide the surgeon with highly specialized tools that extend his/her performance, therefore improving the overall quality of the surgical treatment [3]. Nevertheless, sometimes interposing a robot between the surgeon and the patient increases the complexity of the procedure, which is usually due to the physical constraints of the robot. For instance, the robot may have many degrees of freedom in order to adapt to the shape of specific anatomical parts, making it difficult to control. Additional constraints appear in minimally invasive surgery, where a limited access to the surgical site implies a poor perception of the area of interest, demanding additional mental workload to the surgeon, who plan and execute movements on the tools by looking at images provided by a camera located inside the body of the patient. An extended list of open problems related with the use of robots in the operating room is reported in [4].

Thus, it seems that classic robot control strategies are not sufficient to handle the complexity of the scenarios presented above. Cognitive approaches are currently being investigated to turn surgical robots into smart tools. Recent results in this context cover the development of advanced control algorithms for robots with many degrees of freedom, automatic movement of surgical tools, obstacle avoidance, navigation aid and simultaneous localization and mapping [4].

In the case of laser surgery of the vocal cords, i.e., laser phonomicrosurgery (LP) [5] surgeons cannot rely on their sense of touch to control the incision process. Rather, they are required to develop a different kind of dexterity, built around the capability of predicting the effects of laser irradiation of tissue.

This abstract discusses the issues related to the use of lasers as surgical tools and how systems based on cognitive approaches can help in mitigating them. The concept and the current state of development of a cognitive supervisory system for laser phonomicrosurgery is presented.

II. Laser Phonomicrosurgery

The interaction between the laser and the tissue is the elemental building block at the core of laser-based surgery. It is through this interaction that incisions and resections are performed. The control of the incision process relies on the experience and dexterity of the surgeon, who intrinsically establishes the state of the interaction and thereby decides the laser actions to perform. The mental workload is intensified by an inadequate perception of the surgical site, as LP is performed through a microscope [6]. Acquiring the skills needed to conduct LP requires extensive training.

Improper operation of the laser may hinder the surgical procedure. Furthermore, it may lead to undesired and potentially dangerous effects. Carbonization is one of those. It occurs when the temperature of tissue increases, due to the energy transferred from the laser [7], beyond 100°C. Carbonization causes pain and longer healing times, diminishing the quality of surgery [6]. Also, it may influence the patient ability to speak normally again.

Nowadays there are no technical solutions for the automatic supervision of the incision process during laser-based surgery. To this end, a predictive model would be necessary, predicting the outcome of the process and analyzing its state. Analytical models of laser-tissue interaction (LTI) are well known [7]. They depend mainly on tissue temperature and water content. At the same time, these variables depend on laser properties as beam focus and power, as well as on laser exposure time and pulse rate. The laser wavelength, and its corresponding absorption and scattering coefficients on the

tissue also determine the emergence of undesired effects like tissue carbonization. Accurate and real-time measurement of some of these variables during LP is not straightforward.

Thus, if a system is supposed to supervise the state of the LTI, it should rely on inputs similar to those used by surgeons (laser location and history of actions) and not on analytical models based on tissue properties.

III. Cognitive Systems for Laser Surgery Supervision

Using a forward model to predict the state of LTI during LP leads to formulate a solution in which analytical modeling is neither convenient nor viable. Accordingly, we propose to use models motivated by the capacity of humans to map and fuse diverse sets of information and infer the state of events.

A. Cognitive Model

Length and depth of an incision depend on the treatment parameters, such as the laser power and the total exposure time. Skilled surgeons have developed the ability to finely configure these parameters in order to get the incision they have planned. The thermal state of the tissue plays a major role during the incision process [7], driving its outcome. We may hypothesize that surgeons have an internal, and probably not explicit, estimation about the thermal state of the tissue. Developing an autonomous system able to predict this state without using a deterministic model can be seen as the design of an artificial cognitive model.

A *cognitive model* generally denotes the combination of a knowledge set with a given cognitive architecture [8]. Such knowledge encapsulates the experience about certain process or entity, while the cognitive architecture specifies how this knowledge is represented, acquired, and processed in order to obtain some specific behaviour.

We have developed a thermal model of tissue based on high-level information such as laser activation, power and pulse mode [9]. The change in temperature due to heat transfer and diffusion are modeled as functions of laser exposure time. The model is parameterized with respect to laser power and assumes constant tissue properties. This model has been extracted using machine learning techniques.

Initial results demonstrated the concept of an artificial cognitive system able to predict the tissue thermal state during laser exposure and it is based on simulated data, generated with a Monte Carlo-based algorithm complemented by a finite difference method for the resolution of heat diffusion [10].

B. Supervising Laser-Tissue Interaction

The cognitive supervisory system is meant to support surgeons, enhancing their perception about the state of LTI, thus facilitating their decision making. This model is not supposed to replace the surgeon perception but to complement it. Fig. 1 shows a diagram describing this concept.

The purpose of this system is to predict the continuous appearance changes of the surgical site that can be observed during LP, by means of image processing (e.g., laser localization, carbonization detection) and artificial intelligence techniques. This functionality will be used to automatically supervise the surgical procedure, generating alarms in case unexpected or unforeseen situations are detected. The focus of the supervisory system falls on the undesired and potentially dangerous situations that may arise during LTI. In this context, tissue carbonization and incision quality are recognized as potential targets for automatic supervision.

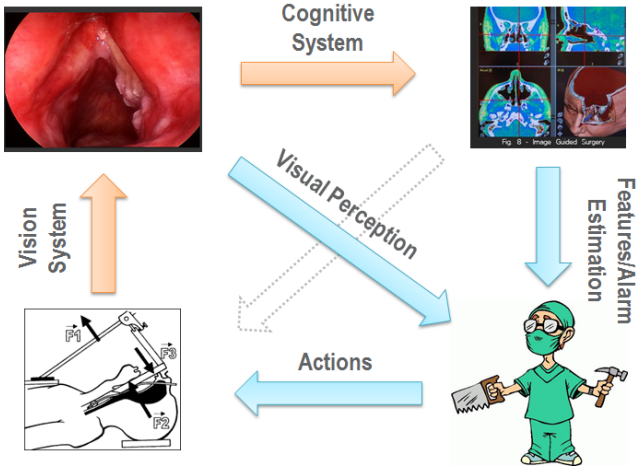

Fig. 1. Cognitive System for supervision of laser surgery. The system provides additional information to the surgeon enhancing the perception on the laser-tissue interaction

At the core of the supervisory system lies the developed model of temperature during LTI [9]. Based on the model of temperature dynamics and the history of laser actions, an autonomous system to avoid tissue carbonization and to supervise the quality of the incision can be implemented. Given the location of the laser beam, the temperature model can be mapped onto the area of interest, activating the input when the surgeon triggers the laser, generating and tracking an estimation of tissue temperature.

IV. Preliminary Results

Initial studies demonstrated that a model based on ML can be obtained mapping the same inputs that surgeons use (i.e, laser actions) to the resulting thermal state of the tissue [9]. Nevertheless input/output data for the model was obtained through simulation, given an analytic description of the temperature dynamics [7],

$$\dot{T} = \kappa \nabla T + \frac{1}{\rho c} S, \tag{1}$$

where T, and $\dot{T}$ represent the tissue temperature and its temporal derivative, while ∇T is the Laplacian operator, describing the spatial change of temperature along the tissue, which conductivity, κ, is approximately the same for liquid water and most tissues ($\sim 1.4 \times 10^{-7} \frac{\mathrm{m}^2}{\mathrm{s}}$). The source of heat per unit of volume and time, S, contributes to the change in temperature weighted by the density (ρ) and the specific

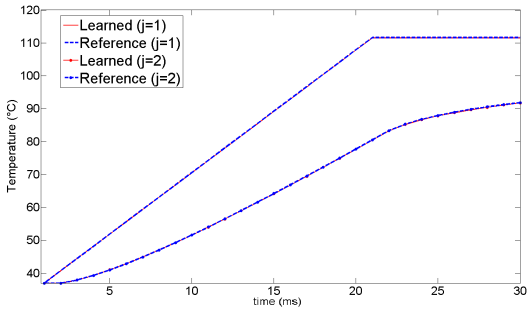

(a) Continuous Laser Mode

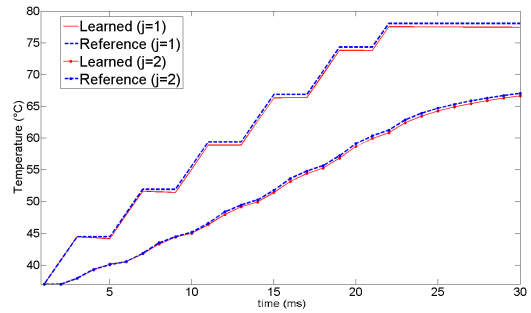

(b) Pulsed Laser Mode

Fig. 2. Temperature dynamics at the center of the tissue at the surface ($j = 1$), and at $z = 0.025$mm, ($j = 2$) for continuous/pulsed type of laser modes. Time response of the reference (blue) and learned (red) models are shown.

heat capacity (c). In pursuance of proving initial concepts in [11], [9], Eq.(1) was solved using Finite Differences (FD) approximation whereas a Monte Carlo approach was used to properly simulate the heat of rate generation (S).

The results presented in Fig. 2 demonstrated that a learned system can reproduce the dynamics of tissue temperature obtained through the solution of the partial differential equation presented in Eq. 1.

V. Conclusion

In this abstract, the concept of cognitive supervisory system for robotic laser surgery was discussed. The system is intended to supervise the laser-tissue interactions that occur during surgery. A model of tissue temperature during laser irradiation is at the core of the system. The model is inspired by the cognitive process that surgeons do when map visual information i.e., location of the laser spot, together with the history of laser actions, to the estimation of temperature in the tissue to avoid carbonization. This is, they decide what actions to do in order to avoid increasing the temperature of the tissue beyond 100°C.

Further investigation and developments are needed to bring the system into a real surgical scenario. Current efforts are focused on the validation of the temperature model. Also, a model able to predict the properties of laser incisions, in terms of depth and width, is being developed. These developments are supported through the collection of experimental data from real laser-tissue interaction.

VI. Acknowledgments

The research leading to these results has received funding from the European Union Seventh Framework Programme FP7/2007-2013 – Challenge 2 – Cognitive Systems, Interaction, Robotics – under grant agreement μRALP N°288233.

References

[1] D. Vernon, "Cognitive system," *Encyclopedia of Computer Vision.*, 2012. [Online]. Available: http://www.vernon.eu/publications/12_Vernon_Cognitive_System.pdf

[2] F. Rodriguez y Baena and B. Davies, "Robotic surgery: from autonomous systems to intelligent tools," *Robotica*, vol. 28, no. Special Issue 02, pp. 163–170, 2010.

[3] R. Satava, "Future directions in robotic surgery," in *Surgical Robotics*, J. Rosen, B. Hannaford, and R. M. Satava, Eds. Springer US, 2011, pp. 3–11.

[4] Cognitive surgical robotics - robotic surgepedia. [Online]. Available: http://rsp.inf.elte.hu/mediawiki/index.php/Cognitive_Surgical_Robotics

[5] L. Mattos, D. Caldwell, M. Dellepiane, and E. Grant, "Design and control of a robotic system for assistive laser phonomicrosurgery," in *Engineering in Medicine and Biology Society (EMBC), 2010 Annual International Conference of the IEEE*, 2010, pp. 5411–5415.

[6] W. Steiner and P. Ambrosch, *Endoscopic laser surgery of the upper aerodigestive tract: with special emphasis on cancer surgery*. Thieme, 2000.

[7] M. Niemz, *Laser-tissue Interactions*. Springer Berlin Heidelberg, 2003.

[8] D. Vernon, G. Metta, and G. Sandini, "A survey of artificial cognitive systems: Implications for the autonomous development of mental capabilities in computational agents," *Evolutionary Computation, IEEE Transactions on*, vol. 11, no. 2, pp. 151 –180, april 2007.

[9] L. Fichera, D. Pardo, and L. S. Mattos, "Modeling tissue temperature dynamics during laser exposure," in *Proceedings of the International Work Conference on Artificial Neural Networks (IWANN)*, 2013.

[10] J. J. Crochet, S. C. Gnyawali, Y. Chen, E. C. Lemley, L. V. Wang, and W. R. Chen, "Temperature distribution in selective laser-tissue," *Journal of Biomedical Optics*, vol. 11, no. 3, pp. 01–10, 2006.

[11] L. Fichera, D. Pardo, and L. S. Mattos, "Supervisory system for robot assisted laser phonomicrosurgery," in *Proceedings of the 35th International Conference of the IEEE Engineering in Medicine and Biology Society (EMBC)*, 2013.

Automated Surgical Task Execution: the Needle Insertion Case

Marcello Bonfè, Nicola Preda
Engineering Department
University of Ferrara, Italy
Emails: {marcello.bonfe, nicola.preda}@unife.it

Cristian Secchi, Federica Ferraguti
Department of Science and Methods for Engineering
University of Modena and Reggio Emilia, Italy
Emails: {cristian.secchi, federica.ferraguti}@unimore.it

Riccardo Muradore, Luisa Repele, Giovanni Lorenzi, Lorenza Gasperotti and Paolo Fiorini
Department of Computer Science
University of Verona, Italy
Emails: {riccardo.muradore, luisa.repele, giovanni.lorenzi, lorenza.gasperotti, paolo.fiorini}@univr.it

***Abstract*—The paper describes a robot control and coordination framework for the automation of surgical tasks. In the proposed framework, surgeons do not interact with robots by means of teleoperation, but they are supported by autonomous robotic assistants. Such robots perform basic surgical actions by combining sensing, dexterity and cognitive capabilities. The goal is achieved thanks to rigorous assessment of surgical requirements, formal specification of robotic system behavior, including multiple arm coordination and human/system interaction, and control software development with *state-of-the-art* component-based technologies. The paper presents an experimental setup composed of two robots operating on a US-compatible phantom, demonstrating the feasibility of the approach.**

I. Introduction

Minimally invasive surgery first and, more recently, surgical robots have brought new perspectives to surgery and have significantly improved the quality of many critical surgical tasks [1], [2]. In this paper we go further by designing an architecture to control a robotic system capable of autonomously executing US-guided insertion of needles into soft bodies, i.e. emulating the surgical procedure for percutaneous cryoablation of small tumoral masses. To validate the proposed software/hardware architecture we prepared an experimental setup, involving two robotic manipulators that autonomously perform the task: one robot holds the needle and moves according to a planned trajectory to perform the puncturing, while the other robot holds an US probe which images are used to intra-operatively guide and control the needle insertion, [3]. Even the pre-operative planning is performed automatically, by means of a software that implements the algorithm proposed in [4]. Since the architecture of the system is modular and component-based by design, the same methodology can be applied to automate other simple surgical tasks. In this way, the robotic system autonomously deals with the simplest tasks and the role of the surgeon becomes that of irreplaceable supervisor. Subsequently, the surgeon can focus his/her attention on the most critical parts of the procedure. In this paper we implement the model presented in [5], where the requirements for a software-intensive and intelligent surgical robots were collected and translated into engineering specifications.

II. Case Study and Robotic Setup

The final objective of the proposed research is to demonstrate the feasibility of robotic automation for some surgical procedures, which have been selected among those that would benefit mostly from the accuracy and repeatability levels achievable by intelligent robots. We focus on percutaneous cryoablation of small tumors, but the same methodology and design approach will be applied in a near future to automated suture of planar wounds. Percutaneous cryoablation requires the use of pre- and intraoperative images (CT, MRI/US) to insert, through the skin, one or more cryoprobe needles into the tumoral mass to be destroyed and to check the real-time position of the tools inside the patient. Trajectory misalignments are usually due to the deformation of soft tissues and organ displacement because of breathing. Thanks to real-time image registration and accurately calibrated mechanical arms, needle insertion will be executed precisely by the robots.

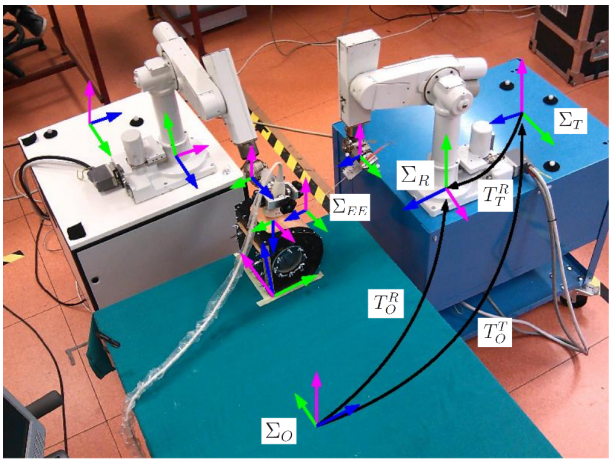

Fig. 1. Experimental setup with coordinate systems and related transformations.

To evaluate practical issues and benefits of cryoablation execution by means of automated robots, an experimental setup has been prepared, as shown in Figure 1. The setup includes two robotic manipulators: the first robot holds the needle, while the second holds the US probe. The end-effectors of both

robots are equipped with specific tool adapters that integrate 6-DOF force/torque sensor. The robots are mounted on two trolleys allowing to move them freely around the surgical bed, i.e. where the phantom replicating the human abdomen is located. Freely movable trolleys improve the setup flexibility, but, on the other hand, they require an accurate registration phase before starting the operation. For this reason an Optitrack system (NaturalPoint, Inc.) using 10 infrared cameras is used to estimate relative coordinate transformations among the robots and the phantom.

III. Control and Supervision Architecture

The autonomous system being designed in this project is composed of the following modules, corresponding also to software units deployed on different computational platforms: a *Surgical Interface*, the *Robot Controllers* and the *Sensing* system with *Reasoning and Situation Awareness* capabilities. Figure 2 shows the overall control and supervisor architecture.

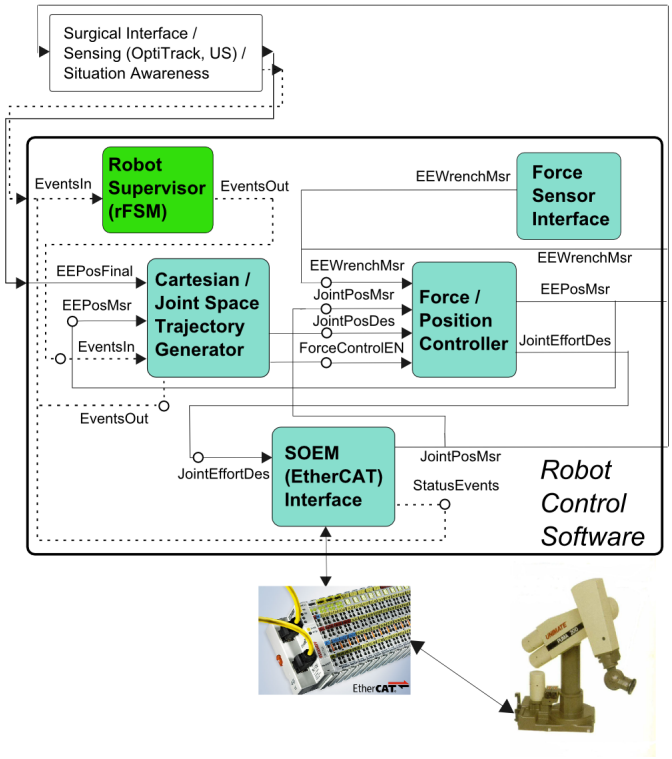

Fig. 2. Control software implementation of the robot holding US probe

In particular, the Surgical Interface is a software-intensive system allowing humans (i.e. surgeons and technicians) to drive the system during both the pre-operative and the intra-operative phase. In the first one, the focus is on detailed planning of the surgical intervention (e.g. enumeration and placement of cryoablation needles for maximal tumor coverage thans to the *cryo-planner* described in [4]). During operations, the interface should provide real-time visual navigation of the surgical scenario and, if necessary, let surgeons take control of the system (e.g. by switching to teleoperated mode).

The Robot Controllers are the units implementing control of surgical actions and tasks sequencing during the intraoperative phase. The event-driven behavior extracted from the goal model is mapped into the control logic of each robot, specified by an UML State Diagram. Safety-critical requirements put a strong demand for strict coordination of these components with both the Surgical Interface and the Sensing/Reasoning module.

Finally, the composite sub-system implementing advanced Sensing algorithms and Reasoning for Situation Awareness provides support to the planning task, during the preoperative phase, and prompt identification of anatomical changes or discrepancy between the tasks being executed and the *nominal* surgical plan. In the latter case, Situation Awareness algorithms (e.g. based on Bayesian Networks and Particle Filters) must signal the occurrence of undesired events and critical situations, so that appropriate corrective actions can be triggered. It is important to remark that even though the Reasoning and Situation Awareness module is not fully implemented in the current setup, both the behavioral specification described in the rest of the section and the distributed architecture presented above are prepared to seamlessly embed it.

The interaction among such system components has been specified with the help UML Sequence Diagrams, which represents scenarios compatible with a given collaborative behavioral specification. An UML Sequence Diagram shows a sequence of events, exchanged among a number of *object lifelines*, implicitly ordered in time from top to bottom. As an example, Figure 3 shows an admissible scenario for the cryoablation execution, focused on needle insertion under US-based monitoring. The scenario includes the adaptation required if the algorithm for needle tip detection fails to evaluate the presence of the needle in the current US image. In this case, the motion of the robot holding the needle is paused and the robot holding the US probe executes a sequence of slow rotations of its end-effector along the three orientation axes (roll, pitch and yaw). If the needle is found during these movements and the insertion can be completed with a small adaptation of motion trajectories, the surgical operation proceeds, otherwise the needle is extracted and the insertion trajectory is replanned.

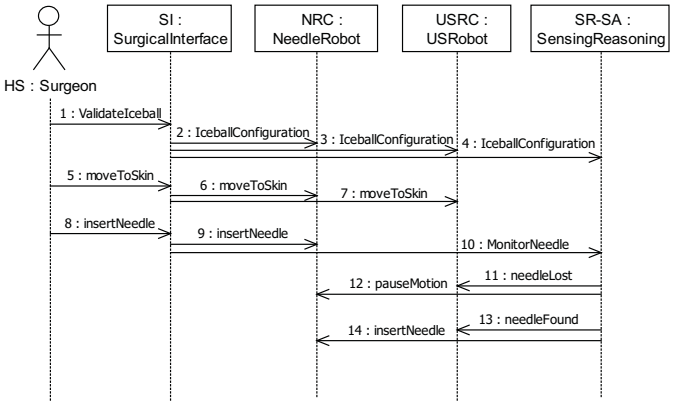

Fig. 3. UML Sequence Diagram of the interaction among system components during cryoprobe needle insertion: scenario in which the US image processing module fails to detect the needle position

IV. Results

In this section the time series of forces and the states of the robots control logic recorded during the experimental phase are reported (see Figures 4 and 5). The proposed experimental setup goes through the following steps triggered by the surgeon through the user interface:

1) The surgeon pushes the Ready button. Both robots move from their nest position to the ready position where the needle and the US probe are mounted.
2) The surgeon pushes the Start button. The robots receive their nominal trajectories and move the needle and the US probe in contact with the phantom.
3) When the surgeon pushes the InsertNeedle button, the robot holding the needle starts the insertion until it reached the target point. In this case the state of its control logic is WaitCryoCycle. However if the surgeon decides to stop the procedure (Stop button) because the needle is not visible in the US image any more, the robot holding the needle performs a sequence of movements of the US probe to bring the needle back on the US images.
4) Since the cryoablation is not available in the current setup, the final step is for the surgeon to push the button Finish to bring the robots back in the Ready state.

Figure 5 shows the force measured by the F/T sensor located on the robot holding the needle along the main axis of the needle. The dashed vertical lines and the numbers help to understand which states of the control logic (Figure 4) are activated.

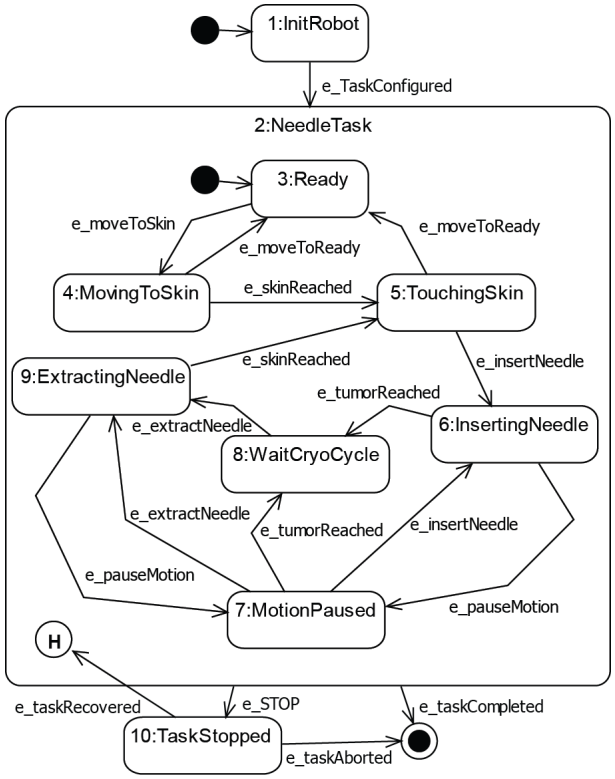

Fig. 4. UML State Diagram of robot control logic for needle insertion in a cryoablation task.

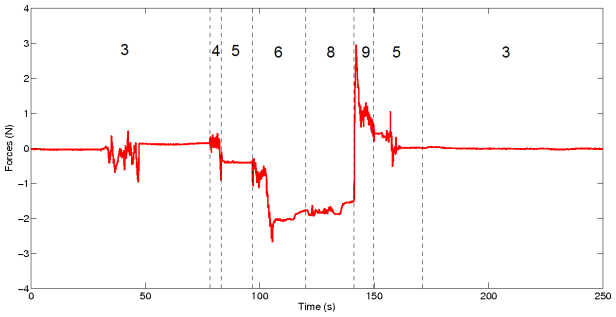

Fig. 5. Force applied to the needle during the emulated cryoblation task.

V. Conclusion

In this paper we presented a robot control and coordination framework for the automation of simple surgical tasks. We formalized the design specifications using a requirements engineering approach and derived the state machines for the control of the robots involved in the operation. Then, we implemented the proposed architecture using component-based design tools, i.e. Orocos framework and rFSM, in order to handle properly the distributed nature of our system.

The goal of these experiments was to show that the technology to execute autonomously basic surgical tasks is available and could be used to improve accuracy. To better reach this critical objectives, a Situation Awareness module that takes care of the uncertainty and manages unexpected events has been implemented on top of the control architecture.

Acknowledgment

The research leading to these results has received funding from the European Union Seventh Framework Programme FP7/2007-2013 under grant agreement n. 270396 (I-SUR).

References

[1] G. H. Ballantyne, "Robotic surgery, telerobotic surgery, telepresence, and telementoring," *Surgical Endoscopy And Other Interventional Techniques*, vol. 16, no. 10, pp. 1389–1402, 2002.

[2] J. Rosen, B. Hannaford, and R. Satava, Eds., *Surgical Robotics: Systems Applications and Visions*. Springer, 2011.

[3] K. Mathiassen, D. Dall'Alba, R. Muradore, P. Fiorini, and O. J. Elle, "Real-time biopsy needle tip estimation in 2D ultrasound images," in *Proceedings of the International Conference on Robotics and Automation (ICRA)*, Karlsruhe, Germany, May 2013.

[4] M. Torricelli, F. Ferraguti, and C. Secchi, "An algorithm for planning the number and the pose of the iceballs in cryoablation," in *Proceedings of the International Conference of the IEEE Engineering in Medicine and Biology Society (EMBC)*, Osaka, Japan, July 2013, submitted.

[5] M. Bonfe, F. Boriero, R. Dodi, P. Fiorini, A. Morandi, R. Muradore, L. Pasquale, A. Sanna, and C. Secchi, "Towards automated surgical robotics: A requirements engineering approach," in *Proceedings of the IEEE RAS & EMBS International Conference on Biomedical Robotics and Biomechatronics (BioRob)*, 2012, pp. 56–61.

this page was intentionally left blank